

DTIC FILE COPY

(Q)

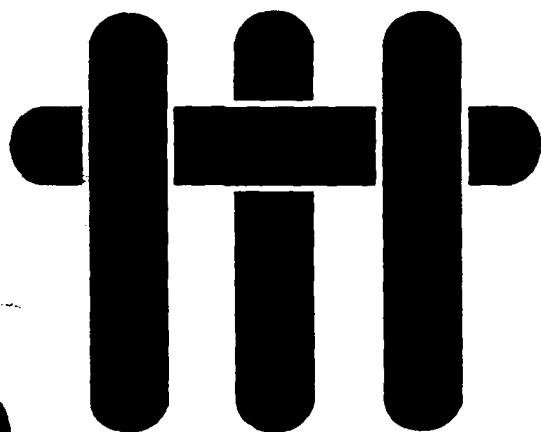
MATERIALS

AD-A223 273

C

TIC
ECTE
18 1990

D



FINAL REPORT

C5
D

to the

DEFENSE ADVANCED RESEARCH
PROJECTS AGENCY

and the

OFFICE OF NAVAL RESEARCH

CONTRACT NO. N00014-86-K-0178

TITLE: High Performance Brittle Matrices and Brittle Matrix
Composites

PERFORMING ORGANIZATION: UC Santa Barbara Materials
Department

PRINCIPAL INVESTIGATORS: A.G. Evans and R. Mehrabian

CONTRACT PERIOD: March 15, 1986 through September 30, 1989

DISTRIBUTION STATEMENT A

Approved for public release
Distribution Unlimited

BOOK 1 OF 2

90 06 14 183

REPORT DOCUMENTATION PAGE

1a. REPORT SECURITY CLASSIFICATION <u>Unclassified</u>		1b. RESTRICTIVE MARKINGS													
2a. SECURITY CLASSIFICATION AUTHORITY		3. DISTRIBUTION/AVAILABILITY OF REPORT <i>See distribution list</i>													
2b. DECLASSIFICATION/DOWNGRADING SCHEDULE															
4. PERFORMING ORGANIZATION REPORT NUMBER(S)		5. MONITORING ORGANIZATION REPORT NUMBER(S)													
6a. NAME OF PERFORMING ORGANIZATION The University of California Materials Department	6b. OFFICE SYMBOL (if applicable)	7a. NAME OF MONITORING ORGANIZATION Office of Naval Research													
6c ADDRESS (City, State, and ZIP Code) College of Engineering University of California Santa Barbara, CA 93106		7b. ADDRESS (City, State, and ZIP Code) 800 North Quincy Street Arlington, VA 22217													
8a. NAME OF FUNDING/SPONSORING ORGANIZATION DARPA/Office of Naval Research	8b. OFFICE SYMBOL (if applicable)	9. PROCUREMENT INSTRUMENT IDENTIFICATION NUMBER N00014-86-K-0178													
8c. ADDRESS (City, State, and ZIP Code) 1400 Wilson Blvd. Arlington, VA 22209		10. SOURCE OF FUNDING NUMBERS PROGRAM ELEMENT NO. PROJECT NO. TASK NO. WORK UNIT ACCESSION NO.													
11. TITLE (Include Security Classification) High Performance Brittle Matrices and Brittle Matrix Composites															
12. PERSONAL AUTHOR(S) Anthony G. Evans and Robert Mehrabian															
13a. TYPE OF REPORT Final Report	13b. TIME COVERED FROM 9/15/86 TO 9/30/89	14. DATE OF REPORT (Year, Month, Day) 12/31/89	15. PAGE COUNT 406												
16. SUPPLEMENTARY NOTATION															
17. COSATI CODES <table border="1"><tr><th>FIELD</th><th>GROUP</th><th>SUB-GROUP</th></tr><tr><td></td><td></td><td></td></tr><tr><td></td><td></td><td></td></tr><tr><td></td><td></td><td></td></tr></table>		FIELD	GROUP	SUB-GROUP										18. SUBJECT TERMS (Continue on reverse if necessary and identify by block number) Phase diagrams, solidification, composites, toughening residual stress. <i>AE</i>	
FIELD	GROUP	SUB-GROUP													
19. ABSTRACT (Continue on reverse if necessary and identify by block number) The primary intent of this research was the development of composites having an acceptable combination of toughness and oxidation resistance. The research was closely coordinated with the DARPA/ONR URI program at UCSB concerned with high temperature, high performance composites. The study comprised three tasks. The first task was to study phase equilibria, solidification pathways and toughness properties of intermetallics, such as oxidation resistant Ti-Al-Ta and Nb-Al-Si alloys, and ceramics. These studies were then combined with interface interaction studies between the matrix microstructure and ductilizing/toughening particulates and fibers. The second task was a basic study of interface structure and chemistry as it relates to the mechanical properties of the interface. The third task involved studies on aluminum and copper matrix composites. These studies were concerned with developing an understanding of creep resistance.															
20. DISTRIBUTION/AVAILABILITY OF ABSTRACT <input checked="" type="checkbox"/> UNCLASSIFIED/UNLIMITED <input type="checkbox"/> SAME AS RPT. <input type="checkbox"/> DTIC USERS		21. ABSTRACT SECURITY CLASSIFICATION Unclassified													
22a. NAME OF RESPONSIBLE INDIVIDUAL Robert Mehrabian		22b. TELEPHONE (Include Area Code) (805) 961-3141	22c. OFFICE SYMBOL												

TABLE OF CONTENTS

Book 1

- | | |
|---|---|
| 1. The High Temperature α Field in the Titanium-Aluminum Phase Diagram | C. McCullough
J.J. Valencia
H. Mateos
C.G. Levi
R. Mehrabian |
| 2. Solidification of Supercooled Intermetallic Powders | C.G. Levi
J.J. Valencia
R. Mehrabian |
| 3. Microstructure Evolution in TiAl Alloys with B Additions: Conventional Solidification | M.E. Hyman
C. McCullough
J.J. Valencia
C.G. Levi
R. Mehrabian |
| 4. Microstructural Development and Mechanical Properties of Cu-Al In Situ Formed Composites | M.L. Borg
J.J. Valencia
C.G. Levi |
| 5. Containerless Processing of Niobium-Based Alloys | K.R. Javed
G.J. Abbaschian |
| 6. Formation and Decomposition of Metastable B2 Phase in Ta-Ti-Al Alloys | Y.S. Kim
K.R. Javed
G.J. Abbaschian |
| 7. Effects of Interfaces on the Design and Oxidation Resistance of High Performance Composites: Processing Pathways-Phase Equilibria and Interdiffusion Reactions | J.H. Perepezko
J.C. Lin
T.J. Jewett
Y.A. Chang |
| 8. Combined Mode I - Mode III Fracture Toughness of Alumina Particulate-Reinforced Aluminum Alloy-Matrix Composites | S.V. Kamat
J.P. Hirth
R. Mehrabian |

STATEMENT "A" per Dr. S. Fishman
ONR/Code 1131
TELECON

6/18/90

VG

For	
RA&I	<input checked="" type="checkbox"/>
AB	<input type="checkbox"/>
ced	<input type="checkbox"/>
RI	
Per Call	
Distribution /	
Availability Codes	
Dist	Aveil and/or Special
A-1	

TABLE OF CONTENTS

Book 2

9.	The Processing and Mechanical Behavior of an Aluminum Matrix Composite Reinforced with Short Fibers	Y.L. Klipfel M.Y. He R.M. McMeeking A.G. Evans R. Mehrabian
10.	Brittle-to-Ductile Transition in Silicon Carbide	G.H. Campbell B.J. Dagleish A.G. Evans
11.	Whisker Toughening: A Comparison Between Al_2O_3 and Si_3N_4 Toughened with SiC	G.H. Campbell M. Rühle B.J. Dagleish A.G. Evans
12.	Finite Cracks in Transformation-Toughened Ceramics	D.M. Stump B. Budiansky
13.	On Toughening by Microcracks	D.K.M. Shum J.W. Hutchinson
14.	Fundamental Solutions for Microcracking Induced by Residual Stress	D.K.M. Shum Y.Y. Huang
15.	Phase Diagram and Solidification Models for the Nb-Al-Si System	D.J. Tilly T. Lu A. Paul R. Mehrabian

SUMMARY

Lightweight intermetallics and ceramics have attractive high temperature properties but are mostly brittle and may be subject to oxidation. The primary intent of this research was the development of such materials having an acceptable combination of toughness and oxidation resistance. The research was closely coordinated with the DARPA/ONR URI program at UCSB concerned with high temperature, high performance composites.

The study comprised three tasks. The first task was to study phase equilibria, solidification pathways and toughness properties of intermetallics, such as oxidation resistant Ti-Al-Ta and Nb-Al-Si alloys, and ceramics. These studies were then combined with interface interaction studies between the matrix microstructure and ductilizing/toughening particulates and fibers. The second task was a basic study of interface structure and chemistry as it relates to the mechanical properties of the interface.

The third task involved studies on aluminum and copper matrix composites. These studies were concerned with the understanding of creep resistance. The aluminum matrix composites were prepared by a new process developed in this contract for direct infiltration of fibers and particulates by liquid aluminum alloys. Uniform fiber/particulate distributions were obtained and related to interface interactions and mechanical properties. The latter involved consideration of the separate and the coupled effects of dispersoids and reinforcements on creep and flow strength.

1. Phase Equilibria and Solidification Pathways in Intermetallics

A major portion of the 1100°C isothermal section of the Ti-Al-Ta phase diagram has been determined based on experimental work on annealed bulk alloys and diffusion couples. Significant inconsistencies were found with previously reported diagrams for the same system. It was established that the η phase field, which terminates at the line compounds $TaAl_3$ and $TiAl_3$ on the binaries, exhibits hyperstoichiometric solubility of Ta and Ti in the ternary system, in agreement with similar findings on the Ti-Al-Nb system. It was also found that the σ and γ phases exhibit substantial ternary solubility. Furthermore, a ternary phase with composition near Ti_2TaAl was reported, but its phase boundaries and relationship with the other fields in the ternary system remains to be clarified.

Diffusion couple studies performed in the course of evaluating the phase diagram were also useful in determining the interdiffusion coefficients of Ta and Al in the β phase. This information has been used for the studies on phase stabilities and interface interactions with reinforcing phases within other DARPA sponsored programs.

Ti-Al-Ta alloys were also subjected to rapid solidification processing using an electromagnetic-levitation/splat-cooling technique. Rapid solidification of Ti-36Al-38Ta, Ti-34Al-39Ta and Ti-44Al-4Cr-29Ta melts resulted in the formation of a metastable ordered B2 phase, which converted to the stable σ and γ phases upon annealing at high temperature. On the other hand, no metastable phase was formed in a Ti-46Al-29Ta alloy.

Work on Nb-Al-Si alloys was motivated by a recent finding that under appropriated processing conditions certain alloys in this ternary system form adherent protective oxides at high temperatures enhancing oxidation

resistance. Furthermore, the solidification microstructures affect this oxidation behavior profoundly, especially since low diffusion rates inhibit homogenization of the as-cast structures at temperatures and times of practical utility. A comprehensive program was thus carried out to first evaluate the equilibrium phase diagram of the system and compare same with experimental data in this program. Second, a ternary alloy solidification model was combined with the phase diagram information to predict the solidification "path" of a number of alloys in the $\text{Nb}_5(\text{Si}, \text{Al})_3$ composition range. In a corollary experimental study, arc-buttons of the alloys were cast and the as-solidified structures characterized by analytical electron microscopy and high temperature X-ray diffractometry. Microsegregation profiles, volume fraction and distribution of the various phases were determined and compared to the calculations. Good agreement was obtained between theory and experiment.

In a related study the niobium-based alloys Nb-7.2Al-59.7Si, Nb-35Al-27Ti and Nb-20Ti-21.3Si were supercooled and splat quenched using the levitation-splat cooling technique. The Nb-35Al-27Ti alloy formed an ordered B2 phase upon rapid solidification, while the formation of the brittle $(\text{NbTi})_5\text{Si}_3$ phase was suppressed upon supercooling of the Nb-20Ti-21.3Si alloy.

2. Matrix Toughening

Process zone and bridging zone mechanisms of matrix toughening have been studied. In particular, short crack effects that arise with process zone toughening have been calculated. These calculations reveal that interaction effects occur between process zones at the two crack tips leading to a reduction in the magnitude of the fracture resistance. The results also

indicate that the strength does not scale simply with the toughness. These solutions thus have important implications for the combined optimization of strength and toughness.

A related investigation of ceramics toughened with whiskers has established both the prevalent contributions to toughness, as well as the realistic toughening potential. The two principal toughening contributions derive from the extra surface energy associated with debonding along the amorphous phase at the interface and energy dissipated as acoustic waves when the whiskers fail in the crack wake. These contributions can lead to toughness of order $K_c \approx 10 \text{ MPa}\sqrt{\text{m}}$. Much larger toughness values could be induced by encouraging frictional dissipation by sliding and pull-out along debonded interfaces.

3. Creep Strengthening

The effects on flow and creep of high aspect ratio reinforcements have been explored by conducting experiments on an Al/Mg alloy reinforced with chopped Al_2O_3 fibers (20% by volume). These experiments have been coupled with plane strain calculations of steady-state flow using incremental plasticity. The reinforcements have been shown to lead to an anisotropy of flow strength between tension and compression, caused by damage in the form of multiple cracks in the fibers. The strengthening in compression (no damage) is substantial and apparently consistent with that predicted by plasticity calculations. The important role of high aspect ratio is thus confirmed. This material also has good toughness and ductility (~6%) because of the high ductility of the matrix alloy, but fracture models have yet to be produced.

A related study concerns processing routes for oxide-dispersion strengthened copper alloys. The oxides of Y, Zr and the rare earths offer alternatives to the conventional $\gamma\text{-Al}_2\text{O}_3$ dispersoids used in ODS copper. These oxides have flourite-related structures and exhibit interfacial characteristics that should lead to an improved ability to pin dislocations. However, these dispersions cannot be produced by conventional internal oxidation, since the alloying elements are not soluble in Cu matrix, but instead precipitate as intermetallic compounds. On the other hand, the intermetallics are much less stable than the corresponding oxides and readily react with the inward-diffusing oxygen releasing Cu and precipitating the oxide. The extent of the reaction and the fineness of the oxide dispersion depends on the intial scale and distribution of the intermetallic, which can be optimized by rapid solidification processing. To explore this opportunity, powders of a Cu-2wt%Y alloy were produced by ultrasonic gas atomization at the National Institute for Standards and Technology, giving segregate spacings on the order of 1 to 2 μm . Y_2O_3 dispersoids on the order of 20nm and ~3 percent in volume fraction were subsequently produced by internal oxidation.

THE HIGH TEMPERATURE α FIELD IN THE
TITANIUM-ALUMINUM PHASE DIAGRAM

C. McCullough, J.J. Valencia, H. Mateos, C.G. Levi, R. Mehrabian
Materials Department, College of Engineering
University of California, Santa Barbara, CA 93106

and K. A. Rhyne
Defense Advanced Research Projects Agency
Arlington, VA 22209

Introduction

Previous investigations of microstructure evolution during solidification of a Ti-50at%Al alloy [1,2] revealed a major disagreement between experimental observations and the recently evaluated version of the Ti-Al phase diagram, Figure 1 [3,4]. While the latter predicts the formation of β (A2) dendrites surrounded by peritectic γ (L1₀) segregate, the experimental evidence strongly indicates that the primary phase is α (A3), i.e. the solid solution based on the hexagonal close packed structure of Ti. Elucidation of the actual solidification path has been an elusive subject as the solid state transformation of either primary phase can in principle result in the α_2 (D0₁₉) + γ lath microconstituent observed in practice, as suggested by Blackburn's experiments on the Ti-33at%Al composition [5].

Primary α formation was first reported by Graves et al [6] in rapidly solidified Ti-Al powders of near equiatomic composition, and was originally ascribed to metastable phase selection resulting from supercooling of the liquid droplets. This hypothesis was supported by the cross-over of the calculated T_0 curves for the α , β and γ phases in the vicinity of 50at%Al, suggesting that metastable α would be competitive with the stable β at relatively modest supercoolings (50-100 K). However, dendrites with hexagonal symmetry were shortly thereafter detected in shrinkage cavities of arc melted buttons [2], e.g. Figure 2, and even ingots as large as 15 kg [7]. Since supercoolings achievable in arc-buttons and ingots are anticipated to be small, the evidence suggested that α may be the stable crystal form in equilibrium with the liquid at the Ti-50at%Al composition.

A two-pronged investigation was undertaken to clarify whether this region of the phase diagram needed revision. The approach involved both high temperature X-ray diffraction of homogenized Ti-50at%Al samples and containerless solidification of the same composition at relatively slow growth rates in order to approach equilibrium.

Alloy Preparation

High purity Ti-50at%Al buttons (<270 ppm O₂) produced by TiMet were cut and remelted in an arc furnace under gettered argon containing less than 0.1 ppb of O₂. Bars 5 and 10 cm long, with a cross section of approximately 1 cm² and oxygen contents of the order of 400 ppm were produced in this manner. The shorter buttons were homogenized for 24 hours at 1270 K in a resistance furnace under gettered argon (<0.1 ppb O₂) at ~50 kPa (0.5 atm). These were then cut into thin slices which were subsequently ground to 300 - 400 μm thickness, electropolished to remove the deformed surface layers and cleaned to minimize any traces of hydride film in the manner described by Hu and Cline [8]. These specimens were used for the X-ray diffraction work and had a typical oxygen content of ~700 ppm O₂. The 10 cm bars were homogenized in situ using a low power level of the arc, cut into 6 mm diameter rods by electro-discharge machining and subsequently ground and ultrasonically cleaned for use in the containerless solidification experiments.

High Temperature X-Ray Diffraction

A Scintag PAD-10 diffractometer fitted with a high temperature stage modified to work under vacuum or inert-gas atmospheres was used for the X-ray work. The diffractometer was operated in the θ - θ mode while the specimen remained stationary on a Ta strip, supported in the chamber by water cooled rods. The sample was heated up both by Ta heating elements surrounding the stage and by resistance heating of the Ta strip on which it rested. The temperature was monitored by a small thermocouple welded onto the sample surface.

Prior to the experiment the furnace was degassed by evacuating and heating up to 1750 K with a pure Ti specimen placed on the stage. The system was considered satisfactory when a pressure of 8 μ torr was maintained at the maximum temperature. The Ti-50at%Al specimen was then positioned in the furnace which was repeatedly evacuated and flushed with gettered argon to ensure an oxygen free environment. The experiment itself was conducted in stagnant gettered argon, close to atmospheric pressure, \sim 0.1 MPa. This approach minimized Al losses while still allowing for sufficient transmission of X-ray intensity to obtain a well-resolved spectrum (Ar appears to be an efficient scattering medium for the incident X-rays).

The specimen was heated following the schedule shown in Figure 3. After reaching each prescribed temperature the specimen was thermally equilibrated for \sim 10 minutes and the X-ray spectrum was subsequently acquired for \sim 5 minutes. Given the thin dimension of the specimen and the fact that most of the signal comes from a surface layer, it was felt that the hold time was sufficient to equilibrate the microstructure, particularly with regard to the $\alpha \leftrightarrow \gamma$ transformation which appears to be relatively fast. The changes in the spectrum at selected temperatures are depicted in Figure 4.

All the peaks in the room temperature spectrum were consistently indexed to the L1₀ structure, indicating that the starting material was single phase γ . This was confirmed by the metallographic examination of the homogenized button, Figure 5(a), which contains relatively large γ grains (200-300 μ m), some of them twinned, but no evidence of a second phase. It should be noted that the coarse-grain structure combined with the relatively small sampling area frequently results in a spectrum different from the one expected for a random polycrystalline specimen. For example, the unusually large $\{111\}_{\gamma}$ peak at about 39° in Figure 4 suggests a strong texture along these planes.

Heating up to 1373 K produced no major changes in the equilibrium configuration--only γ was detected in the spectrum. The first noticeable change occurred at 1623 K, when a small $\{0111\}_{\alpha}$ peak appeared near $2\theta = 40^\circ$ indicating the presence of the hexagonal α phase. The phase has been indexed as α instead of α_2 since the α_2/α transus temperature has been reasonably well established at \sim 1400 K [3]. Note also that the $\{111\}_{\gamma}$ peak remained quite strong, suggesting that the system was in a two-phase ($\alpha + \gamma$) field but still near the boundary of the single phase γ . Increasing the temperature to 1673 K led to a major loss of intensity in the $\{111\}_{\gamma}$ peak and the disappearance of most of the weaker γ peaks. The α peaks became stronger and more numerous, clearly indicating that the system was well within the ($\alpha + \gamma$) field at this temperature. Further heating to 1723 K resulted in the elimination of all the γ peaks within the spectrum, indicating that the system had moved into a single phase α region. The strong increase in intensity of the $\{0111\}_{\alpha}$ peak accompanied by the disappearance of some of the weaker peaks, e.g. $\{01\bar{1}0\}_{\alpha}$, $\{1\bar{1}\bar{2}0\}_{\alpha}$ and $\{1013\}_{\alpha}$ at 36°, 63° and 71°, respectively, suggest the development of a texture due to preferential growth of the $\{0111\}_{\alpha}$ orientations at high temperatures. The heating was terminated at 1723 K to avoid melting the specimen.

Upon cooling to 1273 K the γ phase peaks reappeared but, contrary to the observations made during heating, a small hexagonal peak at \sim 36° still remained in the spectrum (not shown in Figure 4). This peak has been indexed to the $\{02\bar{2}0\}$ plane of the α_2 phase, since the temperature is below the α/α_2 transus. The $\{02\bar{2}0\}_{\alpha_2}$ peak was observed even after cooling to room temperature and was associated with a small aluminum loss during the experiment. The composition of the specimen determined by EDS was 48.3to.9 at%Al and the microstructure of the sample, shown in Figure 5(b), contained the typical ($\alpha_2 + \gamma$) lath structure characteristic of the decomposition of α . It was thus concluded that the change in composition during the experiment moved the alloy from the single phase γ to the ($\alpha_2 + \gamma$) field in the phase diagram.

Containerless Solidification Experiments

Solidification of Ti-50at%Al rods at controlled rates was carried out using a floating-zone approach in gettered argon at pressures slightly over atmospheric, \sim 0.1 MPa. The rod specimen was held at both ends by a rigid frame and moved through a stationary induction coil fitted with

a concentrator plate in order to localize the heating in a small segment (~ 1 cm). In this configuration, the molten zone bridges the two solid halves of the specimen and is held by surface tension. Higher temperature gradients were introduced to maintain a stationary molten zone by cooling the lower interface with jets of gettered argon (<0.1 ppb O₂). The solidification rate could then be related to the velocity of the moving rod, which was precisely controlled by an Instron 1122 crosshead drive. Lengths varying from 1 - 2 cm were solidified at rates ranging from 17 to 830 $\mu\text{m/s}$ (1 - 50 mm/min). Longitudinal and transverse metallographic sections of these samples were prepared for optical and SEM examination.

At the lower solidification rates (17 - 33 $\mu\text{m/s}$) the solidification structure is largely homogenized in-situ as evidenced by the absence of segregate (γ), Figure 6(a). The microstructure consists of large columnar grains containing the typical $\alpha_2 + \gamma$ transformation product with a lath spacing of ~ 1 μm . Increasing the solidification rate to 83 $\mu\text{m/s}$ yields a cell-like structure presumably arising from extensive coarsening of the dendrites, Figure 6(b). About 6 vol% of segregate with spacings of the order of 100 μm is retained in the microstructure, clearly delineating the transformed primary phase. The average compositions of the dendrites and segregate measured by EDX were 49 and 54 at%Al, respectively.

Increasing the rod velocity above 83 $\mu\text{m/s}$ causes a loss of directional growth observed at lower velocities, suggesting the development of growth centers in the liquid ahead of the interface. On the other hand, the dendritic structure is now retained and the volume fraction of segregate increases to $\sim 12\%$ as the time available for coarsening and homogenization is reduced. However, the composition of the constituents is not significantly different, even at the highest velocity where the dendrites and segregate had aluminum contents of 48 and 55 at%, respectively.

Figure 6 also shows examples of dendrites clearly revealing the hexagonal growth symmetry in zones where the rod velocity was 330 and 830 $\mu\text{m/s}$. While Figure 6(d) shows equiaxed growth, the dendrite in 6(c) grew with a primary stem along a $\langle 10\bar{1}0 \rangle_\alpha$ direction and the secondary arms along two of the other $\langle 10\bar{1}0 \rangle_\alpha$ directions at 60° from the main axis. This is different from the dendrite shown in the shrinkage cavity of an arc-button, Figure 2, where the primary stem grows along the $[0001]_\alpha$ direction and the secondary arms are perpendicular to the main axis. Note also that the secondary spacing is 40-50 μm in Figure 6(c), while that in Figure 2 is 20-25 μm , suggesting that even the higher solidification rates in the floating-zone approach are significantly slower than those characteristic of the arc-buttons and any potential supercooling effects would consequently be diminished.

Discussion

The results of this investigation strongly support the hypothesis that the crystalline form in equilibrium with a liquid TiAl alloy of equiatomic composition is a disordered solid solution based on the A3 crystal structure of α -Ti. It is believed that the high temperature X-ray diffraction experiments represent conditions fairly close to equilibrium while minimizing oxygen contamination. The equiatomic alloy was shown to be single phase γ between 300 and ~ 1623 K and single phase α at 1723 K and above, with a two phase $\alpha + \gamma$ field between ~ 1623 and ~ 1723 K. Further, no evidence of β was detected at high temperature, in spite of the small aluminum loss during the analysis. X-ray diffraction of alloys with a leaner Al content, to be reported in a separate publication, confirm that β is indeed present at high temperatures at compositions as high as 46 at%Al. Thus, the technique is reliable to detect both α and β at high temperatures.

Even though the X-ray experiments did not go up to the solidus temperature (estimated ~ 1753 K), the solidification experiments also indicate that the primary phase evolving from the liquid is α . Since local equilibrium is anticipated at the liquid solid interface and bulk liquid supercooling is unlikely in these experiments, it is concluded that the phase in equilibrium with the liquid is α and not β , contrary to the indications of the current phase diagram.

In light of these findings and those of our previous paper [1], it is evident that the phase diagram needs to be revised to include a high temperature α field in equilibrium with the liquid phase. Thus, the α/β transus field is likely to terminate at a peritectic reaction, $L + \beta \rightarrow \alpha$, rather than the peritectoid $\beta + \gamma \rightarrow \alpha$ indicated by the published phase diagram. In addition, the associated $\alpha + \gamma$ field does not terminate at the peritectoid, but rather at a second peritectic $L + \alpha \rightarrow \gamma$. The suggested changes are schematically illustrated in Figure 1 and are consistent in principle with the earlier diagram proposed by Willey and Margolin [9]. It should be noted, however, that the earlier version identified the high temperature hexagonal phase as α_2 (D₁₉).

Conclusions

Evidence from high temperature X-ray diffraction and solidification experiments has definitely established that the phase in equilibrium with a liquid Ti-50at%Al alloy is the hexagonal close packed solid solution based on the structure of α -Ti, rather than the body centered cubic form indicated by the existing phase diagram. The latter must then be revised to include a high temperature α field and probably a second peritectic reaction $L + \alpha \rightarrow \gamma$.

Acknowledgements

The authors would like to thank Prof. Galen Stucky and Dr. Michael Eddy for their help in the conduct of the X-ray experiments. The support of the Defense Advanced Research Projects Agency (DARPA) through grants URI-N00014-86-K-0753 and N00014-86-K-0178, supervised by Dr. P.A. Parrish and monitored by Dr. S.G. Fishman of the Office of Naval Research, is gratefully acknowledged.

References

1. J.J. Valencia, C. McCullough, C.G. Levi and R. Mehrabian, *Scripta Metall.*, 21, 1341 (1987).
2. C.G. Levi, J.J. Valencia and R. Mehrabian, in *Processing of Structural Metals by Rapid Solidification*, eds. F.H. Froes and S.J. Savage, ASM, Metals Park, OH, (1987).
3. J.L. Murray, in *Binary Alloy Phase Diagrams*, ed. T.B. Massalski, ASM, Metals Park, OH, (1986), p. 173.
4. J.L. Murray, *Metall. Trans. A*, 19A, 243 (1988).
5. M.J. Blackburn, in *The Science, Technology and Application of Titanium*, eds. R.I. Jaffee and N.E. Promisel, Pergamon Press, London (1970), p. 633.
6. J.A. Graves et al, *Scripta Metall.*, 21, 567 (1987).
7. W.J. Boettigner, private communication.
8. H. Hu and R.S. Cline, *Trans. AIME*, 242, 1013 (1968).
9. L.A. Willey and H. Margolin, in *Metals Handbook*, 8th ed., v. 8, ASM, Metals Park, OH, (1973), p. 264.

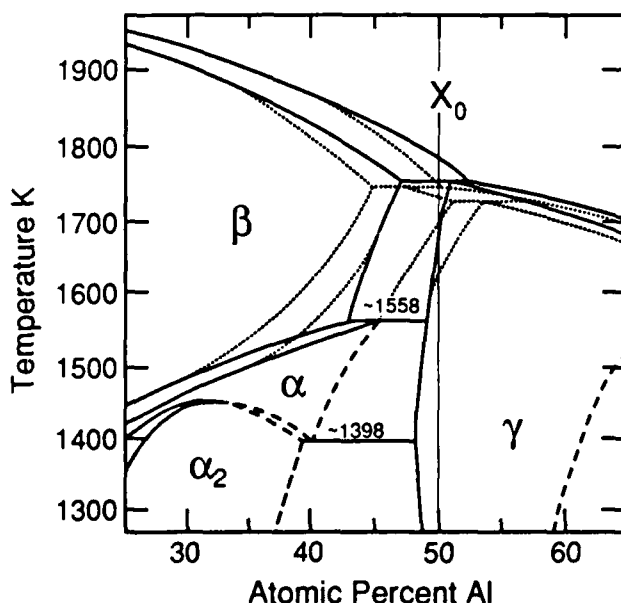


FIG. 1. Section of the Ti-Al phase diagram under investigation. The solid lines correspond to the current version [3] while the dotted lines follow an earlier diagram [9] which is more consistent with our results.



FIG. 2. Hexagonal dendrite in the shrinkage cavity of a Ti-50at%Al alloy arc-melted button. Note the striations along the basal plane arising from the solid state transformation of α into the $\alpha_2 + \gamma$ lath microconstituent.

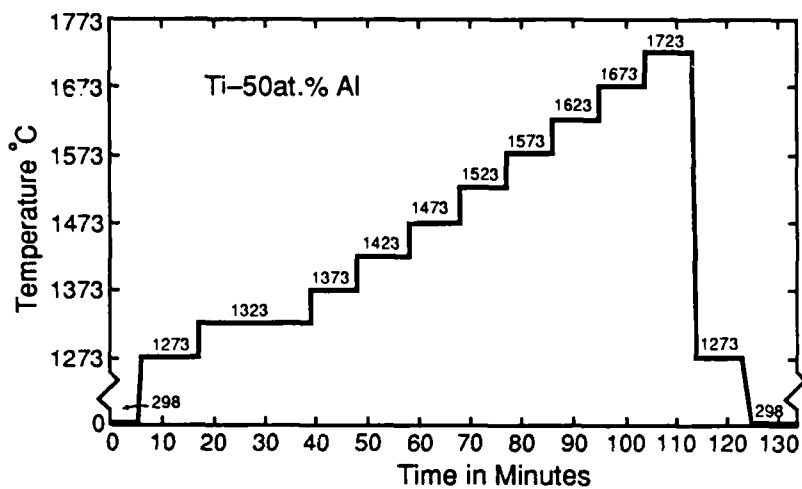


FIG. 3. Heating and cooling schedule of the Ti-50at%Al alloy specimen used for the high-temperature X-ray diffraction experiment.

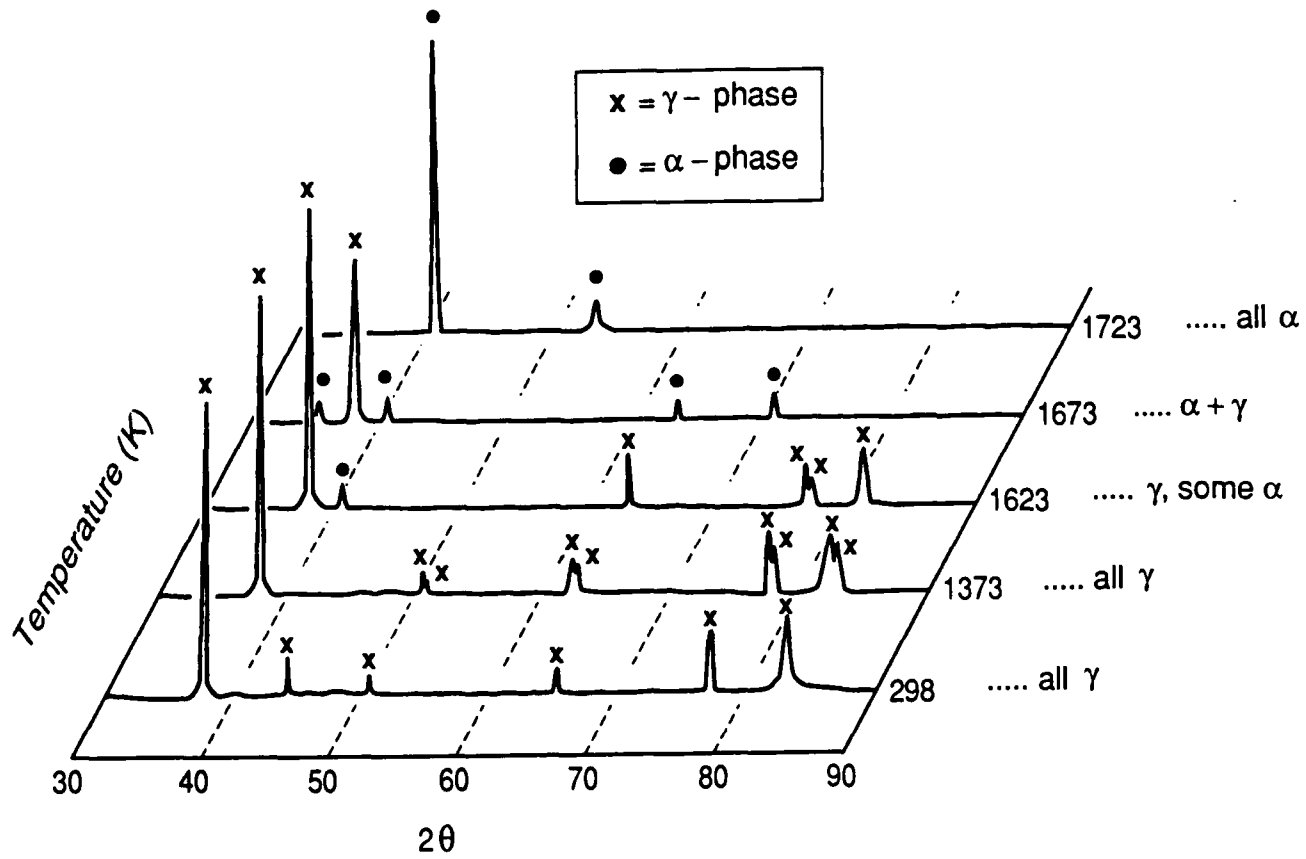


FIG. 4. X-ray diffraction spectrum of the Ti-50at%Al alloy specimen at selected temperatures. Note the transition from γ to α between 1623 K and 1723 K. The largest peaks are $\{111\}_\gamma$ at 39° and $\{01\bar{1}1\}_\alpha$ at 40° .

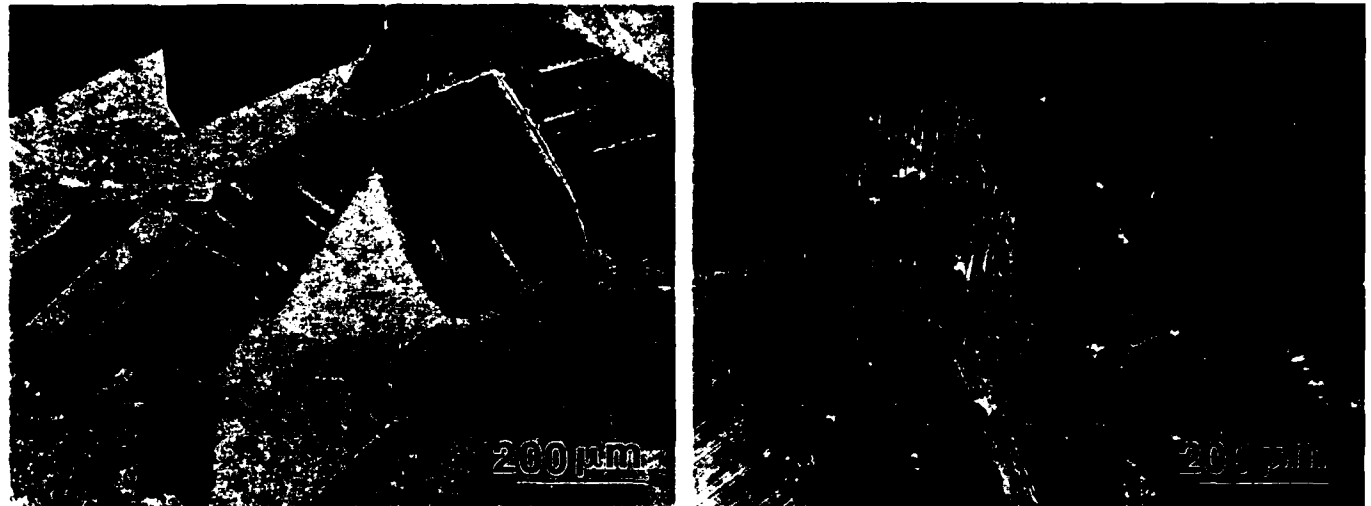


FIG. 5. Optical micrographs of the homogenized Ti-50at%Al alloy used for the high-temperature X-ray diffraction studies: (a) before and (b) after the experiment.

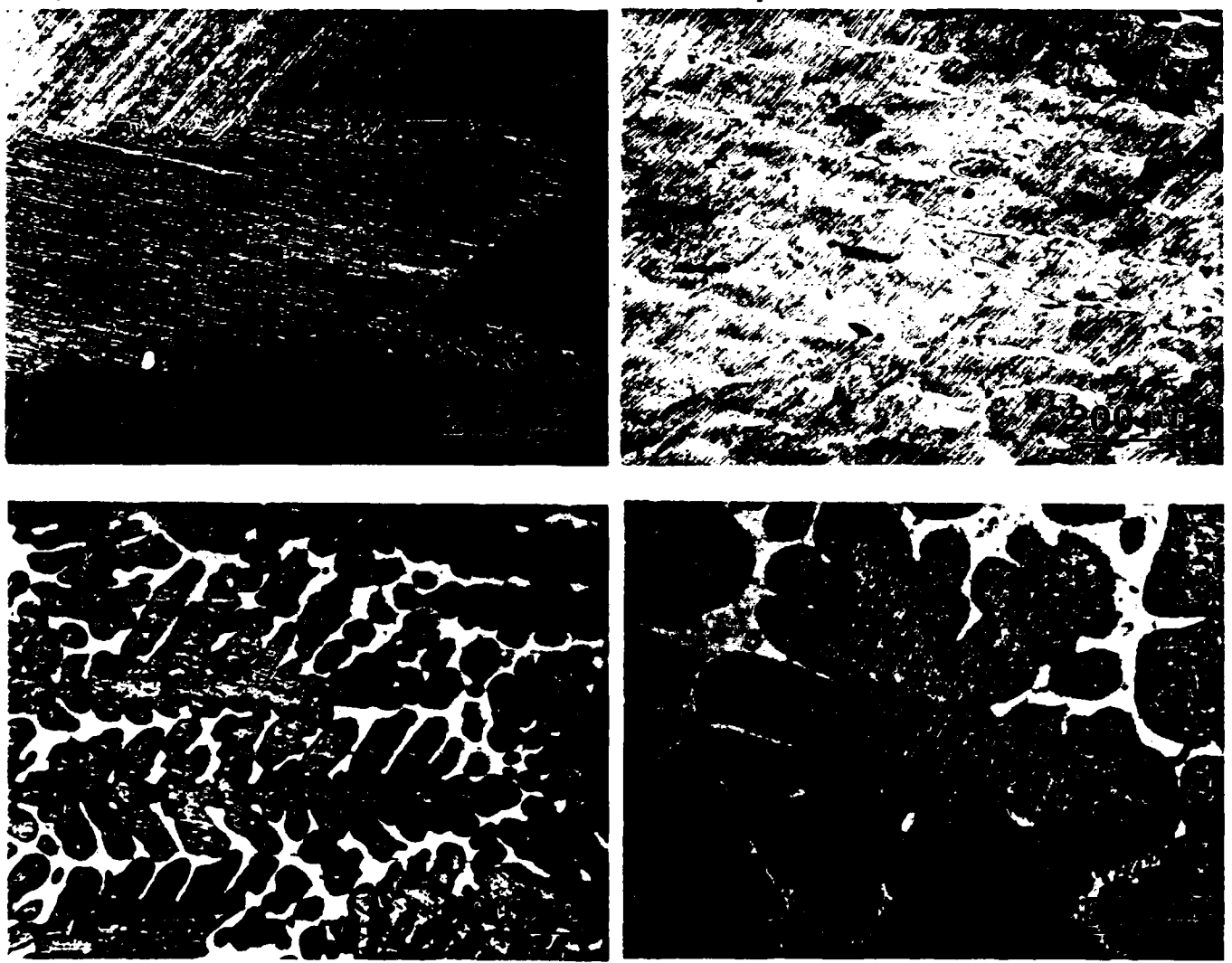


FIG. 6. Solidification microstructures produced by the floating-zone method: (a) Homogenized grains at 17 $\mu\text{m/s}$ showing only $\alpha_2 + \gamma$ lath; (b) directional cells/dendrites at 83 $\mu\text{m/s}$; (c) "columnar" hexagonal dendrite growing along a $<10\bar{1}0>_\alpha$ direction at 330 $\mu\text{m/s}$ and (d) equiaxed hexagonal dendrite showing the full six-fold symmetry from the region solidified at 830 $\mu\text{m/s}$.

SOLIDIFICATION OF SUPERCOOLED INTERMETALLIC POWDERS

by

C.G. Levi, J.J. Valencia and R. Mehrabian
Departments of Materials and Mechanical Engineering
University of California
Santa Barbara, CA, 93106

ABSTRACT

Rapid liquid to solid transformations in intermetallic-forming Ti-Al powders at different levels of supercooling are examined. An overview is first given of solidification with and without equilibrium at the solid-liquid interface. Thermal history of supercooled droplets of Ti-Al alloys is considered emphasizing the interplay between phase selection processes, recalescence and solute redistribution. Experimental observations on Ti-(10-50)at%Al alloy ultrafine (<1 μm) and coarse (>38 μm) powders as well as arc-melted buttons and splats are described. It was found that buttons and possibly the coarse powders between 48 and 50at%Al solidify as a dendrites surrounded by γ segregate. The dendrites further transform in the solid state to a lath structure consisting of $\gamma_T + \alpha_2$. The hexagonal dendrites, which are also observed in 40-80 μm splats of Ti-50at%Al, are formed in a region of the presently accepted phase diagram denoting β as the primary solidification phase. A second type of microstructure observed in all powders with compositions between 38 and 42at%Al is single phase martensite, suggesting the formation of a parent β phase from the liquid. Ultrafine powders and splats ranging in composition from 10-45at%Al appear to solidify to relatively homogeneous β which transforms first to martensite and then orders to α_2 upon cooling in the solid state.

ORDERED INTERMETALLIC COMPOUNDS have long been attractive as high temperature structural materials. They exhibit strong bonding, often partially covalent or ionic, which translates into stiffness retention at higher temperatures. Further, the higher activation energies for diffusion in ordered structures account for improved creep/stress-rupture behavior as well as other diffusion-controlled properties [1].

Titanium aluminides have received substantial attention in the search for lighter, higher

temperature materials for aircraft engines. Amongst the intermediate phases identifiable in the Ti-Al phase diagram of Figure 1, Ti_3Al (DO_{19}) has probably been the subject of the most intense research, e.g. [3]. On the other hand, the equiatomic TiAl (Ll_0) is much stiffer than Ti_3Al , with a Young's modulus at 1200 K higher than that of Ti at room temperature [4]. In addition, it has adequate creep resistance up to 1300 K and forms an alumina-rich scale that could allow it to serve uncoated up to about 1100 K [1].

The application of both aluminides is limited by their low temperature brittleness [5]. However, the ductility of TiAl has been shown to increase rapidly above 973 K as superdislocations become unpinned [6]. The fabricability of these materials is further hindered by a tendency to form massive embrittling segregates when processed by conventional ingot metallurgy.

Rapid solidification (RSP) offers an avenue to circumvent some of the processing problems of intermetallics and opens new "pathways" to alloy development. For example, macrosegregation problems are eliminated and the scale of the microstructural features, such as grain sizes and dendritic spacings, is substantially refined. Moreover, a potential exists for enhancing the formability and fracture toughness of these alloys by RSP. This could include extended solid solubility of ternary additions, production of metastable phases from the melt through alternate phase selection processes and/or incorporation of desirable second phases like fine dispersoids and/or ductile particles [3,7].

The goal of this paper is to explore some of the potential microstructural benefits of rapid solidification in Ti-Al alloys containing primarily Ti_3Al and/or TiAl intermetallics (30 - 50 at%Al). In addition to their practical relevance, alloys in this composition range offer an excellent opportunity for fundamental studies on the evolution of metastable microstructures. Available thermodynamic data reveals a wealth of possibilities for metastable phase formation both during solidification as well as the ensuing trans-

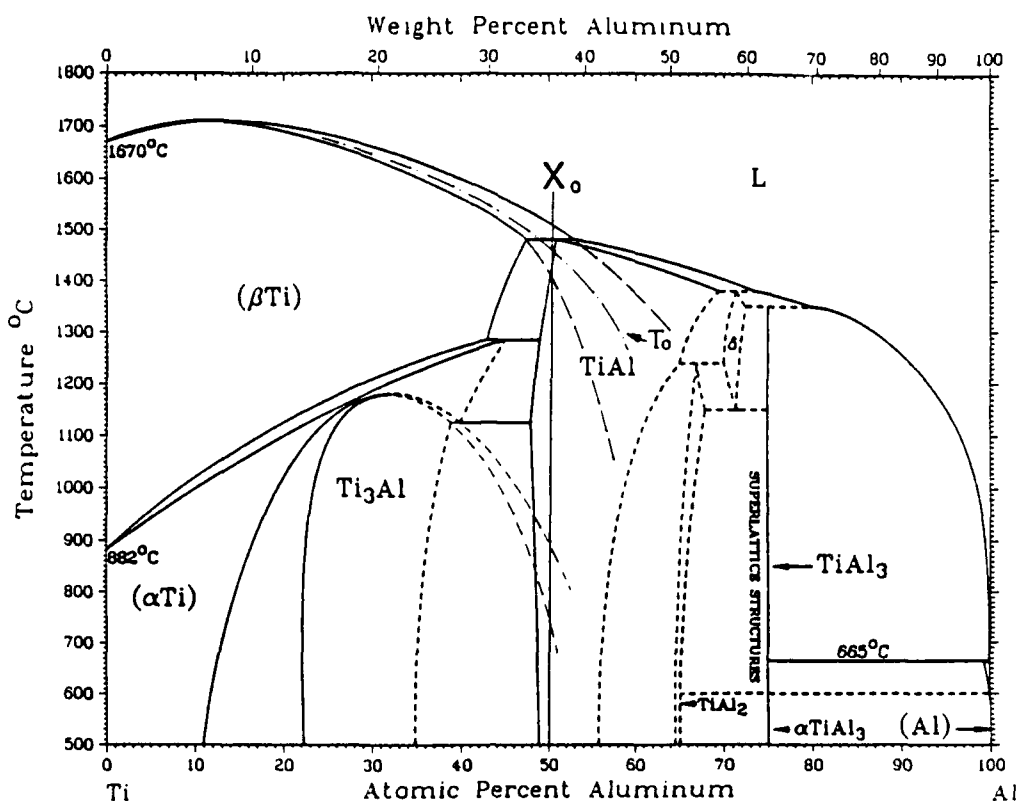


Fig. 1 - Titanium-Aluminum phase diagram showing the T_0 curve and metastable extensions of the liquidus and solidus lines for the liquid- β equilibrium. Metastable extension of the α_2 (Ti_3Al) field up to 50at%Al is schematically shown. From Ref. [2].

formations in the solid state. Topics of further interest are the differences in solidification kinetics and in mechanisms of solute trapping between ordered and disordered phases.

The first part of this paper addresses theoretical concepts in microstructural evolution as applied to the Ti-Al system. The conventional mode of solidification with local equilibrium at the interface is briefly reviewed to set a framework for the analysis of metastable effects generated by increasing the supercooling, hence solidification rate. Alternate "pathways" for microstructure evolution are then discussed in terms of phase selection and solute redistribution.

The second part of the paper deals with microstructural observations in rapidly solidified powders of various sizes and compositions. Microchemical characterization of powders produced by atomization of a Ti-50at%Al alloy in vacuum revealed Al losses in the droplets which resulted in a continuous distribution of compositions from 10-50at%Al. While discouraging from a processing point of view, this finding provided an unusual opportunity for exploring a wide range of alloys in the phase diagram under identical processing conditions. The powder microstructures are discussed in the light of the theoretical concepts as well as corollary experimental observations made on arc-melted buttons and splats.

THEORETICAL CONSIDERATIONS

SOLIDIFICATION UNDER LOCAL EQUILIBRIUM - As a first step in describing the solidification and subsequent solid state transformation "pathways" for the range of alloys noted above we start with the equilibrium phase diagram shown in Figure 1. Dendritic solidification in the absence of bulk supercooling, no significant barrier to nucleation, and local equilibrium at the solid-liquid interface should result in the formation of disordered BCC solid solution (β) followed by the transformation of the interdendritic liquid into the peritectic phase (γ). Figure 2 shows the solid and liquid compositional "pathways" for a Ti-40at%Al alloy, in the middle of the range of interest.

If there were no significant barriers to nucleation, the first solid to form (β) would have a composition $k_\beta X_0$, where $k_\beta = 0.9$ is the equilibrium partition coefficient for the $L \rightarrow \beta$ transformation, and $X_0 = 0.4$ is the initial alloy composition. As solidification proceeds the liquid and solid compositions follow the equilibrium liquidus and β solidus lines down to the peritectic temperature. If the kinetic hindrance to the nucleation of γ - $TiAl$ were also negligible within the time scale of the process, the β dendrites would be immediately surrounded by a layer of γ ,

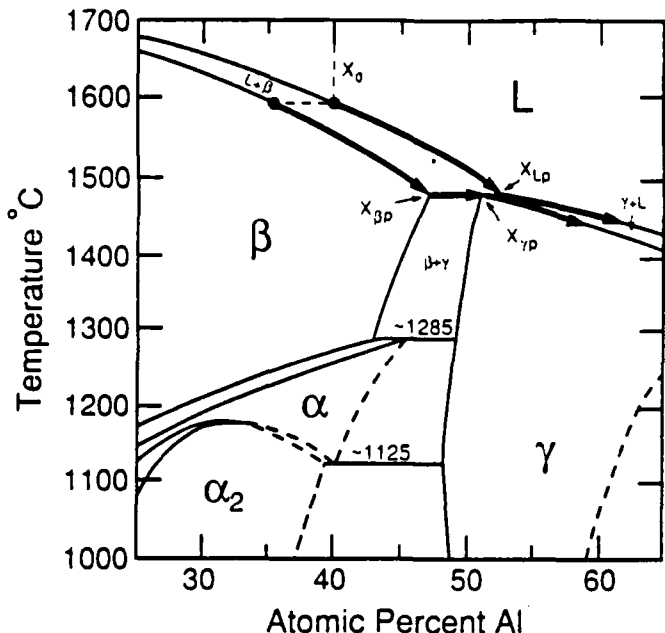


Fig. 2 - Solidification "pathway" of Ti-40at%Al at conventional (slow) rates. Local interfacial equilibrium and negligible nucleation barriers for both phases are assumed.

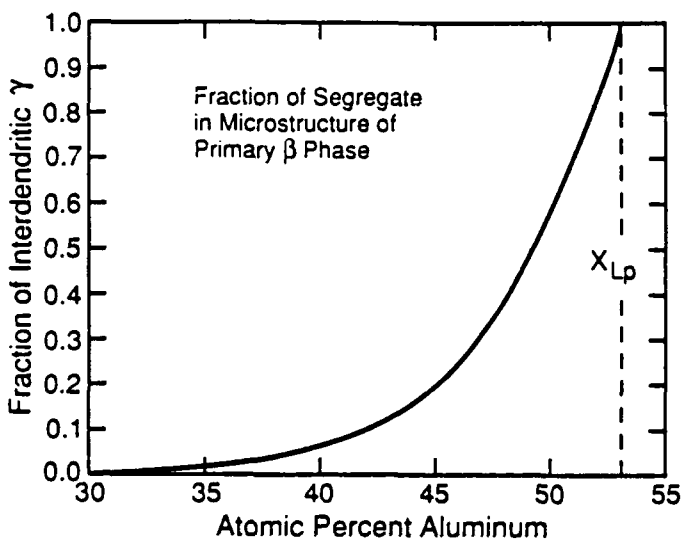


Fig. 3 - Weight fraction of interdendritic γ as a function of alloy composition when solidification occurs with formation of primary β phase. Alloys beyond 53at%Al are expected to form primary γ .

preventing further progress of the diffusion-controlled invariant reaction. The remaining liquid would thus be in local equilibrium with the γ phase and solidification would continue down the liquidus and γ -solidus lines. The resulting microstructure should consist of interdendritic γ in a matrix of primary β which may further transform in the solid state.

Solute redistribution in this case can be approximately described by Scheil's equation [8]. Both segregation profile and weight fraction of interdendritic γ can thus be calculated. Figure 3 shows the calculated weight fraction of γ as a function of initial alloy composition. It ranges from 0.005 to 1.0 for alloys between 30 and 53 at%Al, the latter being the reported liquid composition at the $L + \beta \rightarrow \gamma$ peritectic.

EXTENDED SOLUBILITY UNDER LOCAL EQUILIBRIUM
The first form of metastability beyond conventional segregation effects would be introduced if the intermetallic γ phase does not nucleate readily at the peritectic temperature. Solidification may still occur with local equilibrium at the interface, following the metastable extensions of liquidus and β -solidus lines shown in Figure 1. The solute concentration in β would then surpass the equilibrium limit of $X_{\beta\text{p}} = 0.475$ and the weight fraction of interdendritic γ would be lower than that predicted by Figure 3. It should be noted that under these conditions the supersaturation of the liquid increases progressively and may eventually reach a sufficiently high level to promote the nucleation of γ . However, this form of extended solubility could also result in a single phase structure, especially for the lower Al contents, because the volume fraction of γ may be significantly reduced due to the high equilibrium partition coefficient of Al in BCC Ti.

METASTABLE PHASE SELECTION - Alternate "pathways" to microstructure evolution in these alloys may involve the suppression of interdendritic γ through the mechanism described above, as well as the formation of other primary phases from the liquid.

Potential metastable solidification "paths" in Ti-Al alloys may be identified with the currently available thermodynamic information on the Ti-Al system [9]. The number of options is apparently optimized at about 50at%Al. According to Murray's evaluation of the phase diagram [9], there are at least 5 solid phases which are thermodynamically feasible for this alloy within a 150 K temperature range below the equilibrium liquidus. The possible phases are the disordered solid solutions BCC (β), HCP (α), and the intermetallics Li_0 (γ), B_2 and D_{019} (α_2).

The driving force for the [partitionless] transformation of liquid to each of the possible solid phases can be calculated from the free energy functions in ref. [9]. A phase selection hierarchy can thus be mapped out as a function of composition and temperature (supercooling) at the moment of nucleation. However, the predicted liquidus and solidus lines, hence the T_0 curves, deviate from the published version of the phase diagram, Figure 1, by as much as 80 K for the 30 to 50at%Al composition range. Therefore, we have adopted the simpler approach of tracing the T_0 curves bisecting the currently accepted two-phase fields. Figure 4 shows the result of this exercise. The map has been limited to those phases

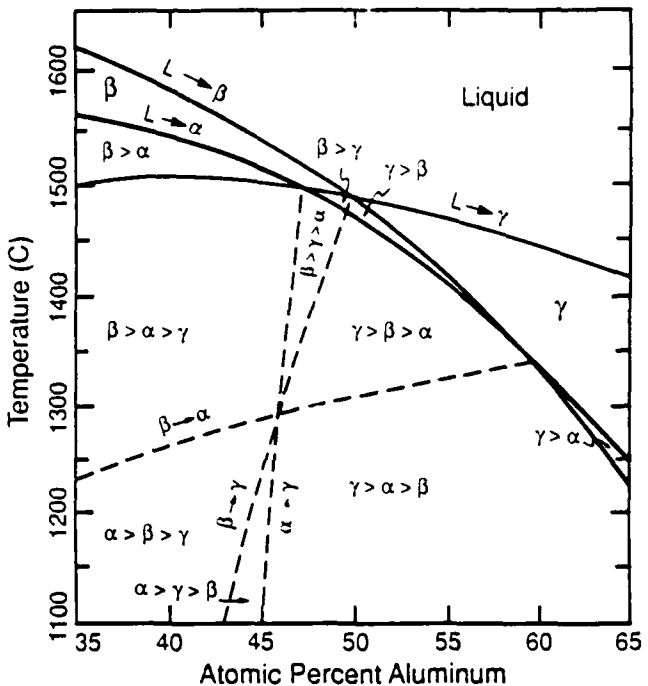


Fig. 4 - Liquid-solid phase selection hierarchy in the Ti-Al system. The curves dividing the different fields are the T_0 temperatures for the $L \rightarrow (\beta, \alpha, \gamma)$ and for the $\beta \rightarrow \alpha$, $\beta \rightarrow \gamma$ and $\alpha \rightarrow \gamma$ solid state transformations.

which have been reported to form from the liquid i.e. β , α and γ [10,11].

Figure 4 indicates that for small supercoolings the primary phase selection should change from β to γ at approximately 50at%Al. Furthermore, all three phases become thermodynamically feasible within ~ 150 K supercooling below the $L \rightarrow \beta$ T_0 curve in the 35-50at%Al composition range. Since the curves are very close to one another at ~ 50 at%Al, there is a higher probability of forming metastable phases from the liquid about this composition.

The intermetallic γ exhibits the strongest driving force for solidification above ~ 50 at%Al in Figure 4. Note, however, that γ is an ordered phase and its transformation kinetics is likely to be more sluggish than that of either disordered phase, and so it could be readily superseded by metastable β or α .

Alloys lean in aluminum exhibit the strongest tendency for β formation from the liquid. On the other hand, the existing thermodynamic data suggests that the likelihood of forming metastable α should increase with aluminum content. However, note in Figure 4 that the level of supercoolings necessary to make α the thermodynamically preferred phase (i.e. nucleation below the $\beta \rightarrow \alpha$ curve) are probably unachievable in practical atomization. Thus, the potential selection of α over β must rely on kinetic factors. The probability for a metastable phase nucleating earlier than the stable one depends on the characteristics of the available sites for nucleation ("motes") as well as any differences in the liq-

uid-solid interfacial energies [12]. Furthermore, when two phases have competitive nucleation kinetics, the dominant one will be determined by the differences in growth velocities, which depend on the driving force for solidification and the difficulty of the transport processes at the interface. For example, it is possible in principle to explain why ordered phases may be superseded by disordered ones based on the easier interfacial rearrangement of the latter. On the other hand, when two disordered phases are competing the limiting rates for interfacial rearrangement are likely to be similar.

To a first approximation, the driving force for solidification in the absence of solute partitioning may be given by [13]

$$\Delta G \sim (\Delta H_0/T_0) (T_0 - T) \quad (1)$$

where ΔH_0 is the latent heat of the alloy at the T_0 temperature. It should be noted that the entropy of solidification $\Delta H_0/T_0$ is significantly larger for α than for β in the composition range of interest. For example, at 50at%Al, $\Delta H_0/T_0$ is 11.1 J/mole K for α and 7.2 J/mole K for β . This suggests that if α were to nucleate preferentially, its growth would be sufficiently rapid to ensure its survival even if β were to appear shortly thereafter.

DEPARTURE FROM LOCAL INTERFACIAL EQUILIBRIUM

One of the benefits of RSP is the potential for extending solid solubility beyond the metastable equilibrium solidus. This is of interest not only for enhancing the chemical homogeneity of the resulting product, but more importantly as a means to produce fine dispersions of stable phases which may be used for high temperature strengthening. In the optimum case it is desirable to produce a microsegregation-free, supersaturated solid of the same composition as the liquid. Although most cases of interest would involve a multiplicity of ternary additions, there are no available treatments of these problems at the present time. We will thus examine the relevant concepts in solute partitioning for the case of binary Ti-Al alloys.

Thermodynamics imposes strict limitations on the range of solid compositions that can form from a liquid of composition X_0 [14]. At the liquidus temperature the only feasible composition is that predicted by the equilibrium solidus. Increasing the interfacial supercooling progressively expands the range of thermodynamically viable solids. Partitionless solidification is only allowed below a critical temperature, T_0 , wherein the free energies of the solid and liquid phases are equal [15]. The T_0 curve for the L-BCC equilibrium in the Ti-Al system is plotted on the phase diagram of Figure 1.

Maintaining the interfacial temperature below T_0 is a necessary but not a sufficient condition to obtain partitionless solidification. If the equilibrium partition coefficient at any supercooling is different from unity, there is a thermodynamic driving force for segregation even

though the system may be below its equilibrium solidus. However, for partitioning to occur the solute must be able to diffuse away from the advancing interface.

Increasing solidification rate results in progressive trapping of solute as the time available for diffusion-controlled partitioning is shortened. The partition coefficient is thus believed to be a monotonic function of interface velocity [16], although the relevant parameters in the relationship are unknown for most systems. In addition, current treatments of solute trapping were developed for dilute systems and are not directly applicable to ordered phases. Further analysis of the mechanisms of solute redistribution and trapping in ordered compounds is necessary before a quantitative description of the phenomenon can be properly addressed.

The critical variables in preventing solute partitioning are thus interfacial temperature and velocity, which are related to each other by the attachment kinetics. In the case of pure metals and disordered solid solutions the attachment kinetics is commonly assumed to be only limited by the collision of atoms with the interface[17]. It is likely, however, that the growth of an ordered phase may involve a significant kinetic hindrance. Hence, the interface velocities at comparable supercoolings may be much lower than those for a disordered phase.

It is well known that solidification of supercooled droplets involves a rising interfacial temperature due to the limitations in dissipating the evolving heat of fusion [18]. Therefore, the extent of fulfillment of the thermodynamic and kinetic conditions for partitionless solidification depends on the evolution of the interfacial temperature and velocity as the transformation progresses, i.e. the thermal history.

THERMAL HISTORY AND SOLUTE REDISTRIBUTION -
The thermal history of different solidification modes can be conveniently described on an enthalpy-temperature diagram [18] such as that for Ti, Figure 5. In a system that is sufficiently small to preclude the development of internal temperature differences, the enthalpy can be taken as the additive contributions of the liquid and solid portions of the system. If the enthalpy is normalized by the heat of fusion, ΔH_M , and the temperature differential with the melting point, $(T-T_M)$, is normalized by a characteristic supercooling, $\Delta H_M/C_L$, where C_L is the heat capacity of the liquid, we obtain a generalized diagram where the only difference between pure materials is a slight variation in the slope of the solid enthalpy line. The melting temperature of pure Ti is designated by the $\theta = 0$ isotherm in Figure 5. Since the enthalpy of pure Ti liquid at its melting temperature is designated as the reference state in this diagram, the dimensionless enthalpies of the liquid and BCC Ti phases at this temperature are zero and minus one, respectively.

Two extreme solidification paths can be illustrated on the upper part of Figure 5 corresponding to pure Ti. Solidification near equili-

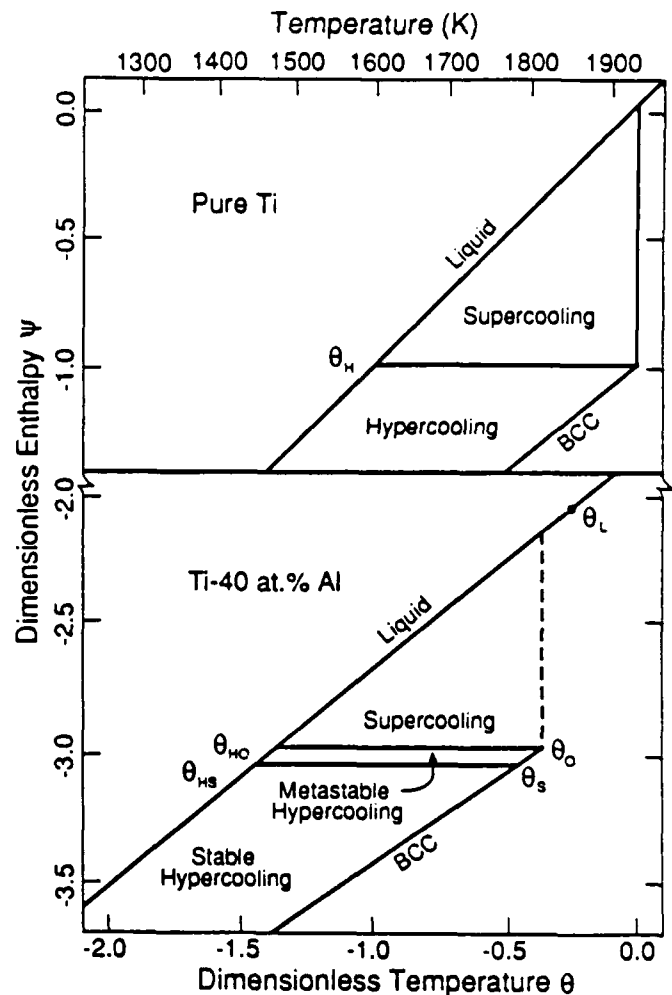


Fig. 5 - Calculated enthalpy-temperature diagram for the liquid and BCC solid phases of pure Ti and the Ti-40at%Al alloy. Hypercooling temperatures are 1600 K ($\theta_H = -1.0$) for pure Ti, and 1471 K ($\theta_{H0} = -1.37$) and 1441 K ($\theta_{HS} = -1.46$) for the alloy. The thermodynamic data used is from reference [9].

brium takes place in an isothermal fashion following the $\theta = 0$ isotherm. On the other hand, if the liquid is supercooled until an amount of enthalpy equivalent to the heat of fusion has been removed, $\theta = \theta_H$, the system can solidify adiabatically following a horizontal path at $\psi = -1.0$ and the liquid is said to be hypercooled. Note that upon adiabatic solidification, the latent heat released must be completely transformed into sensible heat, resulting in recalescence.

A more common situation in rapid solidification is one wherein nucleation occurs at some intermediate supercooling, $\theta_H < \theta_N < 0$, and heat is continuously extracted from the system. The thermal history is then a function of the initial supercooling and the relative rates at which heat is generated, related to the interfacial kinetics, and that at which heat is removed, depen-

dent on the efficiency of the external cooling.

In many pure metals and disordered phases the attachment kinetics is so active that little heat can be removed in the time scale of the process. Thus, the system recalesces in an almost adiabatic fashion up to a temperature at which the rates of latent heat release and removal can be balanced. Interface velocities are much higher during than after recalescence, and rapid solidification is not associated with high cooling rates, but high heating rates. On the other hand, if the alloy were to grow in an ordered fashion, the kinetics might be more sluggish and the external heat transfer could be sufficiently competitive to slow down the recalescence.

Given the irrelevant role of external heat extraction during recalescence, the key to metastable phase formation and increased solute supersaturation is to enhance the supercooling prior to nucleation. Dividing the metal into fine droplets is a common approach in achieving large supercoolings since the heterogeneous nucleation catalysts are isolated into a small fraction of the total volume [12]. Decreasing the size of the droplets further increases undercoolability by both reducing the time available for nucleation and the volume of material in which a successful nucleation event can take place. It is commonly assumed that the enhanced cooling rate associated with decreasing the particle size plays a more important role in suppressing the onset of nucleation than in slowing down the recalescence. However, recent calculations reveal that achievable supercoolings are primarily dependent on the nature of the active nucleation sites and the benefits from increasing cooling rate are relatively modest [19].

Consider now the changes in the thermal characteristics of the system introduced by the addition of an alloying element. The enthalpies of the liquid and the BCC Ti-40at%Al solid solution, calculated from the best thermodynamic information available at this time [9], are compared with the equivalent data for pure Ti in Figure 5. The liquid and solid enthalpy lines for the alloy are displaced downward because the dimensionless variables are referred to the pure Ti at its melting point. The negative deviations result mainly from the large contributions of the non-ideal mixing as well as the replacement of half the Ti atoms in the BCC lattice with Al, which has a lower heat of fusion than Ti.

The major effect of alloying on the thermal behavior of the system during solidification is associated with changes in the heat of fusion. An effective heat of fusion is defined as the enthalpy difference between liquid and solid at their equilibrium liquidus and solidus temperatures, respectively. It consists of a latent heat component, which is the vertical distance between liquid and solid enthalpy lines at the solidus temperature, and a sensible heat component associated with the melting range.

As in the pure metal, a hypercooled regime may be reached when all the effective heat of fusion has been removed from the system prior to

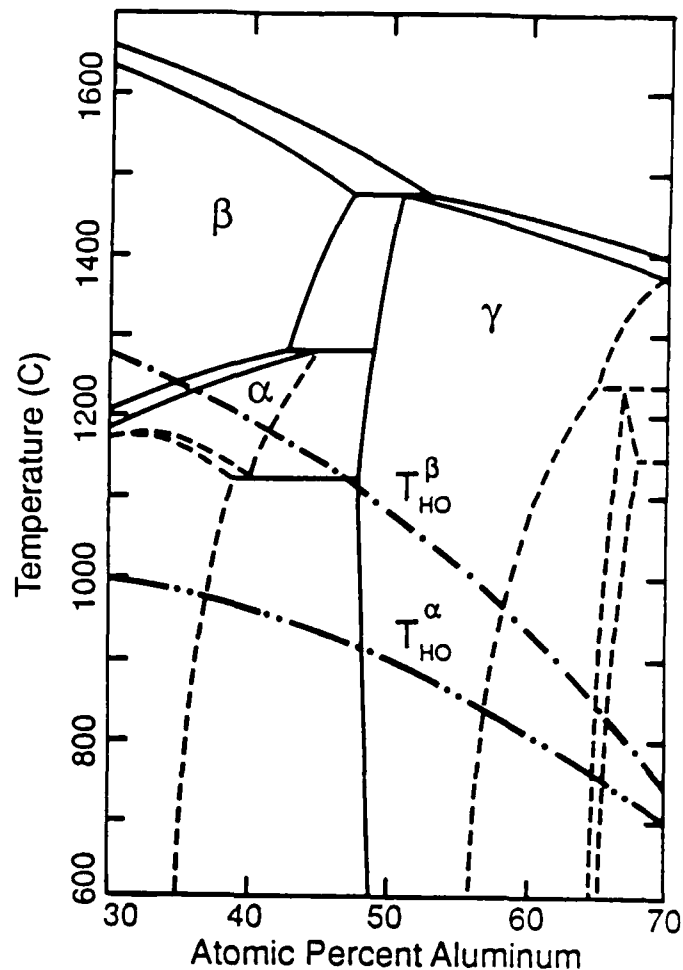


Fig. 6 - Critical supercoolings to reach metastable hypercooling of α and β phases in Ti-Al alloys. Thermodynamic data is from ref. [9].

nucleation and recalescence produces a solid at or below its solidus temperature. On the other hand, one may define a critical supercooling to prevent adiabatic recalescence above the T_0 temperature, thus ensuring that the thermodynamic condition for partitionless solidification is fulfilled at all times. The system could in principle solidify adiabatically, but recalescence would result in a metastable solid which would have to be rapidly cooled below T_S to prevent remelting. Thus, stable (T_{HS}) and metastable (T_{HO}) hypercooling temperatures can be defined for the Ti-Al alloy of Figure 5 (θ_{HS} and θ_{HO} in dimensionless terms). Figure 6 shows the critical nucleation temperatures to achieve metastable hypercooling for the α and β phases within the composition range of interest. Note that α requires much higher supercoolings before complete partitionless solidification may become feasible due to the much higher latent heat predicted from the thermodynamic functions.

MICROSTRUCTURAL OBSERVATIONS

EXPERIMENTAL - The materials used in this research were arc-melted from high purity Ti sponge (99.98%, <700 ppm O₂) and Al pellets (99.9%). Melting was done under argon processed through a desiccator and an oxygen getter; the oxygen content of the furnace atmosphere was maintained below 10⁻⁷ ppm. The material was processed by a containerless electrohydrodynamic (EHD) atomization technique [20] using thin rods cut from the buttons by electro-discharge machining. Powders ranging in size from about 10 nm to over 300 μm were collected and examined by X-ray diffraction, scanning and transmission electron microscopy. In addition, microsplats were generated by impacting ultrafine supercooled droplets on a copper substrate during atomization. Larger splats were produced in a hammer and anvil device under an Ar atmosphere of similar purity.

MICROSTRUCTURES OF COARSE POWDERS - Cross sectional views of coarse powder (38 to ~300 μm) microstructures examined are shown in Figure 7. The structures range from distinctly dendritic to martensitic, the latter appearing as single phase or with varying degrees of second phase segregate. A relatively small fraction of single phase powders with no discernible evidence of martensite were also detected. Table 1 summarizes the incidence of the different microstructures as a function of particle size.

Table 1 - Microstructures detected in Ti-Al alloys between 38 and 50at%Al.
(% of total particles in range)

	Size Range (μm)			
	150-300	106-149	75-105	53-74
Dendritic	85	52	40	37
Martensitic	13	44	52	51
Featureless	2	4	10	12

EDX analysis revealed average composition variations ranging from 38 to 50at%Al. Dendritic powders have an average composition of 48-50at%Al and exhibit arm spacings on the order of 7-10 μm, Figure 7(b). Martensitic powders have an average composition of 38 to 48at%Al and are commonly single phase, Figure 7(c), although those in the higher compositions (>42at%Al) tend to show small amounts of segregate. Featureless single phase powders are typically in the 40-44at%Al range.

The composition variations in the powders are due to superheat coupled to the vacuum environment unique to the EHD atomization technique, which results in evaporation of Al from the liquid pool as well as from the molten droplets. Increasing surface to volume ratio with decreasing powder size results in a corresponding decrease in aluminum content, and a lower incidence of the dendritic morphology. As a consequence of this observation, microstructural analysis of each individual powder microstructure was pre-

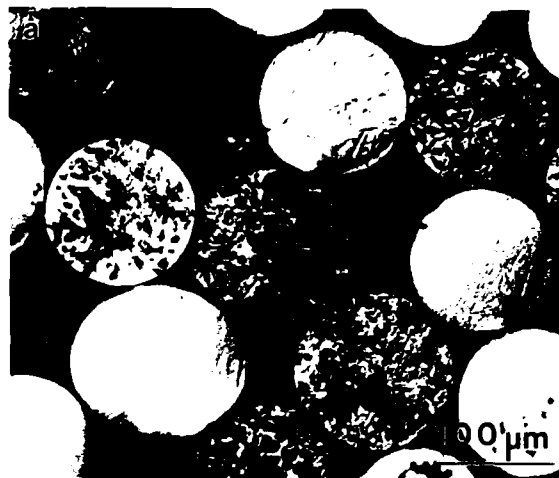


Fig. 7 - Polished section of EHD powder revealing at least two distinct solidification morphologies (a). (b) is a typical dendritic microstructure and (c) is a single phase martensitic microstructure.

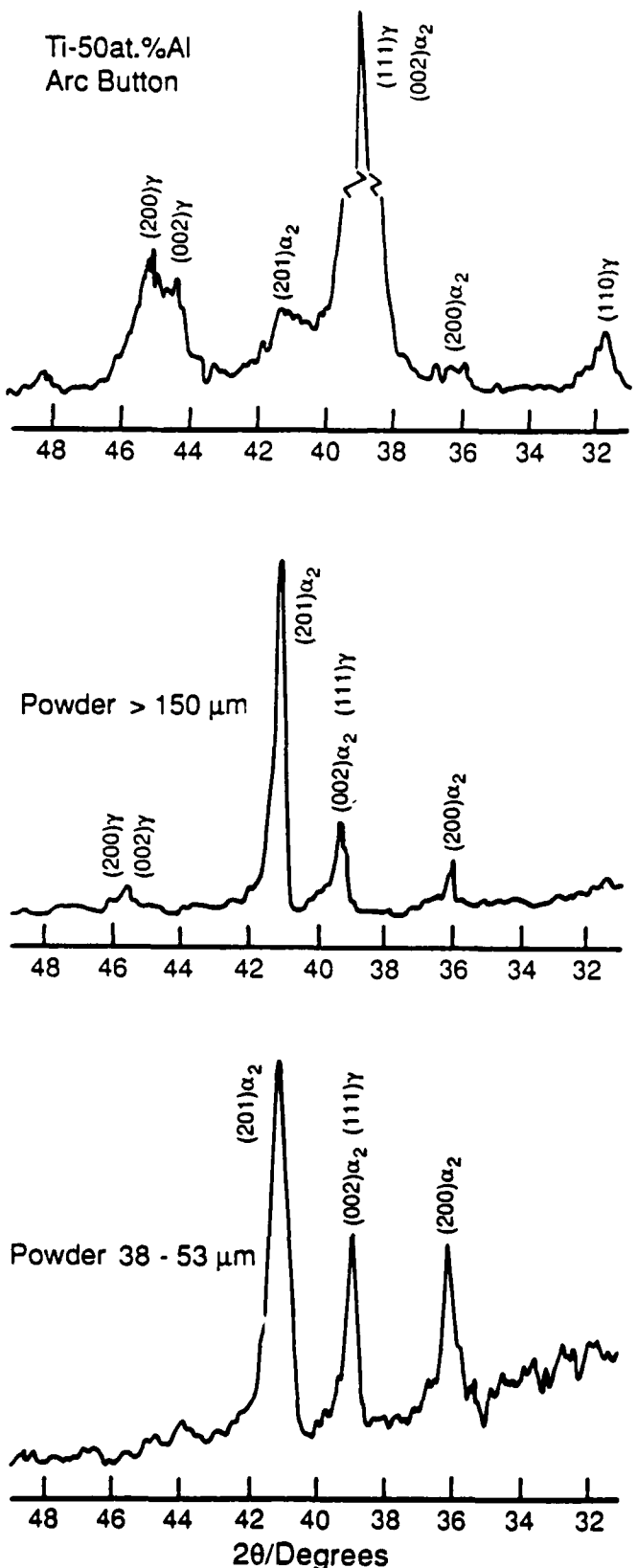


Fig. 8 - X-ray diffraction scans of the as-cast button and EHD atomized powders in the coarsest and finest size ranges. Note the reduction in the $(111)\gamma$ peak and the enhancement of the $(201)\alpha_2$ peak from the button to the finer powder.

ceeded with EDX analysis of its average composition. The initial alloy composition of the arc-melted buttons used for the production of the powders was verified to be within 0.5% of the stoichiometric Ti-50at%Al.

X-ray diffraction analysis of the buttons and powders in two extreme size ranges, $>150 \mu\text{m}$ and $38-53 \mu\text{m}$, are shown in Figure 8. The phases detected in all cases were the ordered intermetallics α_2 plus γ , which are the equilibrium phases expected from the phase diagram for compositions between 35 and 49at%Al. It should be noted that the distinction between α and α_2 by X-ray diffraction was not always conclusive as the superlattice reflections of $D0_{19}$ have inherently low intensities and sometimes overlap with the stronger γ peaks. The identification of the phase as α_2 was primarily supported by TEM work.

A relative measurement of the proportion of these phases in the microstructures may be obtained by comparing the $(201)\alpha_2$ and the $(111)\gamma$ peaks, which correspond to the 100% intensity reflections for both phases. The $(111)\gamma$ peak, which overlaps with the $(002)\alpha_2$ peak, is much stronger in the button pattern, even though the relative sensitivity scale was lower than that used for the powders. On the other hand, the $(201)\alpha_2$ peak is clearly dominant in the finer powder pattern but not very pronounced in the button. One may thus conclude that the γ phase is predominant in the as-cast structure of the arc-melted button while the finer powders are primarily α_2 .

The microstructure of the Ti-50at%Al arc-melted buttons is dendritic with spacings on the order of $20-25 \mu\text{m}$, as shown in Figure 9. TEM analysis [10] confirmed the X-ray finding that the structure consists of $\gamma + \alpha_2$. The core of the dendrite exhibits a lath structure of γ_T twins intermixed with α_2 , see Figure 10. The designation of γ_T denotes γ formed from solid state transformation. The interdendritic region consists of twin-free grains of γ . Average compositions of these constituents were 47at%Al for the dendrite core and 55at%Al for the segregate.

A rather surprising observation in the button microstructures is shown in Figure 11. These are SEM views of a shrinkage cavity which reveal that the dendrite arms are not orthogonal, as would be expected in the solidification of primary β , but generally lie at 60° with respect to each other. Furthermore, the surface relief in this figure correlates with the $\gamma_T + \alpha_2$ lath structure of the dendrite cores shown in Figure 10. One may thus conclude that while the dendrite microstructures of polished samples in Figure 9(a) do not unequivocally reveal a hexagonal growth pattern, the combination of angled dendrite arms in this figure and the SEM views in Figure 11 indicate formation of α dendrites during solidification surrounded by γ segregate. Also, the calculated weight fraction of γ in Figure 3, where the primary phase is assumed to be disordered β , is 0.56 for 50at%Al, whereas measured interdendritic γ in the button is ~ 0.12 .

The coarse dendritically solidified EHD powders exhibit structures similar to those of the

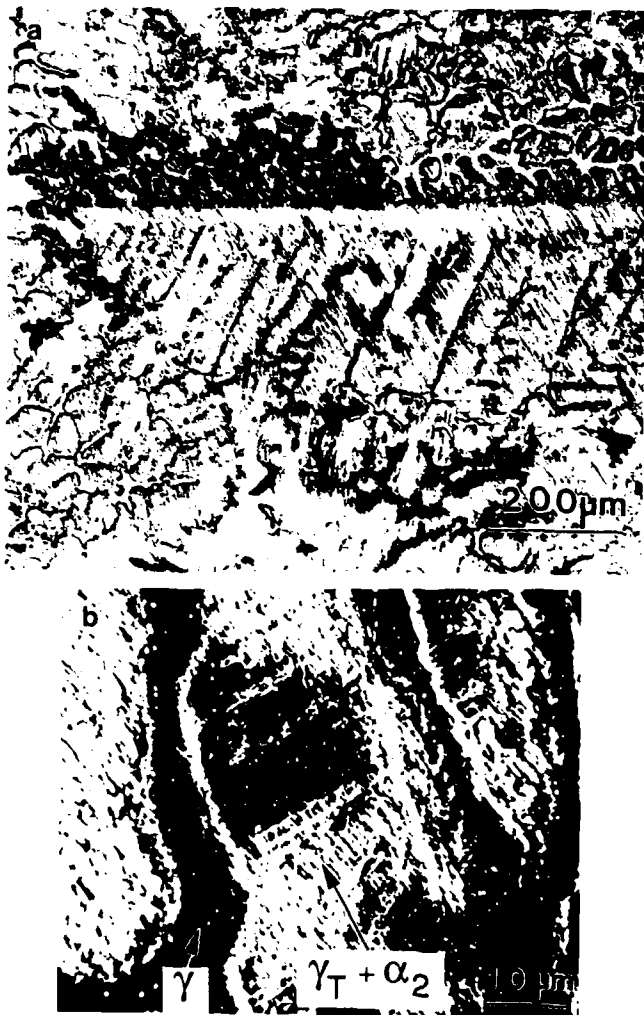


Fig. 9 - Microstructure of arc-melted button of Ti-50at%Al alloy. Primary dendrites have transformed to a lath structure and are surrounded by interdendritic segregate (γ).

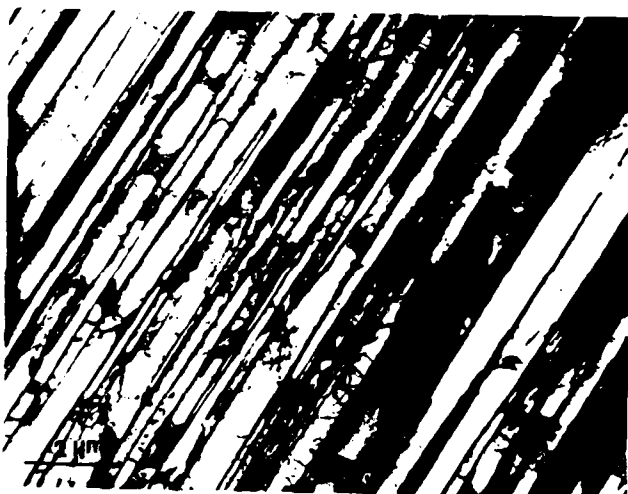


Fig. 10 - TEM view of lath structure characteristic of dendrite cores in the arc-melted button. The laths consist of γ twins and α_2 intermixed layers parallel to the basal plane of α_2 [10].



Fig. 11 - SEM views of a shrinkage cavity in a Ti-50at%Al arc-melted button where hexagonal dendrites are shown to grow from the liquid. The surface striations are parallel to the basal plane of the α dendrite. (From reference [10]).

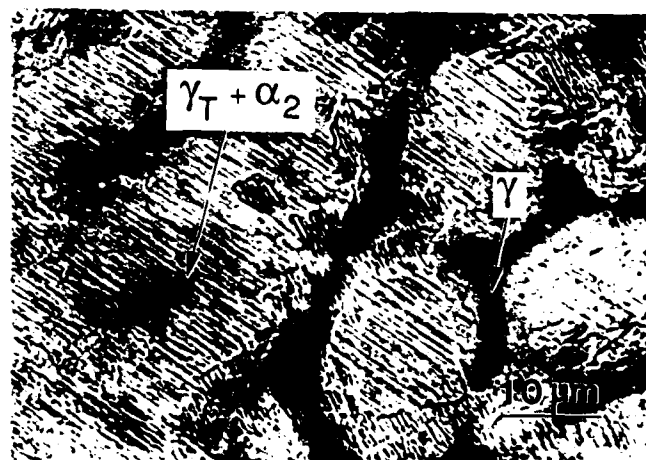


Fig. 12 - Microstructure of dendritically solidified powder (48-50at%Al) with a lath dendritic core and γ segregate. Note the similarity to the button structure in Figure 9(b).

arc-melted buttons, albeit with finer arm spacings. Figure 12 shows an example of (transformed) $\gamma_T + \alpha_2$ dendrites surrounded by interdendritic γ . The finer dendrite spacings (7-10 μm) are consistent with reduction in local solidification time as the size of the "casting" decreases. However, the benefits are somewhat limited by the modest cooling rates characteristic of atomization in vacuum (10^2 - 10^3 K/s for the coarse powders).

A more significant difference between the microstructures of buttons and coarse powders is an apparent reduction in the amount of interdendritic γ phase, from 0.12 to 0.07. In addition, the average composition of the transformed dendrites, determined by EDX, is slightly higher (49at%Al) than that of the button, and that of the interdendritic γ is correspondingly lower (53at%Al). This is consistent with a solidification "path" in which the thermally-activated nucleation of γ is delayed by the faster cooling prevalent in the powders. The average composition of the primary phase increases as the solubility is extended along its metastable solidus.

Perepezko et al [11] have recently found that phases other than BCC can be competitive during the solidification of TiAl. They detected evidence of hexagonal dendritic growth ($L \rightarrow \alpha$) in metallographic sections of drop-tube processed TiAl powders. Similar structures have been observed by the authors on TiAl splats produced in a hammer and anvil device, see Figure 13.

Microstructural observations of coarse EHD powders in Figure 7(a) reveal that, in addition to the dendritic structure of Figure 7(b) and 12, there are particles that show a radically different response to etching, Figure 7(c). These single phase powders appear to be homogeneous in composition and have a structure characteristic of the martensitic transformation. Extensive microchemical analysis of these powders has revealed that they are depleted in aluminum and range in composition from 38 to 42at%Al. It is suggested that the powders solidified as disordered β and then transformed to hexagonal martensite (α') upon cooling in the solid state. As previously noted, there are more complex variants of these microstructures as well as "featureless" powders which are still under investigation.

MICROSTRUCTURES OF ULTRAFINE POWDERS AND SPLATS - Typical microstructures of ultrafine ($<1 \mu\text{m}$) powders and splats produced by EHD are shown in Figure 14. Microchemical analysis on several splats reveals a composition between 38 and 45at%Al. These were solidified on a copper substrate introduced in the flight path of the liquid droplets. The original droplet sizes calculated from splat thickness and diameters were on the order of $\sim 1 \mu\text{m}$. The ultrafine ($<0.5 \mu\text{m}$) powders had a composition range of 10 to 33at%Al, consistent with increasing aluminum loss due to the higher surface area and the longer flight times.

The diffraction patterns index consistently to a hexagonal lattice and, where enough informa-



Fig. 13 - Microstructure of a hammer and anvil splat clearly showing hexagonal dendritic growth on the surface. Note the 60° angle between primary and secondary arms.

tion could be gathered, to the (DO_{19}) structure of α_2 . In general, powders and splats show a lath microstructure, albeit with variations in morphology and scale from one to another. While detection of the solidification grain structure is obscured by the solid-state transformation, powders like the one in Figure 14(a) appear to have solidified from a single nucleation event. Most splats, which are larger in volume and solidified on a copper substrate, show evidence of multiple nucleation with a grain size on the order of 500 nm, see Figure 14(b).

A potential path to these microstructures involves the partitionless solidification of liquid into BCC which transforms to martensite upon cooling from the maximum recalescence temperature. As the supersaturated hexagonal martensite cools further it enters the Ti_3Al phase field, see Figure 1. Thus, it has the option of ordering to the hexagonal DO_{19} structure, requiring only short-range atomic rearrangements. Although there is no BCC phase left in the microstructure, the sequence of events is supported by preliminary observations of an APB sub-structure inside the laths, which would suggest ordering from a disordered hexagonal structure whose morphology is consistent with the martensitic transformation of β -Ti.

SUMMARY OF SOLIDIFICATION "PATHS"

Microstructure evolution in rapidly solidified Ti-Al alloys offers a number of variants that open a host of possibilities for future alloy development. This could include selective addition of ternary elements which would promote formation of alternate primary phases, dispersions and other second phases. Thus, the subsequent behavior of these alloys during consolidation and service may be improved.

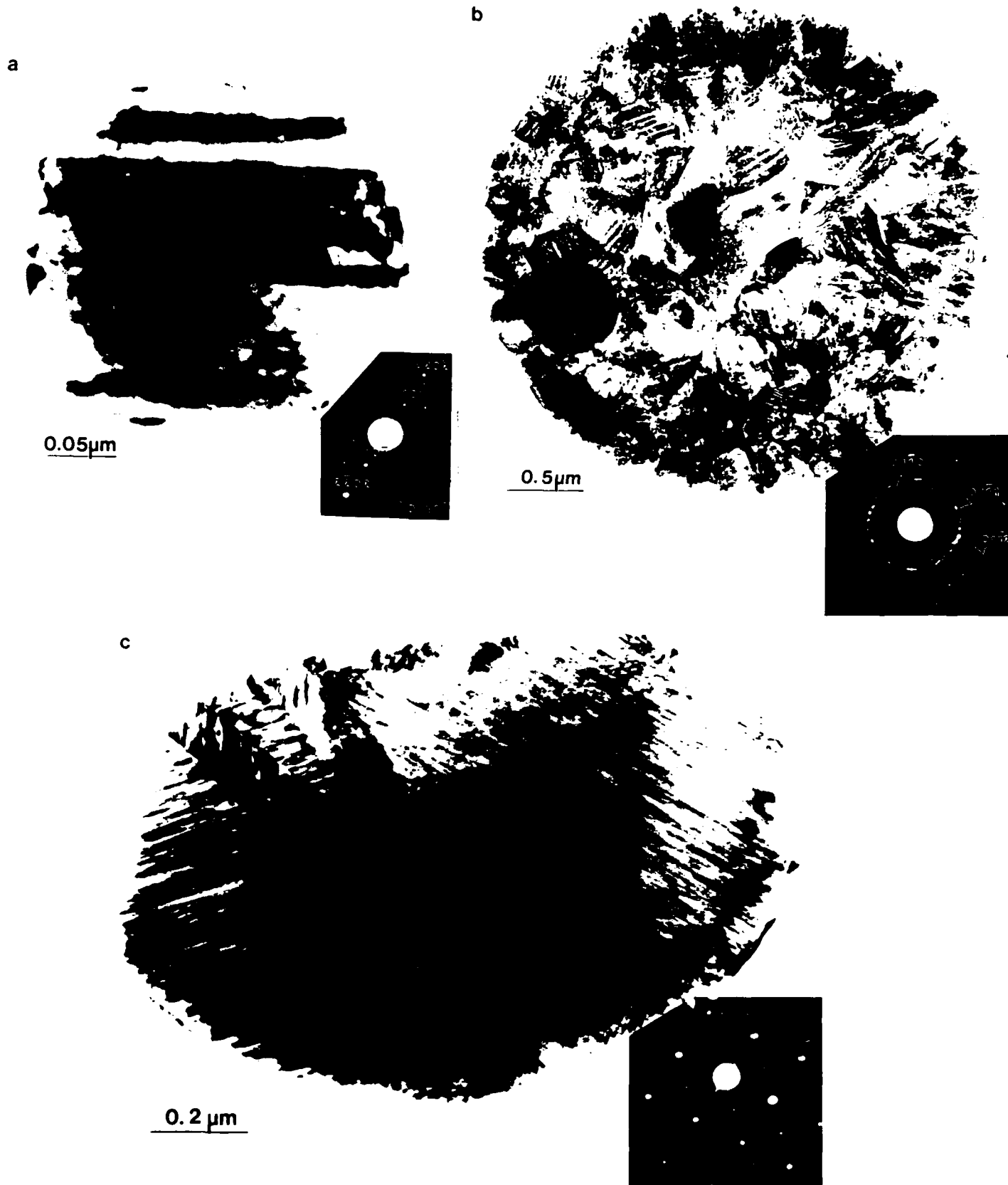
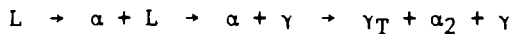


Fig. 14 - Microstructures of ultrafine Ti-Al alloy powder (a) and splats (b) and (c) produced by electrohydrodynamic atomization in vacuum. The powder shows no evidence of prior β boundaries, clearly distinguishable in the splat (b). The smaller splat (c) probably solidified as a bicrystal, with a resulting grain size comparable to that in (b); other boundaries were introduced during the solid state transformation. Note the differences in the scale and morphology of the laths.

To summarize the potential solidification "paths" we can separate the problem into phase selection and solute redistribution. Arc-melted buttons of Ti-50at%Al form primary α dendrites and interdendritic γ segregate. The α phase subsequently transforms to $\gamma_T + \alpha_2$. Thus, the transformation "path" can be denoted as:



Dendritic Ti-(48-50)at%Al coarse powders show as-solidified microstructures similar to the arc-melted buttons albeit with a lower fraction of interdendritic γ . However, the dendritic morphology does not unequivocally correspond to the hexagonal patterns observed in the buttons and hammer and anvil splats. One could postulate that the primary phase may have been β which subsequently transformed to α and then to the $\gamma_T + \alpha_2$ lath structure. If α is a metastable phase in this range, however, it is difficult to justify that the higher cooling rates in the powders led to the stable β phase while the buttons formed the metastable α .

Current thermodynamic information suggests that supercoolings of 50-80K below the equilibrium β liquidus are required for the formation of primary α from the liquid (Figure 4), not a likely event in arc-melted buttons. Hence, more accurate thermodynamic data is needed before this inconsistency can be resolved.

Coarse powders of 38-42at%Al with uniform martensitic structures are believed to follow the transformation path



with possible subsequent ordering of the hexagonal α' to α_2 ($D0_19$). Solidification in the absence of supercooling and no hindrance to nucleation at the peritectic temperature predicts volume fractions of γ between 0.04 and 0.10 for this composition range. Therefore, these powders were either initially supercooled to the extent of producing significant solute trapping, or the nucleation of γ was suppressed while solidification occurred with local interfacial equilibrium following the metastable extensions of the β liquidus and solidus, as previously noted.

It is expected that fine powders and splats experienced significant supercoolings prior to solidification of primary β . The lower Al contents in these particulates coupled with the significantly higher calculated supercoolings for α formation, see Figure 4, lend credence to the transformation "path" similar to that of the martensitic coarse powders.

ACKNOWLEDGEMENTS

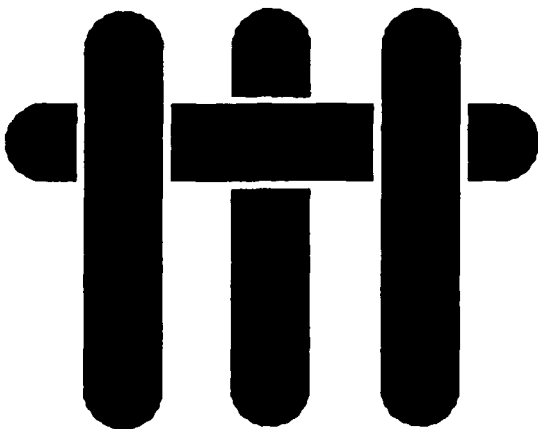
This work was sponsored by the Defense Advanced Research Projects Agency, supervised by Dr. P. Parrish and monitored by the Office of

Naval Research contracts N00014-86-K-0753 and N00014-86-K-0178. The authors are grateful to Prof. John Perepezko for stimulating discussions and to Drs. Colin McCullough and Cindy Elliot for assistance with the TEM work.

REFERENCES

1. H.A. Lipsitt, in "High Temperature Ordered Intermetallic Alloys", ed. by C.C. Koch, C.T. Liu and N.S. Stoloff, p. 351, MRS, Pittsburgh, PA (1985).
2. J.L. Murray, in "Binary Alloy Phase Diagrams", ed. by T.B. Massalski, p. 173, ASM, Metals Park, OH (1986).
3. R.G. Rowe, J.A. Sutliff and E.F. Koch, in "Rapid Solidification Technology for Titanium Alloys", ed. by F.H. Froes, D. Eylon and S.M.L. Sastry, p. 239, The Metallurgical Society, Warrendale, PA (1986).
4. R.E. Schafrik, Metall. Trans. 8A, 1003-6 (1977).
5. H.A. Lipsitt, D. Shechtman and R.E. Schafrik, Metall. Trans. 6A, 1991 (1975).
6. D. Shechtman, M.J. Blackburn and H.A. Lipsitt, Metall. Trans. 5, 1373 (1974).
7. F.H. Froes and R.G. Rowe, in "Titanium Rapid Solidification Technology", ed. by F.H. Froes and D. Eylon, pp. 1-20, The Metallurgical Society, Warrendale, PA (1986).
8. E. Scheil, Z. Metallk. 34, 70 (1942).
9. J.L. Murray, "Calculation of the Ti-Al Phase Diagram", submitted to Metall. Trans.
10. J.J. Valencia, C. McCullough, C.G. Levi and R. Mehrabian, to be published in Scripta Metall.
11. J.H. Perepezko, private communication.
12. W.J. Boettinger and J.H. Perepezko, in "Rapidly Solidified Crystalline Alloys", ed. by S.K. Das, B.H. Kear and C.M. Adam, pp. 123-129, The Metallurgical Society, Warrendale, PA, (1985).
13. C.G. Levi, "Thermal Considerations in the Recalescence of Supercooled Powders", to be published in Metall. Trans. A.
14. W.J. Boettinger, S.R. Coriell and R.F. Sekerka, Mat. Sci. Engr. 65, 27-36 (1984).
15. J.C. Baker and J.W. Cahn, in "Solidification", pp. 23-58, American Society for Metals, Metals Park, OH (1969).
16. M.J. Aziz, J. Appl. Phys. 53, 1158-67 (1982).
17. D. Turnbull, Metall. Trans. 12B, 217-229 (1981).
18. C.G. Levi and R. Mehrabian, Metall. Trans. 13A, 221-234 (1982).
19. C.G. Levi, "The Evolution of Microcrystalline Structures in Supercooled Powders", to be published in Metall. Trans. A.
20. J.F. Mahoney, S. Taylor and J. Perel, in Proceedings of the IEEE/IAS Annual Conference, Electrostatic Processes, Chicago, IL (1984).

M A T E R I A L S



MICROSTRUCTURE EVOLUTION IN TiAl ALLOYS WITH B ADDITIONS: CONVENTIONAL SOLIDIFICATION

by

M.E. Hyman, C. McCullough,
J.J. Valencia, C.G. Levi and R. Mehrabian

Materials Department,
College of Engineering
University of California,
Santa Barbara, California 93106

MICROSTRUCTURE EVOLUTION IN TiAl ALLOYS WITH B ADDITIONS:

CONVENTIONAL SOLIDIFICATION

by

M.E. Hyman, C. McCullough, J.J. Valencia, C.G. Levi and R. Mehrabian¹

ABSTRACT

Solidification microstructures of arc-melted, near-equiautomic TiAl alloys containing boron additions are analyzed and compared with those of binary Ti-Al and Ti-B alloys processed in a similar fashion. With the exception of the boride phase, the matrix of the ternary alloy consists of the same α_2 (DO_{19}) and γ ($L1_0$) intermetallic phases found in the binary Ti-50at%Al alloy. On the other hand, the boride phase, which is TiB ($B27$) in the binary Ti-B alloys, changes to TiB_2 ($C32$) with the addition of Al. The solidification path of the ternary alloys starts with the formation of primary α ($A3$) for an alloy lean in boron (~1at%), and with primary TiB_2 for a higher boron concentration (~5at%). In both cases the system follows the liquidus surface down to a monovariant line where both α and TiB_2 are solidified concurrently. In the final stage, the α phase gives way to γ , presumably by a peritectic-type reaction similar to the one in the binary Ti-Al system. Upon cooling, the α dendrites order to α_2 and later decompose to a lath structure consisting of alternating layers of γ and α_2 .

¹ M. Hyman is Research Assistant and C. McCullough and J.J. Valencia are Assistant Research Engineers, Materials Department; C.G. Levi is Associate Professor of Materials and Mechanical Engineering and R. Mehrabian is Dean of Engineering and Professor of Materials, University of California, Santa Barbara, CA 93106.

INTRODUCTION

Titanium aluminides are under investigation as candidate materials for advanced aerospace airframe and propulsion components. Like other intermetallics, they exhibit high modulus retention with temperature because of the strong bonding and enhanced creep resistance due to the high activation energy required for diffusion in ordered alloys [85Lip]. The low density of titanium aluminides makes them particularly attractive when compared to superalloys on a strength/weight basis [88Bla]. In addition, the high aluminum content increases oxidation resistance by promoting the formation of an alumina-rich film on the surface.

Among the Ti-Al intermetallics, alloys based on the γ -phase exhibit the most promising potential for high temperature applications. The γ -phase has the $L1_0$ structure of nominally equiatomic stoichiometry, but possesses a relatively wide range of homogeneity (49 to 66 %Al¹) [86Mur]. γ -TiAl remains ordered up to near its melting temperature, estimated between 1725 K [73WiM] and 1753 K [86Mur], and shows a higher modulus at 1273 K than Ti does at room temperature [85Lip]. γ -TiAl is lighter and stiffer, and has better creep and oxidation resistance than α_2 -Ti₃Al (DO_{19}) [77Sch,85Lip]. Although both intermetallics suffer from low toughness and ductility at room temperature, γ -TiAl is the more brittle and difficult to process of the two. The very limited plasticity of TiAl has been ascribed to the pinning of the 1/6[112] partial dislocation, which not only hinders slip by reducing the mobility of the [101] and [011] superdislocations, but is also the operating dislocation in twinning [75LSS,85Lip]. On the other hand, these partial dislocations become unpinned at ~973 K facilitating slip and twinning and consequently increasing the duc-

¹ All compositions in atomic percent unless otherwise specified.

tility. Thus, a brittle to ductile transition near 973 K is reported, with the dominant fracture mode changing from cleavage at room temperature to intergranular at 1073 K [80SaL].

Prospects for toughening γ -TiAl are primarily based on crack bridging, either by weakly-bonded fibers in the manner described by Evans et al [85MCE], or by incorporation of ductile phases. Promising results have been achieved in the latter case by dispersing Nb-alloy ductile particles in TiAl using powder metallurgy techniques [88El1]. However, ductile-phase toughening is likely to produce a concomitant reduction in creep resistance.

Improvements in creep properties can be addressed by incorporation of hard second phase particles of two distinct size scales. Firstly, small dispersoids would interact with dislocations to reduce the dislocation-cell size to dimensions comparable to the dispersion spacing and hence improve creep resistance. Numerous rare earth (e.g. Er, Nd, Y) and compound forming metalloids (e.g. B, C, Si) have been added to Ti alloys for dispersion strengthening [84SPB,87RoF]; however, there are only a few reports of dispersoid-forming additions to intermetallics. Since the alloying additions of interest have low solubilities in the solid matrix, the approach normally involves rapid solidification to produce a supersaturated solid solution, followed by solid state precipitation during cooling, consolidation and/or subsequent heat treatment. Stable rare-earth-oxide dispersions produced by RSP have been shown to improve yield and tensile strength, creep resistance and stress-rupture life of titanium at temperatures up to 973 K [84SPB]. However, dispersoid strengthening in α and α_2 -base alloys is limited by rapid coarsening above the α/β transus, due to the more open structure of the bcc Ti solid solution and the disordering of α_2 . On the other hand, the γ -phase does not disorder or transform at high temperatures and should in principle offer a much higher resistance to coar-

sening of dispersoids than the leaner aluminum compositions.

Based on continuum mechanics considerations, reinforcements with dimensions appreciably larger than the dislocation-cell size can also contribute to improved creep resistance. The analysis indicates a creep rate

$$\dot{\epsilon} = A(f,s) (\sigma/\sigma_0)^n \quad (1)$$

where n and σ_0 represent the creep coefficients of the matrix and A is a measure of the effect of the reinforcement, depending on its volume fraction, f , and shape factor, s [88Eva]. Reduced creep rate is predicted for reinforcements on the size scale of $>10 \mu\text{m}$, with rods and discs being more effective than spheres. Since A is a direct multiplier of the matrix creep rate, greater improvement is expected in TiAl, which already has good creep resistance. The relevant matrix microstructure dimension changes from dislocation-cell size to grain size as the operating mechanism changes from dislocation motion to diffusional creep. In the latter case, either large grains are needed or the reinforcement size needs to exceed the grain size of the matrix for improved creep resistance.

The present investigation was motivated on the foregoing discussion. It deals with additions of B to γ -TiAl alloys to obtain stable high temperature dispersoids. The size, shape, composition and crystal structure of the borides are studied by extending the current understanding of microstructural evolution during conventional (relatively slow) solidification of binary Ti-B alloys to the ternary compositions near the binary Ti-Al γ field. Two forthcoming papers will discuss the effects of supercooling and rapid solidification on the microstructure of the boron-containing aluminides, as well as the stability of the dispersoids produced and the effect on mechanical properties.

PHASE EQUILIBRIA

The binary Ti-B system, Figure 1, exhibits three intermetallic compounds¹ in addition to the terminal phases [86MLS]. As expected from Hume-Rothery considerations, the elements should have very limited mutual solubility in each other [86BoF]; the B/Ti atomic radius ratio is 0.66, highly unfavorable for either interstitial or substitutional solid solution. The maximum equilibrium solubility of B is <1% in β -(Ti) at the eutectic temperature, 1813 K, and ~0.2% in α -(Ti) at the peritectoid temperature, 1157 K [86MLS]. Boron is classified as an α -stabilizer, but in reality has a negligible effect on the α/β transition temperature due to its low solubility. On the other hand, solubility extensions as high as 10% B in α -(Ti) have been reported by rapid solidification and ascribed to increased interstitial solubility [86Wha]. It is not clear, however, whether the primary β -phase could accommodate that much B in its interstitial sites, which are considerably smaller.

The highly refractory titanium borides are all based on the same building block: the trigonal prismatic array of six Ti atoms with a B at the center [77Lun]. In the case of TiB_2 the prisms are in a "close packed" array, sharing all their faces with neighboring prisms, see Figure 2. The resulting C32 structure can also be visualized by stacking close packed Ti planes (A) with graphite-like boron planes (H) in an AH AH sequence along the c-axis of the crystal. On the other hand, in the B27 structure of TiB the trigonal prisms are closely packed in only one direction, forming columns with a rectangular base and a central chain of boron atoms whose axis is the [010] direction of the crystal [54DeK]. To account for stoichiometry these columns are only con-

¹ The existence of Ti_3B_4 is still a subject of debate and was not observed in the present experiments.

nected at their edges, with four columns surrounding a boron-free "pipe" of Ti atoms with a trapezoidal cross section, as shown in Figure 2. These crystallographic differences will become relevant in our discussion of the growth morphology of primary borides, see below.

The high temperature equilibrium in the γ -forming range of the Ti-Al phase diagram has been a subject of much debate. An earlier version suggested the presence of a double peritectic cascade, $L + \beta \rightarrow \alpha_2$ and $L + \alpha_2 \rightarrow \gamma$, about the equiatomic composition [73WiM]. However, a more recent thermodynamic assessment predicted a single peritectic $L + \beta \rightarrow \gamma$ with γ forming by a peritectoid reaction between β and γ at a lower temperature [86Mur]. A host of new experimental evidence strongly supports the double peritectic predicted by the earlier diagram, but with α as the intermediate phase instead of α_2 , as shown schematically in Figure 3 [88McC]. Thus, the primary solidification phase in alloys containing ~ 48 to ~ 55 % Al is believed to be the α -(Ti) solid solution (A3), which transforms peritectically to γ upon cooling. Under non-equilibrium conditions the primary α -dendrites transform instead to a lath structure consisting of twin-related variants of γ intertwined with α_2 .

Most of what is known about the ternary Ti-Al-B diagram is limited to the Al-rich corner, which is of interest in the grain refinement of aluminum alloys with TiB_2 additions. There is reasonable agreement that the ternary diagram is divided by a quasibinary equilibrium between (Al) and a diboride, which is TiB_2 according to Maxwell and Hellawell [72MaH] but $TiAl_2B_6$ according to Mondolfo [76Mon]. On the other hand, there is considerable disagreement regarding the solubility of Al in TiB_2 , with some authors suggesting that there is a continuous series of solid solutions between AlB_2 and TiB_2 , which are isomorphous [71MaM, 83ABK], and others indicating that there is negligible mutual solubility [72MaH, 76JoP]. However, this discrepancy is only marginally

relevant to our alloys, which are near the Ti-Al binary. It is generally accepted that there is a region of ternary equilibrium between TiB_2 , $TiAl_3$ and (Al) just below the melting temperature of Al [72MaH, 76Mon]. The primary phases are TiB_2 on the quasibinary side and $TiAl_3$ near the Ti-Al side, with a line of two-fold saturation descending toward the Al-corner and terminating at a ternary reaction $L + TiB_2 + TiAl_3 \rightarrow (Al)$, which is placed at 938 K [76Mon].

EXPERIMENTAL

There are several experimental complications in preparing Ti-Al-B alloys of accurate composition in a reproducible manner. The first one relates to the large differences in melting temperature between TiAl (~ 1750 K) and the available material for alloying, which may be elemental B (2365 K) or TiB_2 (3500 K) in powder form. If either material is added to TiAl the liquid must be significantly superheated to accomplish dissolution and homogenization in a reasonable time. However, the vapor pressure of Al is sufficiently high at the process temperatures to cause significant losses by evaporation and an unpredictable variation in the final composition. Thus, the alloys must be prepared by first dissolving B or TiB_2 in Ti to produce a Ti-B master alloy and then adding the Al to reach the desired composition. Since the B concentrations in these studies were relatively low, the process temperatures during the Al addition were of the order of the eutectic temperature between Ti and TiB_2 , Figure 1, resulting in minimal and more predictable Al losses.

The second problem arises because of contaminants present in the boron sources. Both high purity elemental boron (99.7%) and TiB_2 (99.5%) can typically contain up to 1200 ppm N and up to 5000 ppm O. As a matter of fact, our initial experiments were made with a batch of "pure" TiB_2 which was later

found to contain as much as 3 - 4 wt% N and a similar amount of O. These contaminants, especially nitrogen, can produce spurious second phases which significantly complicate the identification of borides and the elucidation of phase sequencing during solidification, as discussed below. Metallic impurities like Si and Fe are also common in both materials, although they were found to be higher in the elemental B. Thus, extreme care must be exercised in characterizing the actual chemical composition of the raw materials to minimize microstructural features which can lead to erroneous conclusions.

All alloys were prepared by arc-melting in gettered argon atmosphere (<0.1 ppb O₂) using high purity Ti ingots (200 ppm O), 99.99% Al pellets and 99.7% pure, 60 mesh elemental B powder (see analysis in Table I). The binary Ti-B alloy buttons were melted and flipped four times using fairly high power and keeping the metal molten for about 2 minutes each time in order to ensure complete dissolution and homogenization. The Al was then added and the buttons were melted and flipped another four times, but using reduced power and holding times to minimize Al losses.

Two binary and two ternary alloys with the compositions given in Table I were produced in the manner described. The binary compositions were selected on the two sides of the eutectic composition (~7 %B) with the hypoeutectic alloy (BLB¹, 1.3% B) producing primary Ti during initial solidification and the hypereutectic alloy (BHB¹, 9.7% B) producing primary TiB. The corresponding ternaries, TLB and THB¹, were designed with an Al:Ti ratio slightly above equiatomic, which in the binary Ti-Al system would lie in the equilibrium single phase γ field.

¹ BLB and BHB refer to binary low boron and binary high boron alloys, respectively. Similarly, TLB and THB refer to ternary low and high boron alloys, respectively.

Extensive characterization of the four alloys was performed by optical metallography, scanning and transmission electron microscopy. A staining technique developed by Fenish [64Fen] for identification of borides in the binary Ti-B system was extended to the ternary system and consistently used in the metallographic analysis. In this technique the specimens are electrolytically etched in a 25vol% NH₄OH solution at 30 V DC using a Buehler Electromet III apparatus. While the α -(Ti) matrix should appear blue with purple overtones, the different borides were reported to stain as follows: orange-rust for TiB, light grey-tan for Ti₃B₄ and yellow-white for TiB₂ [64Fen]. The photomicrographs were taken in a Nikon Epiphot Metallograph using Ektachrome 50 color slide film.

Boride particles were also prepared for examination using two different matrix dissolution techniques. The boride morphology may be revealed by deep etching a polished section in hot sulfuric acid, but the process was found to be rather slow. Extraction of the particles was accomplished by electrolytic digestion of the matrix using a 7vol% solution of HCl in methanol and a voltage of 20 V DC. The residue was filtered, washed first in 75vol% HNO₃, and subsequently in a solution of 30 g ZnCl₂, 25 ml HNO₃ and 100 ml H₂O to remove hydrides, rinsed in methanol and air dried. SEM was performed in a JEOL-840 microscope equipped with a Tracor EDS analysis system and the TEM in a JEOL-2000FX microscope equipped with Tracor EDS and Gatan EELS systems.

MICROSTRUCTURES OF BINARY ALLOYS

Optical photomicrographs of the stained solidification microstructures are given in Figure 4. As expected from the phase diagram, the hypereutectic BHB alloy contains large primary TiB particles which appear golden yellow¹, Figure 4(a), in a matrix of eutectic α -(Ti) + TiB. The primary boride is highly faceted and exhibits a hollow needle morphology, as shown in Figure 5(a), with typical transverse dimensions upwards of 10 μm and lengths of 100 μm or more. The calculated amount of primary boride is about 5 vol% and corresponds reasonably well with the experimental observations. The eutectic monoboride also exhibits a faceted needlelike morphology, with typical dimensions up to 2 μm across and 10 - 50 μm in length. Note that some of the coarser eutectic needles are also hollow, as shown in Figure 5(b), in spite of their much finer scale when compared with the primary TiB. The relative amount of eutectic monoboride should be about 8 vol% according to the phase diagram.

The low-boron hypoeutectic alloy, BLB, exhibits primary β -(Ti) growth as indicated by the orthogonal dendritic pattern characteristic of bcc growth in Figure 4(b). The interdendritic segregate is eutectic Ti + TiB, with a size scale and morphology comparable to those in the hypereutectic alloy, BHB. The calculated amount of eutectic segregate is approximately 10 vol%, which seems consistent with that observed in the microstructure.

Transmission electron microscopy revealed three types of second phase particles in the binary Ti-B alloys, all needlelike and indexing to the orthorhombic structure of TiB (B27) with lattice parameters $a = 612 \text{ pm}$, $b = 306 \text{ pm}$

¹ The colors do not correspond exactly to those described by Fenish, who indicated that the actual hues could vary with composition and etching conditions. We also found them to change with the type of film and illumination. Nevertheless, the darker shade of yellow shown by TiB when compared with TiB_2 is relatively consistent with Fenish's scale.

and $c = 456$ pm. In all cases the needle axis was found to be parallel to the [010] axis of the B27 cell, see Figure 2. The matrix is polycrystalline α -(Ti) resulting from the solid state transformation of the solidified β -phase.

The primary monoboride needles, observed only in the BHB alloy, are single crystals with occasional stacking faults. Figure 6 shows a cross section of a primary needle with [010] and [011] zone axis patterns (ZAP). Analysis of several ZAPs indicated that the crystallographic facets in these needles are always of the type (100), (101) and (101). There is no evident crystallographic relationship between the primary borides and the surrounding matrix, but apparently there is one with the α -Ti trapped inside the needle. For the case of Figure 6 the relationship was found to be close to

$$(10\bar{1}1)_\alpha // (201)_{\text{TiB}}$$

$$(10\bar{1}\bar{1})_\alpha // (001)_{\text{TiB}}$$

$$(1\bar{2}10)_\alpha // (010)_{\text{TiB}}$$

and when this is translated through the Burgers relation for the $\beta \rightarrow \alpha$ transformation, the orientation relationships become exactly

$$(001)_{\text{TiB}} // \{0\bar{1}1\}_\beta$$

$$(010)_{\text{TiB}} // \{111\}_\beta$$

$$(100)_{\text{TiB}} // \{\bar{2}11\}_\beta$$

The second boride morphology observed in TEM corresponds to the eutectic TiB needles, shown in Figure 7. The eutectic structure is only poorly developed in the hypoeutectic BLB alloy, with clusters of needles appearing in the prior β interdendritic spaces, as shown in Figures 4(b) and 7(a). The hypereu-

tectic BHR alloy reveals a much more defined eutectic morphology, Figure 7(b), with needles 10 to 20 μm long extending through the transformed β -(Ti) matrix. The needles are all single crystals with their axis parallel to the [010] direction of the B27 unit cell, see Figure 7(c). In tilting to this zone axis, Figure 7(f), all fringing effects at the particle/matrix interface disappear, giving rise to sharply defined boundaries which indicate that the planes enclosing this crystal lie perpendicular to the plane of the image. The eutectic needles typically have an elongated cross section, ≤ 500 nm thick and $\leq 2 \mu\text{m}$ wide, where the long faces are consistently (100) planes and the shorter planes forming a wedge shape are (101) and (10 $\bar{1}$), as indicated in Figure 7(d). Stacking faults and/or twins are often seen running across the crystal, seemingly parallel to the (100) faces. As with the primary borides, the eutectic needles had no orientation relationship with the surrounding α -(Ti) matrix or the prior β -(Ti).

Closer examination of Figure 7(c) reveals a third type of TiB needle, much finer than the eutectic particle next to it. These particles had typical dimensions of 100-200 nm thick and up to $\sim 5 \mu\text{m}$ long, and were consistently found within the α -(Ti) grains. Figure 8 shows a region of α -(Ti) viewed down the [0001] direction, containing three variants of the fine TiB needles at 60° from each other. The SAD patterns in this figure show $[0001]_{\alpha}$ and $[001]_{\text{TiB}}$ zone axes, clearly revealing the following orientation relationship between the needles and the matrix

$$\begin{aligned}(010)_{\text{TiB}} & // \{1\bar{2}10\}_{\alpha} \\(100)_{\text{TiB}} & // \{10\bar{1}0\}_{\alpha} \\(001)_{\text{TiB}} & // (0001)_{\alpha}\end{aligned}$$

Furthermore, the long axes of the needles, which were indexed as $[010]_{\text{TiB}}$, are parallel to the close-packed directions on the α -(Ti) basal plane, $\langle 11\bar{2}0 \rangle_\alpha$. However, assuming a Burgers relation for the $\beta \rightarrow \alpha$ transformation, it may be demonstrated that there is no specific relationship between these fine TiB needles and the prior β -(Ti). It was thus concluded that these finer needles must have formed as a result of solid state precipitation within the α phase during cooling.

MICROSTRUCTURES OF TERNARY ALLOYS

The most evident feature of the ternary alloy micrographs in Figure 4 is that, as in the case of the binaries, the higher boron alloy THB contains large primary boride particles whereas the leaner one, TLB, does not. It is also evident that the borides have a different morphology and stain a lighter yellow color, indicative of TiB_2 according to the staining procedure of Fenish [64Fen]. It should be noted, however, that the color coding developed for boride identification in binary Ti-B is not necessarily applicable to the ternary alloys, where the presence of Al could affect the nature of the film produced by the electrolytic etching. Nevertheless, the TEM analysis described below confirms that the boride in this case is indeed TiB_2 , confirming that the staining technique may be extended to the ternary system.

Apart from the presence of the borides, the matrix microstructure has essentially the same constituents as in the binary Ti-Al alloy, namely α dendrites transformed upon cooling to a mixture of $\alpha_2 + \gamma$ laths and surrounded by γ segregate [87Val]. Typical TEM views of the metallic phases are shown in Figure 9. The lath constituent has an average spacing of $\sim 1.2 \mu\text{m}$, comparable to that observed in a binary arc-button of similar composition [87Val], but con-

tains a higher γ/α_2 ratio; the thicknesses of the γ and α_2 regions in Figure 9(b) are approximately 1 μm and 0.1-0.2 μm , respectively. The average composition of the lath constituent is 48 to 49 %Al and that of the interdendritic γ -segregate is 53 to 55 %Al. In general, the aluminum content is higher in both phases for the alloy richer in boron, since more of the Ti is combined in the borides; the estimated Al:Ti ratio in the matrix is about 1.11 and 1.04 for the higher (5.4%B) and lower (0.9%B) boron alloys, respectively. The measured amount of interdendritic segregate (predominantly γ) also increases significantly, going from ~5 vol% in the TLB alloy to ~25 vol% in the THB alloy. Finally, the segregate spacings in the ternary alloys were significantly coarser than those in the binary alloys, e.g. 106 μm for TLB versus 16 μm for the BLB material.

The primary TiB_2 particles in the THB alloy are somewhat smaller, 10 to 20 μm across, than the primary borides in the binary alloy and exhibit a blocky morphology instead of the needle shape characteristic of TiB --compare Figures 4(a) and (c). Figure 5(c) shows an SEM view of primary TiB_2 particles extracted by electrolytic dissolution of the matrix. Note the clear hexagonal symmetry of the crystal and the stepwise growth along the c-axis. It was also observed that these borides tend to grow in clusters, Figure 5(c), and are invariably found within the lath microconstituent of the matrix, Figure 4(c), suggesting that they acted as nucleation sites for the α phase. The relative amount of primary TiB_2 in the THB alloy was less than 5 vol%.

The ternary alloys also contain a needlelike boride, typically 0.5 to 2 μm thick and 5 to 20 μm long, observed both within the transformed dendrites and the interdendritic segregate, as shown in Figures 4(c) and (d). Furthermore, a phase in the form of thin (<<1 μm) curly plates, Figure 5(d), was sometimes observed within the γ segregate in the ternary alloys, and occasion-

ally in combination with the lath structure.

Both the blocky and needlelike boride particles were identified as TiB_2 by TEM analysis, with lattice parameters for the C32 cell of $a = 303 \text{ pm}$ and $c = 323 \text{ pm}$. Furthermore, EDS and EELS spectra showed no detectable Al in these phases. Figure 10 shows a thinned area of primary TiB_2 , approximately 10 by 20 μm in size, with hexagonal symmetry. The [0001] and [1 $\bar{2}$ 13] ZAPs presented indicate that the c-axis of the C32 structure is perpendicular to the plane of the image, and that all the crystal facets are prism planes of the type {10 $\bar{1}$ 0}. No clear evidence was found of an orientation relationship between the primary TiB_2 and either phase in the lath structure, or the parent α -phase.

Figure 11 shows longitudinal and transverse views of TiB_2 needles within the lath structure. Diffraction trace analysis indicates that the long axis of the needle is parallel to the [0001] direction in the C32 crystal, and the facets observed in Figure 11(b) are again {10 $\bar{1}$ 0} prism planes. As with the primary diboride, no orientation relationship was evident between the needles and the surrounding matrix. Similar observations were made for the diboride within the interdendritic segregate.

TEM views of the curly plates detected in the ternary alloys are given in Figure 12. These were found to contain only Ti and B, although a few specimens showed traces of Al in EDS, with a crystal structure that has been tentatively identified as tetragonal. The sparse population of these phases has prevented a conclusive identification up to now. Boride precipitation in the solid state, clearly evident in the binary Ti-B, has not been observed so far in the ternary alloys.

It is appropriate at this point to show an example of the microstructural features that may arise from an excessive level of nitrogen in the ternary alloys. The specimen in Figure 13 was prepared with TiB_2 inadvertently conta-

minated with about 3 wt% nitrogen. The primary borides, which are still TiB_2 , are frequently covered by multiple flakes with a hexagonal crystal structure and a Ti:Al ratio of 2. It is believed that these phases are nitrides of the type $(Ti_2Al)_xN_y$ or perhaps more complex boronitrides, although further clarification of the issue was not pursued. Furthermore, the tetragonal curly phases were much more numerous in the contaminated alloy, suggesting that their origin could be associated with the everpresent N. However, microchemical analysis revealed no nitrogen in any of the curly plates. On the other hand, significant amounts of Al (Ti:Al \sim 2) were detected in the tetragonal phase found in the contaminated alloy, while that in the THB and TLB alloys rarely showed any Al.

DISCUSSION

Elucidation of the solidification "path" for γ -TiAl alloyed with boron appears to be reasonably straightforward¹, although a quantitative description is hindered by the shortage of information on phase boundaries and invariant reactions in the relevant regions of the ternary diagram. It is quite evident that the liquidus surface is dominated by the very high melting temperature of TiB_2 (\sim 3500 K) and that it drops down rapidly from the quasibinary Al- TiB_2 to a line of monovariant equilibrium below the melting temperature of γ -TiAl (\sim 1750 K). This monovariant line must be close to the binary Ti-Al side of the ternary diagram, given that as little as 5 %B produces primary TiB_2 , however in a small volume fraction. It is not clear at this time whether this line terminates at a ternary eutectic or follows a peritectic cascade, similar to

¹ Phase sequencing during solidification of the binary alloys is presumed to be readily deduced from the phase diagram and is not discussed.

the one shown in the binary diagram, until it merges with the $TiB_2 + TiAl_3$ line near the Al-rich corner [76Mon].

Solidification of these alloys can thus start with the formation of primary TiB_2 or primary α -(Ti), depending on the boron content, with the liquid composition descending down the liquidus surface until it meets the monovariant line, whereupon both α -(Ti) and TiB_2 appear to grow from the liquid. Upon nucleation of γ in the interdendritic spaces, the last liquid solidifies as a mixture of γ , TiB_2 and perhaps the still unidentified tetragonal phase. It is not clear, however, whether the latter is a true phase in the ternary Ti-Al-B system or it is associated with contamination effects from the small amounts of N present in the boron. Moreover, the transformations of the solidification structure upon cooling appear to be limited to the decomposition of the α -(Ti) phase into the lath mixture of $\alpha_2 + \gamma$.

The evolution of TiB_2 as the equilibrium boride in the γ alloys offers a greater potential for dispersion strengthening vis-a-vis the formation of TiB in the Ti-rich α or α_2 alloys. Not only are the γ alloys insensitive to disordering and phase transformations that accelerate dispersoid coarsening at high temperature, but TiB_2 should be a more stable dispersoid than TiB as reflected by their respective melting temperatures. On the other hand, it may be more difficult to suppress the nucleation of TiB_2 in a supercooled melt in order to produce a supersaturated α -(Ti) solid solution. Undercooling experiments to be reported in a forthcoming paper will address this issue.

The differences in boride morphologies can be rationalized to some extent based on their crystal structure and the stage of the solidification process during which they evolved. In the case of TiB , the preferred growth direction is always [010], which is the axis of the boron chains formed by the stacking of trigonal prisms, see Figure 2. The (010) planes perpendicular to this di-

rection also have a 1:1 stoichiometry, providing sites for the attachment of both Ti and B atoms on the same plane. Consider now the facets of the needle crystals. If the bond strength in TiB is B-B > Ti-B > Ti-Ti as estimated from the interatomic distances [54DeK], one would expect Ti planes bounding the B chains in the crystal to have lower interfacial energies and thus be exposed to the liquid. Figure 14 shows that the packing density of Ti atoms decreases in the following order: (100) > (101) and (10 $\bar{1}$) > (001). Note also that growth along [100] involves alternating B and Ti planes, whereas growth along [001] involves planes of equiatomic stoichiometry. One can thus conclude that the (001) planes are likely to exhibit the fastest growth, leaving the crystal bound by the (100) and {101} type facets. It is not clear, however, why the TiB needles are hollow, although this type of morphology has been associated with dendritic-like growth instabilities in Ti₅Si₃ [71CrY] and Cu₆Sn₅ [65Dav, 71CrY].

The blocky morphology of primary TiB₂ shown in Figure 4(c) may also be related to its crystal structure. In this case the trigonal prisms are closely packed in all directions, with growth along the [0001] and <1100> directions involving alternating Ti and B layers in both cases. It may be argued that the basal plane should have a lower lateral growth velocity than the prism plane, based on its higher relative packing density (1.23:1). However, the interplanar spacing between basal planes (328 pm) is larger than that between prism planes (262 pm) by an equivalent amount, such that the growth velocity normal to the plane should be approximately the same in both cases, barring any significant differences in attachment kinetics. Indeed, the primary crystals growing unconstrained from the melt tend to have fairly equiaxed shapes, as shown in Figure 4(c). The larger flat prismatic facets suggest that the two-dimensional nucleation process of the layers may be easier on the basal plane,

but a physical rationale for this preference could not be elucidated from the information available.

The needlelike eutectic growth of TiB is not surprising in view of the crystallographic considerations outlined for the primary monoboride. On the other hand, the TiB_2 evolving in conjunction with α -(Ti) and γ -(TiAl) through the monovariant and/or invariant reactions in the ternary system is markedly different from the primary diboride. While the crystal facets are identical in both cases, the secondary TiB_2 grows preferentially along the [0001] axis of the C32 structure. This may be ascribed to the constraint imposed by the metallic phase growing concurrently with the boride; Jackson and Hunt's treatment of coupled eutectic growth predicts a rod-like morphology for the second phase when its volume fraction is relatively small [66JaH].

Finally, the solid state precipitation of TiB in the binary alloys poses an interesting question. The experimental evidence suggests that the TiB needles must have formed by precipitation within the α -(Ti) + TiB field, even though the solubility of B in β -(Ti) decreases more significantly with temperature. One may hypothesize that the cooling rate in the arc-melting process is sufficiently high to prevent the precipitation of TiB when cooling through the β -(Ti) + TiB field, but not to suppress the $\beta \rightarrow \alpha$ transformation, which can be quite rapid. TiB may thus precipitate from the supersaturated α upon further cooling, developing the observed orientation relationship.

SUMMARY

Boron additions to γ Ti-Al alloys offer some potential benefits for dispersion strengthening when compared with α and α_2 based alloys. Not only is the γ matrix stable and ordered up to very high temperatures, with the conse-

quent reduction in diffusion rates, but the reinforcing boride phase changes from TiB in the α alloys to a much more stable TiB₂ in the γ alloys. Thus, if the diboride were to be finely dispersed by rapid solidification, it should be more stable to coarsening than the monoboride.

Except for the presence of the diboride phases, solidification of the TiAl-(0.9 to 5.4)%B results in a similar matrix microstructure to that of the binary γ alloy. The primary phase is α -(Ti) for the leaner boron content and TiB₂ for the higher boron alloy. In either case, the liquid composition moves down the liquidus surface until it reaches a monovariant line, probably of the type L \rightarrow α + TiB₂, wherein both phases appear to solidify concurrently. Solidification ends with the formation of γ in the interdendritic spaces, again mixed with TiB₂ plus a still unidentified tetragonal phase. It was shown that the amount of segregate increases with B content, presumably because more of the Ti is combined in the diboride, leading to a higher Al:Ti ratio in the matrix.

ACKNOWLEDGEMENTS

This research was sponsored by the Defense Advance Projects Agency under grant N00014-86-K-0178, monitored by the Office of Naval Research. The program director at DARPA is Dr. P.A. Parrish and the program monitor at ONR is Dr. S. Fishman. Discussions with Prof. A.G. Evans are gratefully acknowledged.

REFERENCES

- [54Dek] B.F. Decker and R. Kasper: **Acta Cryst.**, 1954, vol. 7, pp. 77
- [64Fen] R.G. Fenish: Report No. NRM-138, Union Carbide Corp., Parma Research Center, Parma, OH, 1964.
- [65Dav] G. J. Davies: in **High Temperature Materials**, John Wiley & Sons Inc., New York, NY, 1965, pp. 603-650.
- [66JaH] K.A. Jackson and J.D. Hunt: **Trans. AIME**, 1966, vol. 236, pp. 1129-42.
- [71CrY] F. W. Crossman and A.S. Yue: **Metall. Trans.**, 1971, vol. 2, pp. 1545-1555
- [71MaM] J.A. Marcantonio and L.F. Mondolfo: **Metall. Trans.**, 1971 , vol. 2, pp. 465-471.
- [72MaH] I. Maxwell and A. Hellawell, **Metall. Trans.**, 1972, vol. 3, pp. 1487-1493.
- [73WiM] L.A. Willey and H. Margolin: in **Metals Handbook**, 8th Ed., vol. 8, American Society for Metals, Metals Park, OH, 1973, p. 264.
- [75LSS] H.A. Lipsitt, D. Shechtman, and R.E. Shafrik: **Metall. Trans. A**, 1975, vol. 6A, p. 1991.
- [76Mon] L. F. Mondolfo: **Aluminum Alloys, Structure and Properties**, Butterworths, London, UK, 1976, pp. 437-9.
- [76JoP] G.P. Jones and J. Pearson: **Metall. Trans.**, 1976, vol. 7B, pp. 223-234.
- [77Lun] T. Lündstrom: in **Boron and Refractory Borides**, ed. V. I. Matkovich, Springer-Verlag Berlin Heidelberg, New York, NY, 1977, pp. 351-376.
- [77Sch] R.E. Schafrik: **Metall. Trans.**, 1977, vol. 8a, pp. 1003-1006.

- [80SaL] S.M.L. Sastry and H.A. Lipsitt: in **Titanium '80: Science and Technology**, vol 2, ed. by H. Kimura and O. Izumi, The Metallurgical Society, Warrendale, PA, 1980, pp. 1231-1243.
- [83ABK] L. Arnberg, L. Bäckerud and H. Klang: in **Solidification Technology in the Foundry and the Cast House**, Bartholomew Press, Surrey, UK, 1983, pp. 89-92.
- [84SPB] S.M.L. Sastry, T.C. Peng and L.P. Beckerman: **Metall. Trans. A**, vol. 15A, 1984, pp. 1465-1474.
- [85Lip] H.A. Lipsitt: **Mat. Res. Soc. Symp. Proc.**, 1985, vol. 39, Materials Research Society.
- [85MCE] D.B. Marshall, B.N. Cox, and A.G. Evans: **Acta Metall.**, 1985, vol. 33, No. 11, pp. 2013-2021.
- [86BoF] H.B. Bomberger and F.H. Froes: in **Titanium Rapid Solidification Technology**, ed. F.H. Froes and D. Eylon, The Metallurgical Society, Warrendale, PA, 1986, pp. 21-43.
- [86MLS] J.L. Murray, P.K. Liao, and K.E. Spear: in **Binary Alloy Phase Diagrams**, ed. T.B. Massalski, ASM International, Metals Park, OH, 1986, p. 392.
- [86Mur] J.L. Murray: in **Binary Alloy Phase Diagrams**, ed. T.B. Massalski, ASM International, Metals Park, OH, 1986, p. 173.
- [86Wha] S.H. Whang: **J. Mater. Sci.**, 1986, vol. 21, pp. 2224-38.
- [87Rof] R.G. Rowe and F.H. Froes: in **Processing of Structural Metals by Rapid Solidification**, ed. F.H. Froes and S. J. Savage, ASM International, Metals Park, OH, 1987, pp. 163-174.
- [87Val] J.J. Valencia, C. McCullough, C.G. Levi and R. Mehrabian: **Scripta Metall.**, 1987, vol. 21, pp. 1341-6.
- [88Bla] M.J. Blackburn: unpublished research.

- [88Ell] C.K. Elliot, G.R. Odette, G.E. Lucas and J.W. Scheckherd: in **High Temperature/High Performance Composites**, Proceedings of the MRS Spring Meeting, Reno, Nevada, 1988 (in press).
- [88Eva] A.G. Evans: unpublished research.
- [88McC] C. McCullough, J.J. Valencia, H. Mateos, C.G. Levi, R. Mehrabian, and K.A. Rhyne: **Scripta Metall.**, 1988, vol. 22 (in press).

Table I. Chemical compositions of the alloys and boron
source materials used in the investigation

	Al	B	Al:Ti	O	N	C	Fe	Cu	Si
	at%	at%	at:at	(all impurities in weight percent)					
BHB alloy		9.7		0.067	0.0061	0.022	0.09		
BLB alloy		1.3		0.063	0.0048				
THB alloy	48.3	5.4	1.04	0.064	0.0097	0.021	0.11		
TLB alloy	50.3	0.9	1.03	0.075	0.0052	0.016			
Boron powder				0.055	0.0078	0.31	0.22	0.017	0.012
TiB ₂ powder				3.27	3.48	1.35			

LIST OF FIGURES

- Figure 1.** Titanium-Boron binary phase diagram from [86MLS]. The maximum solubility of B in β -(Ti) is <1% at the eutectic temperature and ~0.1% at the peritectoid, while that in α -(Ti) is ~0.2%.
- Figure 2.** Schematic of the atomic packing in TiB and TiB_2 . Note the relationship between the crystal structures and the basic trigonal prismatic arrangement of Ti atoms around each B atom. The TiB projection is on the (010) planes, and the shaded area represents the cross section of a boron-free "pipe". The TiB_2 projection is on the (0001) plane.
- Figure 3.** Schematic of the modified Titanium Aluminum phase diagram in the vicinity of the γ -field. The solid-solid equilibrium between β , α and γ has been based on high temperature X-ray diffraction experiments between 42 and 50 at%Al [88McC]. The liquidus and solidus approximately correspond to those suggested by [73WiM], while the α_2 and $\alpha_2 + \gamma$ fields are depicted as in the recently assessed phase diagram [86Mur].
- Figure 4.** Optical photomicrographs of the as-cast alloys prepared by electrolytic staining: (a) BHB alloy, Ti-9.7B, (b) BLB alloy, Ti-1.3B, (c) THB alloy, Ti-48.3Al-5.4B, (d) TLB alloy, Ti-50.3Al-0.9B. Note the differences in color and morphology between the primary borides in (a) and (c).
- Figure 5.** SEM views of the different boride morphologies in the binary and ternary alloys. (a) Deep etched surface of the BHB alloy showing a hollow TiB needle; (b) TiB eutectic needles, some of which are also hollow; (c) Cluster of primary TiB_2 particles extracted from the THB alloy clearly revealing the hexagonal symmetry; and (d) Secondary boride phases in the ternary alloys.
- Figure 6.** Cross sectional TEM view of a primary TiB single crystal needle showing [010] and [011] zone-axis patterns. The facets of the crystal were invariably of the (100), (101) and (101) type.
- Figure 7.** TEM images of eutectic TiB particles in the binary alloys: (a) is from the interdendritic segregate in the BLB alloy, while (b) shows a well developed eutectic morphology in the BHB alloy. (c) and (d) are longitudinal and transverse views of eutectic needles, accompanied by their respective ZAPs in (e) and (f). Note the correspondence between the crystallographic facets of the needle in (d) and those of the primary TiB in Figure 6.
- Figure 8.** Three variants of TiB needles precipitated in the solid state with their corresponding diffraction patterns. The plane of the image is parallel to the basal plane of the α -(Ti) matrix. The [010] axes of the three needles fall on the basal plane and are parallel to the $\langle 11\bar{2}0 \rangle$ directions of α -(Ti).

- Figure 9. Ternary alloy matrix showing the $\alpha_2 + \gamma$ lath structure characteristic of transformed α -(Ti) dendrites, in contact with interdendritic γ segregate, (a). The lath constituent in (b) is predominantly γ , with a typical spacing of $\sim 1.2 \mu\text{m}$.
- Figure 10. Cross sectional TEM view of a primary TiB_2 single crystal showing the [0001] and [1 $\bar{2}$ 13] zone axis patterns. The plane of the image is parallel to the basal plane and the facets are all of the type {1010}.
- Figure 11. Longitudinal (a) and transverse (b) views of secondary TiB_2 needles in the ternary alloys, with their corresponding ZAP's. The axis of the needle is parallel to the c-axis of the C32 structure and the facets in (b) are all prism planes.
- Figure 12. TEM images of the curly-plate second phases tentatively indexed as having a tetragonal structure.
- Figure 13. SEM view of the primary TiB_2 in a ternary alloy contaminated with nitrogen. Note the petal-like phases of composition $(\text{Ti}_2\text{Al})_x\text{By}$ attached to the boride particles.
- Figure 14. Relationship between the atomic arrangement in TiB and the macroscopic facets shown by the monoboride needles. The crystal is believed to preferentially expose Ti faces to the melt.

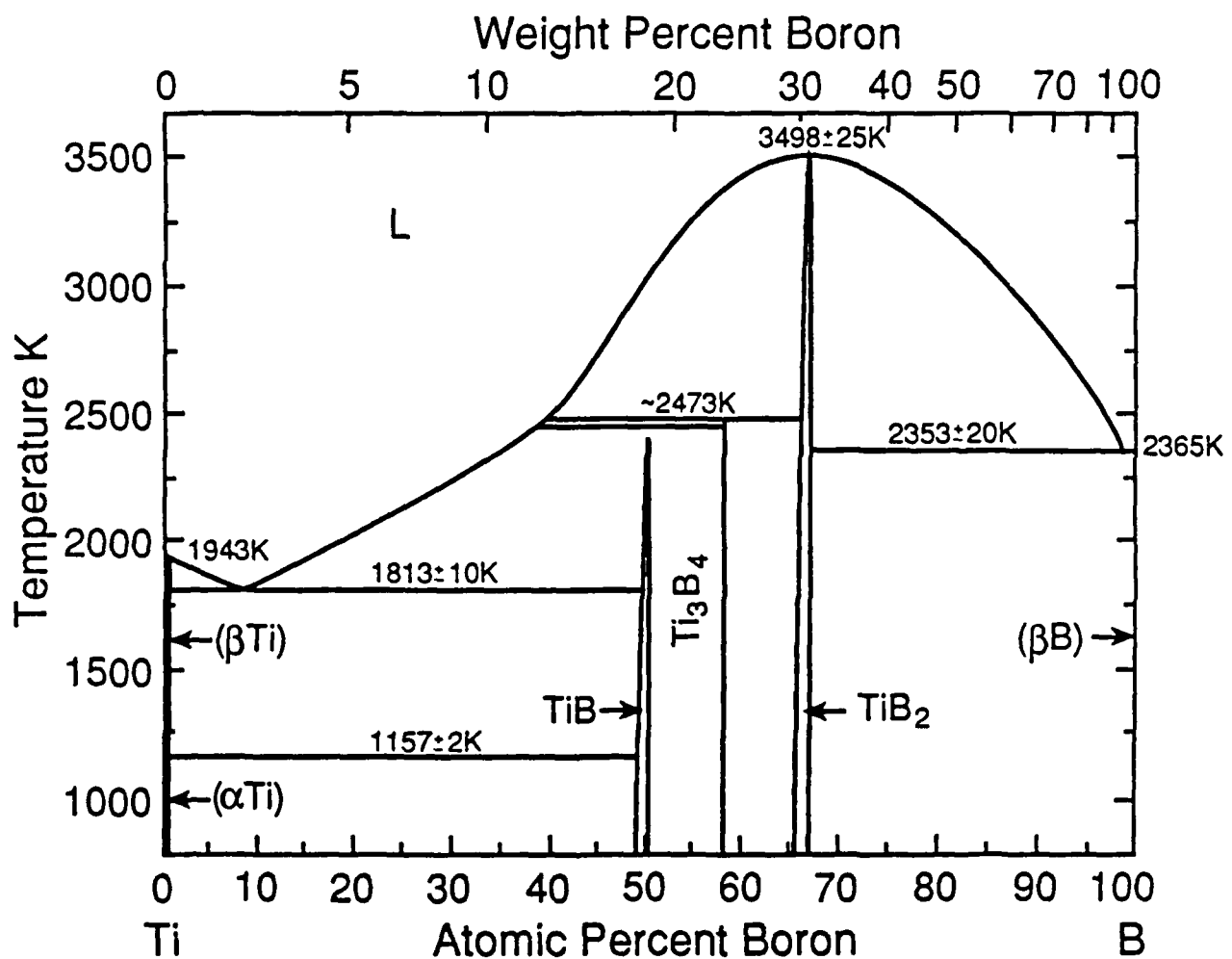


Figure 1. Titanium-Boron binary phase diagram from [86MLS]. The maximum solubility of B in $\beta\text{-}(\text{Ti})$ is <1% at the eutectic temperature and ~0.1% at the peritectoid, while that in $\alpha\text{-}(\text{Ti})$ is ~0.2%.

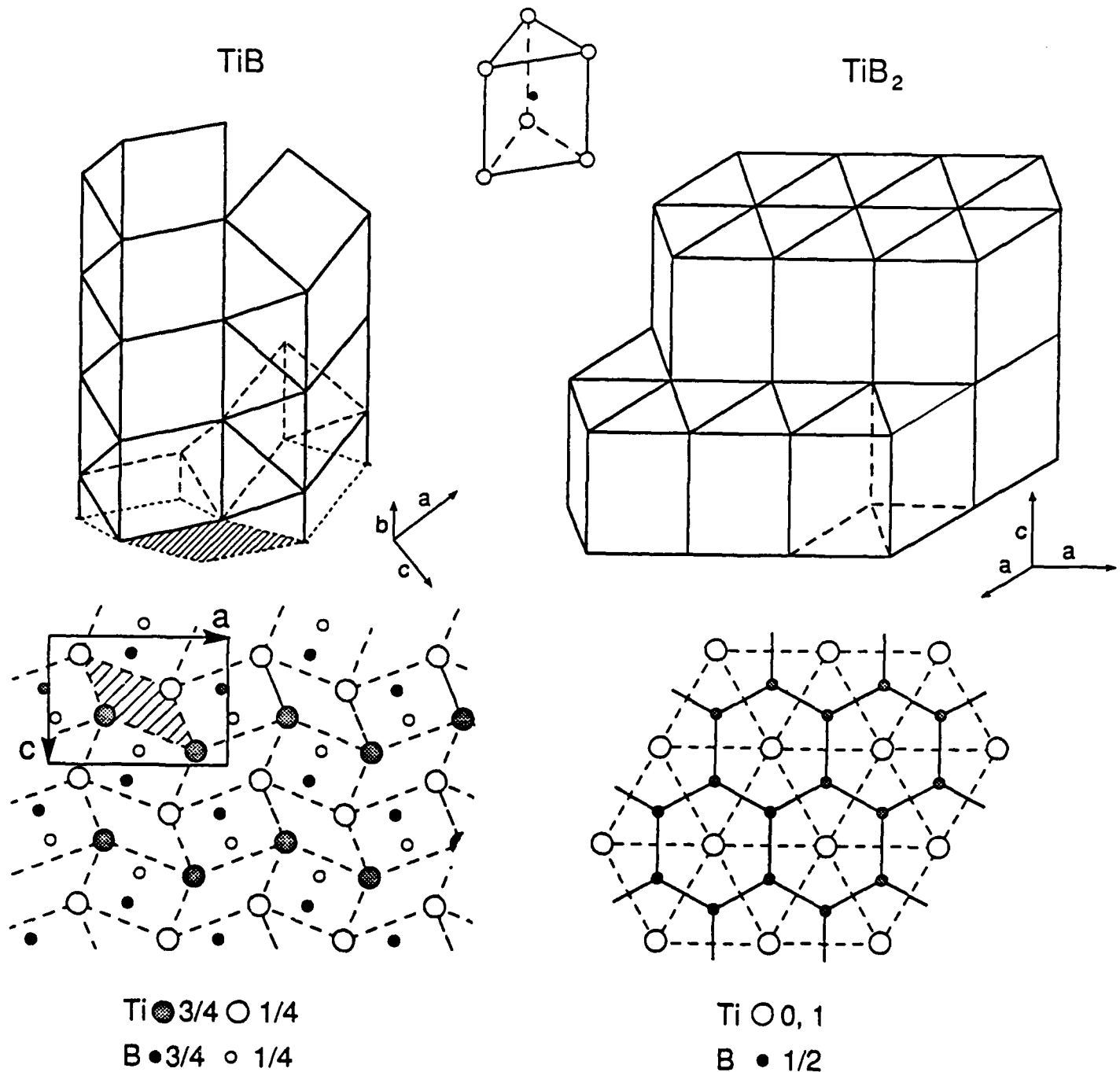


Figure 2. Schematic of the atomic packing in TiB and TiB_2 . Note the relationship between the crystal structures and the basic trigonal prismatic arrangement of Ti atoms around each B atom. The TiB projection is on the (010) planes, and the shaded area represents the cross section of a boron-free "pipe". The TiB_2 projection is on the (0001) plane.

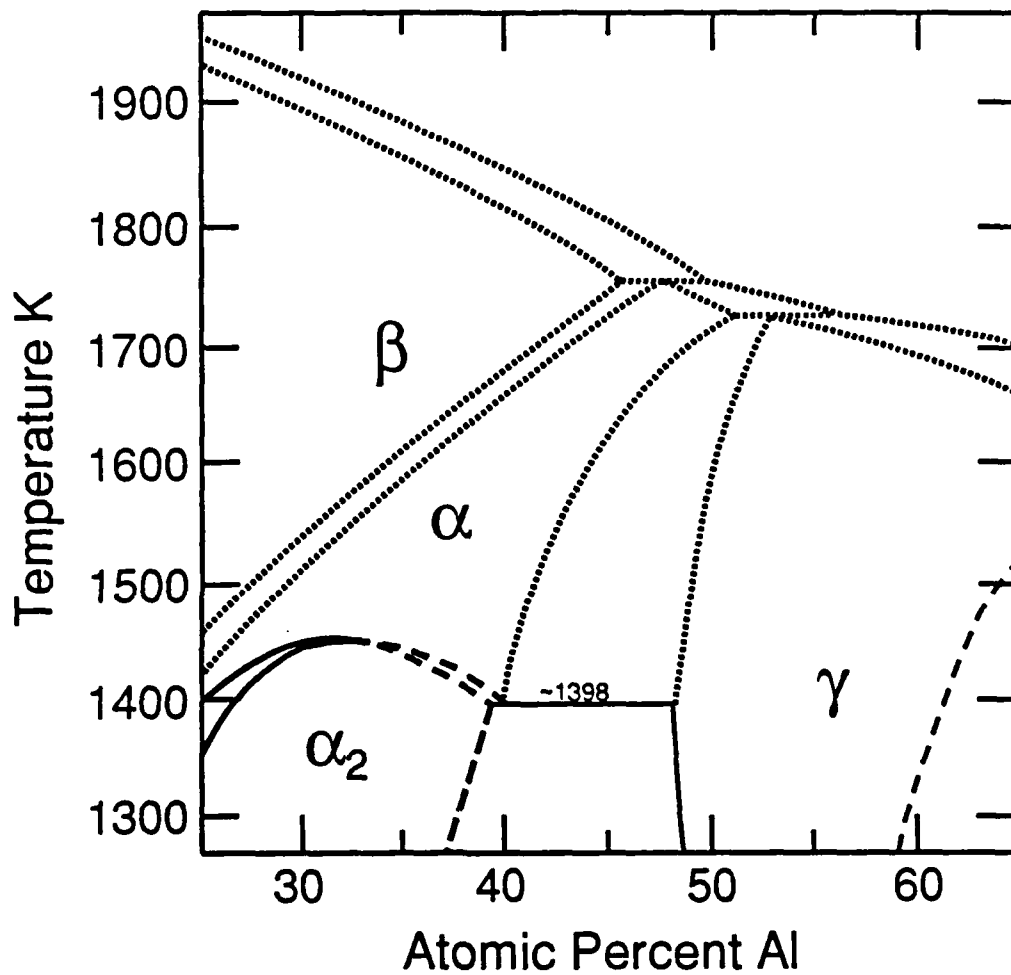


Figure 3. Schematic of the modified Titanium Aluminum phase diagram in the vicinity of the γ -field. The solid-solid equilibrium between β , α and γ has been based on high temperature X-ray diffraction experiments between 42 and 50 at%Al [88McC]. The liquidus and solidus approximately correspond to those suggested by [73WiM], while the α_2 and $\alpha_2 + \gamma$ fields are depicted as in the recently assessed phase diagram [86Mur].

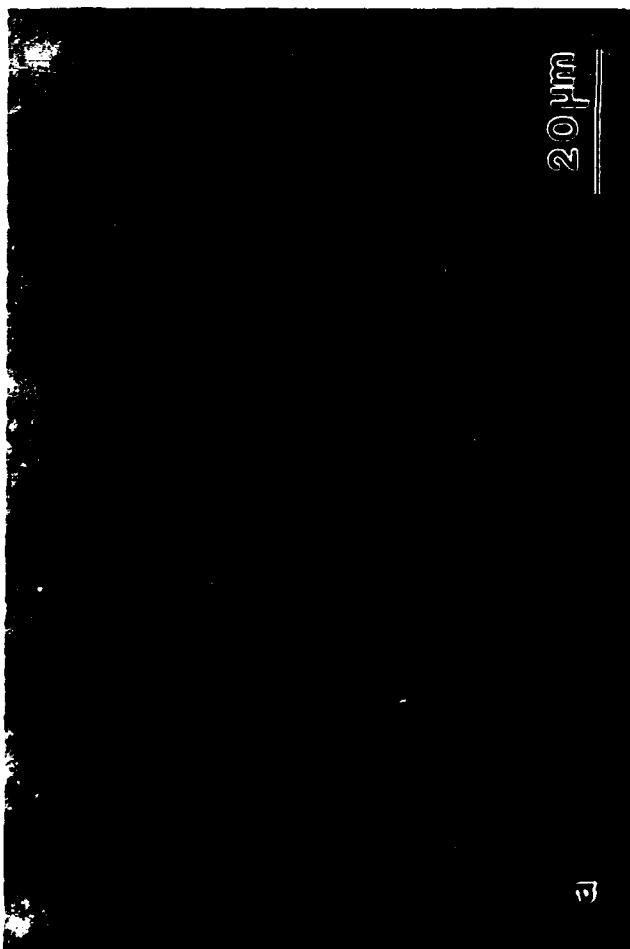


Figure 4. Optical photomicrographs of the as-cast alloys prepared by electrolytic staining: (a) BH alloy, Ti-9.7B, (b) BLB alloy, Ti-1.3B, (c) THB alloy, Ti-48.3Al-5.4B, (d) TLB alloy, Ti-50.3Al-0.9B. Note the differences in color and morphology between the primary borides in (a) and (c).

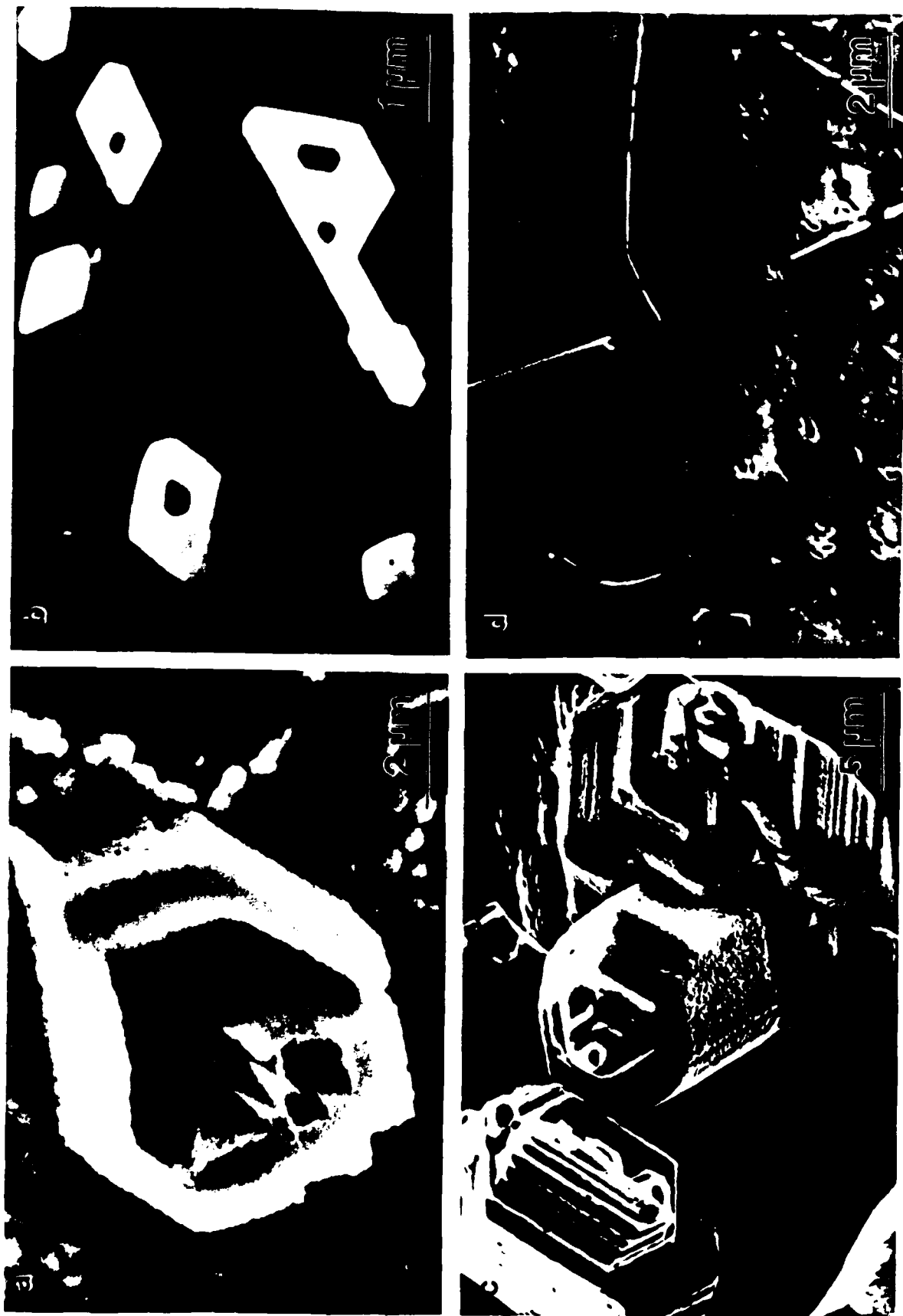


Figure 5. SEM views of the different boride morphologies in the binary and ternary alloys. (a) Deep etched surface of the BH₂ alloy showing a hollow TiB needle; (b) TiB eutectic needles, some of which are also hollow; (c) Cluster of primary TiB₂ particles extracted from the THB alloy clearly revealing the hexagonal symmetry; and (d) Secondary boride phases in the ternary alloys.

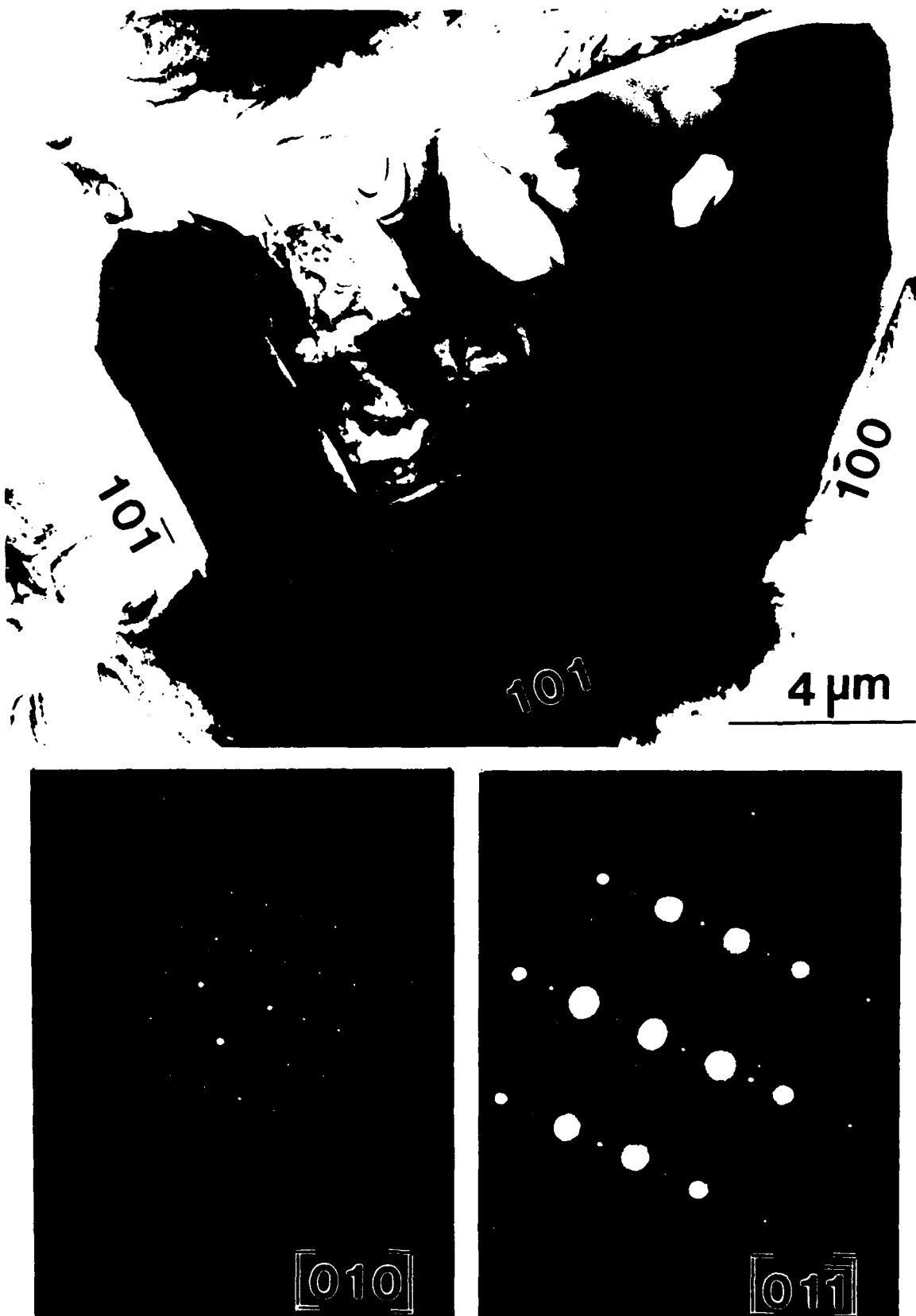


Figure 6. Cross sectional TEM view of a primary TiB single crystal needle showing [010] and [011] zone-axis patterns. The facets of the crystal were invariably of the (100), (101) and (10̄1) type.

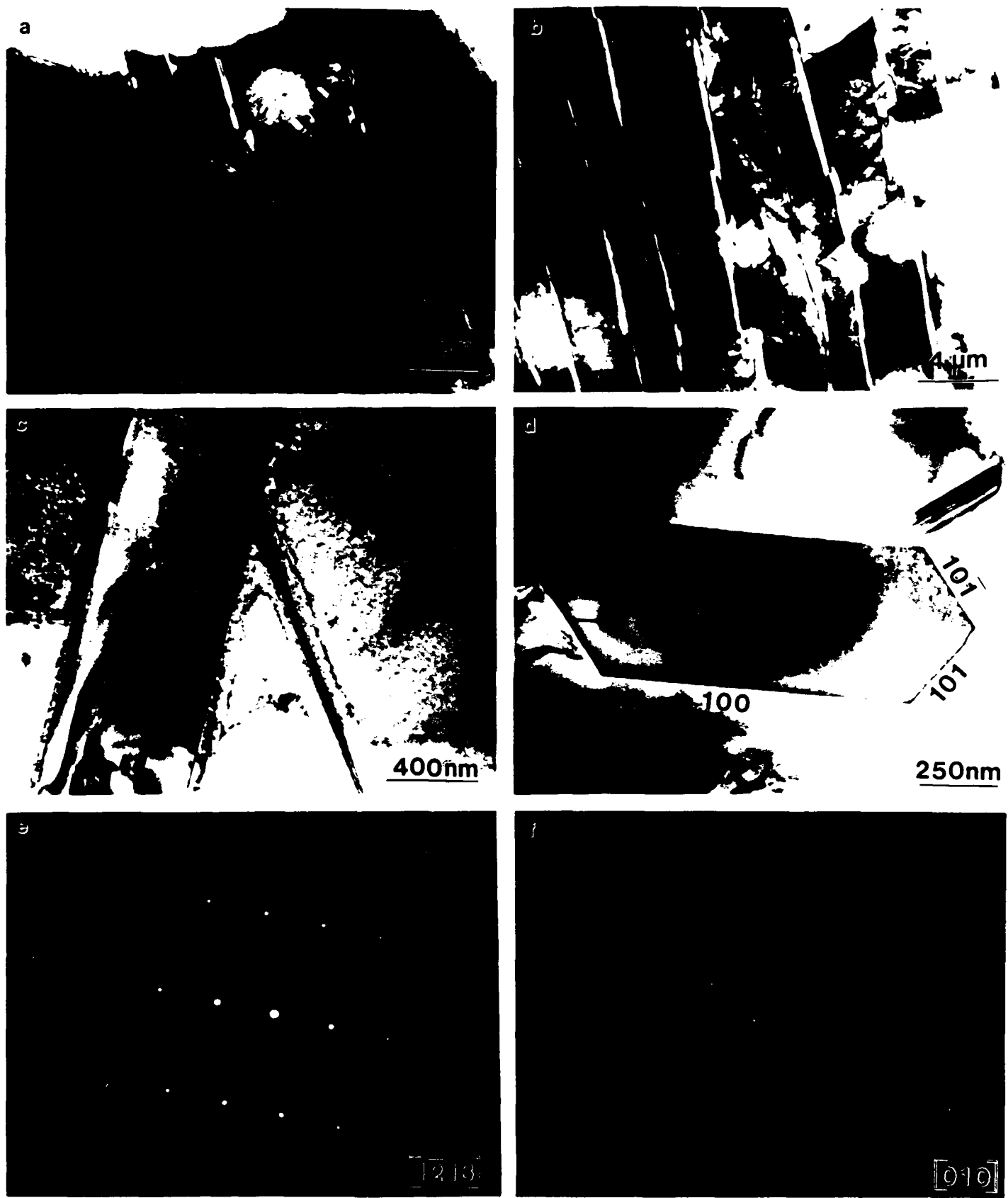


Figure 7. TEM images of eutectic TiB particles in the binary alloys: (a) is from the interdendritic segregate in the BLB alloy, while (b) shows a well developed eutectic morphology in the BHB alloy. (c) and (d) are longitudinal and transverse views of eutectic needles, accompanied by their respective ZAPs in (e) and (f). Note the correspondence between the crystallographic facets of the needle in (d) and those of the primary TiB in Figure 6.

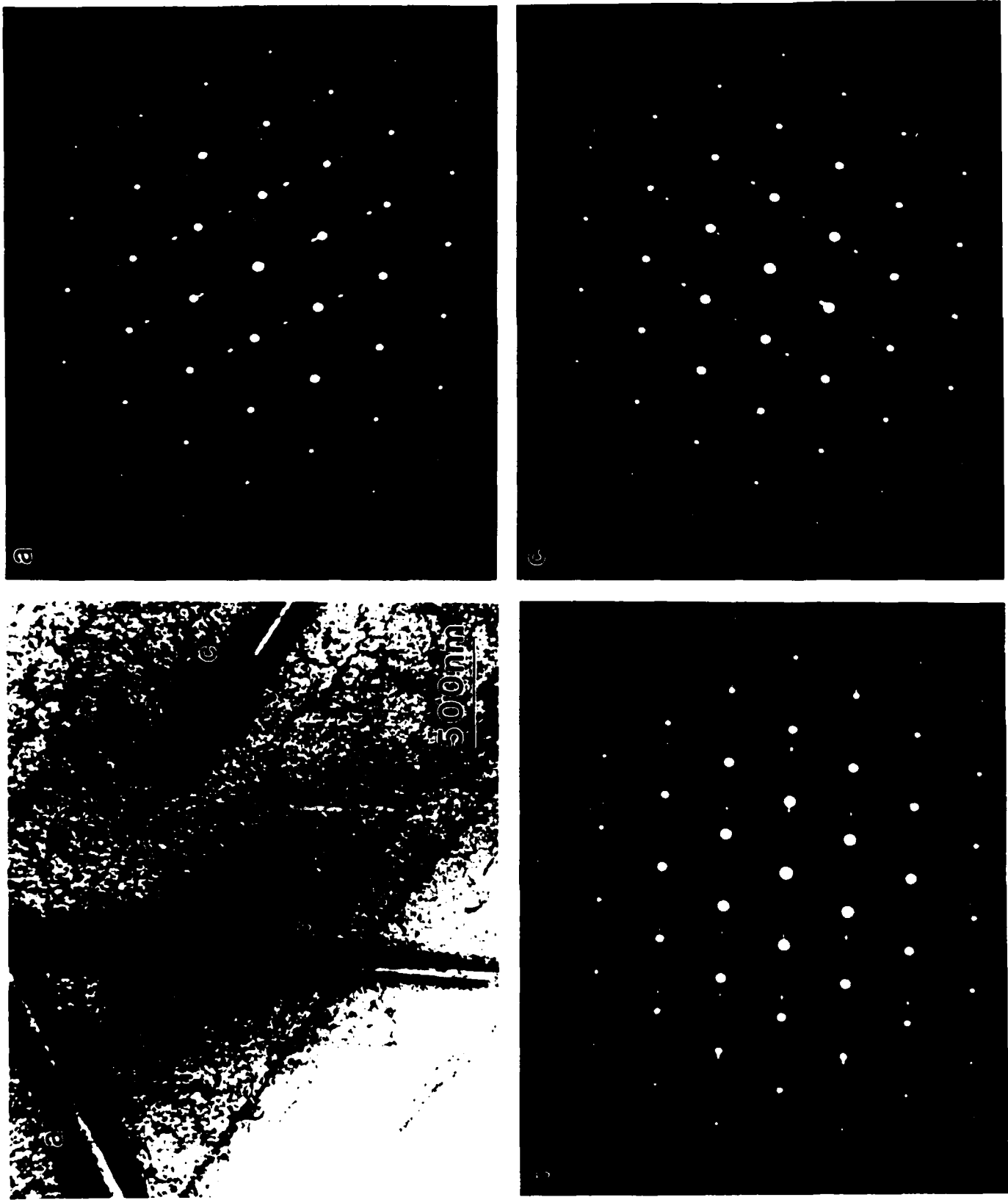


Figure 8. Three variants of TiB needles precipitated in the solid state with their corresponding diffraction patterns. The plane of the image is parallel to the basal plane of the α -(Ti) matrix. The [010] axes of the three needles fall on the basal plane and are parallel to the $\langle 11\bar{2}0 \rangle$ directions of α -(Ti).

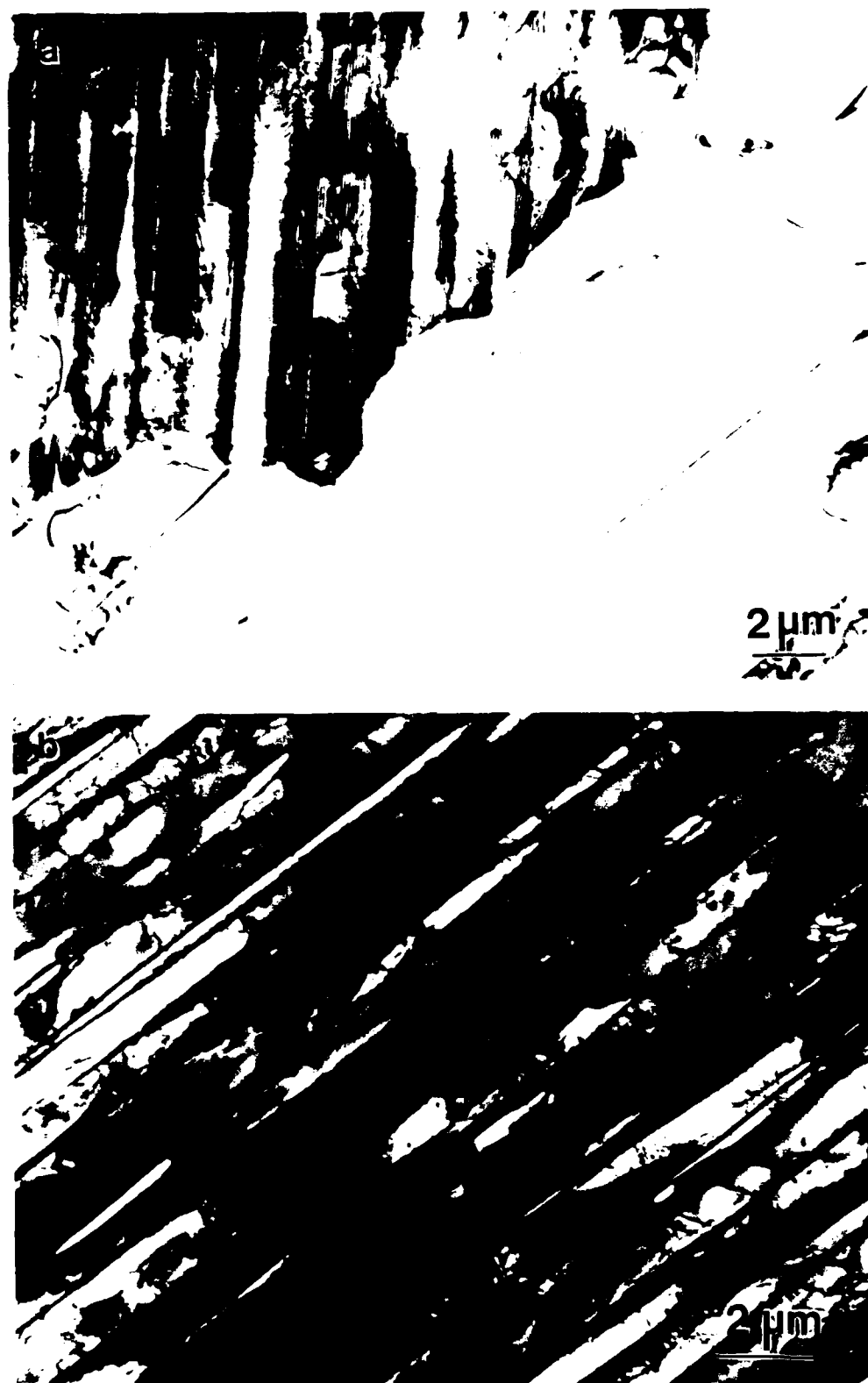


Figure 9. Ternary alloy matrix showing the $\alpha_2 + \gamma$ lath structure characteristic of transformed α -(Ti) dendrites, in contact with interdendritic γ segregate, (a). The lath constituent in (b) is predominantly γ , with a typical spacing of $\sim 1.2 \mu\text{m}$.

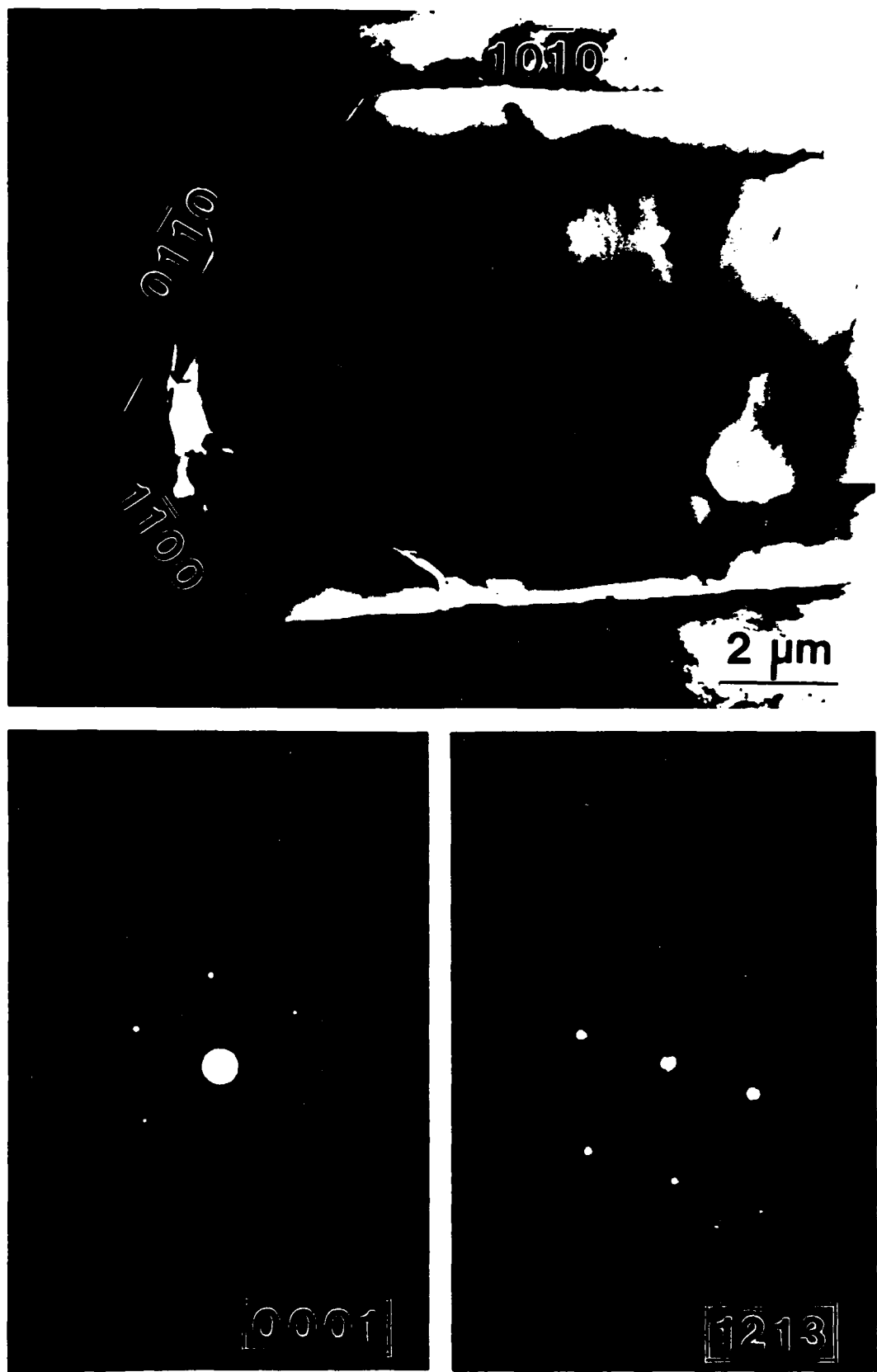


Figure 10. Cross sectional TEM view of a primary TiB_2 single crystal showing the $[0001]$ and $[1\bar{2}13]$ zone axis patterns. The plane of the image is parallel to the basal plane and the facets are all of the type $\{1010\}$.

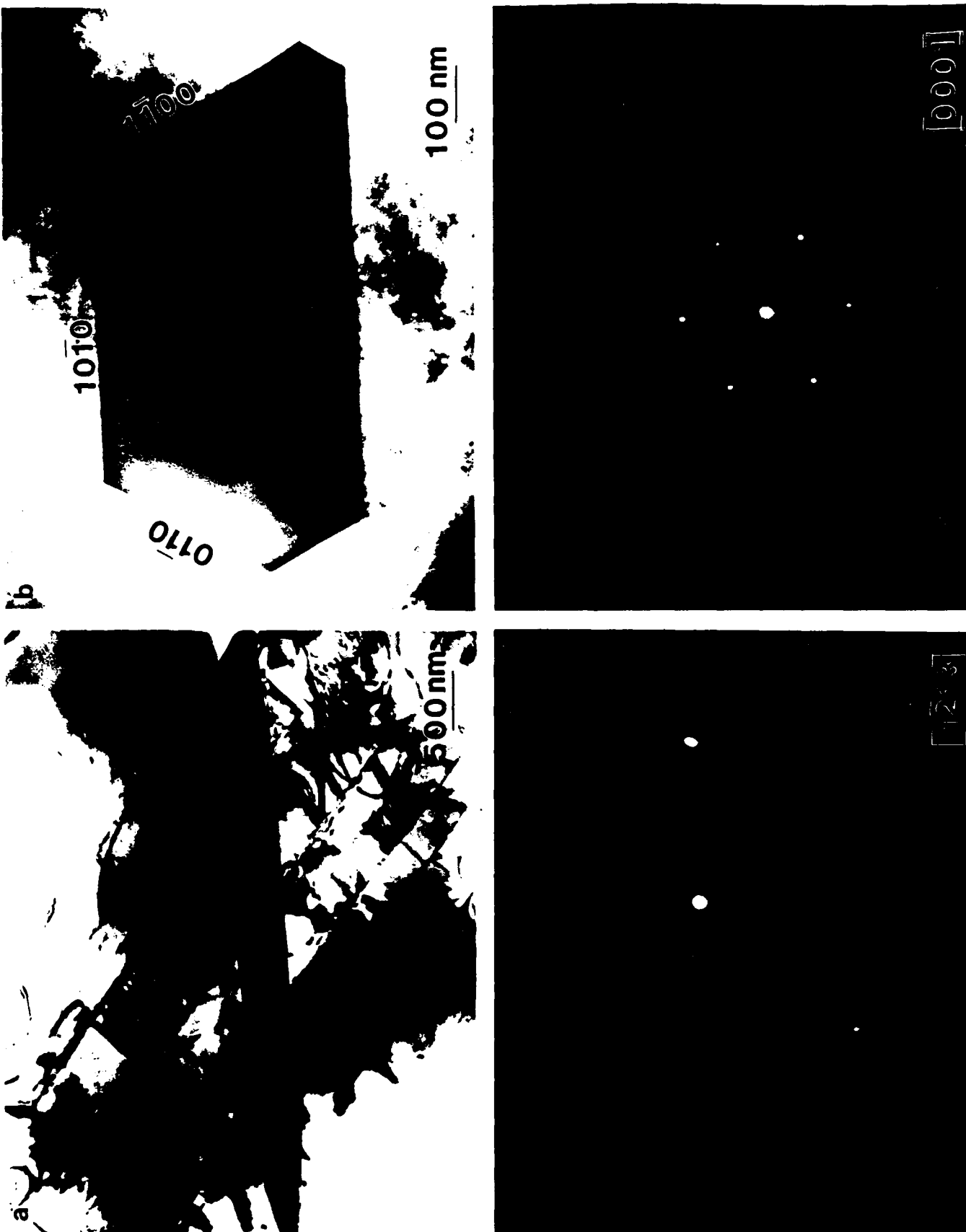


Figure 11. Longitudinal (a) and transverse (b) views of secondary TiB_2 needles in the ternary alloys, with their corresponding ZAP's. The axis of the needle is parallel to the c-axis of the C32 structure and the facets in (b) are all prism planes.

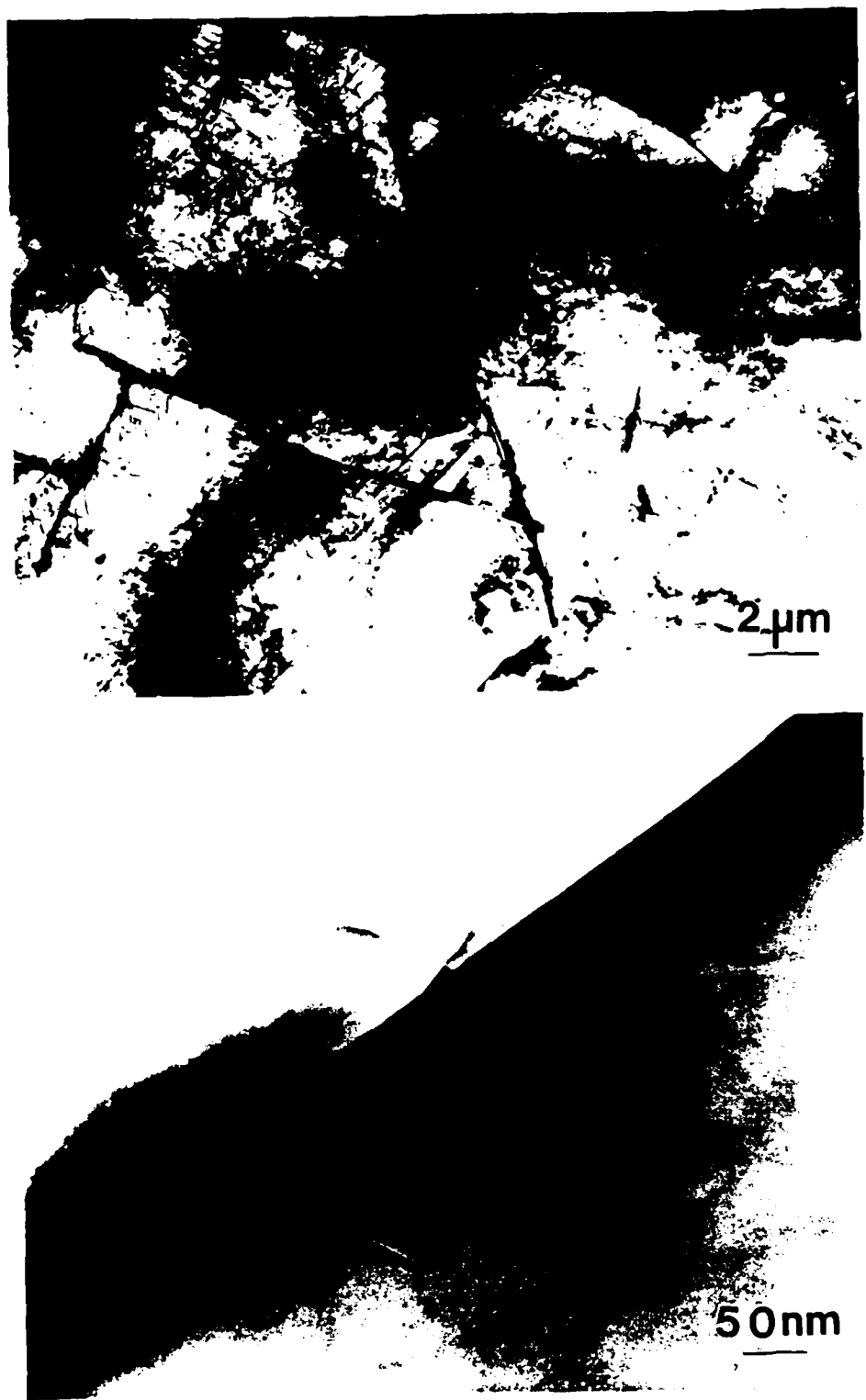


Figure 12. TEM images of the curly-plate second phases tentatively indexed as having a tetragonal structure.

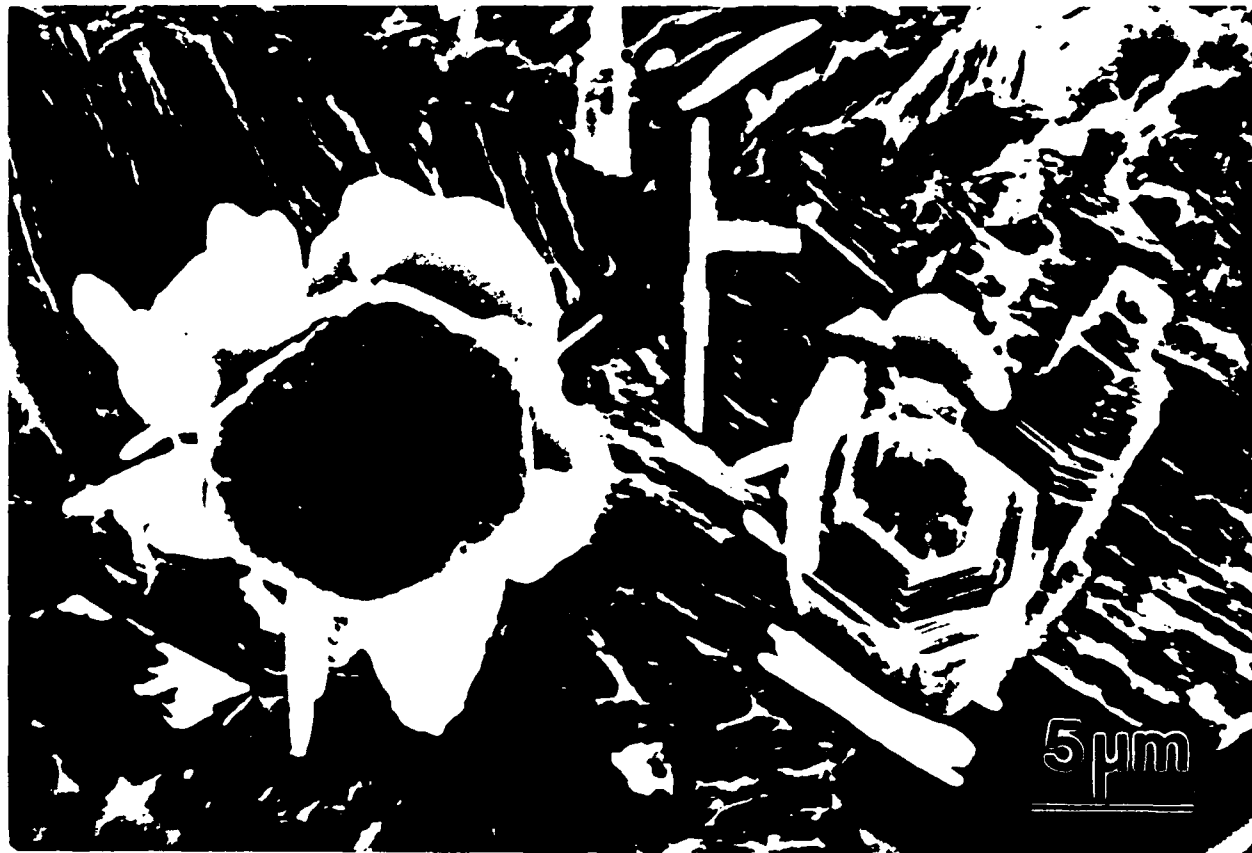


Figure 13. SEM view of the primary TiB_2 in a ternary alloy contaminated with nitrogen. Note the petal-like phases of composition $(\text{Ti}_2\text{Al})_x\text{By}$ attached to the boride particles.

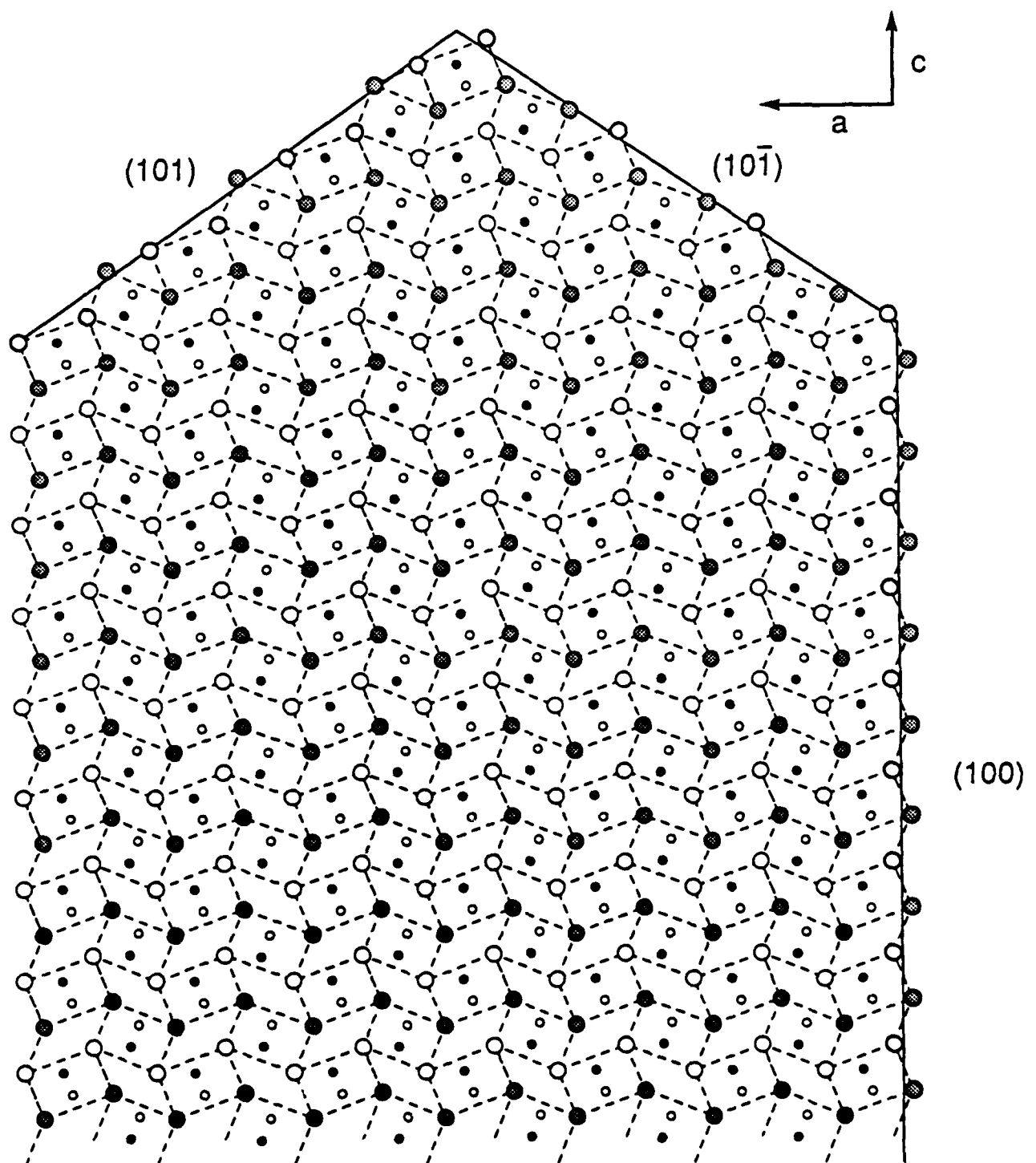


Figure 14. Relationship between the atomic arrangement in TiB and the macroscopic facets shown by the monoboride needles. The crystal is believed to preferentially expose Ti faces to the melt.

MICROSTRUCTURAL DEVELOPMENT AND MECHANICAL PROPERTIES
OF Cu-Al IN-SITU FORMED COMPOSITES

M. L. Borg, J. J. Valencia and C. G. Levi

Materials Department
Department of Mechanical and Environmental Engineering
University of California
Santa Barbara, CA 93106

Abstract

Highly deformed in-situ composites of a two-phase Cu-8.3%Al eutectic alloy have been produced by conventional casting (CC) and directional solidification (DS) followed by extensive mechanical working. As-cast microstructures are dendritic/cellular and exhibit spacings on the order of 23 μm for conventional casting and 185 to 136 μm for directional solidification at 3 and 6 cm/hr, respectively. Cold working up to true strains of $\epsilon = 5.3$ (99.5% CW) was possible in the CC structure, leading to filament spacings as fine as 1 - 2 μm . Mechanical testing of samples deformed to $\epsilon > 3$ revealed that tensile strengths achieved in both CC and DS materials are higher than those observed in any other composite systems explored to date, notably Cu-Nb and Cu-Fe, at equivalent cold work strains. It is believed, however, that most of the strengthening arises from work hardening of the matrix, with limited contribution of the second phase filamentary dispersion.

Solidification Processing of Eutectic Alloys
D.M. Stefanescu, G.J. Abbaschian and R.J. Bayuzick
The Metallurgical Society, 1988

Introduction

In-situ formed filamentary composites are a class of materials produced by extensive deformation processing of two-phase alloys. Desirable microstructures consist of an extremely dense (10^6 - 10^{10} /cm²) and uniform dispersion of very thin (5 - 100 nm) metallic filaments in a metallic matrix [1]. These composites are of interest primarily because of their enhanced work hardening behavior; achievable strengths are higher than those expected from a rule of mixtures calculation based on the strength of the individual constituents with the same amount of cold work strain [2]. Furthermore, the work hardening rates of these materials commonly increase with deformation up to true strains on the order of 10 (99.995% CW), whereas in most systems reinforced by non-deforming dispersoids the initially rapid work hardening rate decreases with increasing strain [3]. In addition to their high strengths, some of these composites may also exhibit attractive magnetic or superconducting properties [1].

The strengthening mechanisms at work in ultrafine filamentary composites are not completely understood, although several hypotheses have been put forward. In general, the strength of these alloys is thought to be associated with the high density of interfaces, but the role of those interfaces is still a subject of debate. It has been shown that the UTS exhibits a Hall-Petch type relationship with the interfilament spacing, suggesting that interfaces act primarily as barriers to dislocation motion [4,5]. On the other hand, it has been proposed that the most significant contribution to composite strength stems from the additional dislocations which are geometrically necessary to accommodate the strain incompatibility between the phases [3,6]. Regardless of the mechanism, it is generally agreed that interfilament spacings in the sub-micron range are desirable to optimize the interfacial area per unit volume and the resulting strength. It is also believed that the phases should be as mechanically disparate as possible, but sufficiently ductile to undergo the extensive deformation associated with composite fabrication [6].

By and large the composite systems most extensively investigated are based on a copper matrix with a bcc second phase, notably Cu-Nb [1,4,7-11], Cu-Fe [5,6,12,13], Cu-Cr and Cu-Mo [14]. Filaments as fine as 10 nm and interfiber spacings ranging from 100 nm in Cu-Nb [9] to a few micrometers in Cu-Fe [13] have been obtained by swaging and drawing arc-cast ingots containing 10 - 30 vol% of second phase. Concomitant room temperature strengths as high as 2230 MPa, or about G/20, have been obtained for Cu-18 vol% Nb deformed to a true strain of ~11.5 (99.999% CW) [1]. This compares with maximum UTS values of ~500 MPa for pure Cu drawn to similar cold work strains [10]. It is also significant that strengthening occurs in many cases below the minimum volume fraction of reinforcing phase required in conventional composites [1].

The present investigation deals with in-situ formed Cu-matrix composites produced by deformation processing of cast structures. The primary objective is to study the effects of solidification microstructure on the material behavior during forming and on the achievable strengths. It is anticipated that if the second phase could be aligned and refined prior to deformation, the interfilament spacings would be finer at any level of cold working strain, thus enhancing the resultant strengthening. While directional solidification appears to be the logical approach to control the size and orientation of the second phase, it has seldom been coupled with mechanical processing, and then only with limited success [2,15]. For example, DS of an Ag-28.1 wt% Cu eutectic alloy followed by wire-drawing up to 99.99% CW showed only a marginal increase in strengthening (<10%) when compared with conventionally cast material cold worked to the same strain [2].

Improvements in microstructural refinement and orientation are optimized in principle by plane-front coupled growth, where spacings may be an order of magnitude finer than those in dendritic/cellular microstructures [16]. However, most of the copper matrix alloys of interest are not suitable for this approach: Cu-Fe is a peritectic system, theoretically unsuitable for coupled growth [16], while Cu-Nb and Cu-Cr are simple eutectics, but the volume fraction of the second phase is minimal at the eutectic composition. Furthermore, all these systems have steep liquidus and the liquid-solid temperature range opens rapidly with increasing composition.

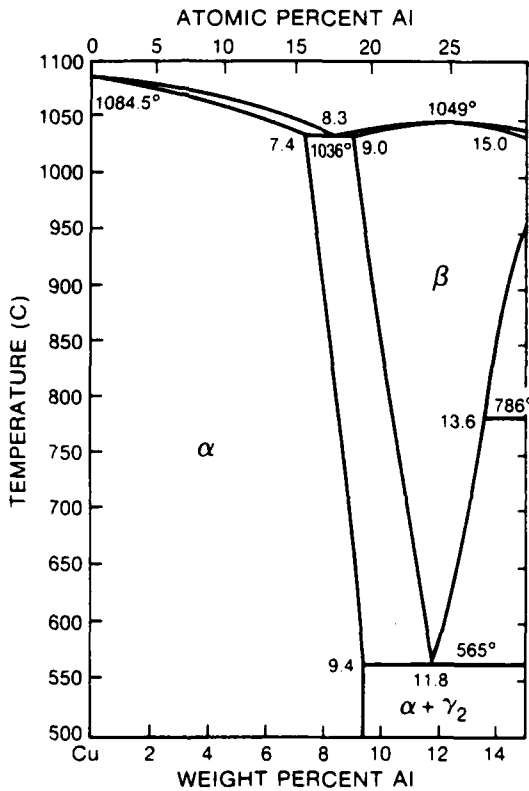


Figure 1 - Cu-rich end of the Cu-Al phase diagram from reference [17]. The eutectic composition is given in a more recent evaluation as 8 ± 0.3 %Al [18]. Note that all the alloys in the eutectic range (7.4 - 9.0 %Al) are single phase at room temperature.

A cursory review of the Cu-X binary phase diagrams reveals that the Cu-Al system selected for this study is the only Cu-matrix eutectic alloy involving a significant amount of a potentially ductile bcc second phase (i.e. the disordered intermetallic β). Figure 1 shows that this system has a reasonably low eutectic temperature and relatively short liquid-solid ranges on both sides of the eutectic composition. However, the $(\text{Cu}) + \beta$ two-phase

field is quite narrow making the microstructure evolution sensitive to small changes in Al content and/or solidification conditions. For example, a negative deviation of 0.5 %Al from the reported eutectic composition (8.3 %Al) would enhance the formability of the alloy as the volume fraction of second phase is cut in half, but it would also require a significant reduction in solidification velocity to maintain coupled growth. Further, the peculiar shape of the (Cu) + β phase field indicates that the 8.3%Al eutectic alloy should be single phase at temperatures below \sim 1023 K (750 °C). Thus, the second phase is prone to dissolve partially during cooling from the solidification temperature.

Experimental

The Cu-Al alloy stock was prepared from electrolytic oxygen-free copper (99.999 %Cu) and high purity Al pellets (99.99 %Al). Melting was carried out by induction in a graphite-clay crucible coated with ZrO₂ mold wash. The melt was protected from oxidation by a CaCO₃ slag and was degassed for over 5 min. with argon injected through a graphite lance. The alloy was superheated 75 K above the eutectic temperature and cast into graphite molds having four 12 mm diameter, 150 mm long cylindrical cavities. The cast rods were cleaned and later used for directional solidification and/or deformation processing.

Given the characteristics of the phase diagram in Figure 1, it was deemed convenient to first explore the effects of Al content on volume fraction of β and growth morphology. To that effect, buttons ranging from 8.0 to 10.0 wt% Al were arc-melted in an argon atmosphere and examined metallurgically. None of the microstructures exhibited regular coupled growth, as shown in Figure 2, but the 8.3 wt% Al button contained about 10 - 15 volume percent of β , which is on the lower end of the range used in most other composite systems (10-30 vol%) [1]. Since the second phase is a disordered intermetallic, conceivably with lower ductility than other reinforcements used so far, it was considered that larger amounts of second phase could hinder the formability of the material. Thus, it was decided to use the Cu-8.3wt%Al alloy for the initial stage of this investigation.

Apparatus

The DS apparatus, shown in Figure 3, consists of a high gradient induction furnace heated by a cylindrical graphite susceptor and powered by a 20 kW, 400 kHz power supply. An alumina crucible (99.8% Al₂O₃, 13 mm I.D. and 305 mm long) containing the Cu-Al alloy is placed inside the susceptor. The whole furnace assembly is housed in a quartz chamber, where an argon flow is circulated from the top to protect both the susceptor and the liquid metal. A superheating of 100 K was typically achieved in the molten alloy away from the growing front; this temperature was held constant during the process. A temperature gradient of \sim 50 K/cm (measured experimentally) was established on the liquid side of the interface by spraying cold water onto the crucible from a insulated stainless steel ring located at the bottom of the susceptor. The crucible is slowly withdrawn from the furnace using an Instron 1122 universal testing machine as a drive, which allowed for precise control of the solidification rate. Two solidification velocities, 3 cm/hr (8 μ m/s) and 6 cm/hr (16 μ m/s), were selected for the initial experiments based on previous experience with other alloy systems [e.g. 2].

Deformation Processing

Prior to deformation processing the conventionally cast and directionally solidified rods were machined down to a diameter of \sim 10 mm (400 mils) in order to remove any superficial oxides and casting defects. The rods were cold worked by swaging, limiting the reduction in area to less than 30% per

step and constantly lubricating the dies with a light oil to keep the sample from overheating. The direction of swaging was reversed in each pass to prevent development of a spiral texture due to the rotating action of the dies [19]. 10 mm long samples for metallographic examination and hardness testing were taken at each swaging step beyond $\epsilon = 1$. Material for about 5 tensile specimens was set aside at selected steps above cold work strains of 2.9.

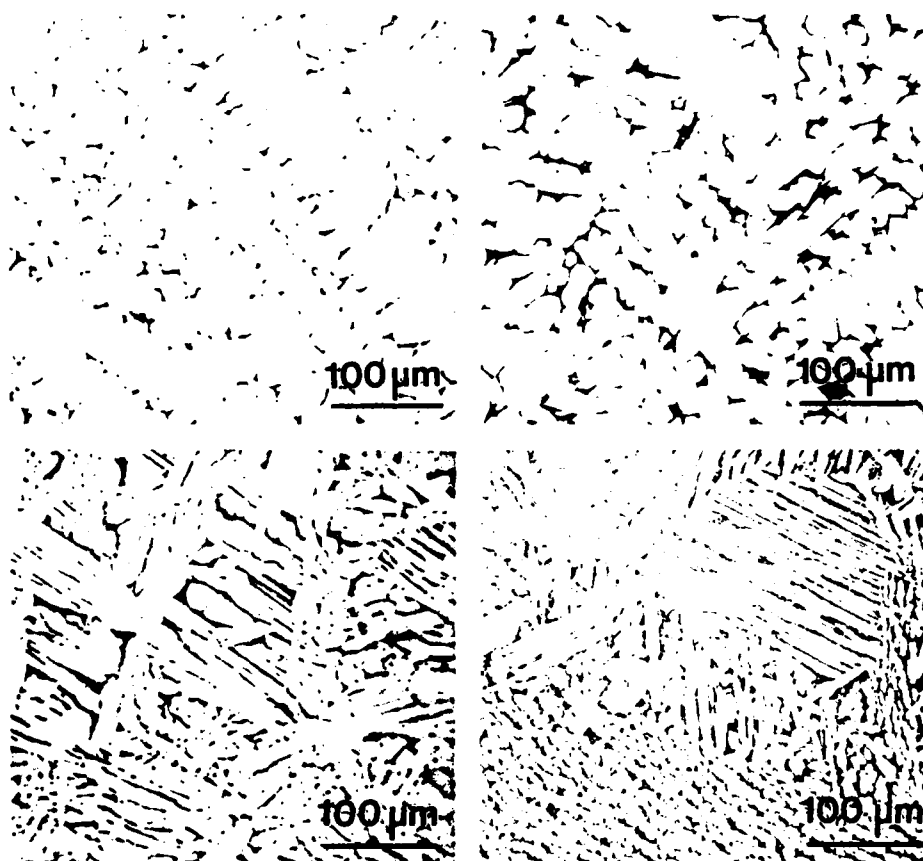


Figure 2 - Solidification microstructures of arc-melted Cu-Al buttons of nominal compositions (a) 8.0%Al, (b) 8.3%Al, (c) 8.6%Al and (d) 10%Al.

Characterization and Testing

Metallographic samples were mounted in conducting phenolic resin, mechanically polished and lightly etched with a FeCl_3/HCl -base solution to reveal the morphology of the second phase. Achieving a good-quality surface for optical examination was particularly difficult since the two-phase alloy does not lend itself to electropolishing or chemical polishing.

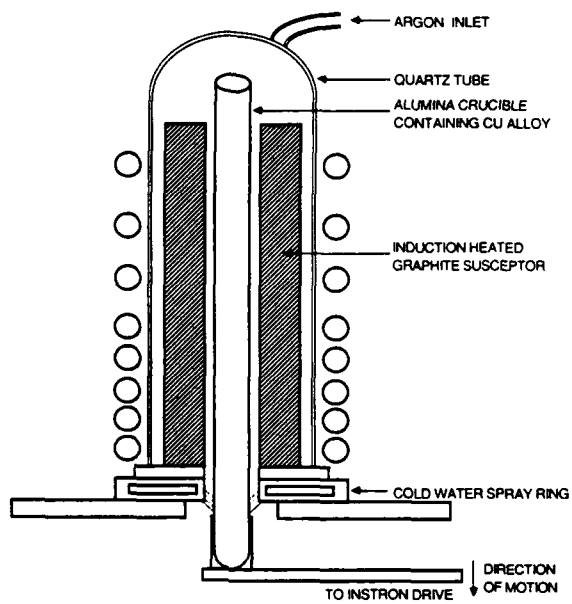


Figure 3 - Schematic of the directional solidification furnace. The crucible is driven by an Instron tensile testing machine and the graphite susceptor is heated by a 20 kW, 400 kHz power supply.

Microindentation hardness testing was performed on samples mounted in transverse orientation in bakelite and mechanically polished. Indentations were made with a Vickers diamond pyramid indenter using a load of 200 grams. Five readings were usually taken from each sample, one in the center and four at half radius around the center. At the higher strains ($\epsilon > 2.9$), however, the number of indentations was sometimes limited by incipient cracking and the small cross sectional area of the specimens.

Tensile testing was performed on an Instron 1122 universal testing machine using standard grips and a crosshead speed of $\sim 20 \mu\text{m/s}$. In order to minimize stress concentrations at the edge of the grips, the ends of the composite wire were sandwiched between two pieces of soft copper sheet. Although an extensometer was used on many of the tests, fracture often occurred outside the gauge length, preventing the accurate determination of yield strength and elongation to failure. The smaller diameter specimens, especially those produced from DS material, often failed at preexisting cracks produced during swaging. In those cases the tests were repeated on the remaining portion of the specimen until a reasonably clean fracture was produced.

Microstructural Development

The solidification microstructures of the conventionally cast (CC) and directionally solidified (DS) rods are shown in Figure 4. It is evident that the interfacial conditions resulted in a dendritic or cellular morphology rather than coupled growth, even though the alloy is at or very close to the reported eutectic composition. In principle, one could argue that for growth

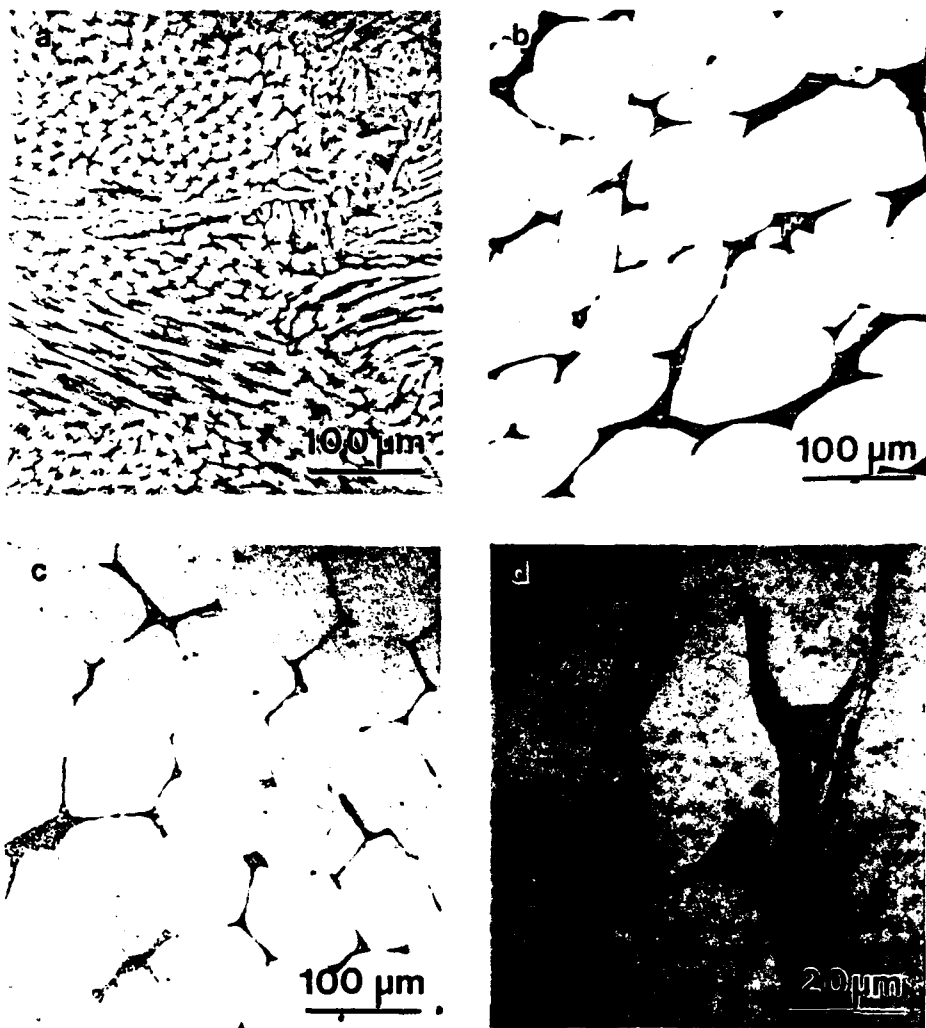


Figure 4 - Solidification microstructures of Cu-8.3%Al (a) conventionally cast, (b) directionally solidified at 6 cm/hr and (c) DS at 3 cm/hr; (d) shows a higher magnification view of a segregate region containing a mixture of (Cu) and β phases.

of (Cu) dendrites or cells to be favored at the eutectic composition, the coupled zone should be skewed towards the β field and the interfacial supercooling should fall out of the coupled zone in the phase diagram [20]. A skewed zone is normally associated with one of the phases growing in a faceted mode, which is not evident in any of the microstructures and would not be characteristic of either of the disordered solid phases involved in this system. Furthermore, it is unlikely that any significant supercooling could

be developed at the relatively low growth velocities used in directional solidification¹.

An alternate hypothesis is that the alloy used is really hypoeutectic, as suggested by the micrographs in Figure 2, where the 8.0, 8.3 and 8.6% alloys are seen to contain primary (Cu) with increasing amounts of β segregate. EDXS analysis of the cast samples revealed the bulk composition of the alloy to be quite close to 8.3%Al, within the accepted range for the eutectic composition specified in a recent evaluation of the phase diagram [18]. On the other hand, the compositions of the primary and segregate phases were found to be ~7.7 and ~12%Al, which are somewhat higher than the values indicated in Figure 1 but agree with the relative amounts of phases observed. Nevertheless, if the 8.3%Al alloy were indeed hypoeutectic, it should still be possible to produce coupled growth at much higher or much lower velocities than those used up to this point, provided that the coupled zone is reasonably symmetric. This approach will be further explored in future activities.

Figure 4 also shows that the segregate spacings in the directionally solidified rods are much larger than that in the conventionally cast one. As expected, the DS ingot grown at the faster velocity exhibits a finer spacing than that solidified more slowly, i.e. $\lambda = 136 \mu\text{m}$ and $185 \mu\text{m}$ for $V = 6$ and 3 cm/hr , respectively. It was rather surprising the product $\lambda^2 V$ was reasonably constant,

$$\lambda^2 V \sim 3 \times 10^{-13} \text{ m}^3/\text{s} \quad (1)$$

since that type of relationship is predicted for coupled eutectics but not for cellular or dendritic growth. Although Equation (1) is not expected to hold over a wide range of velocities, it does suggest that the growth rate would have to be substantially increased (i.e. $V \sim 200 \text{ cm/hr}$) in order to refine the DS structures to the level observed in the CC rods. Further increments, of course, could result in coupled growth with a more significant reduction in microstructural scale.

The larger segregate areas in the directionally solidified material, such as that in Figure 4(d), are sometimes found to be a mixture of phases rather than single phase β . This could be ascribed to coupled growth in the intercellular regions during solidification [20] or to solid state decomposition of the β phase as it goes through the (Cu) + β field during cooling. Although the issue has not been resolved, most of the β regions are single phase and occasionally show evidence of a martensitic transformation, e.g. Figure 4(d), suggesting that the regions where phase separation is observed form during solidification. After deformation, these (Cu) + β areas become bundles of second phase ribbons with some primary phase included.

Microstructure evolution during deformation processing is illustrated in Figure 5 for the CC and the DS rod solidified at 6 cm/hr . In the conventionally cast structure, the cold work progressively develops the alignment and refinement of the microstructure, reducing the interfiber spacing from $23 \mu\text{m}$ in the as-solidified structure to $\sim 3 \mu\text{m}$ after a deformation strain of 3.3 (95% CW). Further cold working to a strain of 5.3 (99.5% CW) decreases the spacing to $1-2 \mu\text{m}$. Although these spacings are comparable to those produced in some Cu-Fe composites [13], they are still coarser than those associated with the highest strengths obtained in Cu-Nb [1].

¹ Data for this system is not available, but relationships between velocity and supercooling established for the (Al)+CuAl₂ eutectic [21] suggest that $\Delta T < 1 \text{ K}$ are typical of the velocities used in these experiments.

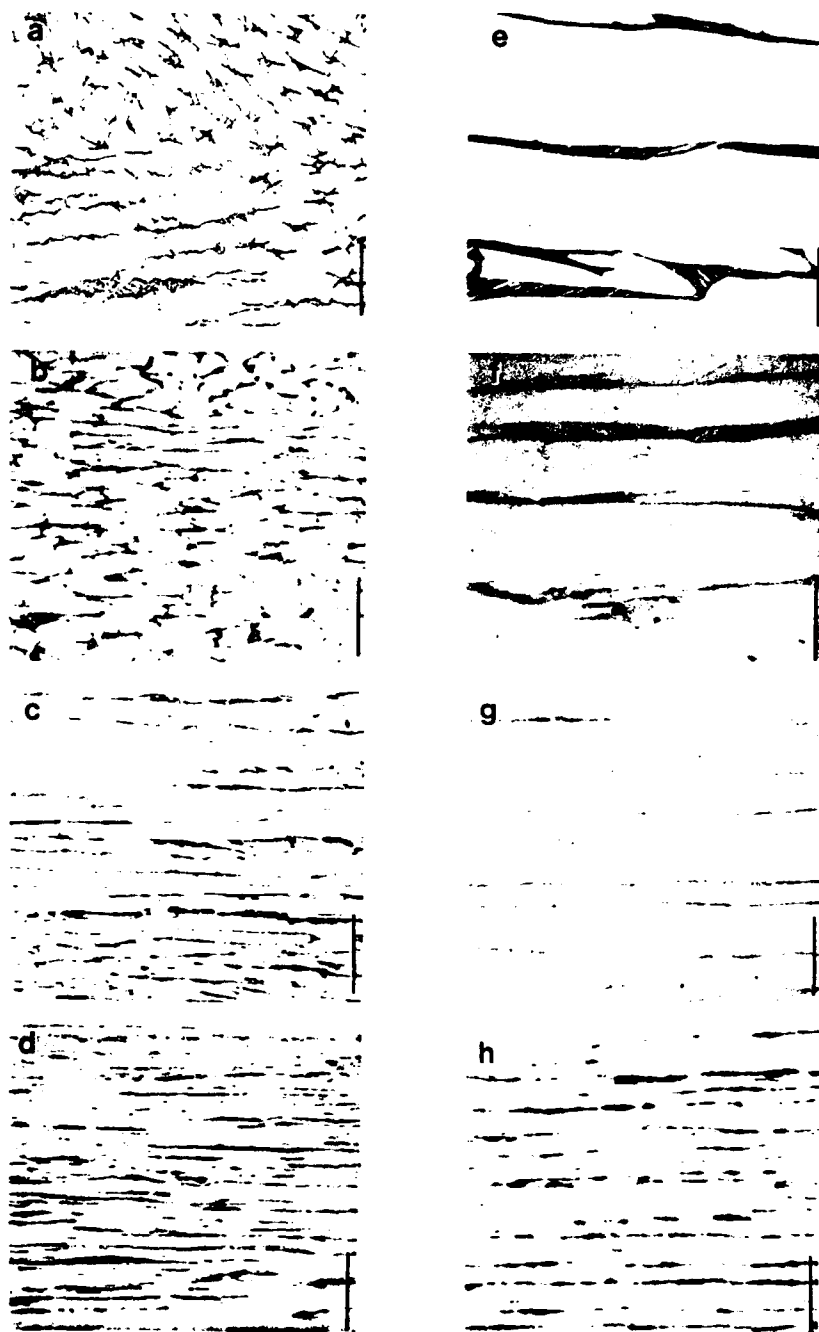


Figure 5 - Microstructure evolution during deformation processing in Cu-8.3%Al CC (left) and DS at 6 cm/hr (right). Cold work strains are 0 (a,e), 1.0 (b,f), 1.9 (c,g), and 3.3 (d,h). Marker bars are 50 μm for (a-d) and 100 μm for (e-h).

As expected from the solidification microstructures, much higher levels of deformation strain would be necessary in the DS rods in order to achieve the spacings observed in the CC microstructures. For example, the DS microstructure in Figure 5, cold worked to a strain of 3.3, exhibits a spacing comparable to that of the CC ingot in the as-cast condition. Further, the long residence time (several hours) in the liquid state associated with directional solidification promotes the formation of porosity defects, in spite of the efforts to control the environment in the DS furnace. In consequence, DS ingots could only be deformed to $\epsilon = 3.3$ before incipient cracking ensued, whereas the CC ingots were readily swaged down to $\epsilon = 5.3$. Thus, the limited benefits expected from pre-alignment of the second phase by DS were overcome by the increased scale and casting defect population of the microstructure, both of which are detrimental to the mechanical properties.

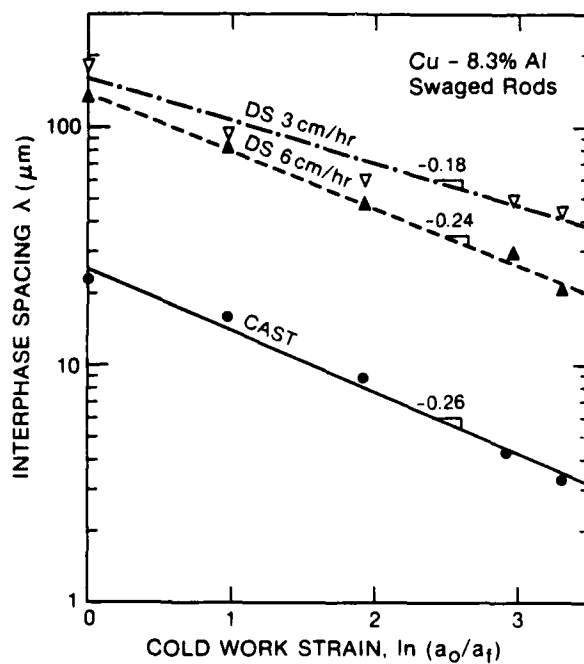


Figure 6 - Effect of deformation processing on interfiber spacing, λ , for conventionally cast and directionally solidified Cu-8.3%Al.

The effect of deformation processing on the interfiber spacing is depicted in Figure 6. A fairly linear trend is observed in all cases, with slopes close to -0.22 ($-0.5/\ln 10$), or

$$\lambda = \lambda_0 \exp(-0.5 \epsilon) \quad (2)$$

This behavior is expected when the deformation is purely axisymmetric, i.e. if the scale of all the microstructural features decreases at the same rate as the cross sectional area of the rods. It is generally agreed that the bcc second phase in these composites undergoes plane strain deformation during

cold working [22], as discussed below. However, the deformation is in general axially symmetric due to the higher number of slip systems active in the textured fcc Cu matrix [13,14]. Departures from axisymmetric behavior have been observed in Cu-Nb and ascribed to the increase in the density of second phase filaments on the cross section of the composite [10].

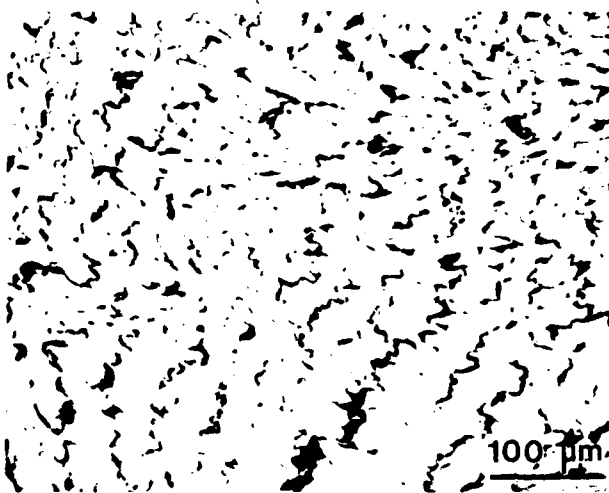


Figure 7 - Transverse view of the directionally solidified alloy (3 cm/hr) after a cold work strain of 3.3. Note the curled ribbon morphology of the second phase.

A transverse view of the microstructure after deformation reveals that the second phase assumes the curled ribbon morphology shown in Figure 7. The morphology arises from the $\langle 110 \rangle$ texture developed in bcc crystals during deformation [22]. When a $\langle 110 \rangle$ direction in a crystal becomes parallel to the rod/wire axis, there are only two $\langle 111 \rangle$ slip directions favorably oriented to accommodate the extension. Since these two directions lie on the same slip plane, further deformation becomes plane strain, producing the ribbon shape. The curling and kinking of the ribbons have been associated with the development of deformation bands within each crystal due to the different rotations of neighboring crystal portions to align a $\langle 110 \rangle$ with the wire axis [19].

Mechanical Properties

Due to the limited availability of material for tensile testing, hardness measurements were used extensively in this work for a preliminary evaluation of the effects of cold working on mechanical properties. The measured hardness of the individual phases in the as-cast DS rod was 80 VHN for the matrix and 230 VHN for the β phase. Reliable microhardness levels for each phase could not be determined in the CC rod due to the finer microstructure, but measurements of the overall hardness of a region containing both phases was found to be around 100 VHN, in reasonable agreement with the value predicted by the rule of mixtures.

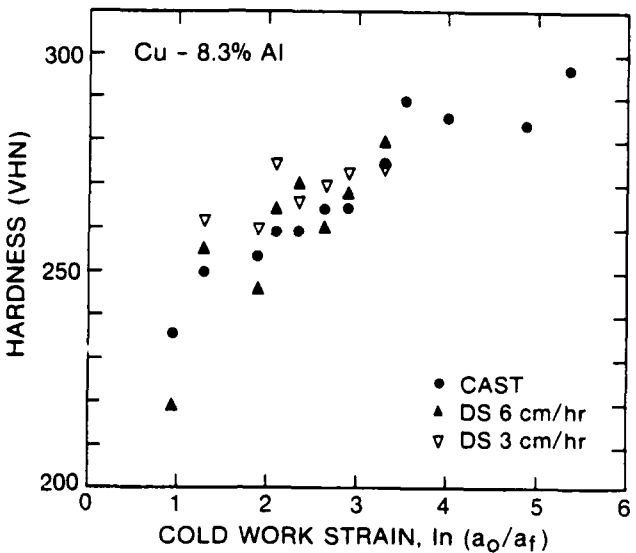


Figure 8 - Work hardening of Cu-8.3%Al CC and DS alloys as a function of true deformation strain.

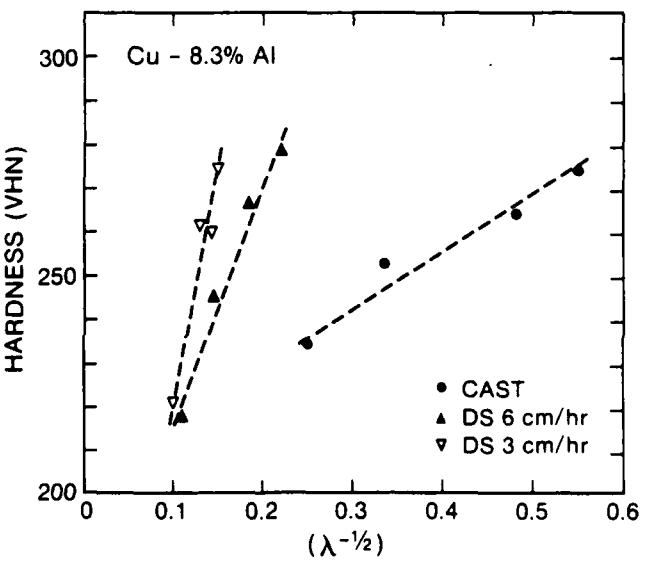


Figure 9 - Vickers hardness as a function of $\lambda^{-0.5}$ for CC and DS Cu-Al composites. The lowest values in each line correspond to a cold work strain of 1.0, whereas the highest values are for $\epsilon = 3.3$.

The effect of the cold work strain on the VHN hardness for the conventionally cast and directionally solidified rods is shown in Figure 8. It was observed that initially the VHN increases rapidly with increasing deformation from ~ 100 in the as-cast condition to about ~ 255 at a strain of 1.3. The trend slows down as cold working proceeds, with the hardness increasing only up to ~ 275 at a strains of 3.3, which was the maximum deformation achieved in the DS rods. The data fall within a relatively narrow band with no clear distinction between the hardness of the CC and DS alloys. Note also that the additional cold working of the CC material led to hardness values as high as 295 VHN.

Following the well established Hall-Petch relationship between UTS and interfiber spacing, we have plotted the VHN number against $1/\sqrt{\lambda}$ for the CC and DS materials in Figure 9. The trends are reasonably linear for the limited range of experimental values depicted. The lowest values correspond to a cold work strain of ~ 1.0 (63% CW) and the highest to a strain of 3.3. As expected from the previous figure, the three composites have approximately the same hardness for equivalent strain levels in spite of the large differences in spacings. This suggests that the observed hardening may be due primarily to cold working of the matrix and that further refinement of the second phase may be necessary for it to have a significant effect.

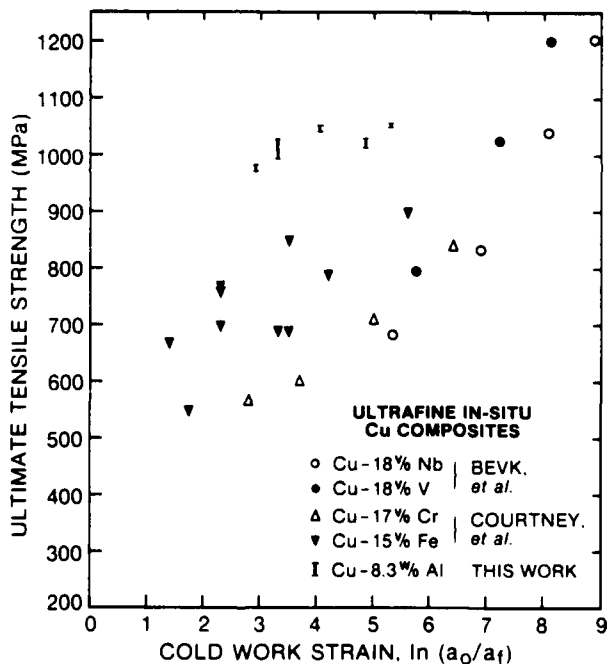


Figure 10 - Ultimate tensile strength as a function of cold work strain for the conventionally cast Cu-8.3%Al alloy compared with other systems reported in the literature [1,6].

The ultimate tensile strength of the conventionally cast material as a function of cold work strain is shown in Figure 10, along with results for other in-situ formed copper-matrix composites reported in the literature [1,6]. These preliminary results are encouraging since the UTS values are significantly higher than those of all the other systems at comparable levels of cold work. Nevertheless, the observed strengths are only about 1/2 of the maximum UTS achievable in the best Cu-Nb composites, which can be cold worked to much higher levels ($\epsilon \sim 12$). It should also be noted that the present materials were deformed by swaging, which is likely to produce lower hardening rates than the drawing process commonly used for the other composites.

Table 1 compares the maximum strengths achieved in the DS Cu-Al composites with those of the CC rods and some relevant standard alloys. As expected from the microhardness data, the UTS values for both CC and DS materials at 95% cold work ($\epsilon = 3.3$) are relatively close, in spite of the differences in spacing. Some insight on whether the matrix work hardening controls the strengthening of these composites may be gained by comparison with a single phase α bronze of similar composition (C61000). If strengthening is due to the matrix, one could argue that both materials should exhibit similar hardening, the differences in UTS arising from the more extensive deformation of the composites.

Comparison of the α bronze with pure copper in Table 1 indicates that the incremental strengthening of the matrix produced by the dissolved Al is 240 MPa in the annealed condition and 170 MPa after 37% CW ($\epsilon = 0.46$). Consider now that pure Cu reaches a saturation UTS of ~ 500 MPa after extensive cold working [10]. The baseline strengthening produced by the matrix work hardening would then be $500 - 240 = 260$ MPa. The large differences between the composite strengths and the saturation UTS of Cu, i.e. 420 to 560 MPa, would then be the incremental contribution of the solute. Aluminum additions above ~ 4.5 wt% have been shown to drastically change the character of the dislocation substructure in copper from cellular to coplanar arrays by reducing the stacking fault energy and hindering cross slip [23,24]. As a consequence, the Hall-Petch effect of the grain size is enhanced [23]. Thus, it is possible that the high composite strengths may result from the increased work hardening rate produced by the Al solute in the matrix, but the additional interfaces in the composite could also have a synergistic contribution to the strengthening.

Table 1 - Tensile strength of Cu-8.3wt%Al composites compared with those of standard Cu alloy rod/wire.

Alloy	Processing	% C.W.	UTS (MPa)
Pure Cu (C10100)	Annealed		240
	Drawn, H04	37	380
Cu-8%Al (C61000)	Annealed		480
	Drawn, H04	37	550
Cu-8.3%Al	CC, Swaged	99.5	1060
	CC, Swaged	95	980
	DS 6cm/hr, Swaged	95	920
	DS 3cm/hr, Swaged	95	950



Figure 11 - Typical fracture surfaces of CC composites after cold work strains of (a) 3.3 and (b) 5.3. The corresponding ductilities are 46% and 10%, respectively.

Figure 11 depicts typical fracture surfaces of tensile test specimens at two different cold work strains. In general, the fractures are microscopically dimpled and exhibit significant macroscopic ductility, but failure seems to be commonly associated with existing cracks in the microstructure. These could result from excessive deformation processing, as in Figure 11(b), but may also arise from porosity and other casting defects. Smaller vertical cracks are probably associated with the jagged appearance of the fracture surface in Figure 11(a).

Conclusions

The heavily cold-worked α - β 8.3% aluminum bronzes exhibit promising strengths when compared with other fcc/bcc copper composites at similar deformation strains. UTS as high as 1060 MPa and hardness values on the order of 295 VHN were achieved in these materials, but analysis of the mechanical behavior suggests that the observed strengthening may be due primarily to cold working of the matrix.

Whereas the conventionally cast material may be cold worked to 99.5% ($\epsilon = 5.3$), the directionally solidified alloys were only formable up to 95% CW ($\epsilon = 3.3$), presumably due to an increased population of casting defects. Spacings as fine as 1-2 μm were achieved in the CC material, but directional solidification at growth rates up to 6 cm/hr resulted in significantly coarser microstructures in the as cast and deformed conditions.

Future efforts in this program are first aimed at clarifying the contribution of the second phase to composite strengthening by processing a single phase alloy of the same composition at comparable cold work strains and studying its mechanical behavior. A second goal is to pursue the development of a finer microstructure by directional solidification, perhaps with minor adjustments in composition. Finally, an alternate route based on rapid solidification, powder metallurgy and deformation processing will be explored.

Acknowledgements

The authors are grateful to Prof. T.H. Courtney, Dr. J.C. Malzahn-Kampe and Prof. R. Mehrabian for enlightening discussions, and to Dr. S.D. Ridder and Mr. F. Biancaniello of the National Bureau of Standards for their assistance with the deformation processing experiments. This work was sponsored by the Defense Advanced Research Projects Agency under Grant N00014-86-K-0178, monitored by the Office of Naval Research. Program Director at DARPA is Dr. P. Parrish and contract monitor at ONR is Dr. S. Fishman.

References

1. J. Bevk, "Ultrafine Filamentary Composites", Ann. Rev. Mater. Sci., 13 (1983), 319-38.
2. G. Frommeyer and G. Wassermann, "Microstructure and Anomalous Mechanical Properties of In-Situ Produced Silver-Copper Composite Wires", Acta Metall., 23(11)(1975), 1353-1360.
3. P.D. Funkenbusch, J.K. Lee and T.H. Courtney, "Ductile Two-Phase Alloys: Prediction of Strengthening at High Strains", Metall. Trans. A, 18A (1987), 1249-1256.
4. J. Bevk, J.P. Harbison and J.L. Bell, "Anomalous Increase in Strength of In-Situ Formed Cu-Nb Multifilamentary Composites", J. Appl. Phys., 49 (12)(1978), 6031-38.
5. P.D. Funkenbusch and T.H. Courtney, "Microstructural Strengthening in Cold Worked In-Situ Cu-14.8 v/o Fe Composites", Scripta Metall., 15 (1981), 1349-1354.
6. P.D. Funkenbusch and T.H. Courtney, "On the Strength of Heavily Cold Worked In-Situ Composites", Acta Metall., 33(5)(1985), 913-922.
7. H.E. Cline, B.P. Strauss, R.M. Rose and J. Wulff, "Superconductivity of a Composite of Fine Niobium Wires in Copper", J. Appl. Phys., 37(1) (1966), 5-8.
8. J. Bevk and K.R. Karasek, "High Temperature Strength and Fracture Mode of In-Situ Formed Cu-Nb Multifilamentary Composites", in New Developments and Applications in Composites, ed. D. Kuhlmann-Wildorf and W.C. Harrigan, (Warrendale, PA: The Metallurgical Society, 1979), 101-113.
9. D.E. Cohen and J. Bevk, "Enhancement of the Young's Modulus in the Ultrafine Cu-Nb Filamentary Composites", Appl. Phys. Lett., 39(8) (1981), 595-597.
10. W.A. Spitzig, A.R. Pelton and F.C. Laabs, "Characterization of the Strength and Microstructure of Heavily Cold Worked Cu-Nb Composites", Acta Metall., 35(10) (1987), 2427-2442.
11. P.J. Lee and D.C. Larbalestier, "Development of Nanometer Scale Structures in Composites of Nb-Ti and Their Effect on the Superconducting Critical Current Density", Acta Metall., 35(10)(1987), 2523-2536.
12. F.P. Levi, "Permanent Magnets Obtained by Drawing Compacts of Parallel Iron Wires", J. Appl. Phys., 31(8)(1960), 1469-1471.

13. J.C. Malzahn-Kampe and T.H. Courtney, "Elevated Temperature Microstructural Stability of Heavily Cold-Worked In-Situ Composites", Scripta Metall., 20 (1986), 285-289.
14. P.D. Funkenbusch, T.H. Courtney and D.G. Kubisch, "Fabricability and Microstructural Development in Cold Worked Metal Matrix Composites", Scripta Metall., 18(1984), 1099-1104.
15. D.G. Kubisch and T.H. Courtney, "The Processing and Properties of Heavily Cold Worked Directionally Solidified Ni-W Eutectic Alloys", submitted for publication.
16. W. Kurz and R.J. Fisher, Fundamentals of Solidification, (Aedermannsdorf, Switzerland: Trans Tech Publications, 1984).
17. T. Lyman et al., eds., Metals Handbook, vol. 8, (Metals Park, OH: American Society for Metals, 1973), 259.
18. J.L. Murray, "The Al-Cu Phase Diagram", Int. Met. Rev., 30(5), 1985, also in Binary Alloy Phase Diagrams, ed. T.B. Massalski, (Metals Park, OH: ASM International, 1986), 103.
19. J.C. Malzahn Kampe: Ph.D. Thesis, Michigan Technological University, 1987.
20. W. Kurz and D.J. Fisher, "Dendrite Growth in Eutectic Alloys: The Coupled Zone", Int. Met. Rev., 1979, Nos. 5 and 6: 177-203.
21. S.M.D. Borland and R. Elliot, "Growth Temperatures in Al-CuAl₂ and Sn-Cd Eutectic Alloys", Metall. Trans. A, 9A (1978), 1063-1067.
22. W.F. Hosford, Jr., "Microstructural Changes During Deformation of [011] Fiber-Textured Metals", Trans. AIME, 230 (1964), 12-15.
23. T.L. Johnston and C.E. Feltner, "Grain Size Effects in the Strain Hardening of Polycrystals", Metall. Trans., 1 (1970), 1161-1167.
24. R.W.K. Honeycombe, The Plastic Deformation of Metals, (London, UK: Edward Arnold Publishers, Ltd., 1968).

PART I

CONTAINERLESS PROCESSING OF NIOBIUM-BASED ALLOYS*

K.R. Javed and G. J. Abbaschian

Materials Science and Engineering
University of Florida
Gainesville, Florida 32611

Abstract

An electromagnetic levitation technique was utilized to study the effects of supercooling and rapid solidification on the structure of niobium-based alloys. Processing conditions included splat quenching and drop casting of supercooled samples. Results indicate that enhanced compositional uniformity and microstructural refinement can be achieved in Nb-27 Ti-35 Al, Nb-20 Ti-21.3 Si, and Nb-7.2 Al-59.7 Si alloys. Results also indicate that an ordered B2 phase is retained in rapidly solidified Nb-27 Ti-35 Al alloys. In the Nb-20 Ti-21.3 Si alloys, formation of the brittle $(NbTi)_3Si_3$ phase can be suppressed when solidified from a critical supercooling. Potential benefits of employing rapid solidification processing to niobium-based alloys are discussed.

* To appear in the proceedings of "The Materials Processing in Space Conference," The Metallurgical Society, October, 1988

Introduction

Refractory metals of group V(B), particularly niobium and tantalum, are receiving increased attention as potential materials for high temperature structural applications. Intermetallic compounds of these metals and their alloys have high melting temperatures, low density, and excellent high temperature creep resistance. However, the alloys also tend to be fairly brittle at ambient temperature. The operating temperature of these new structural materials are expected to be in the range of 800-1500°C. In order to operate in this temperature regime, the new alloys must have melting temperatures in the 1400-2500°C range. Several intermetallic compounds of niobium, tantalum, and their alloys possess such melting temperatures. However, the mechanical behavior of these alloys and their relationship to different processing techniques, micro- and macro-alloying have not been studied to a great extent. Most of these alloys oxidize above 650°C, with catastrophic results[1]. Therefore, adequate oxidation resistance is also required, and must be an integral part of the alloy development program. High temperature oxidation resistance can be achieved either by coating with other compounds, e.g. silicides, or by forming a protective layer by selective oxidation of one or more of the alloying element[1,2].

Conventional casting of these high melting alloys often leads to the formation of embrittling segregates during slow cooling, as in the case of ingot casting [3]. It has been shown in a number of studies [3-6] that mechanical behavior at high temperature is strongly dependent on both the structure and chemistry of the alloy. It has also been shown that for certain alloy systems, rapid solidification processing can lead to improved mechanical properties [3]. This improvement in properties is a direct consequence of microstructural refinement and compositional homogeneity that can be achieved via rapid solidification. Other effects of rapid solidification include solid solubility extension, creation of metastable crystal structure, and massive solidification.

Since the early 60's, workers in this field have been concentrating on achieving higher cooling rates, principally for the purpose of forming metallic glasses [7]. However, in the past 10-15 years a significant amount of attention has also been focused on rapidly solidified crystalline alloys, especially iron, nickel, aluminum, and titanium based alloys[8-10]. For example, melt spinning and powder atomization techniques are capable of reaching cooling rates of up to million degrees per second. Such high cooling rates can give rise to large supercoolings, estimated to be up to 100K, prior to solidification. For bulk metallic samples, the techniques mentioned above are not applicable. Since the material has to be small in at least one dimension in order to allow for the rapid removal of the heat liberated during solidification. However, high supercooling in bulk metallic samples can be obtained by the electromagnetic levitation melting technique[11-14]. This in turn causes solidification with high interfacial velocities.

It has been shown that long range ordering can produce a significant effect on mechanical behavior in some alloy systems [5]. Ordering can improve mechanical properties by altering ductility and strain-hardening rates [15]. Ordered alloys are characterized by their high yield and fracture stress that are maintained up to high temperature relative to unordered alloys. Partially covalent and ionic bonding is predominant among these alloys, and are responsible for their high temperature strength. Mechanical behavior of ordered alloys are strongly influenced by the motion of the superlattice dislocations and their interaction with grain boundaries, precipitate particles, and antiphase boundaries (APB).

Recently, Cahn and coworkers [5,6] have shown that antiphase domains (APD) form only when the order-disorder transition temperature is below the freezing temperature. They recognized that the addition of the solutes in Ni-Al-X alloys, which lower the order-disorder transition temperature to below the freezing temperature, improves ductility because the APD's became finer. However, more systematic studies are needed to determine the effect of antiphase domains on ductility in ordered alloys.

From the above mentioned studies it is evident that room temperature ductilities of intermetallic compounds and their alloys can be altered by alloying and proper processing. The current research project has been undertaken to study the effect of supercooling and rapid solidification in a containerless inert environment using levitation melting for a number of niobium alloys. In particular Nb-Ti-Al, Nb-Al-Si, Nb-Ti-Si, and more complex niobium Nb-Ti-Al-Cr-V alloys were studied. This paper will review some of the results and explore the potential benefits of rapid solidification on structure, morphology, and chemical homogeneity in these alloys.

Experimental

Large multiple pass arc melted buttons each weighing about 200-250 gms were prepared in a high purity inert gas environment. The alloy buttons were broken into smaller pieces, each weighing approximately 1.2-1.5 gms. The alloy pieces were arc melted again in a furnace chamber, which was mechanically purged and backfilled at least three times with gettered argon gas, oxygen content on the order of 10^{-11} ppm, using a titanium-getter gas purifier. Following arc melting, samples were levitated in an electromagnetic levitation coil. Details of the electromagnetic levitation technique have been reported elsewhere [11-14,16]. A single color pyrometer, calibrated with pure niobium as a standard, was used to monitor the levitated sample temperature. The temperature accuracy is estimated to be $\pm 10^{\circ}\text{C}$. The thermal histories of the samples were recorded from the pyrometer readings. The levitated samples were then quenched either on a copper hearth or in a moving piston type splat cooler.

The processed samples were examined by x-ray diffraction, optical and transmission electron microscopy. Compositional analysis was performed in a JEOL JXA-733 electron microprobe using wavelength dispersive spectroscopy with pure standards. Thermal treatment of selected alloys was conducted in quartz capsules that were purged with argon then sealed.

Results and Discussion

Nb-Ti-Al System

The arc melted button alloys with an overall composition of Nb-27 Ti-35 Al (at.%) showed a two-phase microstructure, as shown in the backscattered electron micrograph in Figure 1. Compositional and x-ray analysis of the alloy showed that the matrix consisted of $(\text{NbTi})_2\text{Al}$ (sigma phase) with a tetragonal structure and an average matrix composition of Nb-26.4 Ti-34.8 Al. Average composition of the niobium depleted second phase was determined to be Nb-28.3 Ti-35.5 Al.

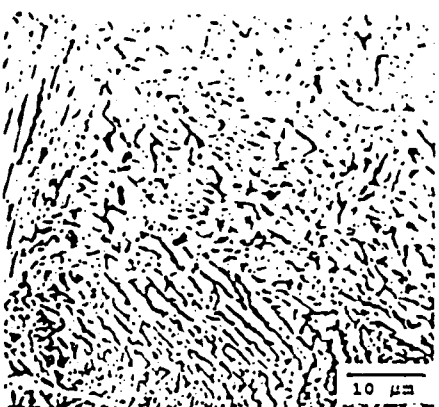


Figure 1 - Micrograph (BEI) of arc melted Nb-27 Ti-35 Al alloy. Gray matrix: $(NbTi)_2Al$ (Sigma) phase



Figure 2 - BEI micrograph of Nb-27 Ti-35 Al alloy showing columnar to dendritic transition. Sample quenched on a cooper hearth from a superheating of 65 K.

A mixed columnar and dendritic morphology was observed when the superheated alloy was quenched on the copper hearth. An example is shown in Figure 2 for a sample which was quenched from a 65 K superheat. The "pancake" shaped sample showed a columnar morphology on the Cu substrate side and a dendritic morphology on the non-contact side. The average composition of the niobium rich dendrites were Nb-26.2 Ti-35.6 Al and the interdendritic regions showed an average Nb concentration of 36.4 at.%. Since the growth morphology is dependent upon the prevailing heat and fluid flow conditions, solidification begins at the bottom surface which was in contact with the copper hearth as nucleation takes place preferentially on that surface. The solidified layer then grows into the melt, resulting in the columnar morphology. The melt surface that was in contact with the purge gas solidified with a randomly distributed equiaxed dendritic morphology. This morphology results from crystals nucleating randomly throughout the melt or from dendrite fragments which are dispersed by the fluid flow. Solidification in this region will also take place at a lower rate because of lower heat transfer condition compared to the substrate side. A sharp boundary region between the columnar and dendritic morphology was evident in the entire length of the cross-sectioned sample.

Various levels of supercooling were obtained in most of the Nb-27 Ti-35 Al alloy samples, with a maximum supercooling of 342 K. Upon solidification, the supercooled Nb-27 Ti-35 Al alloys showed a single phase microstructure. Thermal history and the corresponding microstructure of a single phase sample that was quenched on the Cu hearth at 331 K supercooling is shown in Figure 3. The Nb concentration was determined to be between 37.6 to 38.2 at.% (average 37.9) in the as-solidified sample. The solidified sample was of nearly spherical shape, indicating that the supercooled liquid either recrystallized prior to impact with the copper hearth, or became mostly solid rapidly before the liquid had time to spread. The grain structure was non-uniform but nearly equiaxed.

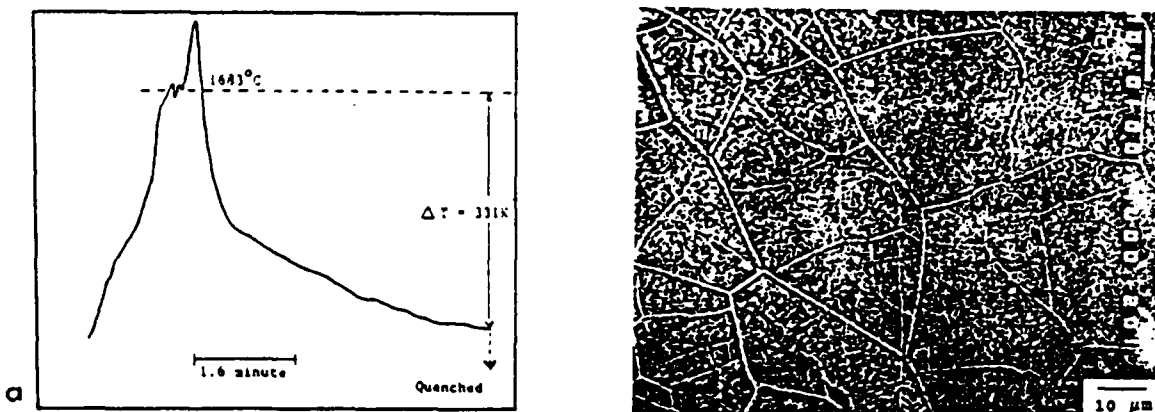


Figure 3: (a) Thermal history of the Nb-27 Ti-35 Al alloy, supercooled 331 K and (b) BEI micrograph showing single phase ordered B2 structure.

Metastable B2 Structure

The microstructure of another supercooled and splat quenched Nb-27 Ti-35 Al alloy was examined by transmission electron microscopy. Figure 4(a) shows dark field TEM micrograph of the sample, which shows antiphase domains (APD). The antiphase domains were found to be uniform throughout the grain interior with APD size of 0.08 - 0.15 microns. These domains indicate an ordered phase which was determined by selected area electron diffraction and x-ray diffraction to be that of an ordered B2 (CsCl), Im3m structure. The lattice parameter was measured to be approximately 3.22 Å.

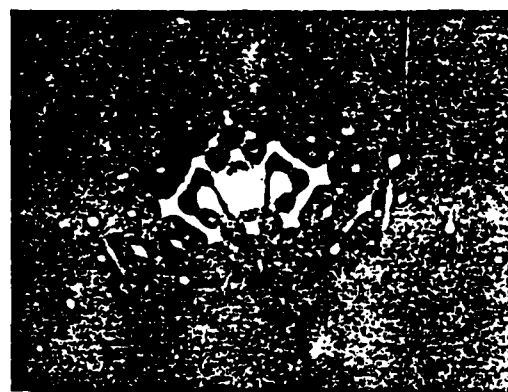
Figure 4(b) shows the presence of superlattice reflections due to ordered structure in an electron diffraction pattern obtained near the $\langle 001 \rangle \beta$ zone [17]. Strong streaking along $\langle 110 \rangle \beta$ with associated $\langle 110 \rangle$ rel rods (extra diffraction spots near the fundamental reflections) surrounding each reciprocal lattice point and very faint maxima at $\langle 110 \rangle \beta$ are also evident in the diffraction pattern. Interestingly, streaking is also observed along $\langle 110 \rangle \beta$ through superlattice reflections. While these observations are not consistent with an ordered B2 structure, observations similar to these have been reported in rapidly quenched Ti_xAl-Nb alloys by Strycor et al. [18] and Ward et al. [19].

It is also found that when two beam conditions are employed with $g = \langle 200 \rangle$ near the $\langle 001 \rangle \beta$ zone, a "tweed" type of contrast is produced in the microstructure as shown in Figure 4(c). The "tweed" structure is observed as

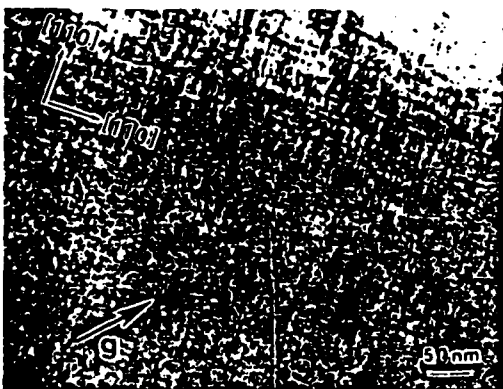
a striation which traces parallel to the $\{110\}$ plane in the microstructure, which are absent whenever the $\{110\}$ plane traces are perpendicular to the operating g vector under two beam conditions. It has been suggested [19] that the occurrence of a tweed microstructure is due to lattice shear strains of type $\langle 110 \rangle <110>$.



(a)



(b)



(c)

Figure 4: (a) dark field TEM of splat cooled Nb-27 Ti-35 Al alloys showing antiphase domains, (b) selected area diffraction pattern of $\langle 001 \rangle \beta$ zone showing ordered B2 structure, and (c) bright field TEM showing "tweed-like" striations--due to lattice shear strains, $g = \langle 200 \rangle$ near $\langle 001 \rangle \beta$ zone.

Annealing of the splat cooled Nb-27 Ti-35 Al alloy at 400°C for 24 hours did not appreciably alter the ordered B2 phase. However, upon continued annealing of the same sample at 825°C for an additional 3½ hours, the metastable B2 structure decomposed to the tetragonal sigma structure. X-ray diffraction scans of the arc melted alloy with tetragonal sigma structure, and the ordered B2 structure of a splat cooled ($\Delta T = 112$ K) alloy are shown in Figures 5(a) and 5(b), respectively. Figure 5(c) shows the x-ray diffraction scan of the same splat cooled alloy after annealing at 825°C for 3½ hours. High temperature x-ray diffraction experiments are currently in progress to determine the ordering transition temperature.

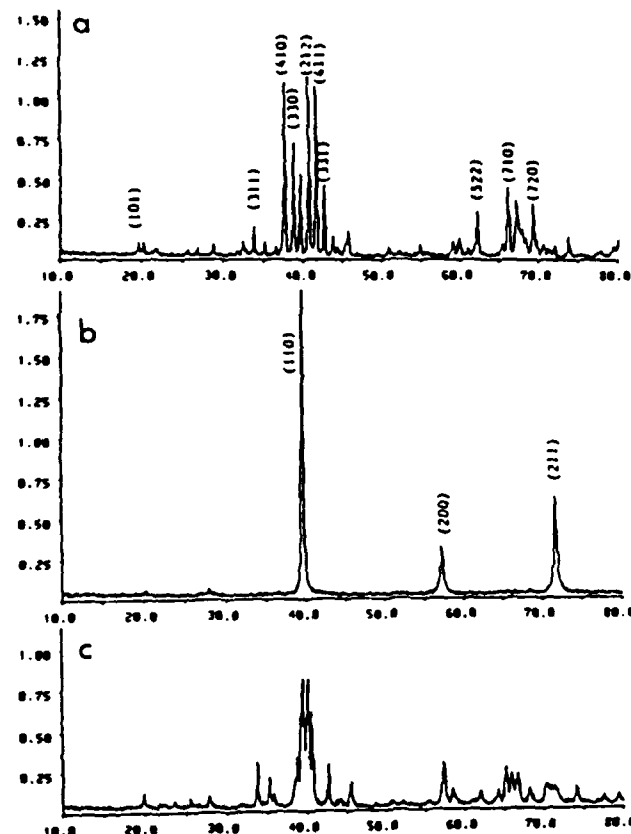


Figure 5 - X-ray diffraction patterns of Nb-27 Ti-35 Al: (a) arc melted alloy, showing tetragonal sigma structure, (b) Ordered B2 structure of a splat cooled sample, (c) XRDA of (b) after annealing at 825°C for 3 1/2 hours.

Phase equilibrium in the Nb-Ti-Al system is poorly understood, primarily because of limited amount of available data. Figure 6 shows the phase field of the BCC phase at 1100°C, as estimated by Bendersky et al. [20], based on experimental data. The estimated BCC field where B2 order exists is shown by the dotted line. They proposed that since no APB's were found from B2 ordering in their study, the B2 phase is an equilibrium phase at 1100°C.

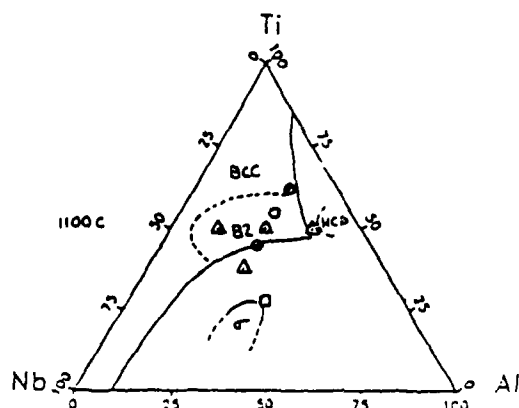


Figure 6 - The estimated single phase field of the BCC phase at 1100°C [20].

Since an ordered B2 phase was observed in the splat cooled Nb-27 Ti-35 Al alloy specimens, it suggests that the B2 phase exists at Nb concentrations of up to 38 at.%. The temperature where this phase exists is above 825°C.

Ward et al. [19] also studied the effect of niobium concentration in melt spun Ti₃Al-Nb alloys. Niobium concentration of 12 to 30 at.% was studied and it was found that both grain size and antiphase domain spacing become finer in high Nb alloys, while the lattice parameter (measured to be approximately 3.24 Å) increased slightly as the Nb content increased. The APD size decreased from 0.4 microns for 12 at.% to 0.2 microns for 30 at.% Nb. The alloy in the current study, which contained 38 at.% Nb, showed even finer APD spacing, as noted above. Two mechanisms have been proposed for the reduction in the APD size [19]. Introduction of additional heavier niobium atoms in the alloy reduces diffusivity in the matrix. Since growth of APD's are diffusion controlled process, higher niobium concentration would reduce APD growth. It is also possible that the ordering transition temperature is decreased with increased niobium content. Consequently, APD's will have less time to grow during cooling.

Rapid solidification (splat cooled from 120 K supercooling) of the Nb-27 Ti-35 Al alloy with 3 at.% Cr and 4 at.% V substituted for Nb also resulted in an ordered B2 structure, as determined by x-ray diffraction. The lattice parameter was measured to be approximately 3.19 Å, compared to 3.22 Å for the Nb-27 Ti-35 Al alloys. The smaller lattice parameter is due to the addition of Cr and V atoms in the alloy, which have smaller atomic radii. It has been shown [2] that the Cr and V addition are beneficial for high temperature oxidation resistance of these alloys. Therefore, any improvement in the room temperature ductility of this series of alloys should be of significant technological importance.

Phase Suppression in Nb-Ti-Si Alloys

The Nb-Ti-Si alloys are attractive, primarily because of their higher melting temperatures compared to the niobium aluminides. However, conventional casting of these alloys results in the formation of the (NbTi)₃Si₃ phase, which is brittle and frequently contains thermally induced cracks. Because of the presence of this phase in the solidified morphology, crack propagation can result in brittle failure.

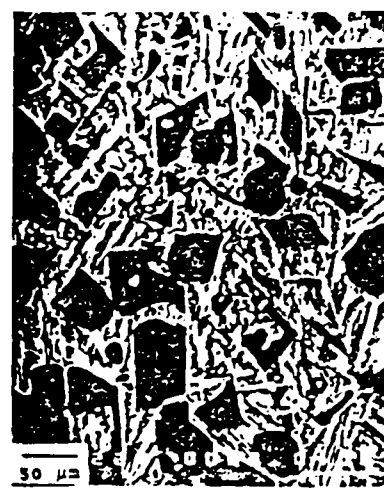
The microstructure of the arc melted samples consisted of dendrites of primary (NbTi)₃Si₃ phase (tetragonal I4/mcm structure) surrounded by the peritectically formed (NbTi)₃Si phase (tetragonal P4₂/n structure) as shown in Figure 7. The last liquid to solidify is the niobium-titanium solid solution



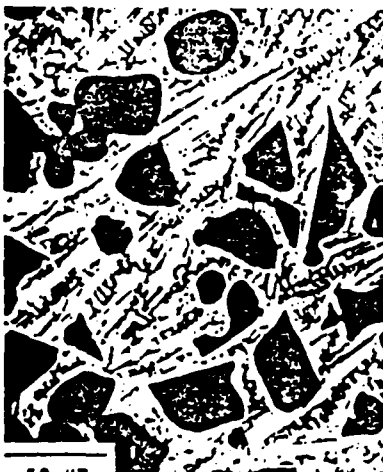
Figure 7 - Microstructure of arc melted Nb-20 Ti-21.3 Si alloy (BEI). Dark phase: (NbTi)₃Si₃. Gray phase: (NbTi)₃Si. White phase: NbTi solid solution.



(a)



(b)



(c)



(d)

Figure 8 - Microstructure (BEI) of supercooled Nb-20 Ti-21.3 Si: (a) 20K, (b) 142K, (c) 188K, and (d) 275K; For the latter sample $(NbTi)_3Si_3$ phase is suppressed.

containing 2-3.2 at.% Si, which appears as the white phase in this figure. The structure showed cracks not only in the $(NbTi)_3Si_3$ phase, but also large cracks that propagated throughout the matrix.

Various levels of supercoolings were achieved for this alloy, with a maximum of 290 K. The series of micrographs presented in Figure 8 show the effect of supercooling. All samples were quenched on a copper hearth, therefore a similar cooling rate can be assumed for all of them. As can be seen in Figures 8(a) - 8(c), at supercoolings of up to 188 K, the solidification begins by the formation of $(NbTi)_3Si_3$ phase. In all three of the above supercooled microstructure morphologies, the primary $(NbTi)_3Si_3$ phase is followed by the formation of the $(NbTi)_3Si$ phase by peritectic reaction. Similar to the arc melted sample, the $(NbTi)_3Si_3$ phase shows cracks at these supercoolings.

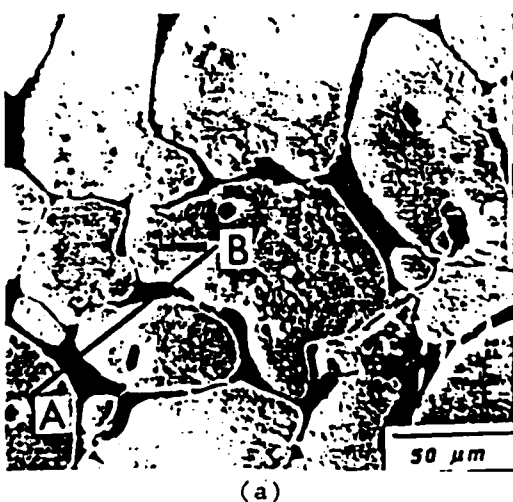
A dramatic change in the microstructure takes place when the sample is supercooled 275 K; the silicon rich brittle $(NbTi)_3Si_3$ phase is completely suppressed, as shown in Figure 8(d). Compositional line scan and x-ray analysis

of the matrix indicated an average alloy composition of Nb-20.3 Ti-21.3 Si and a tetragonal structure. Based on these results, the critical amount of supercooling required for the suppression of the $(NbTi)_3Si_3$ phase is between 188 and 275 K. Although the $(NbTi)_3Si_3$ phase is the thermodynamically stable primary phase, at large supercoolings nucleation of this phase is not viable. The dominant nucleating phase beyond the critical supercooling is determined by the nucleation kinetics at that temperature and growth velocities, which are dependent on the driving force for solidification and attachment kinetics.

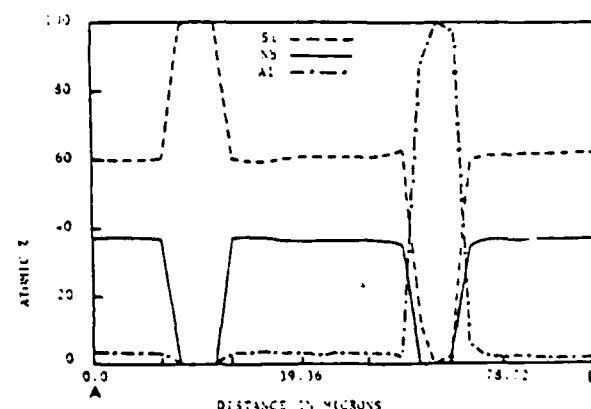
Niobium Aluminum Silicides

The arc melted Nb-7.2 Al-59.7 Si alloy, shown in Figure 9(a), consisted mostly of grains of $Nb(SiAl)_2$ (orthorhombic $TiSi_2$ type structure). A compositional line scan profile of the alloy is shown in Figure 9(b) which was taken across line A-B of Figure 9(a). From the linescan and the corresponding micrograph, it can be noted that the intergranular region consists of two phases: the black phase is almost pure Al (99.97 at.% Al), and the dark gray phase is Si (up to 99.9 at.%). Niobium concentration in the grain interior varies between 35.9 to 37 at.%. As evident from Figure 9(a), the $Nb(SiAl)_2$ phase solidified first and with continued cooling, the remaining liquid transformed to Si and Al solid solutions.

Substantial microstructural and compositional homogeneity was achieved when the alloy was solidified on the copper hearth from the supercooled state, as shown in Figure 10. The average composition of the processed alloy was determined to be Nb-6.6 Al-54.6 Si. Microprobe analysis of the processed alloys also revealed some Al losses during levitation. Figure 10(a) shows the microstructure of the alloy at 247 K supercooling. The compositional linescan shown in Figure 10(b), was taken across the line C-D of Figure 10(a). The micrograph shows formation of niobium rich faceted $Nb_3(SiAl)_3$ phase (the white phase in Figure 10(a)) in a $Nb(SiAl)_2$ matrix. The niobium concentration in the matrix varied from 36-37.9 at.% and Si concentration ranged from 59.8 to 62 at.%. The concentration of Al in the $Nb_3(SiAl)_3$ phase is between 2-2.3 at.%.



(a)

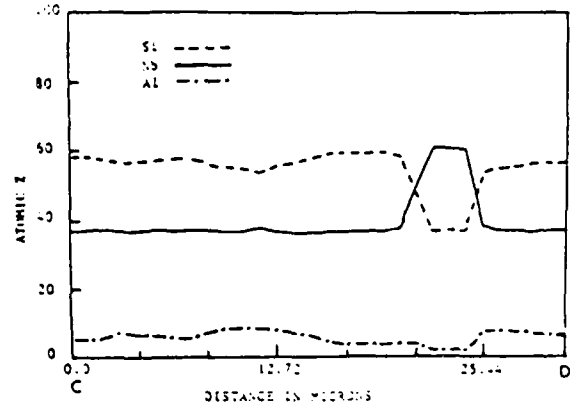


(b)

Figure 9: (a) Electron micrograph (SEI) of Nb-7.2 Al-59.7 Si alloy and (b) compositional linescan showing Si and Al in the intergranular regions.



(a)



(b)

Figure 10: (a) Microstructure of Nb-6.6 Al-54.6 Si alloy quenched on a copper hearth, supercooled 247 K. White phase: Nb_5Si_3 , Gray phase: $\text{Nb}(\text{SiAl})_2$, and (b) compositional linescan of the sample across the line C-D.

In contrast with the arc melted samples, no Al or Si rich phase in the intergranular region was observed in the supercooled sample. It is possible that the Al-rich phase was eliminated because of the 0.6 at.% Al loss in the processed alloy. The micrograph (Figure 10(a)) also reveals some shrinkage porosities in the matrix as well as around the $\text{Nb}_5(\text{SiAl})_3$ phase. During rapid cooling of the supercooled liquid, $\text{Nb}_5(\text{SiAl})_3$ phase nucleates first. The remaining liquid is Si rich and Nb depleted, resulting in the formation of $\text{Nb}(\text{SiAl})_2$ phase.

Summary

The following conclusions can be drawn from the current experimental investigation of the niobium based alloys using a containerless processing technique:

- (1) Increased compositional homogeneity and microstructural refinement can be achieved in ternary Nb-27 Ti-35 Al, Nb-20 Ti-21.3 Si, and Nb-7.2 Al-59.7 Si alloys upon supercooling followed by rapid solidification.
- (2) A single phase microstructure is obtained in supercooled and rapidly solidified Nb-27 Ti-35 Al alloys. An ordered B2 structure, with an average APD size of approximately 0.08-0.15 μm , was retained during solidification of the alloy. The B2 to sigma transformation temperature is above 825°C for this composition. An ordered B2 structure was also found in Nb-27 Ti-35 Al-3 Cr-4 V alloys when splat cooled from 120 K supercooling.
- (3) Formation of the brittle $(\text{NbTi})_5\text{Si}_3$ phase can be suppressed in highly supercooled Nb-20 Ti-21.3 Si alloys. The critical supercooling required for the suppression of the $(\text{NbTi})_5\text{Si}_3$ phase is between 188 K and 275 K.

- (4) During bulk supercooling of Nb-7.2 Al-59.7 Si, the low melting interdendritic phases (Al and Si solid solutions) are eliminated, and the faceted intermediate $Nb_3(SiAl)_3$ phase becomes the primary nucleating phase.

Acknowledgement

The authors would like to acknowledge support of this research by Pratt and Whitney, West Palm Beach, FL and the University of California at Santa Barbara. Special thanks are due to R.J. Hecht and R. Mehrabian for their valuable discussions and contributions.

References

- [1] Wadsworth, J., Nieh, T.G., and Stephens, J.J., Int. Mat Reviews, p. 131, vol. 33, 1988.
- [2] Perkins, R.A., Chiang, K.T., and Meier, G.H., Air Force office of Scientific Research, Contract No. F49620-86-C-0018 (1987).
- [3] Rowe, R.G., Taub, A.I., and Froes, F.H., in Rapid Solidification Processing, Principles and Technologies, IV, p. 149, Mehrabian and Parrish (Eds.), Claitor Publishing, 1986.
- [4] Koch, C.C., in High Temperature Ordered Intermetallic Alloys, p. 397, Koch, Liu, and Stoloff (Eds.), MRS, 1984.
- [5] Cahn, R.W., in High Temperature Ordered Intermetallic Alloys II, p. 27-38, Stoloff, Koch, Liu, and Izumi (Eds.), MRS, 1986.
- [6] Cahn, R.W., Siemers, P.A., Geiger, J.E., Bardhan, P., as-reported in ref. [5].
- [7] P. Duwez, Trans. ASM, Vol. 60, p. 607, 1976.
- [8] Inoue, A., Tomioka, H., and Masumoto, T., Met. Trans., p. 1367, vol. 14A, 1983.
- [9] Adam, C.M., and Lewis, R.E., in Rapidly Solidified Crystalline Alloys, p. 157, Das, S.K., Kear, B.H., and Adam, C.M., (Eds.), TMS Publications, 1985.
- [10] Olson, G.B., and Bourdeau, R.C., ibid, p. 185.
- [11] Munitz, A. and Abbaschian, G.J., in Undercooled Alloy Phases, p. 23-48, Collings and Koch (Eds.), TMS Publications, 1986.
- [12] G.J. Abbaschian and E.C. Ethridge, "Containerless Electromagnetic Levitation Melting of Cu-Fe and Ag-Ni Alloys," NASA TM-82553, September 1983.
- [13] G.J. Abbaschian and M.C. Flemings, Metall. Trans. A., 1983, 14A, 1147-1157.
- [14] J.A. Patchett and G.J. Abbaschian, Metall. Trans. B, 1985, 16B, 505-511.

- [15] Stoloff, N.S., in High Temperature Ordered Intermetallic Alloys, p. 3, Koch, Liu, and Stoloff (Eds.), MRS, 1984.
- [16] Amaya, G.E., Patchett, J.A., and Abbaschian, G.J., in Grain Refinement in Casting and Welds, p. 51-65, Abbaschian and David (Eds.), TMS Publication, 1982.
- [17] Hoelzer, D., Ph.D. Research in Progress, University of Florida, Gainesville, FL.
- [18] Strychor, R., Williams, J.C., and Soffa, W.A., Met. Trans., p. 225-234, vol. 19A, 1988.
- [19] Ward, C.H., Broderick, T.F., Froes, F.H., Jackson, A.G., Rowe, R.G., in Processing of Structural Metals by Rapid Solidification, p. 243-246, Froes and Savage (Eds.), ASM Publications, 1986.
- [20] Bendersky, L.A., and Boettinger, W.J., MRS Fall Meeting, November 28-December 3, Boston, MA, 1988.

PART II

Formation and Decomposition of Metastable B2 Phase in Ta-Ti-Al Alloys

By

Y. S. Kim, K. R. Javed, and G. J. Abbaschian
Department of Materials Science
and Engineering
University of Florida
Gainesville, FL 32611

Abstract

The effect of solidification processing on the microstructure of Ta-Ti-Al and Ta-Ti-Al-Cr alloys were investigated using an electromagnetic levitation apparatus combined with a splat quencher. The alloys containing 32 to 40 at. % Al contained the metastable ordered β (B2) phase upon splat quenching of the superheated melt. Subsequent annealing in the range of 1000 to 1300°C resulted in the decomposition of the metastable phase into a stable two phase mixture of σ and γ . The effects of annealing temperature on the microstructure and mechanical properties were also investigated.

1. Introduction

In recent years, there has been a great deal of interest in the potential use of intermetallics for high temperature structural applications. The silicides and aluminides of refractory metals are particularly attractive for these applications because of their high melting temperature, and superior creep and oxidation resistances [1-3]. However, intermetallic compounds have inherently poor toughness due to their atomic bonding characteristics and complex crystal structures. Thus the practical use of these intermetallics depends on improving their toughness without sacrificing their creep and oxidation properties.

Several approaches have been attempted to improve their toughness, including microstructural control [4] and compositing [5]. With microstructural control, the shape and morphology of the constituent phases, which usually are composed of a ductile phase and a brittle hard phase, were modified in order to improve their toughness. In the compositing method, intermetallic materials have been used as the matrix in order to exploit their superior creep and oxidation resistances. Based on their high strength, relatively low density, and the ability to form a protective oxide layer at high temperatures, various compositions in Nb-Ti-Al and Ta-Ti-Al alloy systems have been of special interest.

In the Nb-Ti-Al alloy system, a region of compositions where the ordered β ($B2$, DO_3) phase is stable has been observed near the titanium rich compositions, as shown in Fig. 1 [6-7]. The $B2$ phase is known to be reasonably ductile at ambient temperatures [4],

which can be advantageous in low temperature manufacturing of components for subsequent high temperature applications. Our experiments, as described in Part I of this report, have shown that it is possible to form a metastable ordered B2 phase via rapid solidification in alloy compositions that are in the $\sigma + \gamma$ two phase field [8]. Furthermore the phase retained at low temperatures has higher ductility and lower strength than the corresponding stable $\gamma + \sigma$ phases. The retained B2 phase is metastable, it decomposes to the stable phases upon subsequent annealing. Also, the size, morphology, and spatial distribution of these stable phases control the fracture toughness. It is, therefore, necessary to optimize the annealing time and temperature in order to improve the fracture toughness of these alloys.

In the Ta-Ti-Al alloy system, the $\sigma + \gamma$ two-phase region is likely to posses the best combination of high melting temperature and high strength compared with the rest of the phase fields in Ta-Ti-Al alloy system. Thus, the alloys in this two phase region are the most promising candidates for high temperature structural applications. However, the presence of the metastable B2 phase region inside the $\sigma + \gamma$ two-phase field or formation of other metastable phase have not been investigated. In this study we have investigated the effect of the cooling rate and alloy composition on the metastable B2 phase formation in Ta-base alloys. Also the effects of the decomposition temperature on the microhardness and fracture toughness of the alloys were investigated.

2. Experimental Procedure

Four Ta-Ti-Al alloys were selected within the two-phase σ + γ field, as shown in Fig. 2. The compositions of the alloys are given in table 1. The alloy samples were arc melted under a gettered argon atmosphere with an oxygen content less than 10^{-11} ppm. Following arc melting, the samples were melted in an electromagnetic levitation apparatus. The details of the electromagnetic levitation technique have been reported elsewhere [10]. A single color pyrometer, calibrated against the melting temperature of pure niobium, was used to monitor the temperature of the levitated sample. The molten samples were then quenched in a moving piston type splat quencher. As shown in Table 1, the alloy compositions after levitation melting are slightly different than those of the arc melted samples due to volatilization of aluminum during electromagnetic levitation melting.

The processed samples were annealed at 1000, 1100, 1200, and 1300°C and analyzed using X-ray diffraction, Transmission Electron Microscopy, and optical microscopy. Also microhardness tests were performed in order to measure the hardness and estimate the toughness as a function of the annealing temperature.

3. Results and Discussion

3.1. Formation of the metastable ordered B2 phase.

Microstructures of arc melted and splat quenched Ta-1 samples are shown in Fig. 3. The microstructure of the arc melted sample consists of three phases with compositions listed in table 2. The electron microprobe analysis indicates that the white phase has a

composition of 38 at.% Ta, 21.3 at.% Ti, and 40.7 at.% Al. This composition corresponds to $(\text{TaTi})_3\text{Al}_2$.¹ This phase is surrounded by the gray phase which is designated as $(\text{TaTi})\text{Al}$. The interdendritic region is the aluminum rich $(\text{TaTi})_4\text{Al}_5$ phase, seen as the dark phase in the micrographs.

A similar three phase microstructure was also observed in the sample after splat quenching from a 75°C superheat. However, the compositions of the phases are slightly different than those of the arc melted samples. For example, the white $(\text{TaTi})_3\text{Al}_2$ phase has an average aluminum concentration of 42.4 at.%, while the gray $(\text{TaTi})\text{Al}$ phase contains 48 at.% Al, and the dark phase, the richest in aluminum, contains 52.9 at.% of aluminum. Although the splat quenched samples exhibited the same three phase mixture as are melted samples, their microstructures were refined significantly, as shown in Fig. 3. X-ray diffraction analysis indicated that the quenched samples contained phases which are mostly likely α_2 , σ , and η . Diffraction pattern for α_2 is shown in Fig. 4. However, the diffraction analysis did not reveal the presence of a metastable B2 phase.

The microstructures of the alloy Ta-2 in the as arc melted and as splat quenched conditions are shown in Fig. 5. In the as arc melted condition, the microstructure consists of two phases, identified using X-ray diffraction analysis as σ and γ . However, upon splat quenching, the microstructure is predominately single-

¹The phase designations are based on the measured compositions.

phase. X-ray diffraction analysis, Fig. 6, indicates the phase to be B2.

Fig. 7 shows a SAD pattern of the matrix of the splat quenched sample. The presence of streaks and superlattice reflections support the x-ray diffraction analysis that the matrix is an ordered phase. A TEM dark field image of splat quenched sample is shown in Fig. 8. As seen in the figure, the anti-phase domain boundary is not visible, suggesting that the order-disorder transition temperature is very close to or the same as the melting point of the alloy. Also, at these high magnifications, a second phase in the form of grain boundaries precipitates is visible.

In alloys Ta-3 and Ta-4, microstructures similar to those of the Ta-2 alloy were observed in the arc melted condition: the microstructure again consisted of two phases, identified as σ and γ . However, upon rapid solidification via splat quenching, the microstructure was predominantly the ordered B2 phase.

Thus, the metastable B2 phase was observed in the splat quenched Ta-2, Ta-3, and Ta-4 alloys. However, in the Ta-1 alloy which has a higher aluminum content, no metastable B2 phase was detected upon splat quenching.

3.2. Decomposition of the metastable ordered B2 phase.

The decomposition behavior of the metastable B2 phase upon annealing is important in controlling the properties of the alloys, since the size and spatial distribution of the stable phases affect the strength and toughness of the alloy. Fig. 9 shows the microstructures of alloy Ta-2 after annealing at 1000, 1100, and

1300°C for two hours. It can be seen that the single metastable B2 phase decomposes into two phases, which were identified as σ and γ , in agreement with the ternary isotherm at 1100°C (Fig. 2). The white phase in Fig. 9 is the tantalum rich σ phase $((\text{TaTi})_2\text{Al})$ which is known to be very brittle, whereas, the black phase is the aluminum rich γ phase $(\text{TiTa})\text{Al}$ which is a relatively ductile intermetallic compound.

Microhardness of the annealed samples was measured using a 200 gram load. As seen in Fig. 10, the microhardness in the as quenched condition shows the lowest value, while subsequent annealing increases the microhardness significantly. This increase corresponds to the decomposition of the soft B2 phase into a harder $\sigma + \gamma$ two-phase mixture. The microhardness decreases slightly with increasing temperature, which may be related to the microstructural coarsening.

In some of the annealed samples, small cracks were observed at the edge of microhardness indentations. As shown in Fig. 11, the crack length tends to decrease as the annealing temperature increases, indicating that the toughness increases with the annealing temperature. This behavior might be due to the coarsening of the relatively ductile γ particles in the σ matrix. However, it should be noted that the lengths of cracks were not long enough to quantify the toughness of the material by the microhardness indentation method. Nonetheless, the crack length data can be used as a qualitative indicator of the fracture toughness.

Qualitatively, as the annealing temperature increases, the microstructure becomes coarser and the toughness increases. Such a trend is commonly attributed to the "bridging toughening mechanism" of brittle matrix by a ductile second phase [11]. According to this mechanism, the toughness of the composite increases as the size of the ductile particle increases. However, for the $\sigma + \gamma$ alloys, the limited ductility of γ phase might not be adequate to produce toughening via the bridging mechanism, and other toughening mechanisms such as crack deflection or branching might be operating. Therefore, determination of the exact toughening mechanism requires further investigation.

5. Summary

For Ta-base alloys, rapid solidification results in the formation of a metastable ordered β (B2) phase upon quenching of the levitated Ta-26Ti-36 Al, Ta-27Ti-34Al, and Ta-23Ti-44Al-4Cr melts. However, no metastable ordered phase was obtained in Ta-25Ti-46Al alloy. Subsequent annealing of the metastable phase resulted in the formation of σ and γ phases. The effects of annealing temperature on the microstructure and mechanical properties were also investigated.

6. Acknowledgements

The authors would like to thanks to Professor Robert Mehrabian and Ralph J. Hecht for their support and discussions. This work was supported by the Defense Advanced Research Project Agency

through the University of California at Santa Barbara and the Pratt and Whitney Corporation.

7. References

1. R. L. Fleischer, High-Temperature Ordered Intermetallic Alloy II, edited by N. S. Stoloff, C. C. Koch, C. T. Liu, and O. Izumi (MRS Proc. 81, Pittsburg, PA 1987) pp 405-410.
2. J. D. Destefani, Advanced Materials & Processes, (2) pp 37-41 (1989).
3. D. M. Dimiduk and D. B. Miracle, High-Temperature Ordered Intermetallic Alloy, edited by N. S. Stoloff, C. C. Koch, .C T. Liu, and O. Izumi, MRS Proc. Boston, MA (1988).
4. J. Casillo, Y.S. Kim, D. T. Hoelzer, and F. Ebrahimi, "Development of Nb-based Intermetallics for High Temperature Structural Applications", TMS Conf. on High Temperature Aluminides and Intermetallics, Indianapolis, IN, Oct., 1989.
5. R. Bowman and R. Noebe, Advanced Materials & Processing, (8) pp 35-40 (1989)
6. C. H. Ward, T. F. Broderick, F. H. Froes, A. G. Jackson, R.G. Rowe, Processing of Structural Metals by Rapid Solidification, edited by Froes and Savage, ASM Publications, pp 243-246, 1986.
7. L. A. Bendersky and W. J. Boettigner, MRS Fall Meeting, Nov. 28-Dec., Boston MA (1988).
8. K. R. Javed and G. J. Abbaschian, Materials Processing in Space, The Metallurgical Society, October, 1988.

9. S. Sridharan and H. Nowothy, Z. Metallkunde, Bd 74, pp 468-472 (1983).
10. J. A. Patchett and G. J. Abbaschian, Metall. Trans. B, 16B, pp 505-511 (1985).
11. B. Budiansky, J. C. Amazigo, and A. G. Evans, J. Mech. Phys. Solids, 36(2), pp 167-187, 1988.

Table 1. The composition of the alloy investigated in this study.
 (All compositions are in at.%)

Alloy	Arc-melted	Levitation Processed
Ta-1	Ta - 24.7 Ti - 45.8 Al	Ta - 25.5 Ti - 45.5 Al
Ta-2	Ta - 26.8 Ti - 33.6 Al	Ta - 25.7 Ti - 32.4 Al
Ta-3	Ta - 26.4 Ti - 35.5 Al	Ta - 26.9 Ti - 33.1 Al
Ta-4	Ta - 23.1 Ti - 44.0 Al - 4.0 Cr	Ta - 22.7 Ti - 40.4 Al - 3.5 Cr

Note: The slight changes in the alloy composition are related to aluminum losses via vaporization during processing.

Table 2. Phase compositional analysis of the alloy Ta-1 using microprobe. (All compositions are in at.%)

Sample	Ta	Ti	Al	Phase*
arc-melted	11.1	32.9	56.0	(TaTi) ₄ Al ₅
	27.6	25.4	47.1	(TaTi)Al
	38.0	21.3	40.7	(TaTi) ₃ Al ₂
splat-quenched	18.4	28.8	52.9	
	25.6	26.4	48.0	(TaTi)Al
	33.2	24.5	42.4	(TaTi) ₃ Al ₂

* : the designation is based on the compositional analysis.

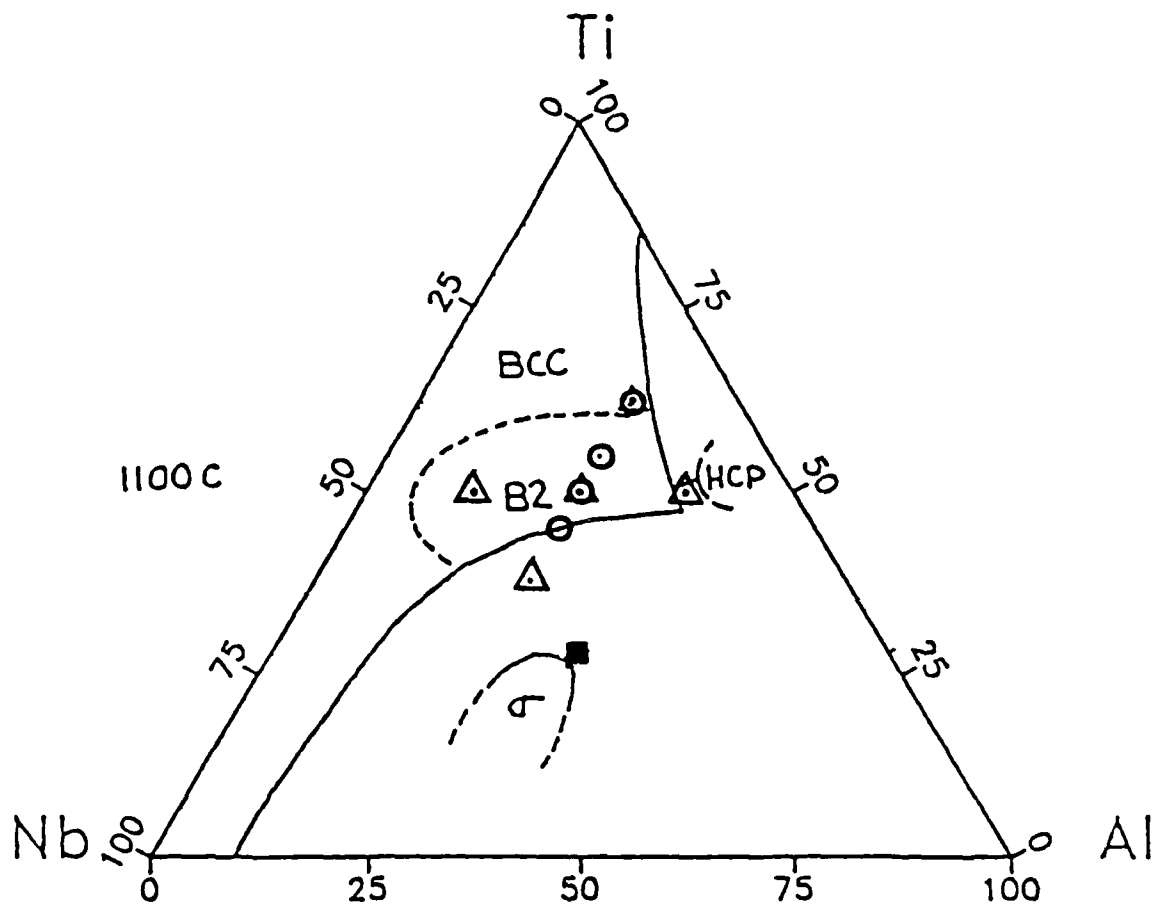


Fig. 1. The estimated single phase field of the BCC phase at 1100°C [7].

- △ Bendersky se al. [7]
- Ward et al. [6]
- Kazi et al. [8]

Ta-Ti-Al PHASE DIAGRAM—1100°C SECTION
(WORK OF SRIDHARAN AND NOWOTNY, 1983)

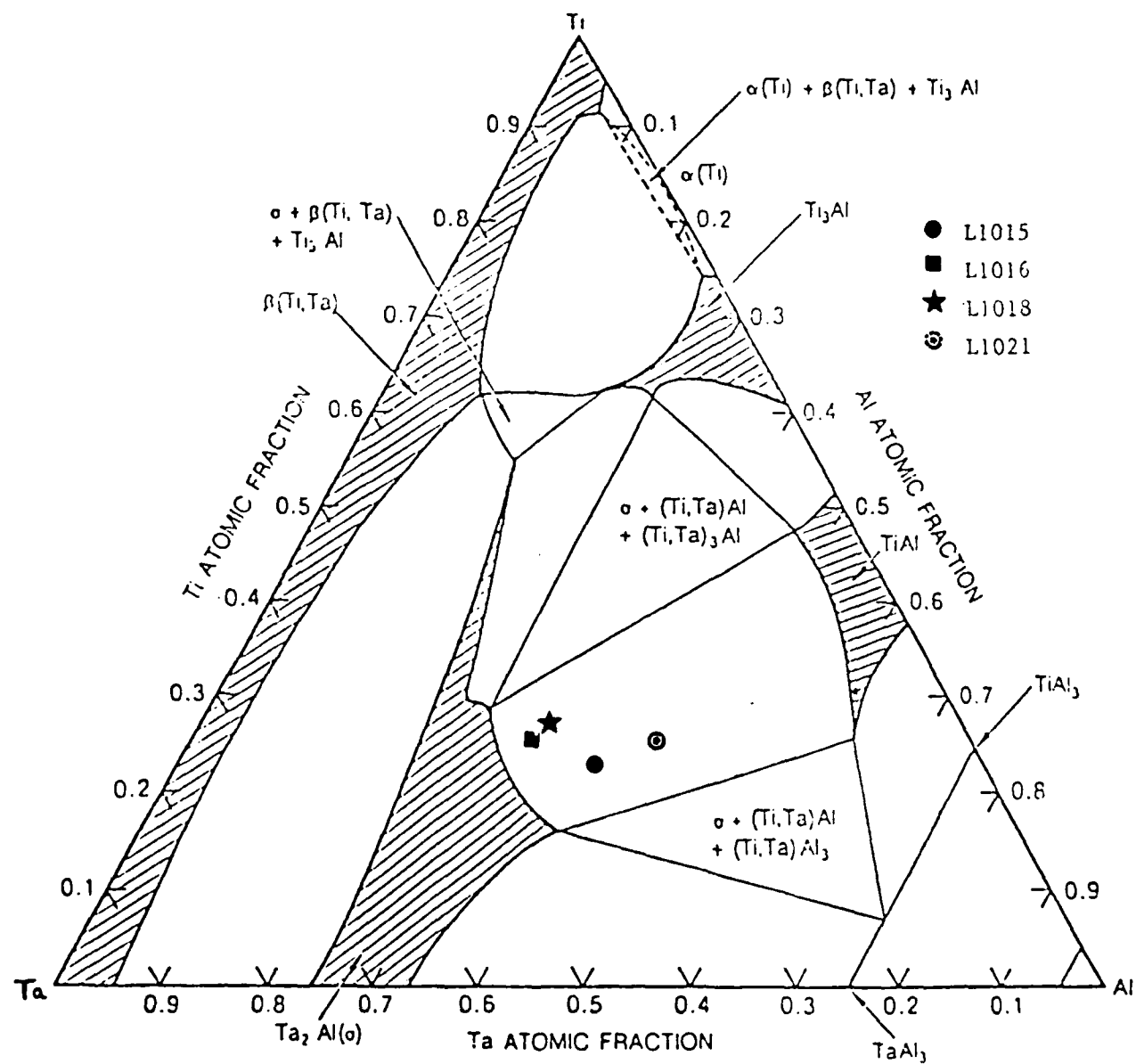
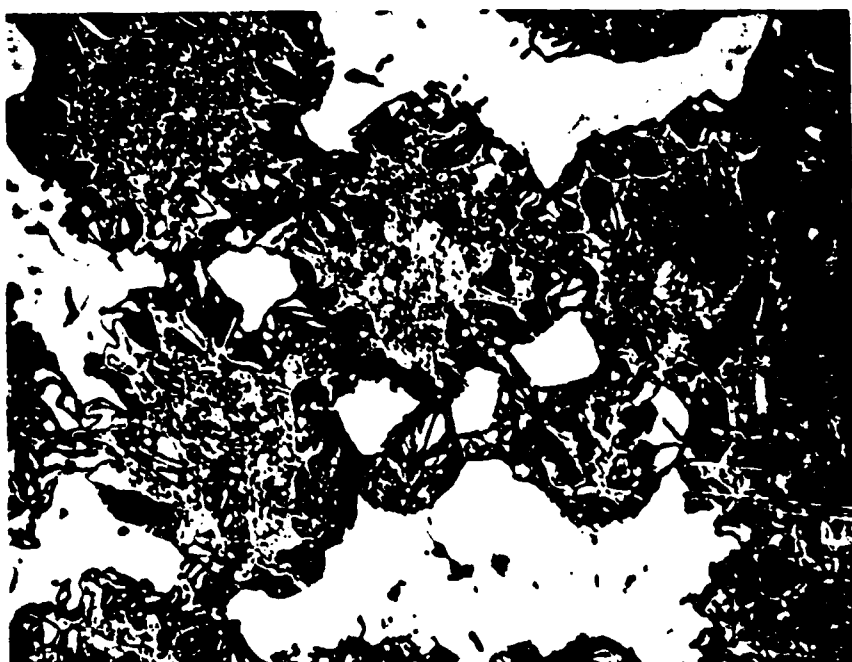
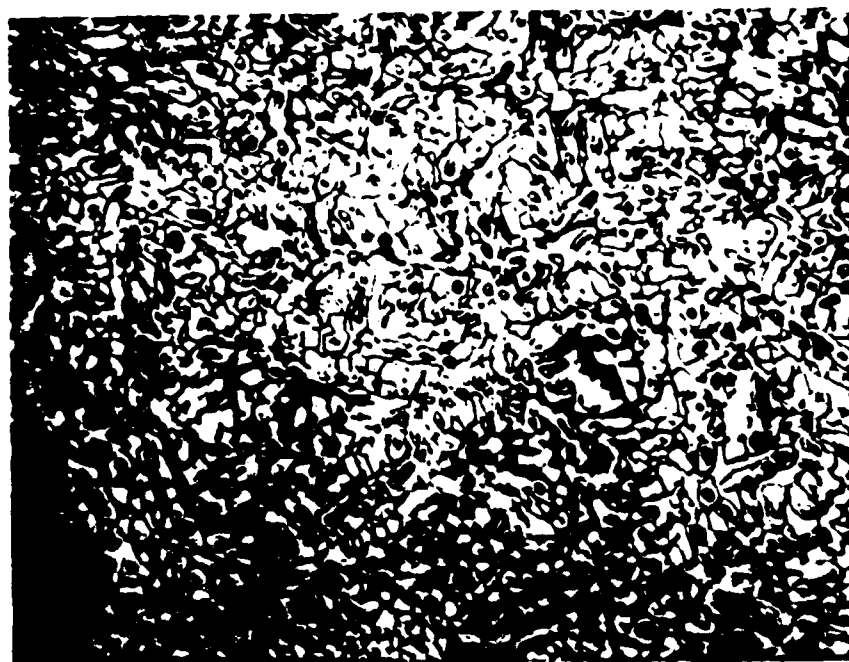


Fig. 2. The ternary Ta-Ti-Al phase diagram at 1100°C. (Sridharan and Noworthy [6])



(a)



(b)

Fig. 3. Optical micrographs of the alloy Ta-1 (a) as arc melted condition and (b) as splat quenched condition.

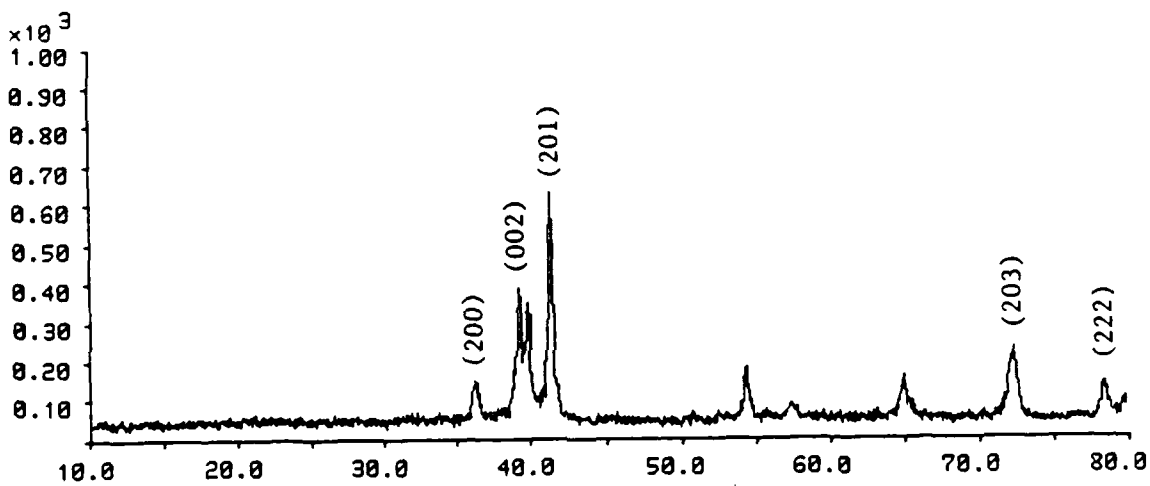
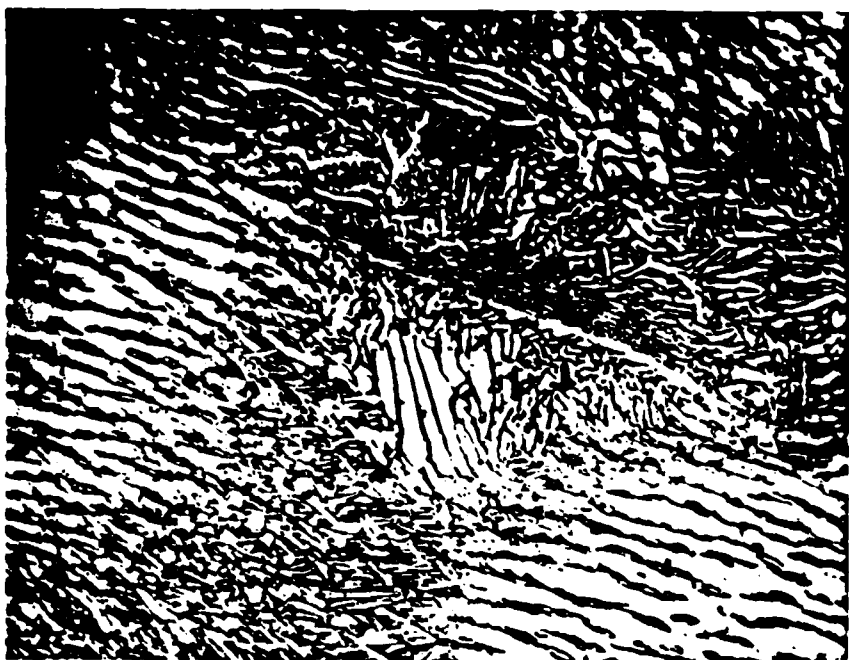
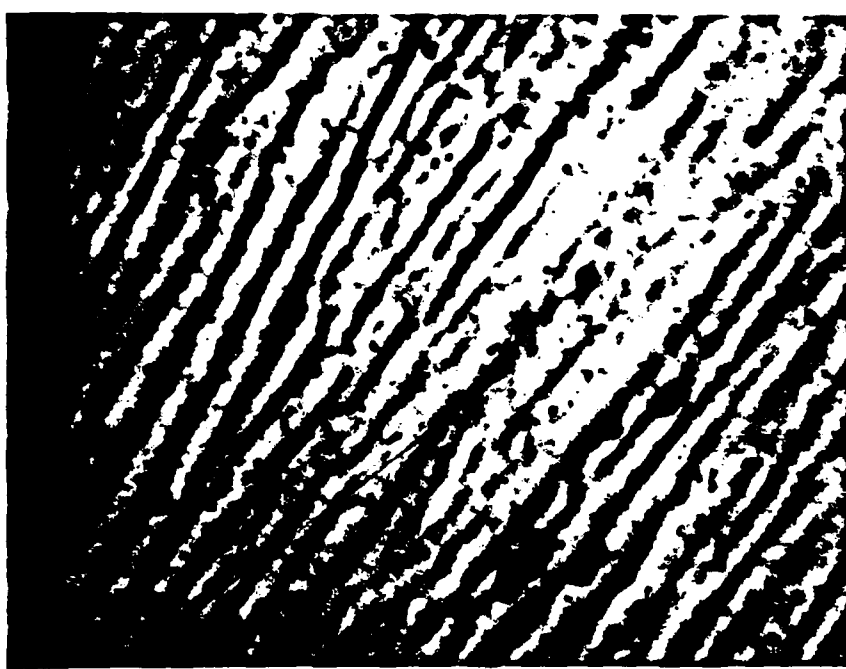


Fig. 4. X-ray diffraction analysis of alloy Ta-1 in as quenched condition. The results indicate the presence of α_2 phase.



(a)



(b)

Fig. 5. Optical micrographs of alloy Ta-2 (a) as arc melted condition and (b) as splat quenched condition.

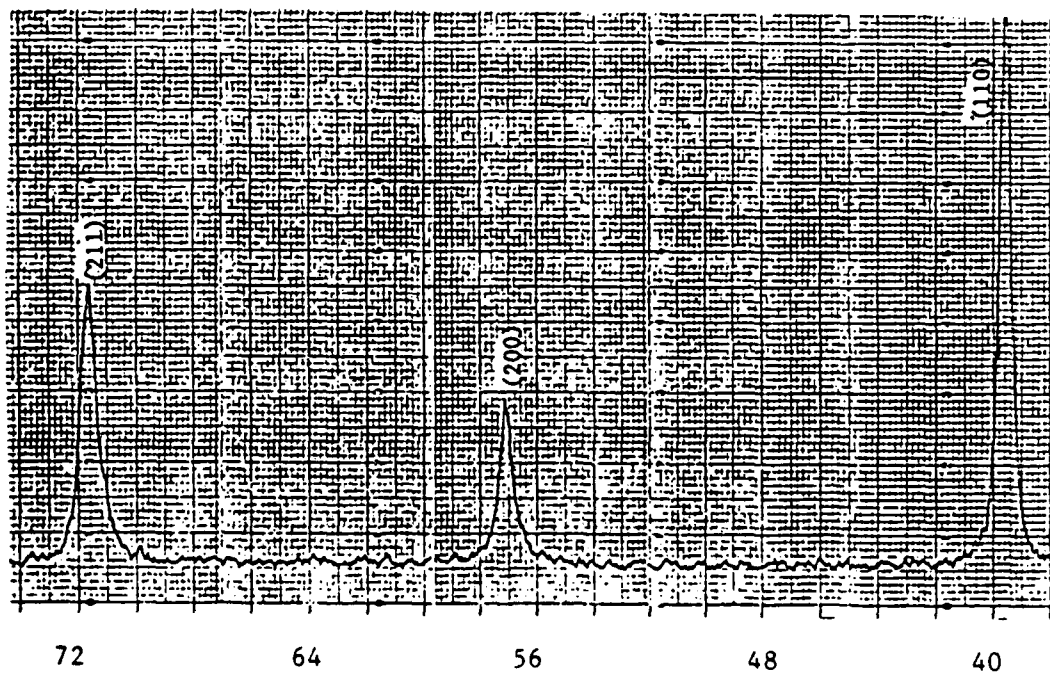


Fig. 6. X-ray diffraction analysis of the alloy Ta-2 in as splat quenched condition. The results show the presence of B2 phase.

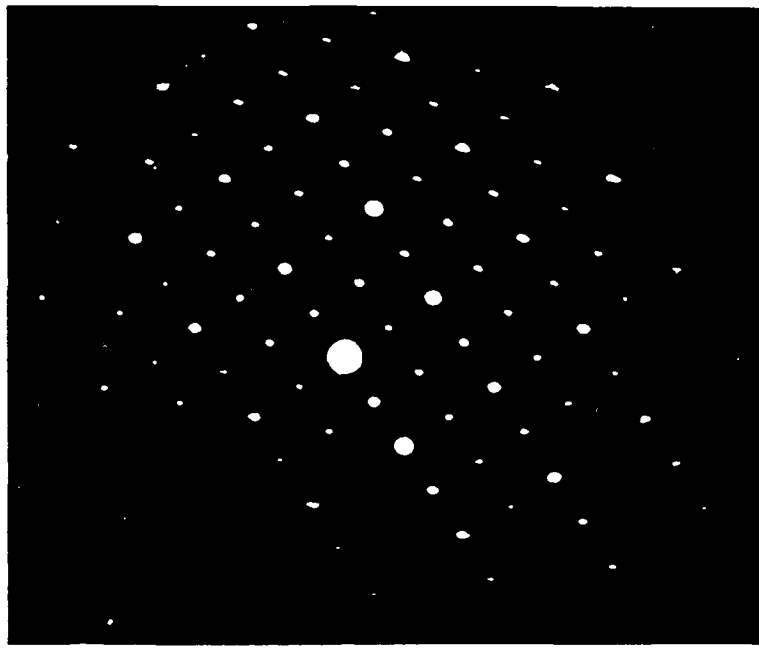
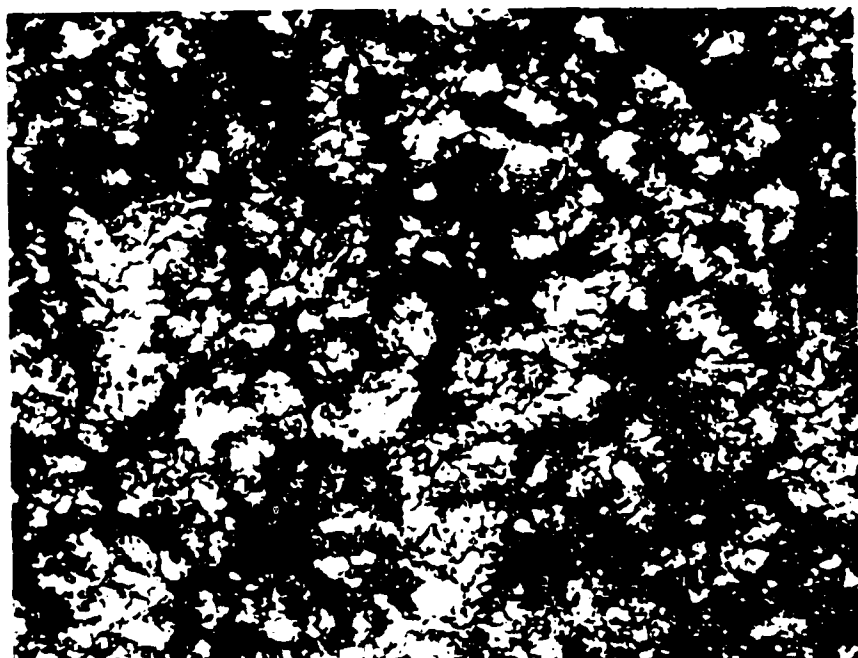


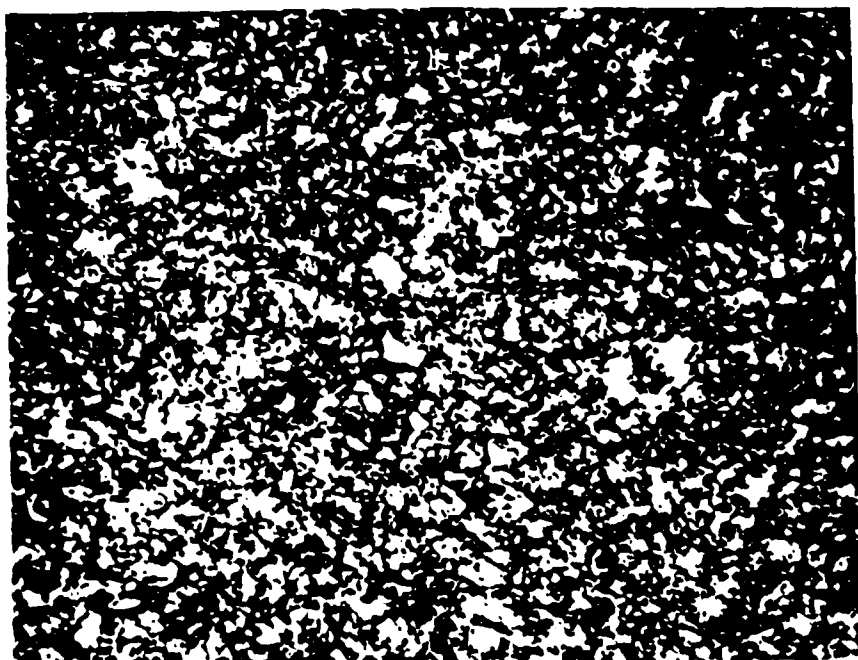
Fig. 7. SAD of matrix of alloy Ta-2. The superlattice reflection is observed suggesting that the matrix is ordered phase.



Fig. 8. TEM micrograph of alloy Ta-2 showing the predominant B2 phase with second phase precipitations at grain boundaries.



(a)



(b)

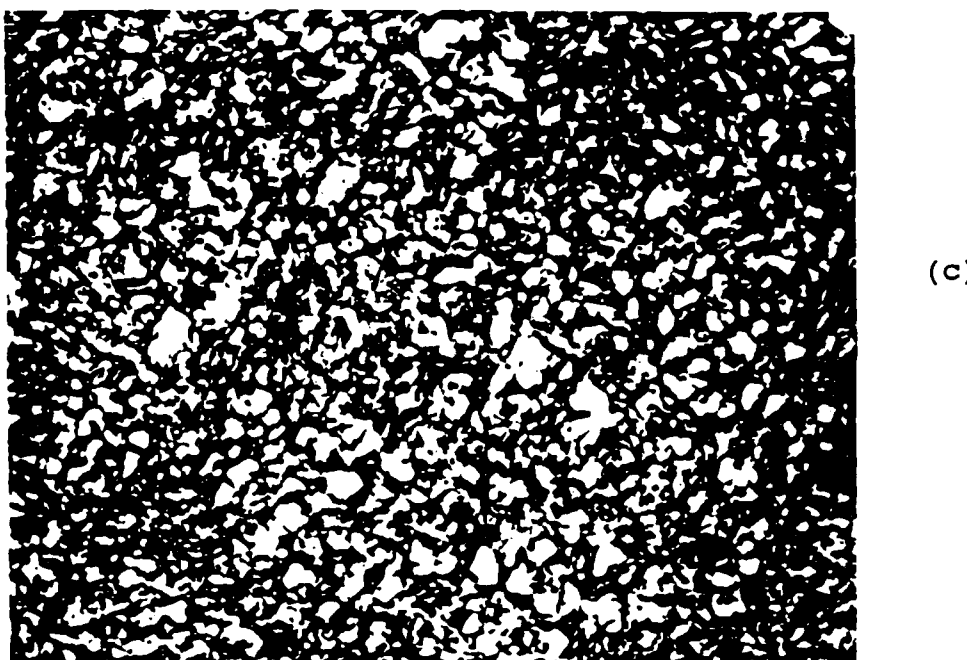


Fig. 9. Optical micrographs of alloy Ta-2 after heat treated at
(a) 1000, (b) 1100, and (c) 1300°C.

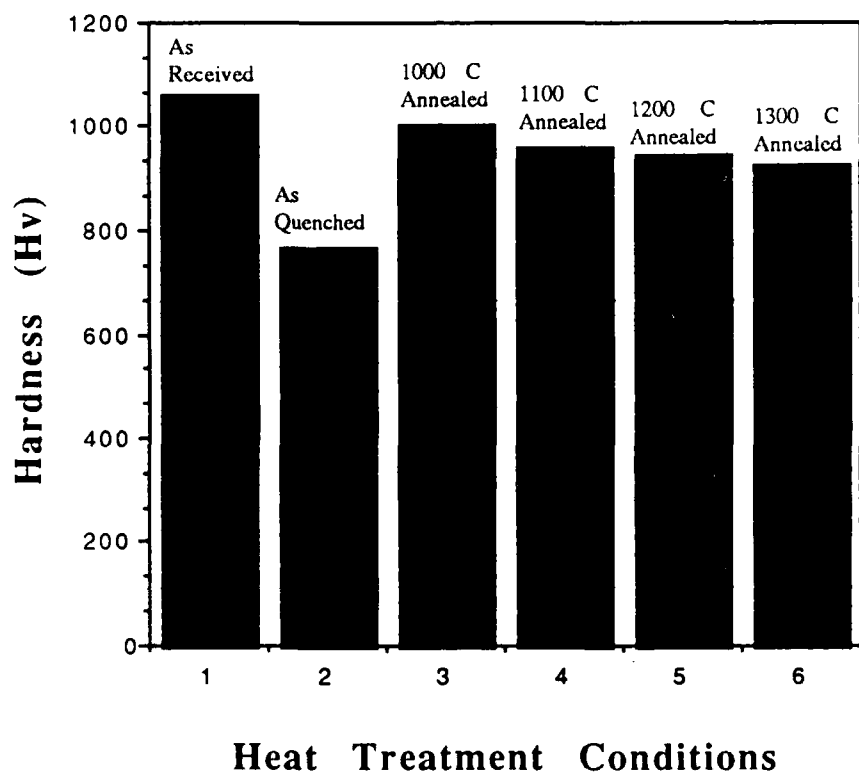


Fig. 10. Microhardness of the alloy Ta-2 after annealing at different temperatures.

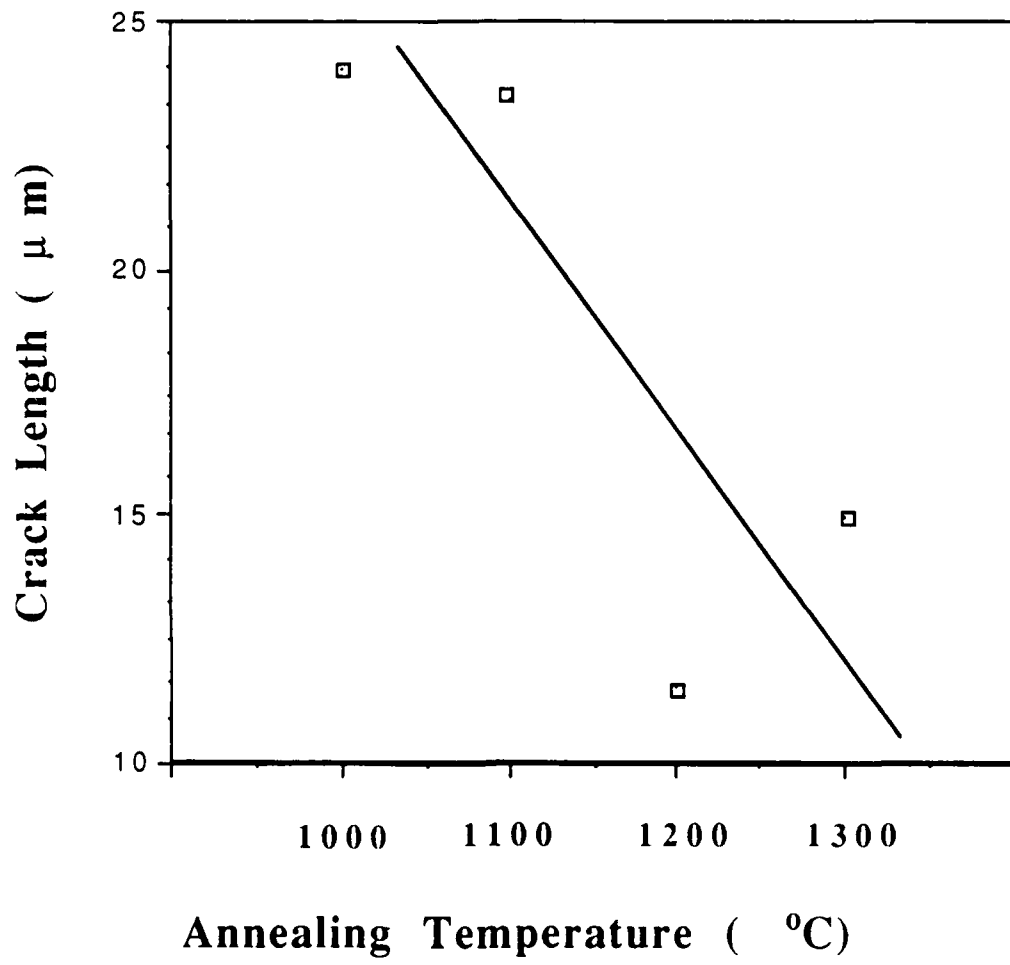


Fig. 11. Crack lengths measured during microhardness tests.
The load used was 1000 grams.

**Effects of Interfaces on the Design and
Oxidation Resistance of High Performance Composites:
Processing Pathways - Phase Equilibria and
Interdiffusion Reactions**

Final Report

(March 15, 1988 - September 30, 1989)

J. H. Perepezko, J.-C. Lin, T. J. Jewett and Y. A. Chang

Department of Materials Science and Engineering

University of Wisconsin-Madison

Madison, WI 53706

**Supported by DARPA through ONR Contract (N00014-86-K-0178) to the
University of California-Santa Barbara with a subagreement
(VB55107-0) to the University of Wisconsin-Madison**

Introduction

The needs for improved high temperature structural materials are widespread with much of the current attention focussed on aerospace applications. For structural materials, high strength and stiffness at elevated temperature are key requirements of the components which must also have some ductility at both elevated and temperatures. Oxidation and corrosion resistance are also needed in terms of microstructure stability. Current materials based on nickel alloys are limited for further improvement since their current operating temperatures are already in excess of 80% of the melting temperature. The development of new intermetallic alloys offers the promise of retaining higher strength at higher temperatures which is required for improved performance.

In the current program the objective is to develop a refractory intermetallic capable of surviving as a structural material in the temperature range of 1400-1600°C. Along with this requirement a lower density than conventional nickel based alloys as well as comparable or superior strength and creep properties at elevated temperatures are necessary. At the onset it is clear that all of these requirements may not be necessarily met by a single monolithic component, but rather such a component could form the basis of a composite material with an engineered microstructure designed to offer a combination of properties in order to satisfy the above mentioned requirements.

The performance of advanced composites and their stability are dominated by characteristics of the internal interfaces. At the same time these interfaces are strongly influenced by the

interaction of the various phases and the material processing pathways employed to produce the interface. Indeed in order to achieve the desirable combination of mechanical and chemical interface stability it is essential to consider material processing variables from the onset of fabrication. Among the most fundamental data needed for the development of a new process or the improvement of an existing one are the relevant phase diagrams both the stable and metastable conditions. In the case of intermetallic matrix composites the phase diagrams that are relevant are at least of ternary order. On the basis of these diagrams it is possible to select combinations of phases which may possess the desirable properties. In addition to phase diagram data, kinetic data are required to understand and control the possible chemical interactions at the interfaces in a composite system.

The research activities at the University of Wisconsin-Madison involve interrelated efforts which have been focussed on the determination of phase equilibria and interdiffusion kinetics in selected high temperature intermetallic systems. In conjunction with the experimental studies several approaches are also being examined to develop models for the analysis of microstructural evolution and to provide a basis for predictive capability during various materials processing steps. A central objective in the studies is the production of composite systems with well controlled microstructural features that have been identified in the structural mechanics model efforts and also in the oxidation

studies. In fact as a result of initial studies by industrial laboratory scientists it has been established that Ta and particular Ta-Ti-Al alloys offer the potential for suitable oxidation resistance for the program temperature range goal. From this basis studies have been initiated to evaluate the phase equilibria in the ternary Ta-Ti-Al system and to evaluate the interdiffusion kinetics for selected alloy phase composition in this ternary system.

Approach

The approach to evaluating phase equilibria and diffusional interactions involves the examination of as-cast and annealed alloys and diffusion couples in the ternary Ta-Ti-Al system. Bulk alloy compositions in the as-cast and annealed (at 1100 and 1400°C for 48 hours) conditions were examined by metallographic techniques (optical and scanning electron microscopy) x-ray diffraction analysis and electron microprobe analysis (EPMA) to identify the coexisting phases and to determine the equilibrated compositions. The analysis of annealed samples was supplemented by comparison with calculated phase equilibria based upon the analysis of the binary Ti-Al, Ti-Ta, and Ta-Al systems from a Thermocalc computation to evaluate the liquidus and relevant isothermal sections in the ternary system at several temperatures. The computer calculation of phase equilibria was conducted at NIST by Dr. Kattner.

For the diffusion couple samples several compositions in the binary Ti-Ta system were sputtered deposited onto a γ -TiAl alloy substrate using a dual source method. The thickness of the

deposited layer varied from 30-150 μm . The interdiffusion experiments were carried out in sealed, argon-filled quartz capsules in order to minimize reaction between the samples and the quartz capsules. The samples were coated with yttria and wrapped with tantalum foil. They were annealed at a fixed temperature for a period of time and quenched in ice-water. The quenched samples were characterized by optical microscopy, SEM and EPMA. In addition to probing the various phase fields for solubility in the ternary system and the identification of possible ternary alloy phases, the diffusion couple experiments provided information on the interdiffusion rates which were obtained from an analysis of the layer growth kinetics as determined by metallographic analysis.

Background

While good progress has been made in clarifying the binary equilibrium diagrams for the alumides especially in the case of the Ti-Al system (1,2). There are still a number of questions that remain to be resolved. For example, in the Ta-Al system previous work has reported existence of only 2 phases, Ta_2Al and TaAl_3 . However, recent studies have indicated a third intermetallic phase between the existing previously reported ones with composition near TaAl ⁽³⁾. The information on the ternary Ta-Ti-Al system is also quite limited. There have been only two reports dealing with the phase equilibria. In 1966 Raman⁽⁴⁾ proposed an isothermal section at 1000°C as shown in Fig. 1 which reveals extensive solubility of the β (bcc), σ , $\alpha_2(\text{D}0_{19})$, $\gamma(\text{L}1_0)$ and complete solubility of the $\eta(\text{D}0_{22})$ phases within the ternary

system. From this limited study no new ternary phases were reported. Subsequently, in 1983 Sridharan and Nowotny (S&N) reported an isothermal section at 1100°C which confirmed the extensive solubility into the ternary system of the various binary phases and the complete miscibility between $TaAl_3$ and $TiAl_3$ but did not consider a third intermetallic in the Ta-Al system between Ta_2Al and $TaAl_3$. This diagram is shown in Fig. 2 and reveals a general correspondence between the 1000 and 1100°C isothermal sections.

Based upon these previous studies a computer analysis of the phase equilibria was initiated to provide working estimates at other temperatures and to obtain an estimate of the liquidus projection in the Ta-Ti-Al system. In the calculation a phase diagram for the Ta-Al system was used which contains only the Ta_2Al and $TaAl_3$ phases. The calculation was performed on the basis of a Thermocalc program available at NIST. The equilibria for the 1100°C isothermal section is shown in Fig. 3 and reveals a general correspondence with results reported by S&N. The isothermal sections at 1300, 1400 and 1500°C are shown in Figs. 4-6. As the temperature increases the existence of the γ - σ equilibria diminishes in extent and at 1500°C is replaced by a liquid phase. This is also shown in the liquidus projection given in Fig. 7 where a peritectic reaction at 1468°C is indicated and a ternary eutectic between the $D0_{22}$, σ and γ phases is shown at 1394°C. Although these calculations are only a first estimate, they do provide a useful guidance in interpreting the alloy solidification pathways, the thermal stability and the structural

evolution during elevated temperature annealing. The results have also provided useful guidance in selecting alloy compositions to test the various phase equilibria indicated at the selected temperatures. In order to provide an evaluation of the previous partial studies of phase equilibria, the initial program was designed to provide a testing of the previous results and new information on the phase equilibria at 1100°C where most of the previous information has been reported.

Isothermal Section of the TaTiAl System at 1100°C (Preliminary Determination and Evaluation)

As noted previously the experimental investigation of phase equilibria at 1100°C in the ternary Ta-Ti-Al system was based upon examination of bulk alloy samples that have been provided by Pratt & Whitney and Lockheed and also upon the tie-line information determined from diffusion couples initially prepared by Pratt & Whitney. The annealing treatments on both bulk alloys ranged from two days at 1100°C to periods of more than a week. The diffusion couple studies varied from 1-90 hours. These studies, although incomplete, do provide a fair assessment of the 1100°C isothermal section and allow for an evaluation of the reliability of the previously published diagrams. In order to provide a clear comparison between current and previously published isothermal section the findings of the current study will be plotted on the previously published diagram. A summary of the alloy compositions that were studied and the phase equilibria findings is given in Table I.

From the aluminum rich corner the first alloy phase encountered is Al_3Ti , Al_3Ta which has a $\text{D}0_{22}$ structure in both the binary TiAl and TaAl system. As reported by S&N the ternary solutions of the two binary phases form a completely soluble system with lattice parameters varying in an almost ideal fashion as shown in Fig. 8. In the current studies two samples (204 and 280) have established the boundaries between the η phase the γ phase as plotted on the diagram in Fig. 9. It is apparent based upon the tie-line information established from these samples that the η phase exhibits some breath in the ternary system with compositions departing from the stoichiometric value of 25 atomic percent aluminum by almost 4 atomic percent towards the TiTa rich alloys. This behavior is very analogous to the observations reported for the Ti-Al-Nb system (6).

The γ phase has been determined to have an extensive range of solubility, of the order of 20 atomic percent along the equiaxial direction in aluminum content. This is confirmed by Sample 204 as part of a 3-phase equilibrium which is illustrated by the micrograph in Fig. 10. Moreover, lattice parameters calculated from x-ray diffraction measurements show only minor changes in the c/a ratio with Ta additions. The third phase in Sample 204 has been tentatively identified as σ . However, not all of the diffraction lines obtain from Sample 204 can be indexed as σ reflections. Due to overlap of the reflections with γ and η phase peaks a positive identification of the third phase has not been possible at this time. It is possible for the

a third phase in 204 to be an extension of the AlTa phase into the ternary system. This is under further investigation at the present time.

Alloys in the two-phase region between σ and γ have shown good promise as candidate alloys for high temperature application. Several compositions in the two-phase $\sigma+\gamma$ region exhibit exceptional oxidation resistance and also display adequately high melting temperatures to satisfy the program goals. With this in mind several alloy compositions within this range were examined by electron probe analysis as well as with microstructural and x-ray diffraction measurements. The microstructure developed in $\sigma + \gamma$ two-phase alloys is illustrated in Fig. 11. The tie-line information determined in these samples is plotted in Fig. 9. Although there is some scatter, perhaps due to incomplete equilibration, the general trend of the measurements is quite clear. The extensive solubility of tantalum in the γ phase is confirmed. Moreover, the tie-lines on the σ side also indicate extensive penetration of the σ phase into the ternary system. The assignment of phase boundaries within the two-phase $\gamma+\sigma$ field was based upon the tie triangle information provided by Sample 204 on the aluminum rich side of the two-phase region. On the titanium rich side the σ boundary was set by three-phase equilibrium between σ , α_2 and a ternary phase, from Sample 203. The γ phase boundary on the titanium rich side of the two-phase region has been placed near the mid-range of the reported tie-line measurements.

Information on the β region has been principally provided by the diffusion couple measurements which are described in detail in a subsequent section. The results of tie-line measurements indicate significant revision of the previously published diagram is necessary. For example, four tie-lines have been established involving a ternary phase near the composition Ti_2AlTa . These tie-lines involve a β -T determination and three α_2 -T determinations as well as the tie-triangle established on Sample 203 between σ α_2 and T. The Microstructure for Sample 203 is presented in Fig. 12 and indicates a decomposition during cooling from high temperatures after solidification as primary β phase and perhaps even after long annealing times. Is clear that either rapid quenching or high temperature measurements will be necessary to define fully the structure of the ternary T phase. However, in analogy with recent findings in the Ti-Al-Nb system it is possible that the T phase may represent a B2 structure.

When the present measurements are compared to the previous diagram reported by S&N as shown in Fig. 9 is clear that the preliminary version reported by S&N requires extensive revision. Not only are the various phase two-phase regions in need of significant modification, but also the previous work has missed some important features of the phase equilibria. For example, the width of the η phase is significantly broader than reported previously. The two-phase $\sigma+\gamma$ region requires extensive modification of the phase boundaries. Since these two-phase alloys have attractive high temperature properties and appear to be ammenable to microstructural variation to minimize any

cracking tendency due to the σ phase, this revision is important. However, perhaps the most significant revision is the presence of a ternary phase near the composition Ti_2AlTa . This phase has been completely overlooked in all previous studies perhaps due to contamination based upon the annealing procedure used or incomplete equilibration times. Another factor of importance is related to the decomposition of this ternary T phase into other phases upon cooling from the equilibration temperature. This may have confused the interpretation in the previous work. However, the diffusion couple measurements provide a retention of the compositional information established during the interface equilibration at high temperature during the $1100^{\circ}C$ annealing treatment. Upon cooling a diffusion couple this compositional information is retained even though the structural identity of the phases involved in the high temperature interfacial equilibrium may have undergone alteration to other structures in the system. This is an important advantage in the use of diffusion couples to establish high temperature phase equilibria information. Nevertheless, structural information is important and efforts are in progress to provide an identification of the structural identity of the T phase. The revised isothermal section at $1100^{\circ}C$ for the Ta-Ti-Al system based upon the current observations is presented in Fig. 13 and includes information from annealed bulk alloy samples as well as the diffusion couple tie-line determinations.

Interdiffusion Kinetics

In most composite systems of interest the kinetics of the chemical interactions and interdiffusional mixing at the composite-particulate matrix interface play a central role in determining the evolution of an overall structure and its mechanical performance. In the present work the interfacial reactions and interdiffusion between the γ TiAl phase and various BCC Ta-Ti alloys were studied to determine the interaction products and phase stability. By carefully monitoring the diffusional interaction and diffusion interface compositions, it has been possible also to obtain tie-line information in Ta-Ti-Al alloys and new information on the diffusivities. It is expected that these results will be of further use in designing composite structures for compatibility of the constituents as well as long term thermal stability at high temperatures. Moreover, the approach of examining diffusion couples provides extremely useful information for phase diagram calculations and also very practical information on the variation of phase solubilities with temperature.

In the present studies the identification of suitable compositions for diffusion couples was based upon a substrate consisting of a TiAl alloys near the Ti limit of the solubility. Various overlayers ranging from pure Ta to high titanium Ta-Ti alloys were placed in contact with the substrate either by a dual source sputter deposition method or through a hipping process

at high temperatures. The overlayer thicknesses ranged from 30 microns to 150 microns for the sputter deposited layers to a bulk diffusion couple pair in the case of the hipped sample.

An example of the starting state of an as-deposited couple is shown in Fig. 14 for a $\beta(\text{Ti}_{82}\text{Ta}_{18})/\gamma$ couple. As noted in the composition profile some interdiffusional mixing occurred during the preparation of the sample which required heating the substrate to temperatures of the order of 400°C in order to release stresses and allow for good adhesion of the overlayer. This minor amount interdiffusional mixing in the as-deposited state however, was not a serious problem in influencing the subsequent development of the phases during interdiffusion at elevated annealing temperatures. For example, the progress of diffusion in this couple as a function time at 1100°C is illustrated in Fig. 15 and Fig. 16. Another couple based on $\beta(\text{Ti}_{78}\text{Ta}_{22})/\gamma$ was also examined for various times at 1100°C and interactions that developed are shown in Fig. 17 and Fig. 18 where the microprobe composition determinations as a function of interdiffusion distance are presented. The appearance of a couple after annealing at 1100°C for 50 hours is indicated in Fig. 17 where a clearly developed layer with a composition corresponding to the α_2 phase is shown with a thickness of the order of 20 microns. It is important to note that the layer appearance is one of a planer more morphology which indicates the development of stable interdiffusion interphases. This feature is of importance in the reliable of determination of tie-line

compositions as well as in determining accurately the layer growth kinetics for the reaction production phase i.e. α_2 structure.

Another example illustrating the development of planar interdiffusion interfaces is shown in Fig. 19 for a $\beta(\text{Ti}_{40}\text{Ta}_{60})/\gamma$ couple after annealing at 1100°C for 90 hours. The planar β/α_2 and α_2/γ interfaces are clearly evident. The composition across the α_2 region is also quite clearly defined. However, after 90 hours of annealing diffusion in the β phase has allowed for penetration of aluminum to the surface. In fact, as the summary in Fig. 20 indicates some Al penetration has developed after a 65 hour anneal at 1100°C . Under such conditions the boundary conditions for solution of the diffusion equation have been modified and are now time dependent so that extensive annealing at high temperatures is not possible for the deposited couples. Nevertheless, these couples still yield very useful and important information about the tie-line compositions between β and α_2 and α_2 and γ . Extended annealing is useful in this regard to insure that an apparent tie-line composition between two adjacent phases that is established early in the diffusion process is maintained after extended annealing. If the initial appearant tie-line composition is modified during annealing, then it is a metastable tie-line which is converted into a stable one during extended annealing treatment.

Another diffusion couple between pure Ta and γ produced by hipping was also examined by annealing at about 1100°C for 100 hours as indicated in Fig. 21. In addition to the development of

an α_2 interphase there is a plateau in the composition distance profile suggesting a ternary phase is present at approximately the composition of Ti_2TaAl . The diffusion path associated with this couple is plotted on the phase diagram in Fig. 22. This diffusion path which is unique in a given diffusion couple as well as the other diffusion paths determined from the TaTi alloy overlayers with γ indicate quite clearly that during the initial interdiffusion there is a flux of aluminum leaving the γ phase and entering the tantalum containing overlayer. With this depletion of the γ phase in contact with the overlayer surface in aluminum content, the conditions for development of an α_2 layer are satisfied. In the case of the Ta/ γ couple, the penetration of aluminum into the Ta layer provides conditions for the development of a σ layer and allows the diffusion path to cross into the ternary phase. As noted previously the tie-line compositions determined from the diffusion couples have been included in the ternary phase diagram plot at 1100°C in Fig. 13.

After extended annealing penetration of aluminum through the β phase occurs in the deposited couples. It is clear that most of the diffusion and interdiffusional mixing occurs in the β phase. As noted by the diffusion pathways as well as the composition profiles reported, relatively small amounts of Ta penetrate into the α_2 and γ phases. In order to allow for a determination of the interdiffusion coefficients a number of additional couples were prepared with compositions noted in Table II. In these cases both short and long term annealing treatments were performed. The shorter term annealing treatments after just

a few hours were used to ensure satisfying boundary conditions at the free surface of the couple and to permit an evaluation of the interdiffusional coefficients. The longer term anneals were used to establish the validity of the tie-line information as referring to stable phase arrangements. In some cases as shown in Fig. 23 where in a Ta_82Ti_{18}/γ couple 2 hours of annealing at $1100^\circ C$ allowed for development of an α_2 layer, but no penetration of aluminum to the outer surface. More extensive annealing of this couple for 48 hours as shown in Fig. 24 did allow penetration of aluminum to the outer surface, but again confirmed the presence of the α_2 composition and the existence of a ternary phase composition. However, even short term annealing treatments did not always succeed as indicated in Fig. 25 for a $Ta_{55}Ti_{45}/\gamma$ couple which was annealed at $1100^\circ C$ for 1 hour. In this case even with short term annealing the diffusion in the β phase overlayer was sufficiently fast to allow for penetration of aluminum to the outer surface. In fact, after 48 hours of annealing complete interdiffusion and penetration resulting in level composition profiles was obtained as indicated in Fig. 26 and served to establish the tie-line relationships which are summarized in Table III.

In order to evaluate the interdiffusional fluxes which is essential in the determination of the coefficients the composition profile measurements were analyzed in terms of the Matano method which is illustrated in Fig. 27. Basically the Matano approach is one that allows for determination of the plane over which the interdiffusional fluxes are balanced between the

pairs in a couple. The importance of this feature may be illustrated by considering the following outline of the Matano analysis. The basic diffusion equations in a ternary system for a two phase arrangement of ternary solutions are given as follows:

$$\frac{\partial C_1}{\partial t} = \frac{\partial}{\partial x} \left[\overset{\sim}{D_{11}} \frac{\partial C_1}{\partial x} \right] + \frac{\partial}{\partial x} \left[\overset{\sim}{D_{12}} \frac{\partial C_2}{\partial x} \right] \quad (1)$$

$$\frac{\partial C_2}{\partial t} = \frac{\partial}{\partial x} \left[\overset{\sim}{D_{21}} \frac{\partial C_1}{\partial x} \right] + \frac{\partial}{\partial x} \left[\overset{\sim}{D_{22}} \frac{\partial C_2}{\partial x} \right] \quad (2)$$

where t is the diffusion time, x is the diffusion distance from the Matano interface, and C_1 and C_2 are concentrations of solutes 1 and 2. The interdiffusion coefficients $\overset{\sim}{D_{11}}$ and $\overset{\sim}{D_{22}}$ are referred to as the major coefficients and $\overset{\sim}{D_{12}}$ and $\overset{\sim}{D_{21}}$ are referred to as the cross coefficients.

With this basis it is possible to proceed to development the relationships to evaluation the Matano plane and the interdiffusion coefficients as given.

In brief the Matano analysis allows for the evaluation of the relevant interdiffusion coefficients used in eqs. 1 and 2 based on the following development. For each component, i ,

$$\left[\frac{\delta C_i}{\delta t} \right]_x = - \left[\frac{\overset{\sim}{\delta J}_i}{\delta x} \right]_t \quad (i = 1, 2, \dots n) \quad (3)$$

but,

$$\left[\frac{\delta C_i}{\delta t} \right]_x = - \left[\frac{\delta x}{\delta t} \right]_{C_i} \left[\frac{\delta C_i}{\delta x} \right]_t = - v(C_i) \left[\frac{\delta C_i}{\delta x} \right]_t \quad (4)$$

where $v(C_i)$ refers to the velocity of propagation of a concentration C_i within the diffusion zone. Hence, Eq. (3) becomes:

$$v(C_i) \left[\frac{\delta C_i}{\delta x} \right]_t = \left[\frac{\delta \tilde{J}_i}{\delta x} \right]_t \quad (5)$$

For both solid-solid and vapor-solid couples, C_i is a function of the Boltzmann parameter, λ , given by x/\sqrt{t}

$$v(C_i) = \left[\frac{\delta x}{\delta t} \right]_{C_i} = - \frac{1}{2} \frac{\lambda}{2\sqrt{t}} \quad (6)$$

Hence, at constant t , Eq. (5) can be written as:

$$\begin{aligned} \left[\frac{\delta \tilde{J}_i}{\delta x} \right]_t &= - \left[\frac{\lambda}{\sqrt{t}} \right] \left[\frac{\delta C_i}{\delta x} \right]_t \\ \int d\tilde{J}_i &= \int - \frac{1}{2} \left[\frac{\lambda}{\sqrt{t}} \right] \left[\frac{\delta C_i}{\delta x} \right] dx \\ &= \int - \frac{1}{2} \left[\frac{\lambda}{\sqrt{t}} \right] \frac{dC_i}{d\lambda} \frac{1}{\sqrt{t}} d\lambda \\ &= \frac{1}{2\sqrt{t}} \int \lambda dC_i \\ &= \frac{1}{2t} \int x dC_i \end{aligned} \quad (7)$$

$$\int_{\tilde{J}_i(+\infty)}^{J_i(x)} d\tilde{J}_i = \frac{1}{2t} \int_{C_i(+\infty)}^{C_i(x)} x dC_i \quad (8)$$

Since J_i is zero as x goes to $+\infty$ or $-\infty$,

$$\tilde{J}_i(x) = \frac{1}{2t} \int_{C_i(+\infty)}^{C_i(x)} x dC_i \quad (9)$$

The integral in Eq. (9) can be evaluated from the concentration profile of component i with $x=0$ located at the Matano plane, which can be determined for solid-solid couples from the relation:

$$\int_{C_i(+\infty)}^0 x dC_i + \int_0^{C_i(-\infty)} x dC_i = 0 \quad (10)$$

From Eq. (10), the interdiffusion flux can be calculated from the composition profile as illustrated in Fig. 27. Moreover, if J_i is expressed by the extended form of Fick's law for an n -component system,

$$J_i = - \sum_{j=1}^{n-1} \tilde{D}_{ij} \frac{\delta C_j}{\delta x} \quad (11)$$

where $(n-1)^2$ interdiffusion coefficients, \tilde{D}_{ij} are defined and can be obtained.

Kinetic studies were carried out using Matano analysis for the couples annealed for short times. The composition and flux profile for two different couples are shown in Fig. 28 and Fig. 29. The flux of Ta is much smaller than that for Ti and Al. With the interdiffusion flux and composition gradient, the four independent interdiffusion coefficients in β phase were determined. These values are given in Table IV where it is

evident that the interdiffusion coefficients are functions of composition and generally decrease by about one order of magnitude as the β phase composition varies from Ta₂₂ Ti₇₈ to Ta₈₂ Ti₁₈. The influence of Ta additions on slowing diffusional processes is also revealed in Fig. 30 which summarizes the measured α_2 layer growth kinetics. The parabolic kinetics demonstrates diffusion controlled growth of α_2 . In addition, the Ta composition in the β phase provides an effective means to control the α_2 layer growth. A reduction in the α_2 layer growth rate by a factor of about 8 is possible based on the results in Fig. 30.

Summary

The research program at the University of Wisconsin-Madison has involved interrelated efforts that have been focussed on the determination of phase equilibria and interdiffusion kinetics in selected high temperature intermetallic systems for use in advanced composites. Based on initial findings the investigation of alloys in the Ta-Ti-Al system has been emphasized in the current work.

The phase equilibria in the Ta-Ti-Al system has been evaluated in annealed bulk alloys and diffusion couples. A major portion of the isothermal section at 1100°C has been determined. Previous reports have been shown to be incomplete. It has been established that the η phase field broadens in ternary alloys and that the σ and γ phases exhibit significant ternary solubility. A ternary phase has been discovered with a composition near Ti₂TaAl which was overlooked in past studies.

The diffusion couple studies have also provided new information on the kinetics of the chemical interactions and interdiffusional mixing at composite system interfaces. For diffusion couples between $\beta(\text{Ta}_x\text{Ti}_{1-x})$ and γ phase pairings a layer of the α_2 phase forms and grows with a planar interface. Several diffusion couples have provided tie-line data which has served to define the extent of the Ti_2TaAl phase at 1100°C. A Matano analysis of the composition profiles and the interdiffusion fluxes has been employed to evaluate the diffusivities in the β phase which range from 10^{-10} to 10^{-11} cm^2/s . The lower range of β diffusivity and the slowest α_2 layer growth kinetics occur for the Ta rich β phase compositions. This composition dependence of the diffusivity provides an effective approach to controlling interdiffusion and thermal stability.

The results of this investigation will serve to guide materials processing strategies to permit the development of composite systems with well controlled and stable microstructural features that have been identified as essential for oxidation resistant structural materials.

References

1. J. C. Mishurda, J. C. Lin, Y. A. Chang and J. H. Perepezko, Mat. Res. Soc. Symp. Proc., 133 57 (1989).
2. C. McCullough, J. J. Valencia, C. G. Levi and R. Mehrabian, Acta Met. 37 1321 (1989).
3. P. R. Subramanian, D. B. Miracle and S. Mazdiyasni (private communication).
4. A. Raman, Z. Metallkde, 57 535 (1966).
5. S. Sridharan and H. Nowotny, Z. Metallkde, 74 468 (1983).
6. T. J. Jewett, J. C. Lin, K. C. Hsieh, N. R. Bonda, Y. A. Chang, and J. H. Perepezko, Mat. Res. Soc. Symp. Proc., 133, 69 (1989).

Table I
Alloy Compositions for Phase Equilibria Evaluation*

Sample Number	Bulk Alloy Composition			Phases Present	Phase Composition		
	Ta	Ti	Al		Ta	Ti	Al
202	23	23	54	σ γ	Not equilibrated		
203	20	47	33	σ	35.7	30.8	33.5
				σ_2	9.7	54.5	35.8
				T	15	51	34
204	25	15	60	η	16.5	13.5	70
				γ	17.1	23.4	59.5
				$\sigma(?)$	45.8	7.9	46.3
280	10	26	64	γ	11.7	39.5	48.8
				σ	43.2	20.8	36
18	46	7	47		Not equilibrated		
1015	25	25	50	σ	43	17.2	39.8
				γ	13.6	32.8	53.6
1016	36.2	25.8	38	σ	39.9	24.6	35.5
				γ			
1017	39	28	33	σ	35.1	29.3	35.6
				T(?)	15.5	49.1	35.4
1018	35	25	40	σ	40.6	22.1	37.3
				γ	16.7	35.7	47.6

*All compositions given in atomic percent

Table II
Phase Arrangements in the $\beta(\text{Ta}_x\text{Ti}_{1-x})/\gamma$ Couples
After Annealing at 1100°C

Couples	β Layer Thickness	Time (hrs)	Phase Arrangement
$\beta(\text{Ta}_{82}\text{Ti}_{18})/\gamma$	30 μ	48	$\beta/\text{T}/\alpha_2/\gamma$
$\beta(\text{Ta}_{82}\text{Ti}_{18})/\gamma$	30 μ	2	$\beta/\alpha_2/\gamma$
$\beta(\text{Ta}_{60}\text{Ti}_{40})/\gamma$	60 μ	90	$\beta/\alpha_2/\gamma$
$\beta(\text{Ta}_{60}\text{Ti}_{40})/\gamma$	60 μ	65	$\beta/\alpha_2/\gamma$
$\beta(\text{Ta}_{60}\text{Ti}_{40})/\gamma$	60 μ	24	$\beta/\alpha_2/\gamma$
$\beta(\text{Ta}_{55}\text{Ti}_{45})/\gamma$	15 μ	48	$\text{T}/\alpha_2/\gamma$
$\beta(\text{Ta}_{55}\text{Ti}_{45})/\gamma$	15 μ	2	$\beta/\alpha_2/\gamma$
$\beta(\text{Ta}_{55}\text{Ti}_{45})/\gamma$	15 μ	1	$\beta/\alpha_2/\gamma$
$\beta(\text{Ta}_{22}\text{Ti}_{78})/\gamma$	60 μ	24	$\text{T}/\alpha_2/\gamma$
$\beta(\text{Ta}_{22}\text{Ti}_{78})/\gamma$	60 μ	28	$\text{T}/\alpha_2/\gamma$
$\beta(\text{Ta}_{22}\text{Ti}_{78})/\gamma$	60 μ	50	$\text{T}/\alpha_2/\gamma$
$\beta(\text{Ta}_{18}\text{Ti}_{82})/\gamma$	250 μ	43	$\beta/\alpha_2/\gamma$

Table III
Tie-lines in Ta-Ti-Al System

T (°C)	x _{Ta}	x _{Ti}	x _{Al}	x _{Ta}	x _{Ti}	x _{Al}	i-j
	i			j			
1100	0.14	0.69	0.17	0.09	0.69	0.22	$\beta-\alpha_2$
1100	0.40	0.43	0.17	0.07	0.66	0.27	$\beta-\alpha_2$
1100	0.43	0.40	0.17	0.06	0.65	0.29	$\beta-\alpha_2$
1100	0.18	0.54	0.28	0.055	0.645	0.30	T- α_2
1100	0.18	0.50	0.32	0.04	0.62	0.34	T- α_2
1100	0.18	0.49	0.33	0.025	0.62	0.355	T- α_2
1100	0.65	0.21	0.14	0.21	0.47	0.32	$\beta-T$

Table IV
Interdiffusion Coefficients in the β Phase of
Ta-Ti-Al System

T(°C)	Couple	D_{Ta-Ta}	D_{Ta-Al}	D_{Al-Al}	D_{Al-Ta}^*
1100	β (Ta.22Ti.78)/ γ	2.9×10^{-10}	1.8×10^{-10}	1.8×10^{-9}	-8.1×10^{-10}
1100	β (Ta.24Ti.76)/ γ	1.9×10^{-10}	6.2×10^{-11}	3.7×10^{-10}	-4.5×10^{-10}
1100	β (Ta.67Ti.33)/ γ	5.7×10^{-11}	2.0×10^{-11}	1.6×10^{-10}	-2.5×10^{-11}
1100	β (Ta.82Ti.18)/ γ	1.0×10^{-11}	9.4×10^{-12}	4.9×10^{-11}	1.7×10^{-11}

*All diffusivities in cm^2/s

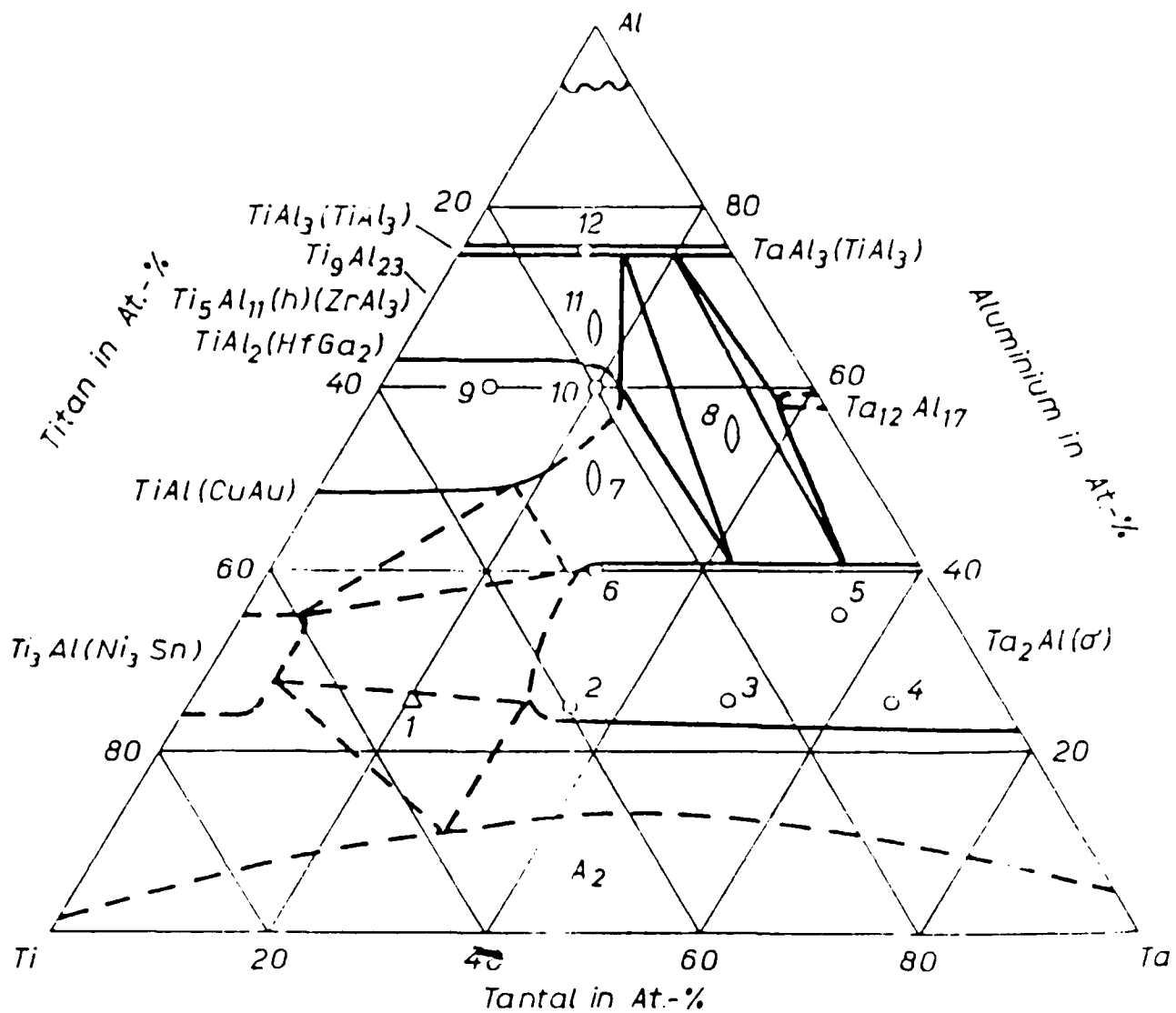


Figure 1 Isothermal section at 1000°C for the Ta-Ti-Al system reported by Raman (4).

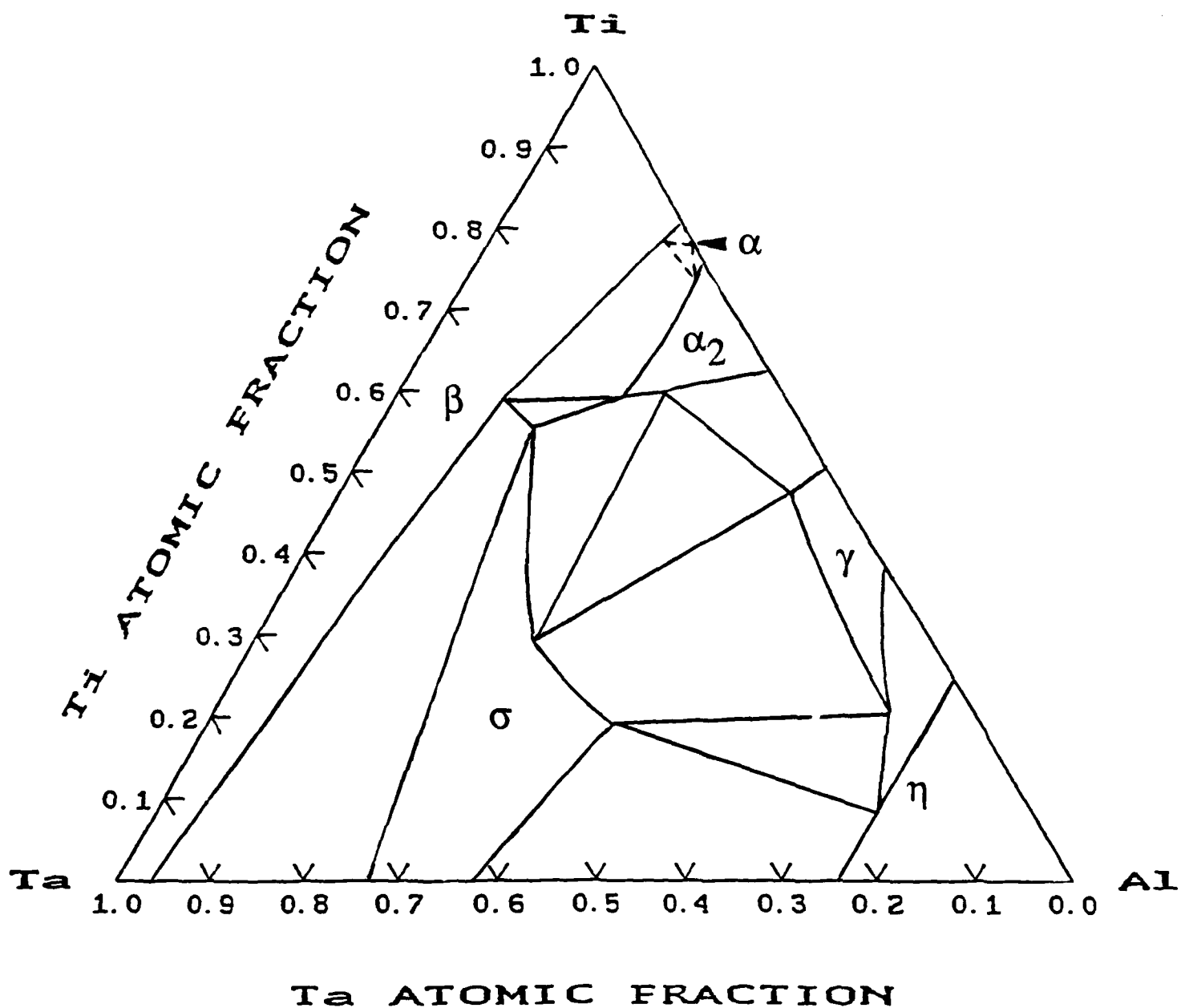


Figure 2 Isothermal section at 1100°C for the Ta-Ti-Al system reported by Sridharan and Nowotny (5).

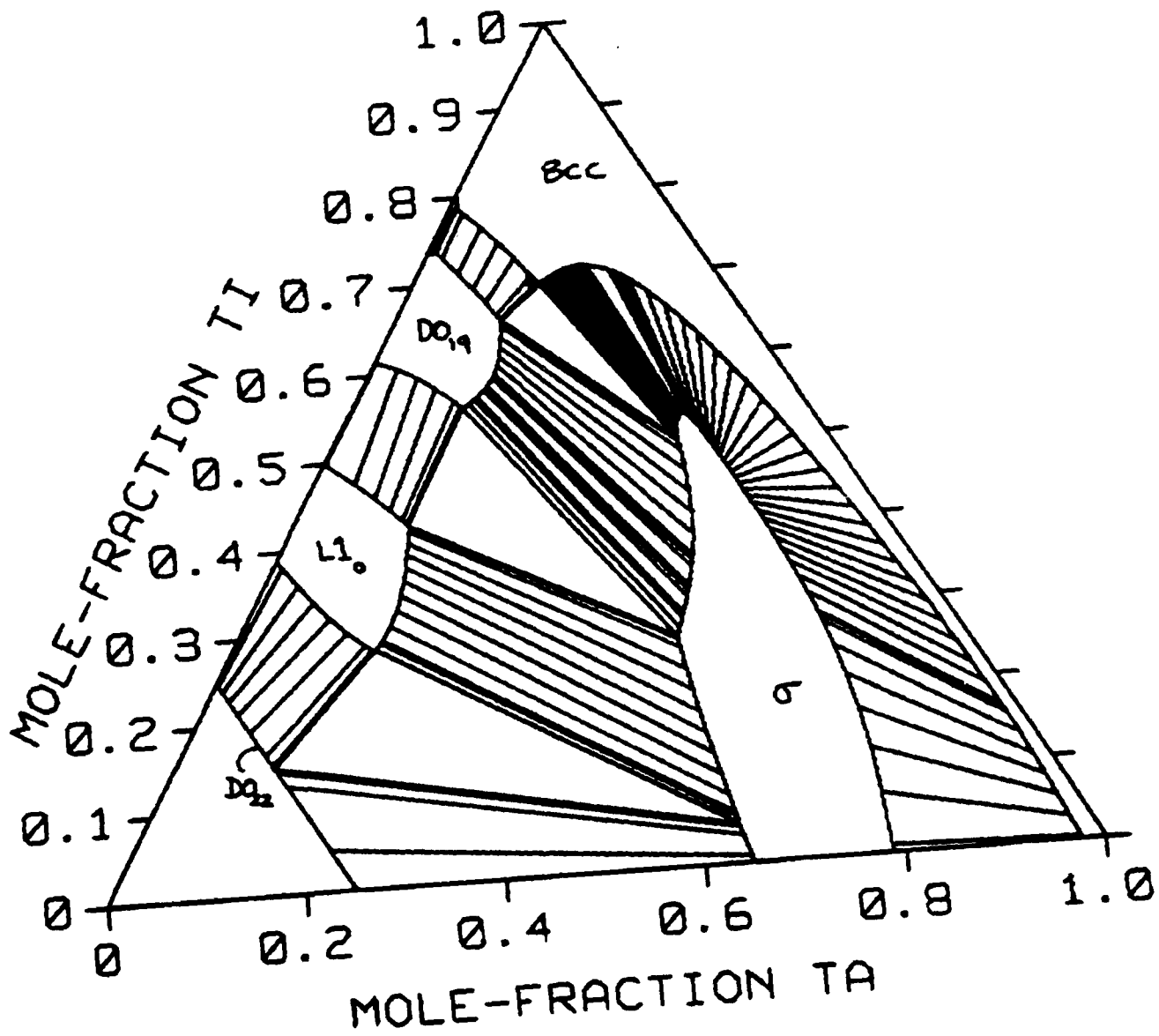


Figure 3 Thermocalc computed isothermal section at 1100°C for the Ta-Ti-Al system (by Kattner).

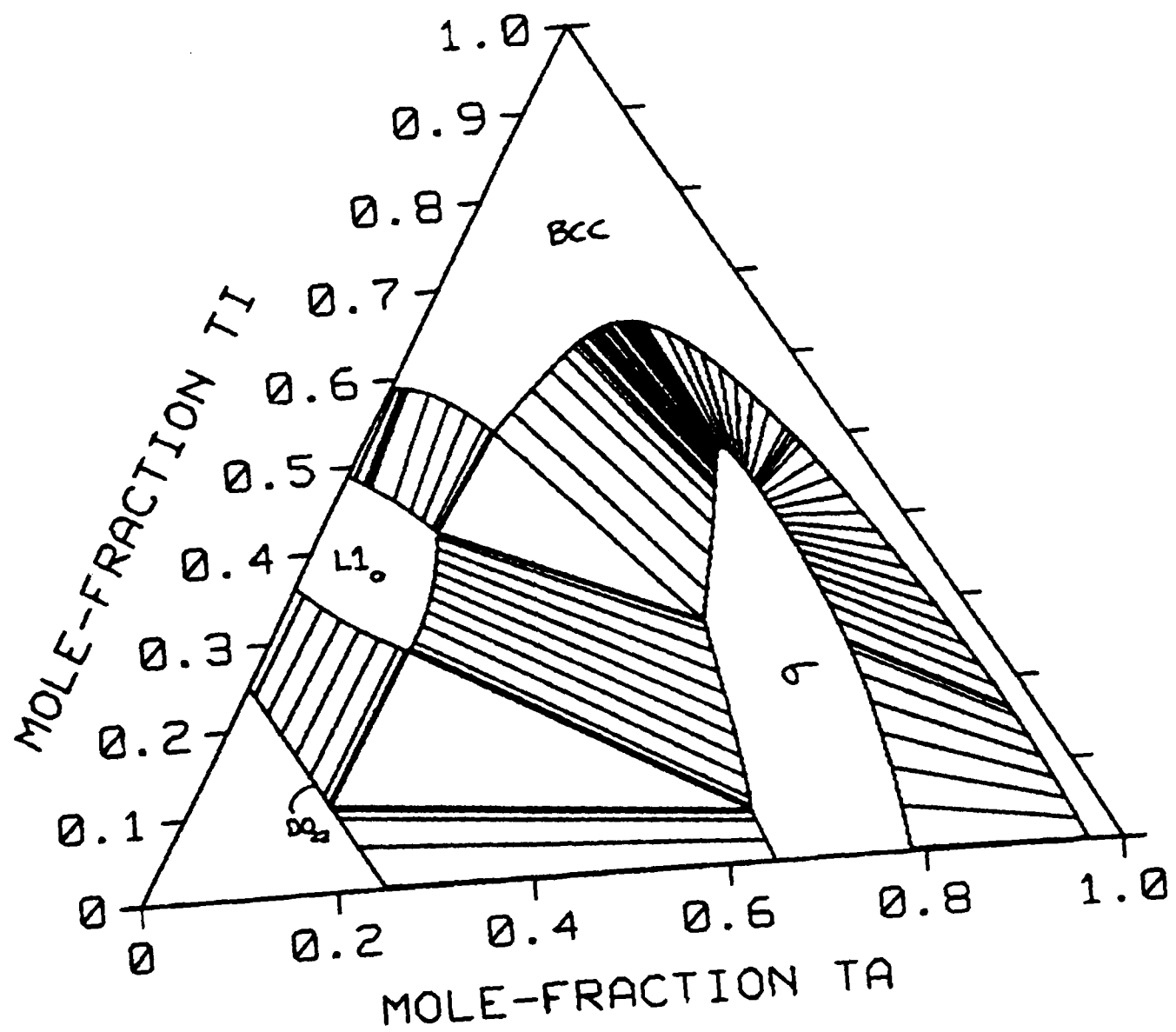


Figure 4 Thermocalc computed isothermal section at 1300°C for the Ta-Ti-Al system (by Kattner).

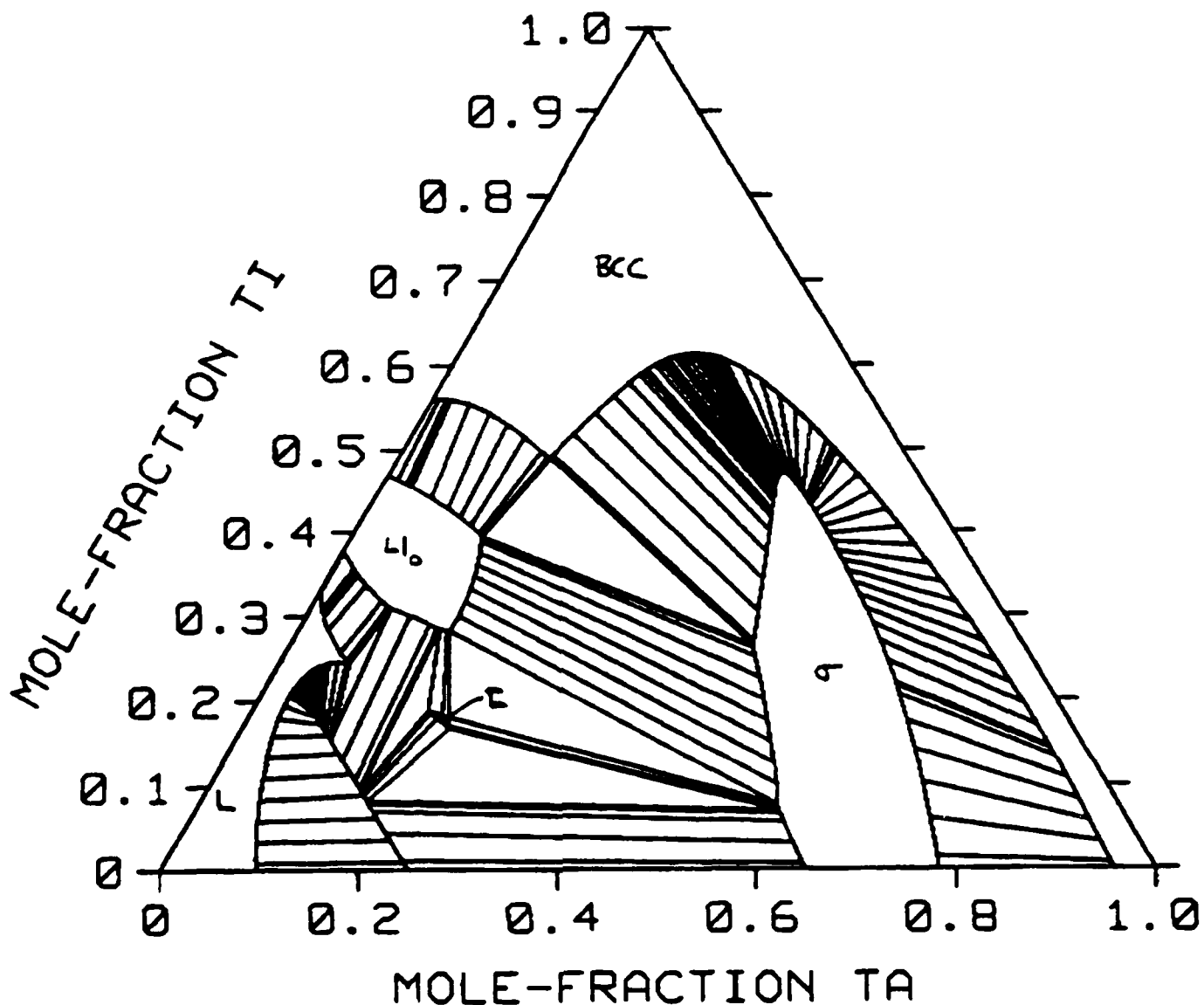


Figure 5 Thermocalc computed isothermal section at 1400°C for the Ta-Ti-Al system (by Kattner).

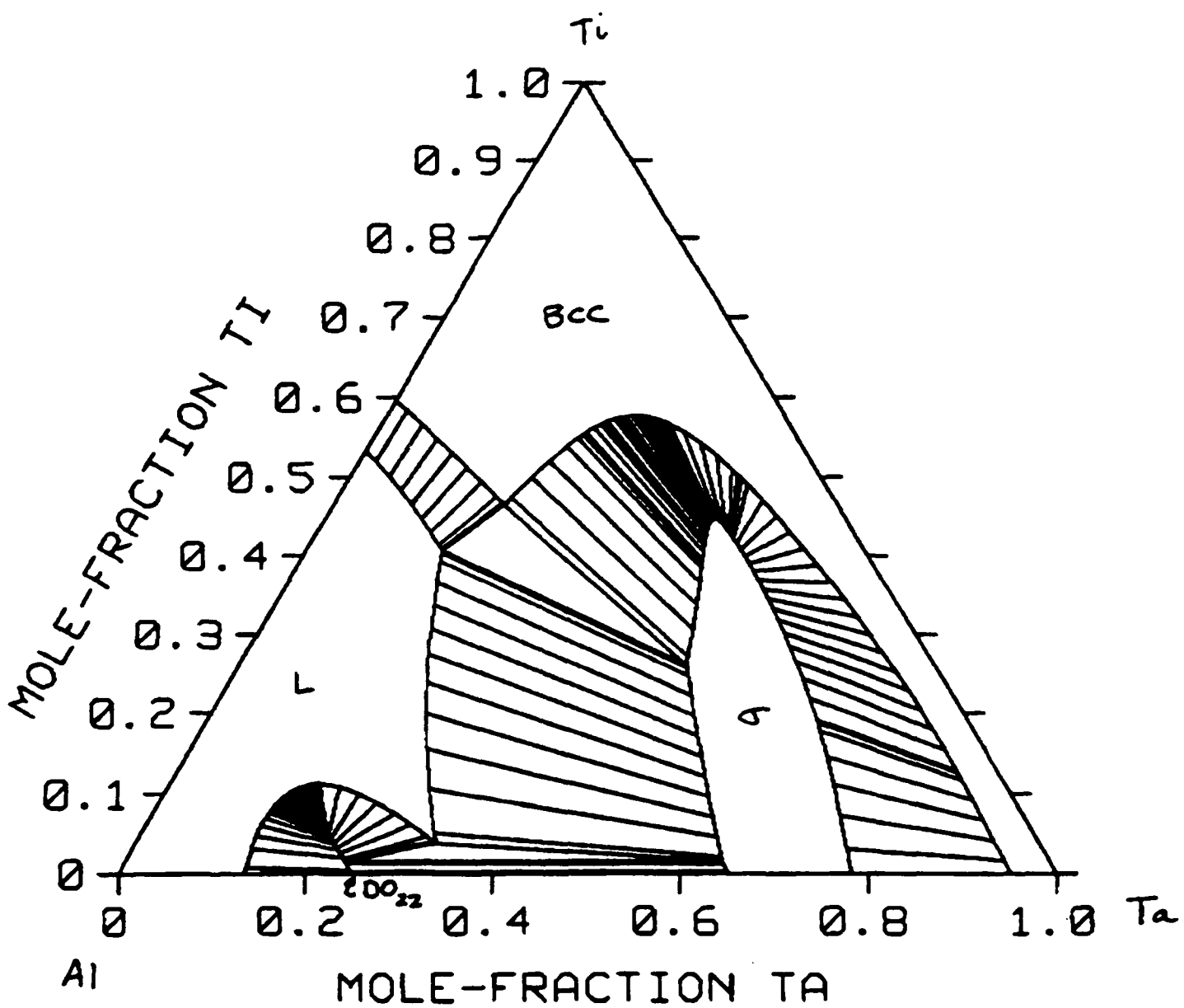


Figure 6 Thermocalc computed isothermal section at 1500°C for the Ta-Ti-Al system (by Kattner).

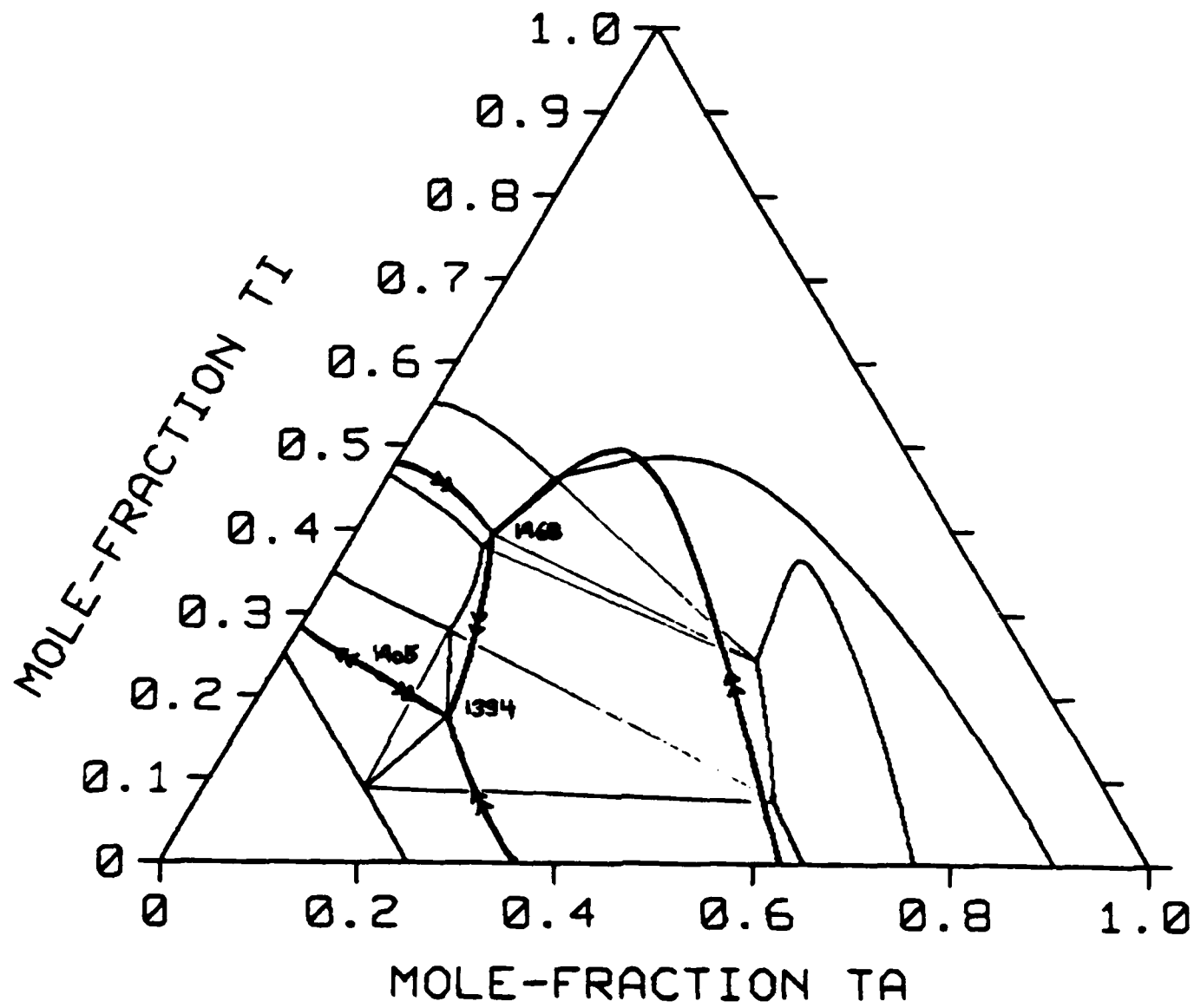


Figure 7 Liquidus projection estimate based on thermocalc computation for the Ta-Ti-Al system (by Kattner).

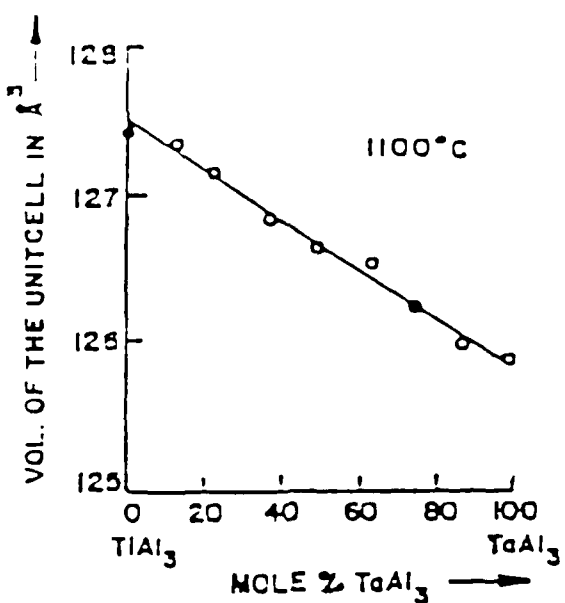
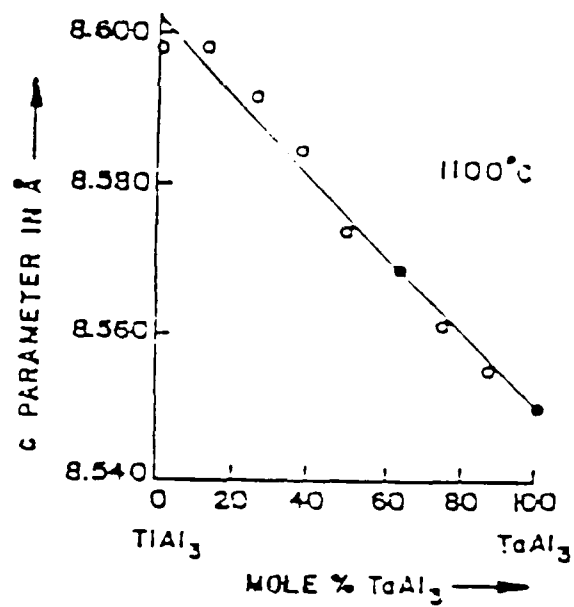
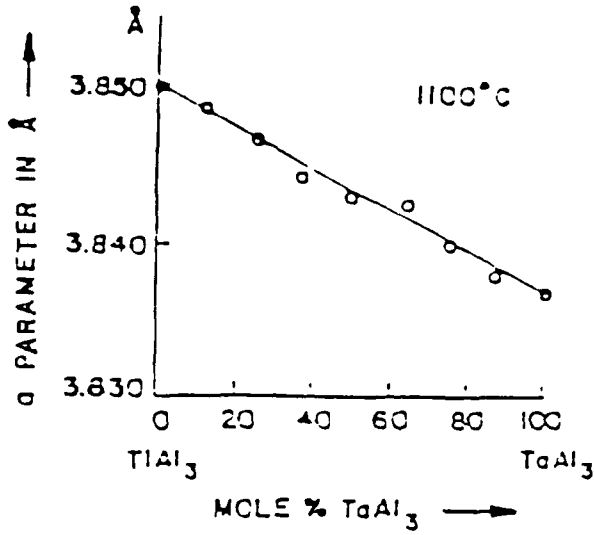


Figure 8 Lattice parameter variation between TaAl_3 and TiAl_3 (5).

TA-TI-AL 1100 C

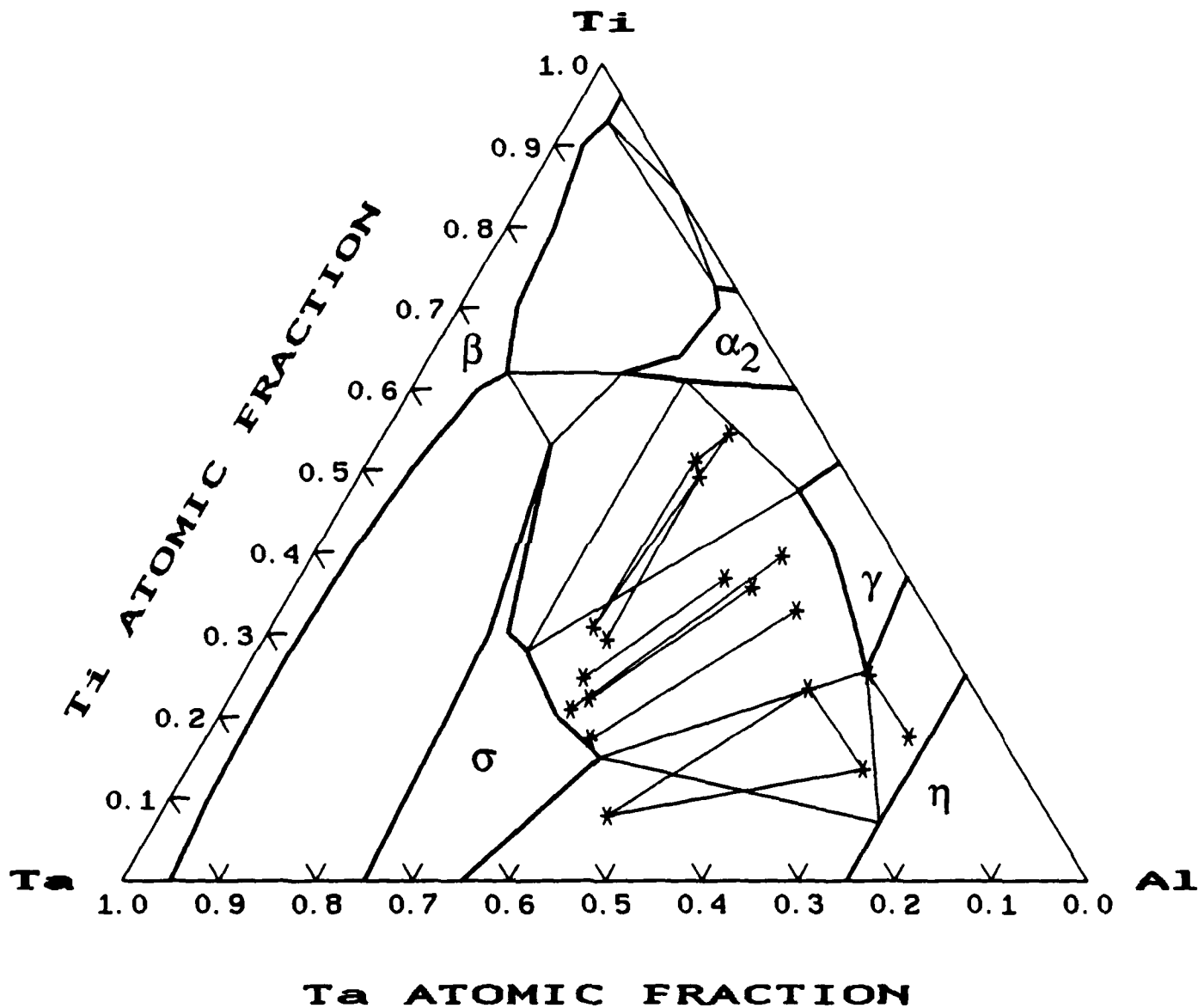


Figure 9 Isothermal section at 1100°C for the Ta-Ti-Al system by S&N (5) compared with bulk alloy phase equilibria results in the current investigation.

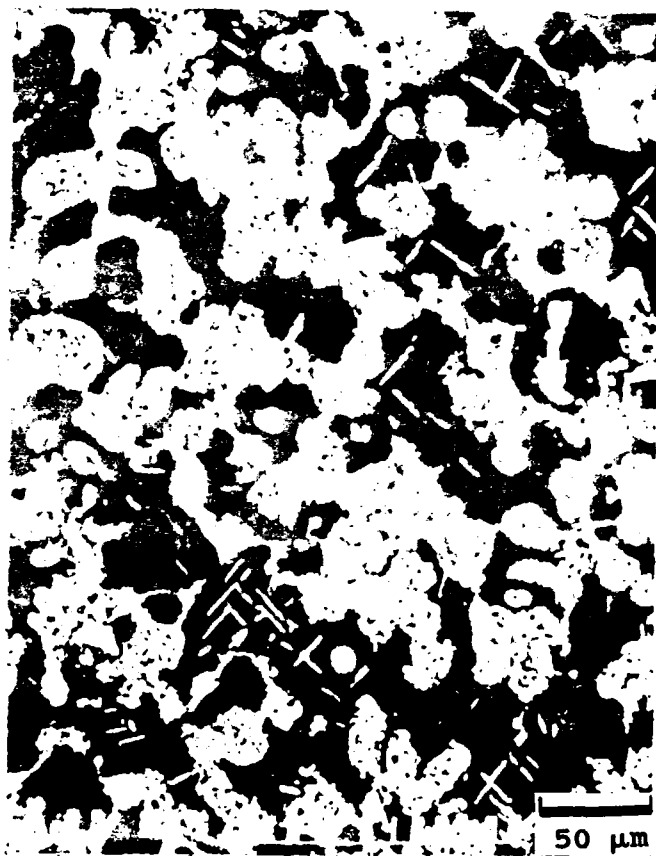


Figure 10 Micrograph of a $\text{Ta}_{25} \text{Ti}_{15} \text{Al}_{60}$ sample after 69 hrs. at 1100°C . Dark phase is η , light gray phase is γ and white phase may be σ or AlTa .

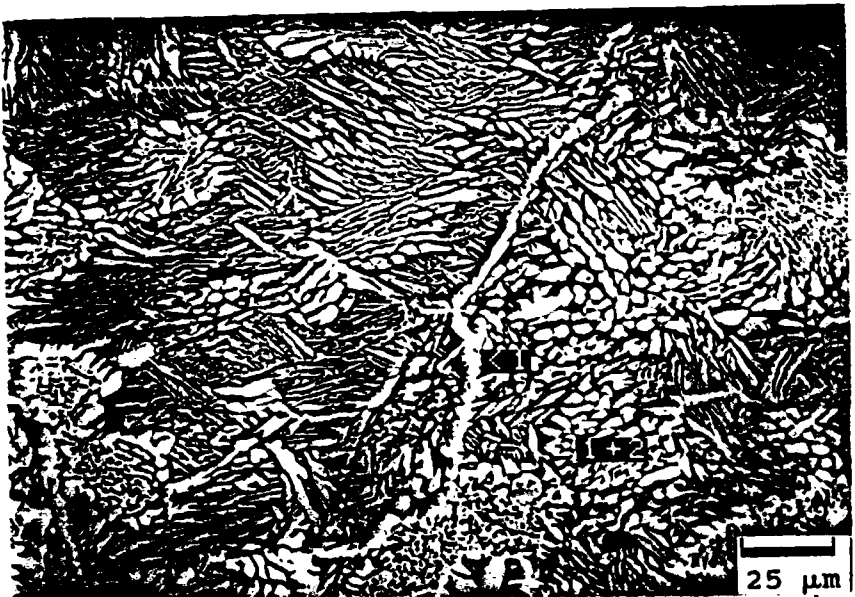


Figure 11 Micrograph of a $Ta_{35} Ti_{25} Al_{40}$ sample in an as-cast condition. The light phase is σ (i.e. #1) with a minor amount of γ between a plate like σ structure. Precipitation of σ at prior grain boundaries suggests that the primary solidification phase was β .

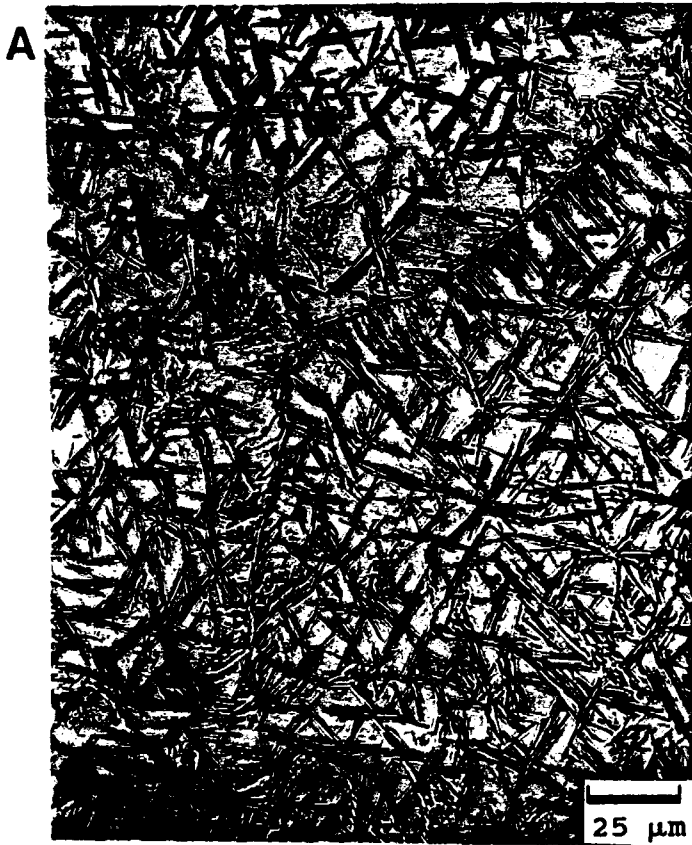


Figure 12 Photomicrographs of a $Ta_{20} Ti_{47} Al_{33}$ sample. a) As-cast condition, with acicular precipitates (probably α_2) outlining prior β phase grains which have decomposed upon cooling. b) Annealed at $1100^\circ C$ for five days showing a block σ phase morphology, with plates of another phase (probably α_2) in a matrix of T phase.

Ta-Ti-Al 1100 C
(Preliminary)

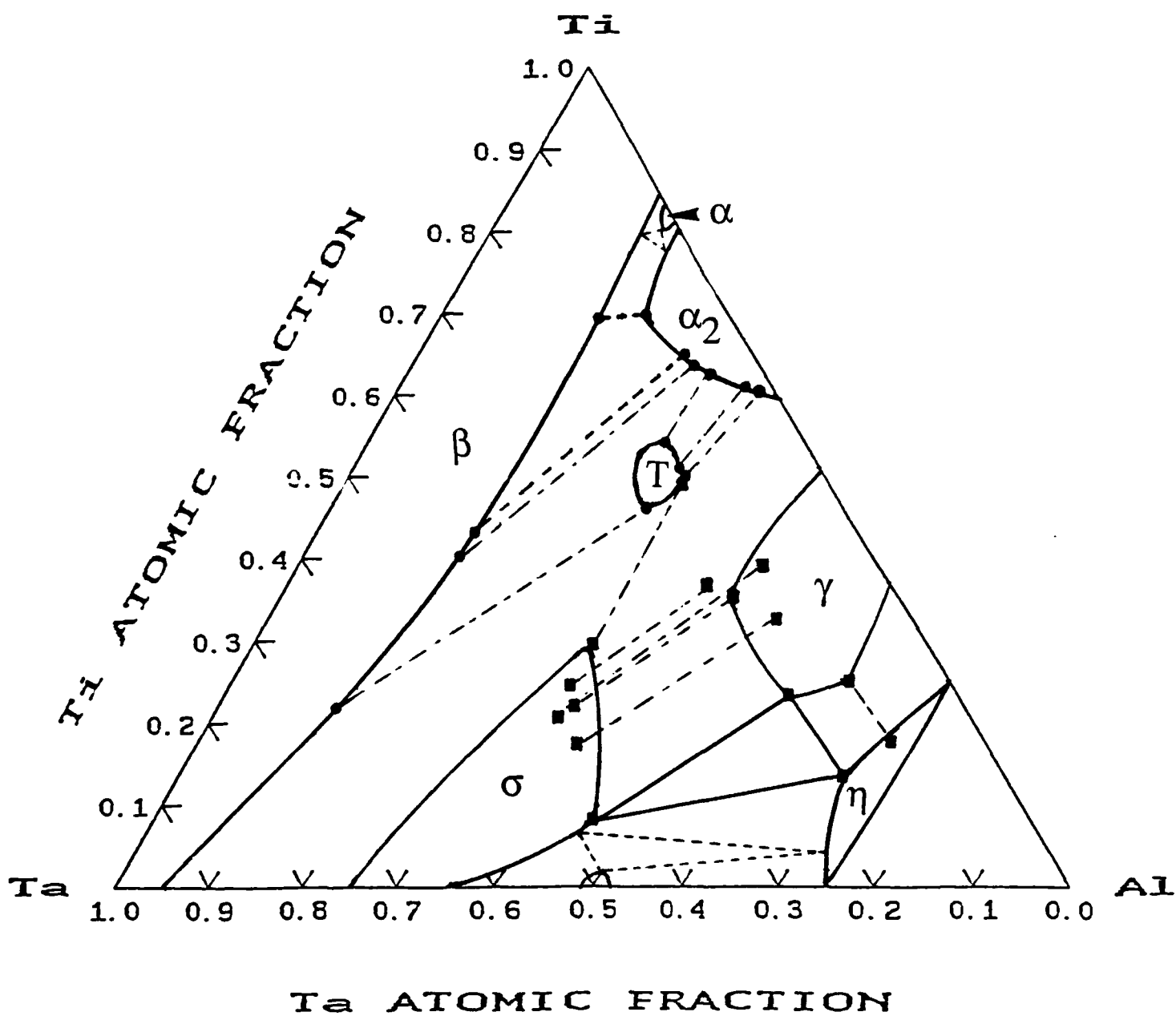
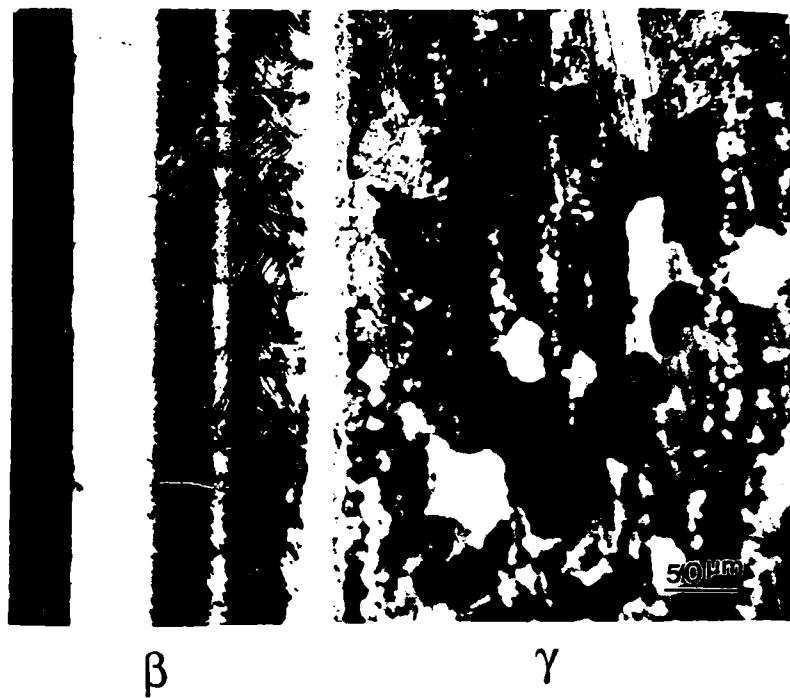


Figure 13 Isothermal section at 1100°C for the Ta-Ti-Al system based upon the current investigation.



β γ

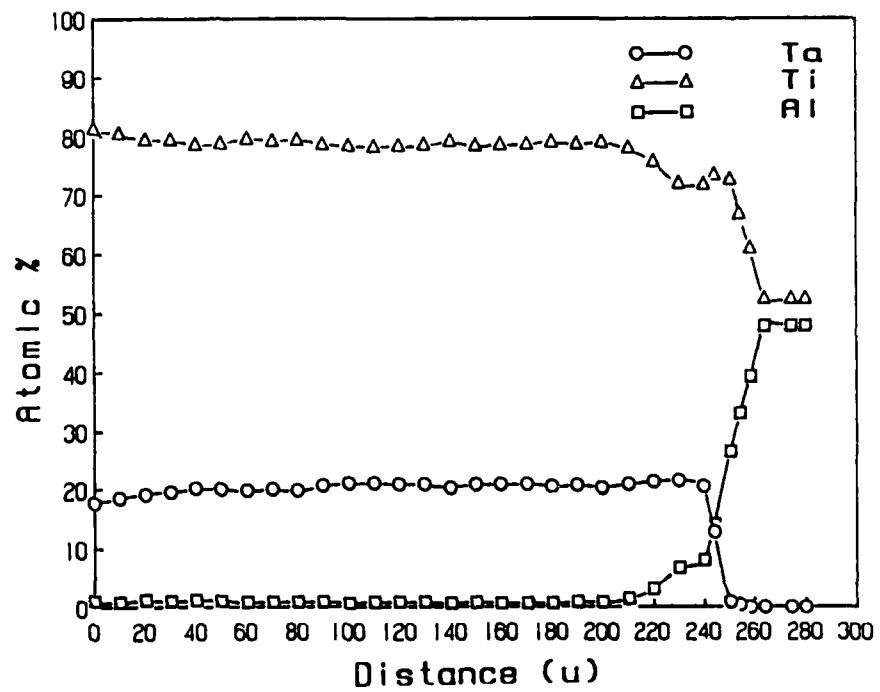
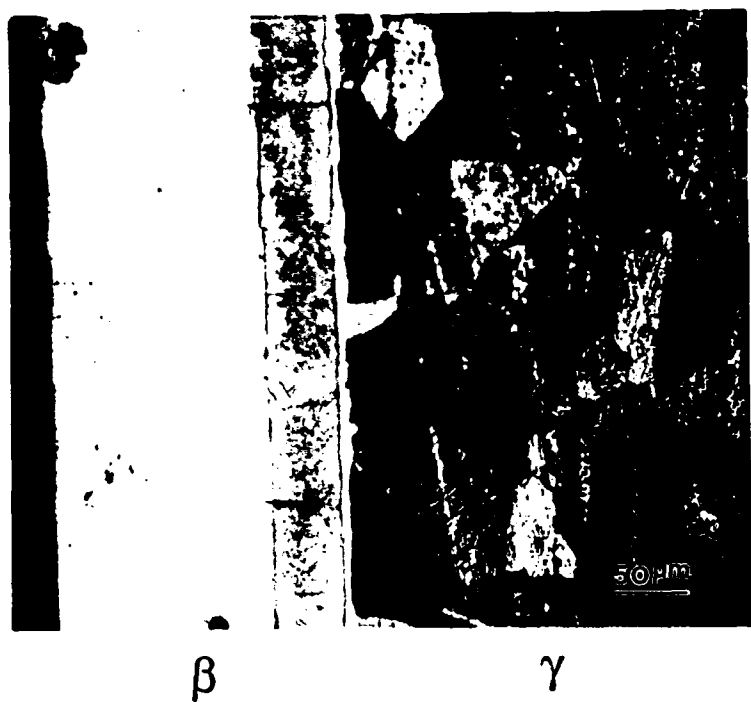


Figure 14 Cross-sectional view of a $\beta(\text{Ti}_{82}\text{Ta}_{18})/\gamma$ diffusion couple and the composition profile for the as-deposited condition.



β

γ

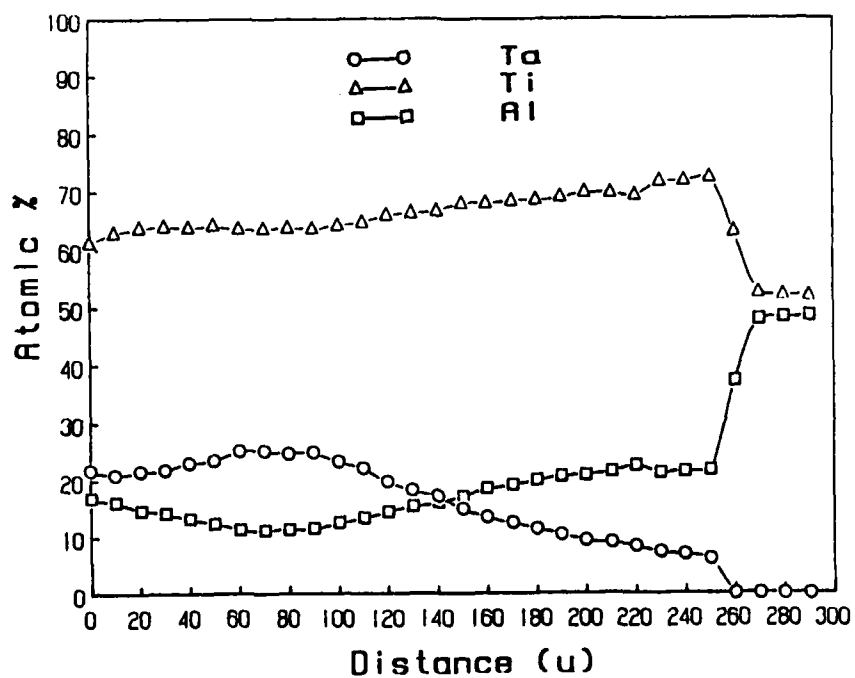
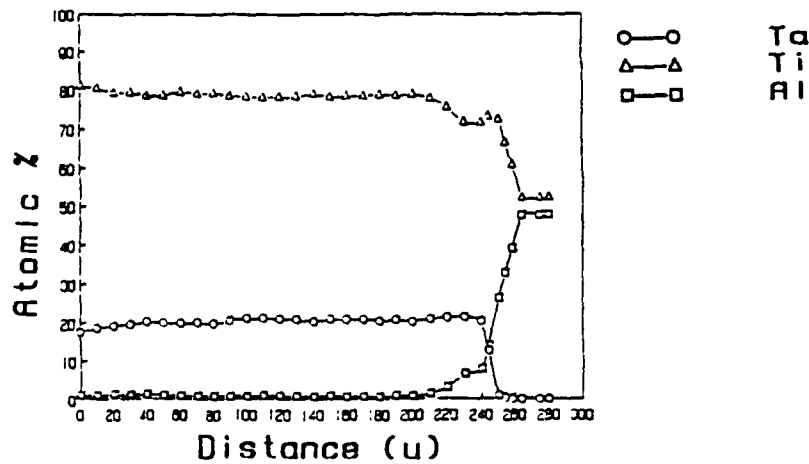
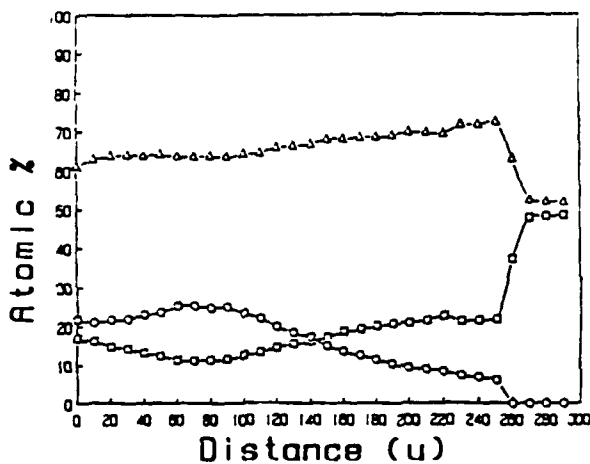


Figure 15 Cross-sectional view of a $\beta(\text{Ti}_{82}\text{Ta}_{18})/\gamma$ diffusion couple and the corresponding composition profile after annealing at 1100°C for 16 hours.

as-deposited



18 hrs



43 hrs

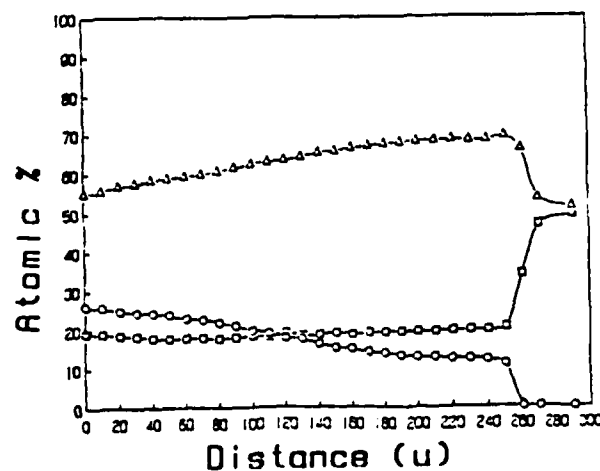


Figure 16 Summary of the interdiffusion behavior for a $\beta(\text{Ti}_{82}\text{Ta}_{18})/\gamma$ diffusion couple.

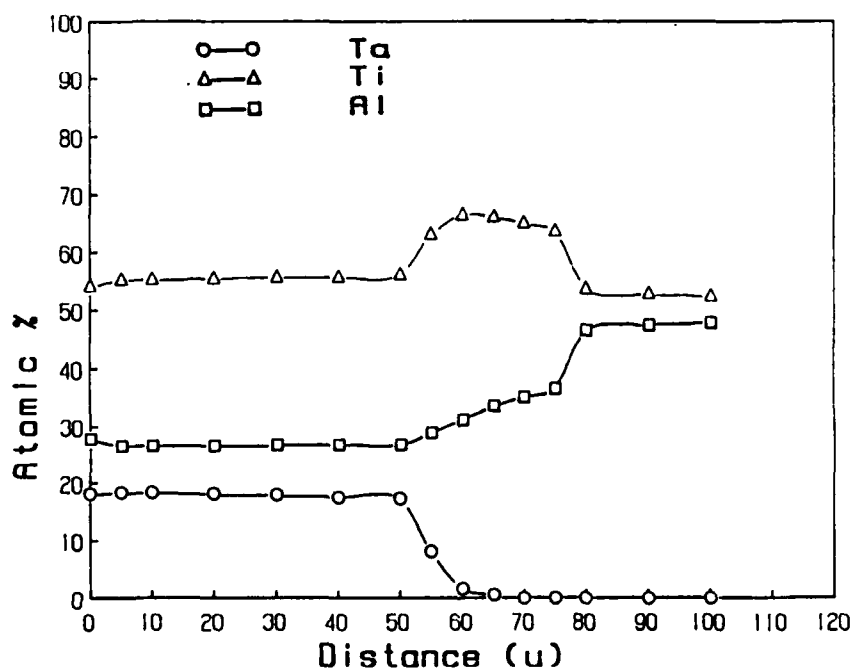
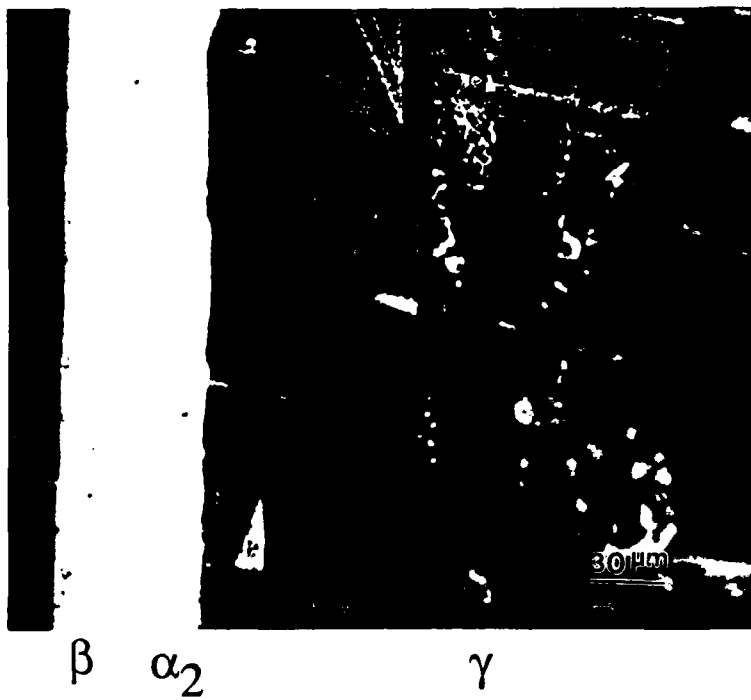
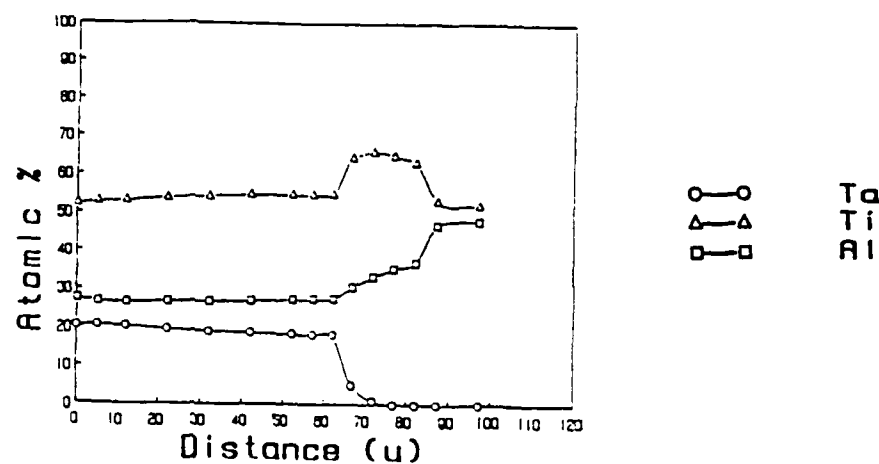
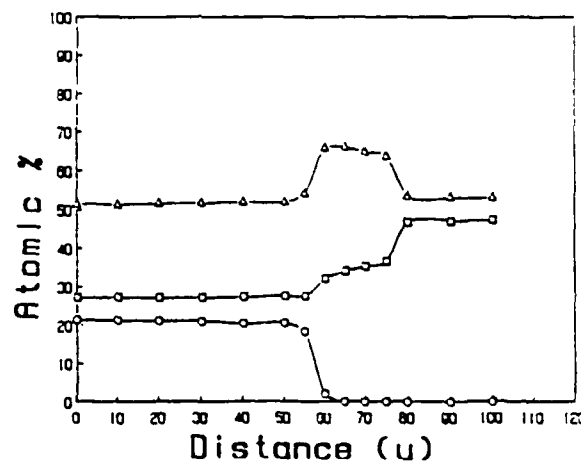


Figure 17 Cross-sectional view of a $\beta(\text{Ti}_{78}\text{Ta}_{22})/\gamma$ diffusion couple and the corresponding composition profile after annealing at 1100°C for 50 hrs.

24 hrs



28 hrs



50 hrs

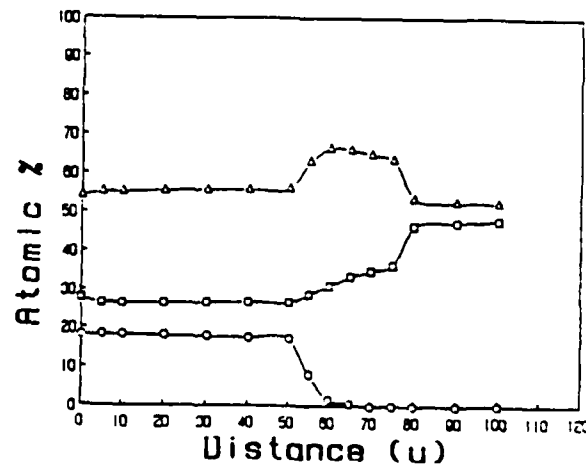


Figure 18 Summary of the interdiffusion behavior for a $\beta(\text{Ti}_{78}\text{Ta}_{22})/\gamma$ diffusion couple.

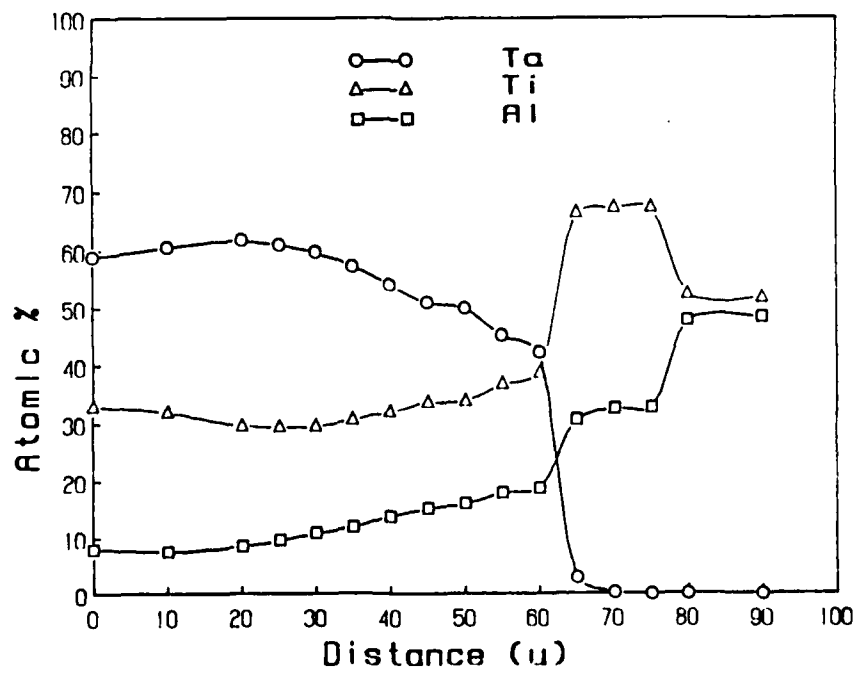
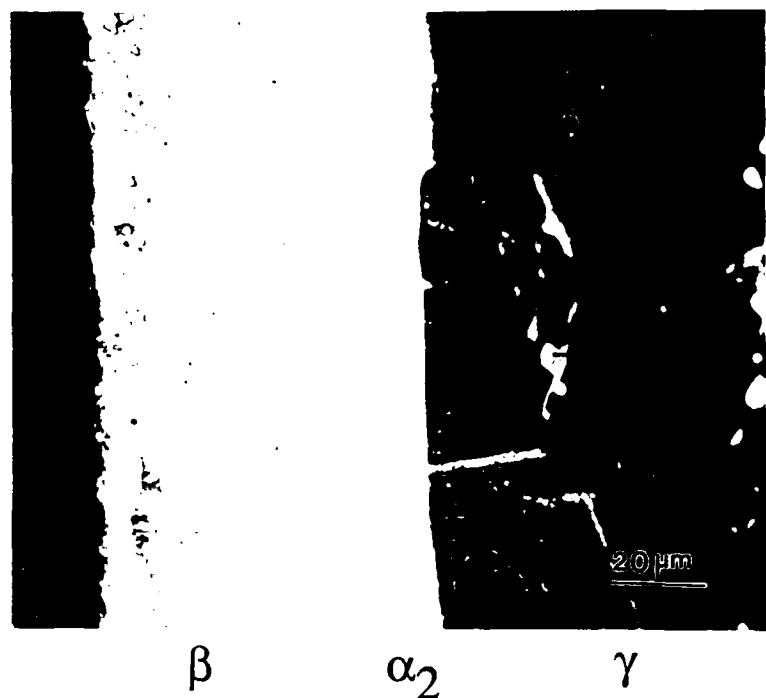
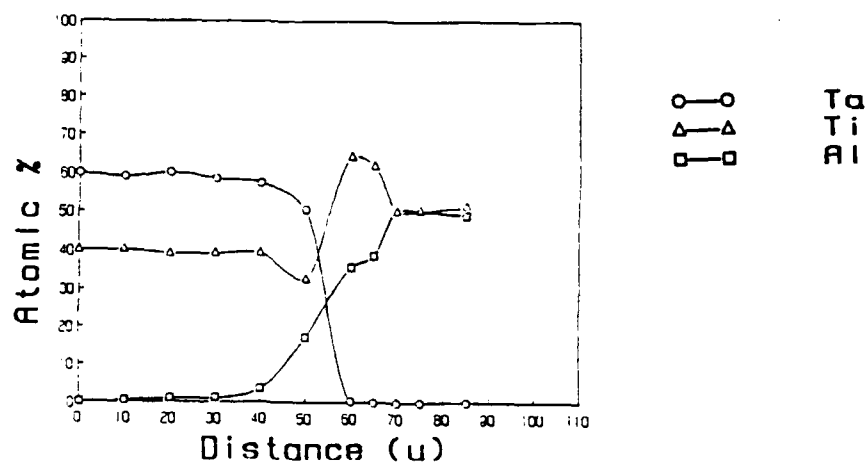
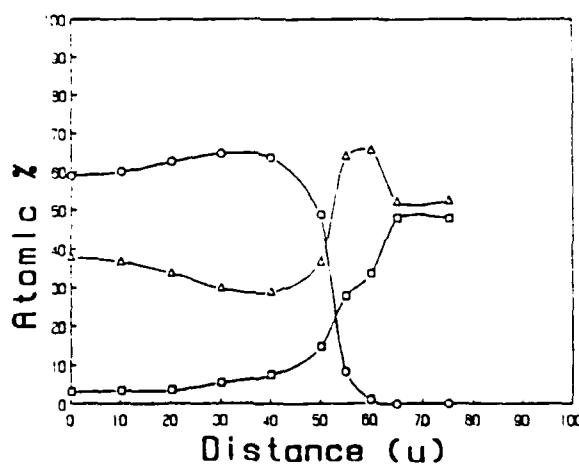


Figure 19 Cross-sectional view of a $\beta(\text{Ti}_{40}\text{Ta}_{60})/\gamma$ diffusion couple and the corresponding composition profile after annealing at 1100°C for 90 hrs.

24 hrs



65 hrs



90 hrs

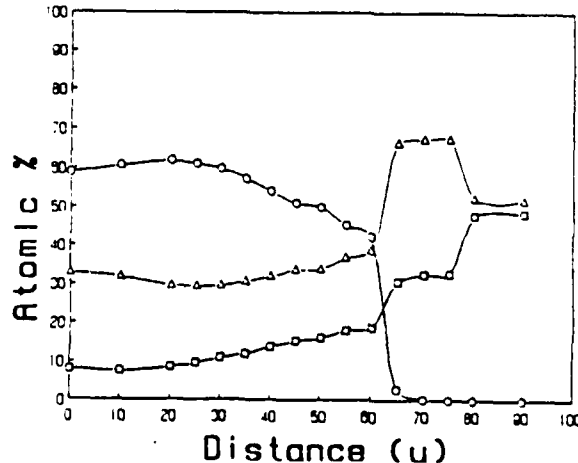
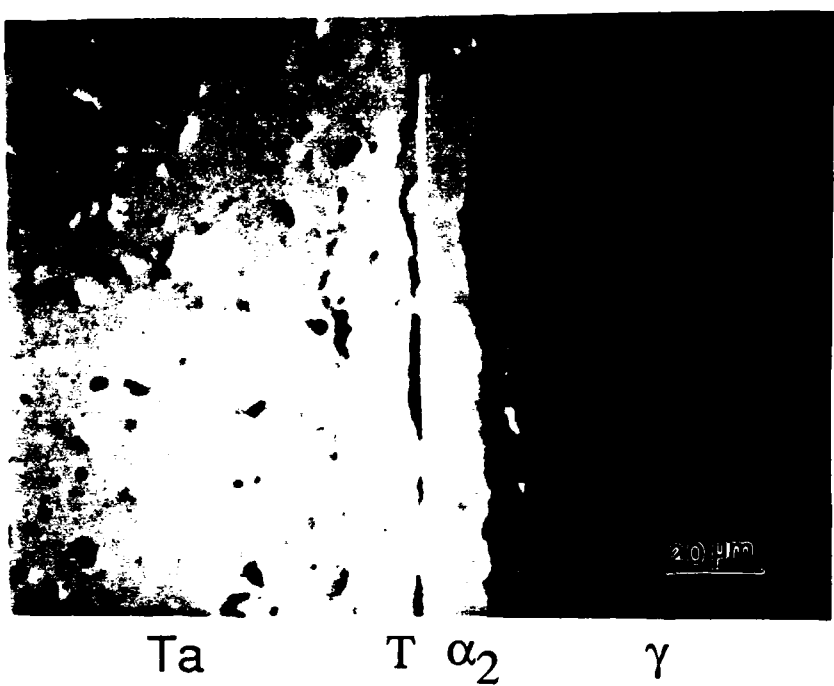


Figure 20 Summary of the interdiffusion behavior for a β (Ti₄₀Ta₆₀)/ γ diffusion couple.



Ta T α_2 γ

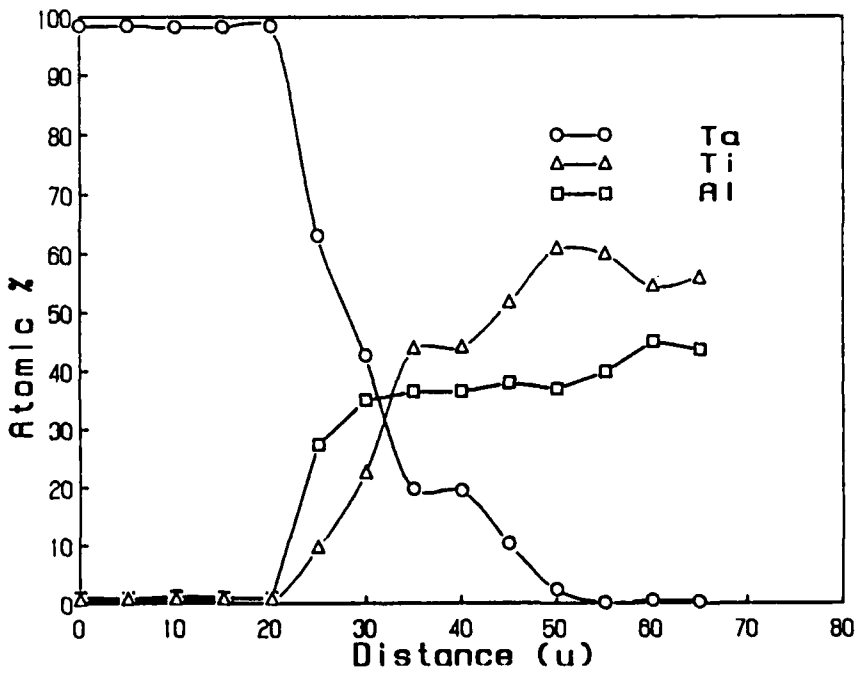


Figure 21 Cross-sectional view of a T_a/γ diffusion couple and the associated composition profile after annealing at 1100°C for 100 hrs.

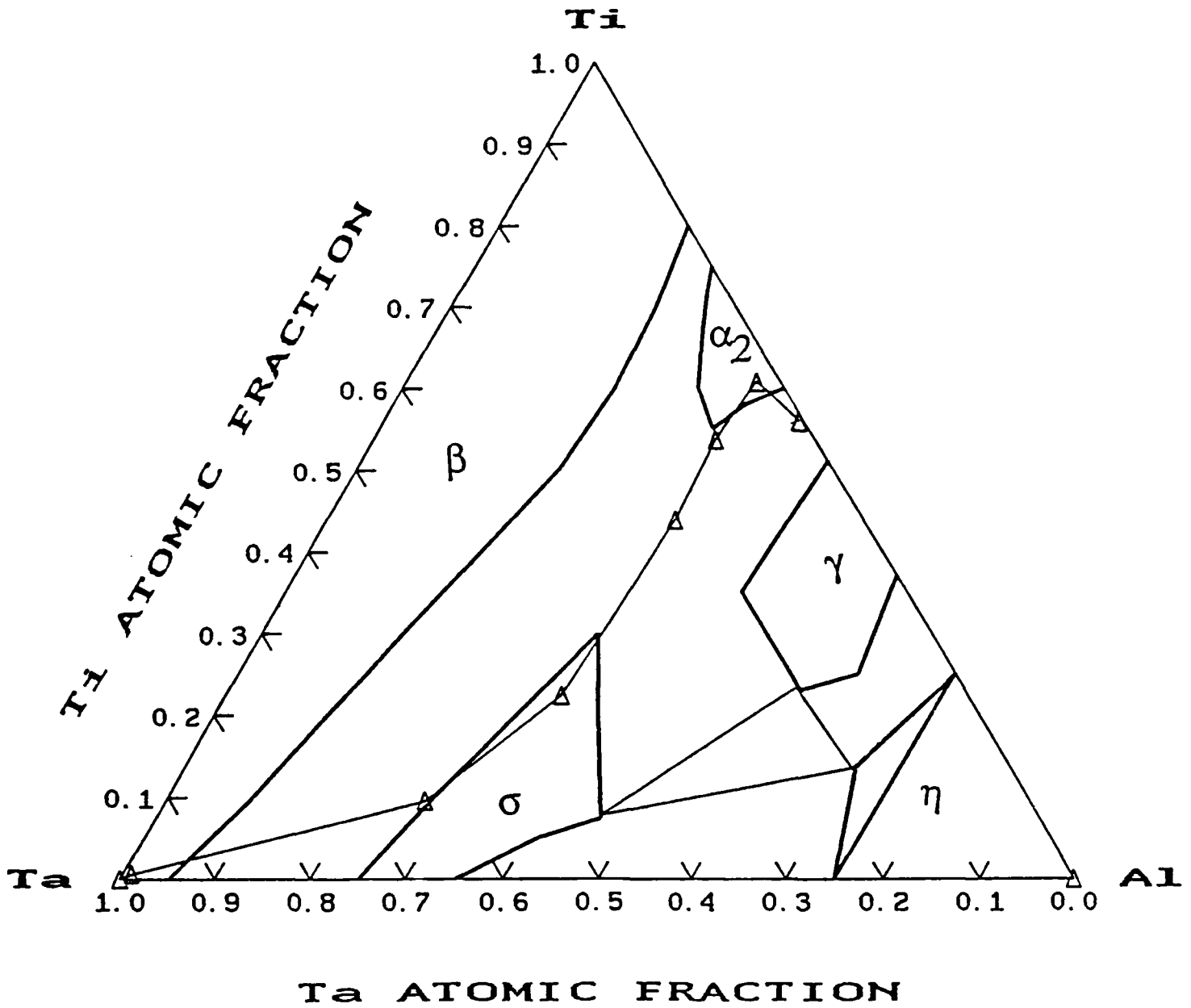


Figure 22 Diffusion path of a Ta/γ diffusion couple annealed at 1100°C for 100 hrs.

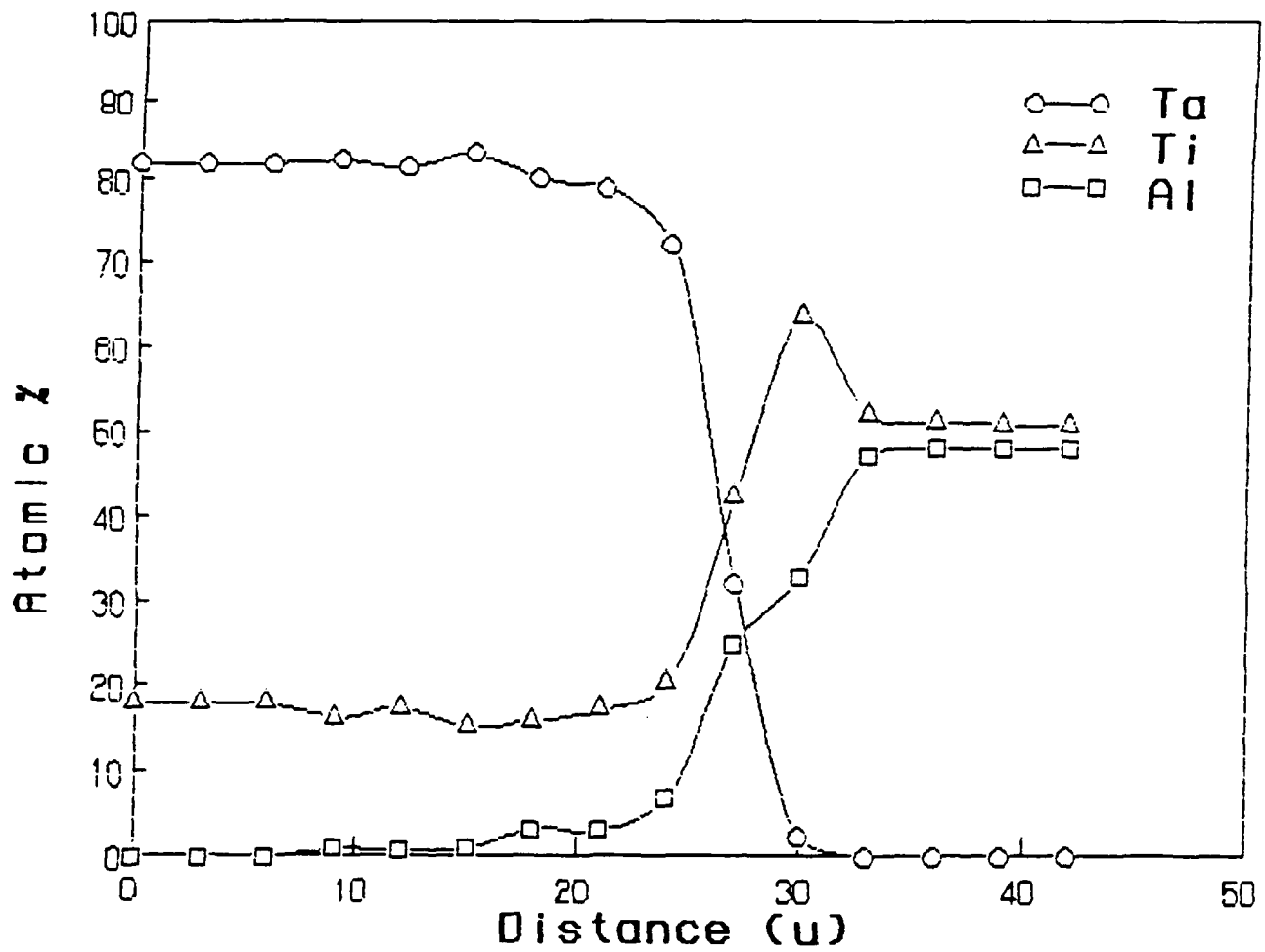


Figure 23 Composition profile for a $(\text{Ta}_{82}\text{Ti}_{18})/\gamma$ couple annealed at 1100°C for 2 hrs.

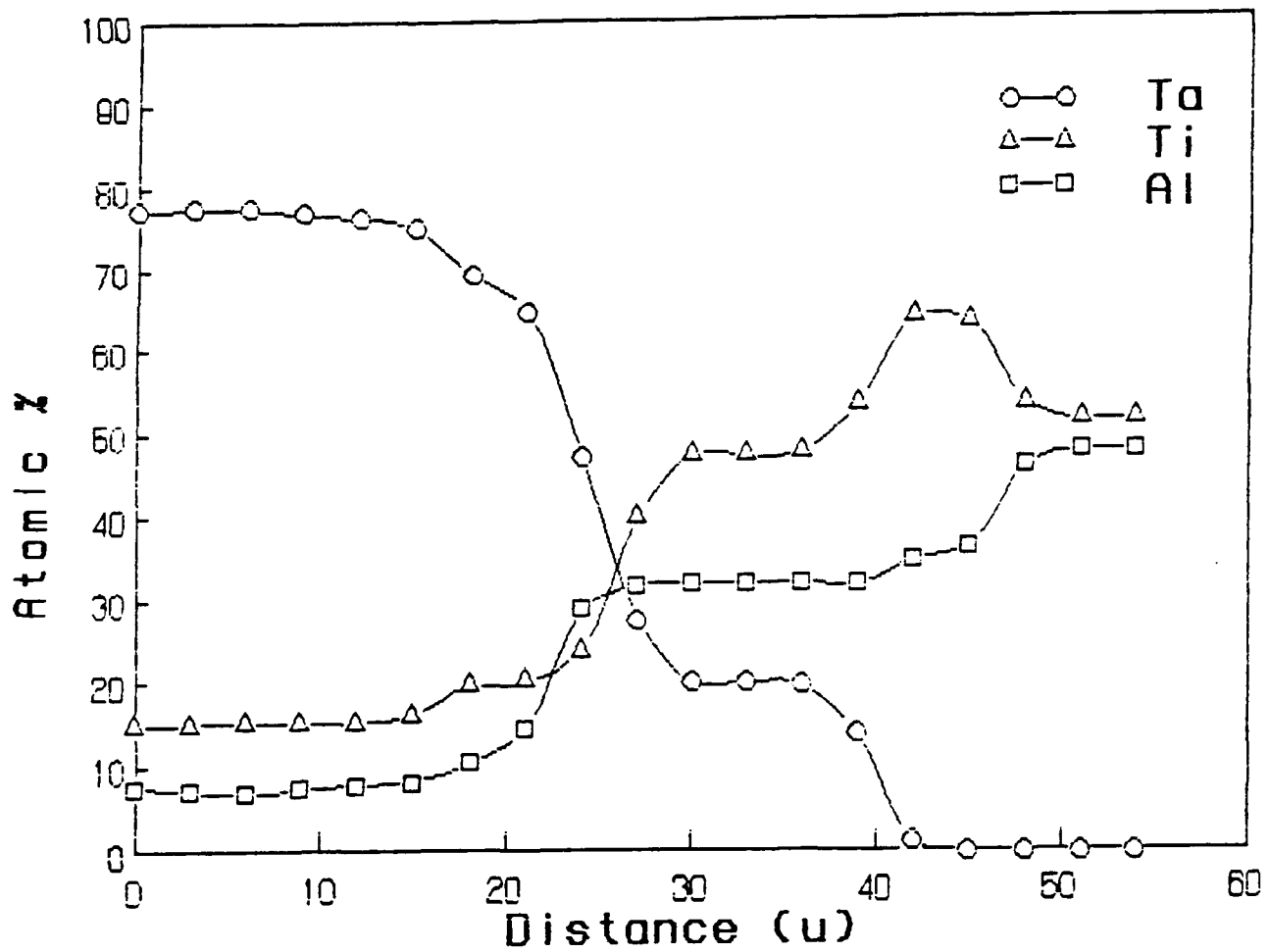


Figure 24 Composition profile for a $(\text{Ta}_{82}\text{Ti}_{18})/\gamma$ couple annealed at 1100°C for 48 hours.

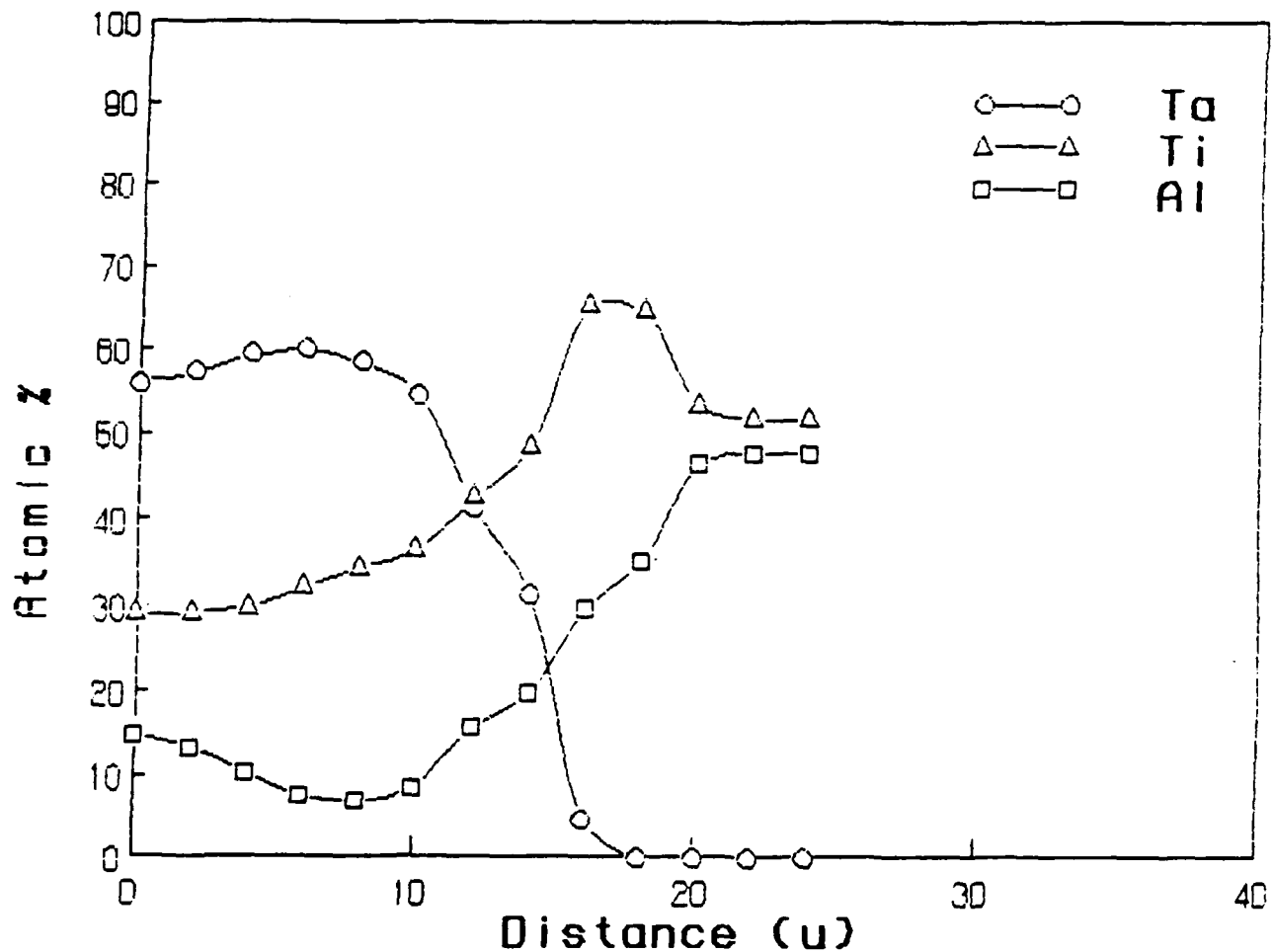


Figure 25 Composition profile for a $(\text{Ta}_{55}\text{Ti}_{45})/\gamma$ couple annealed at 1100°C for 1 hr.

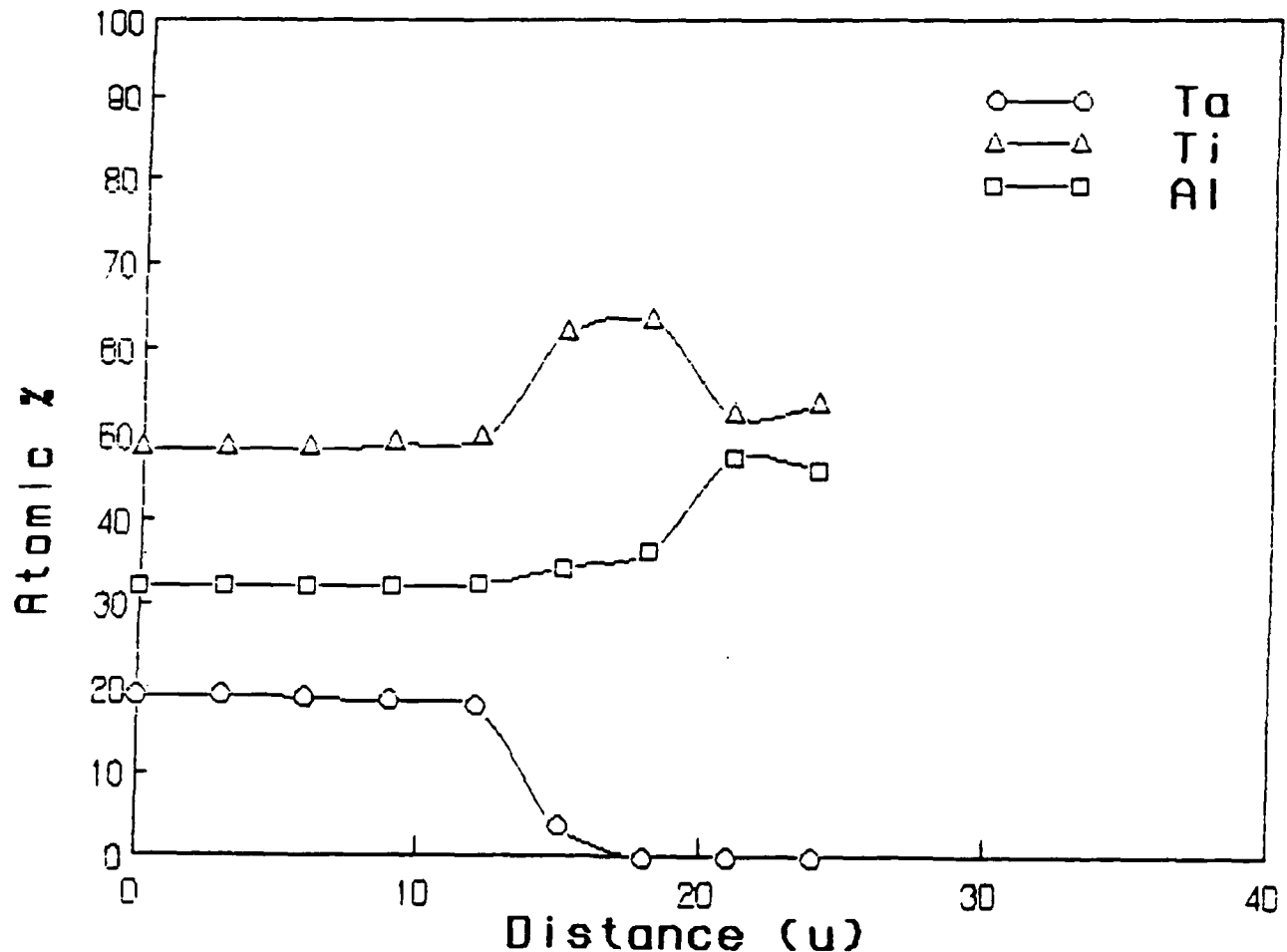


Figure 26 Composition profile for a $(\text{Ta}_{55}\text{Ti}_{45})/\gamma$ couple annealed at 1100°C for 48 hrs.

Matano Analysis

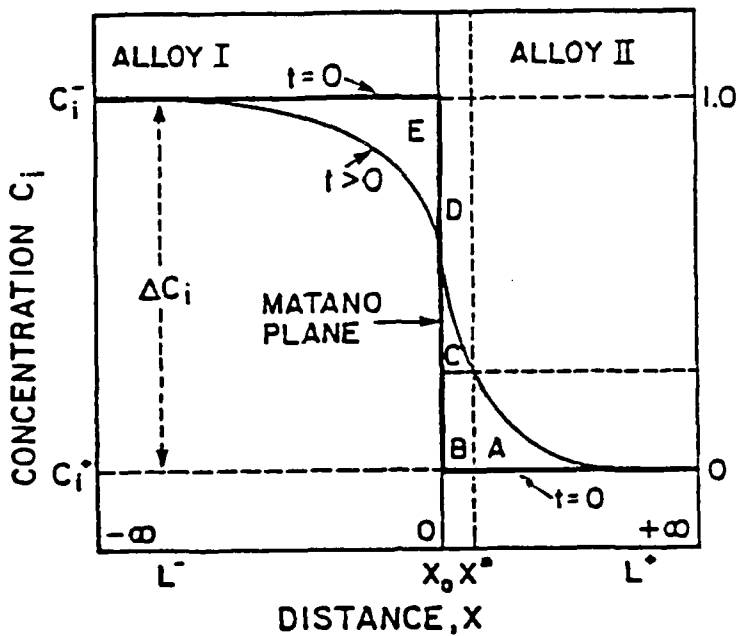


Figure 27 Schematic illustration of the basis of the Matano analysis in which an equal area construction is used to establish the Matano plane.

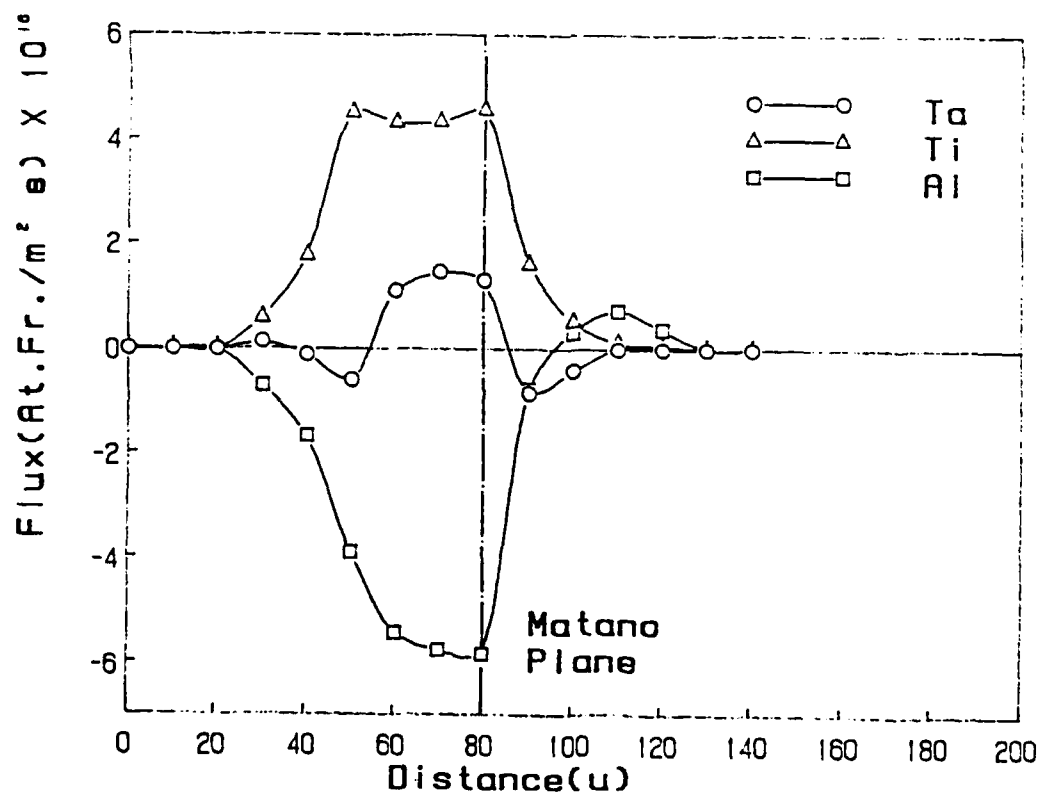
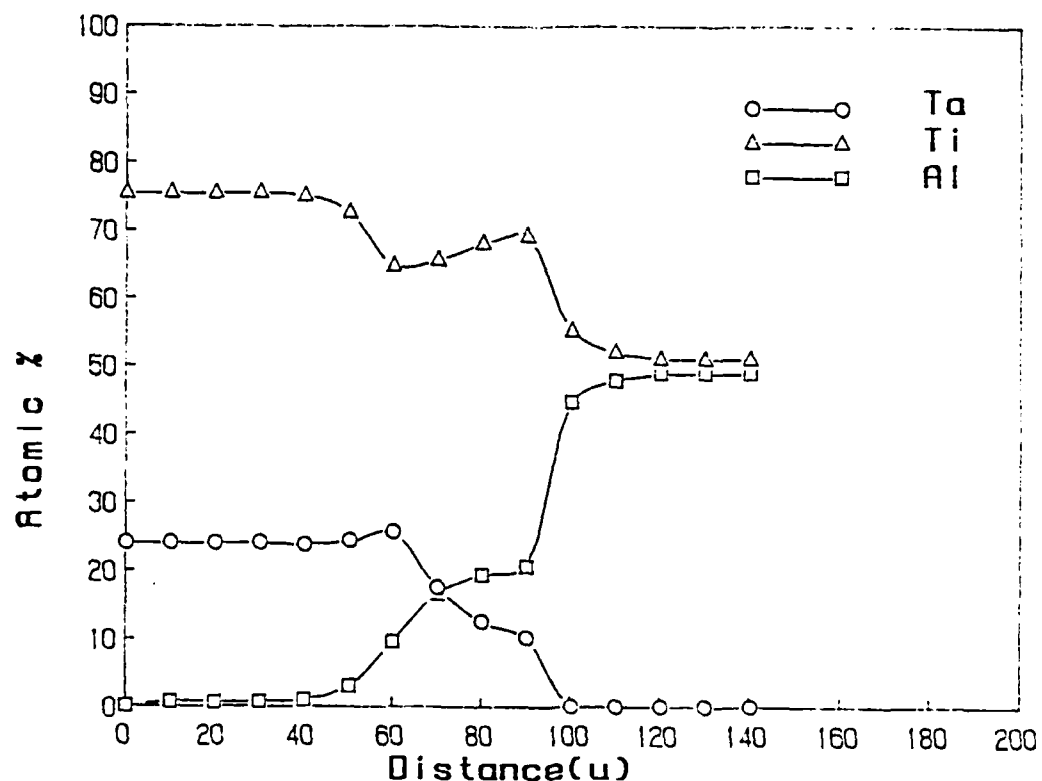


Figure 28 Composition profile and Matano analysis of component fluxes for a $\beta(\text{Ta}_{24}\text{Ti}_{76})/\gamma$ couple annealed at 1100°C for 1 hr.

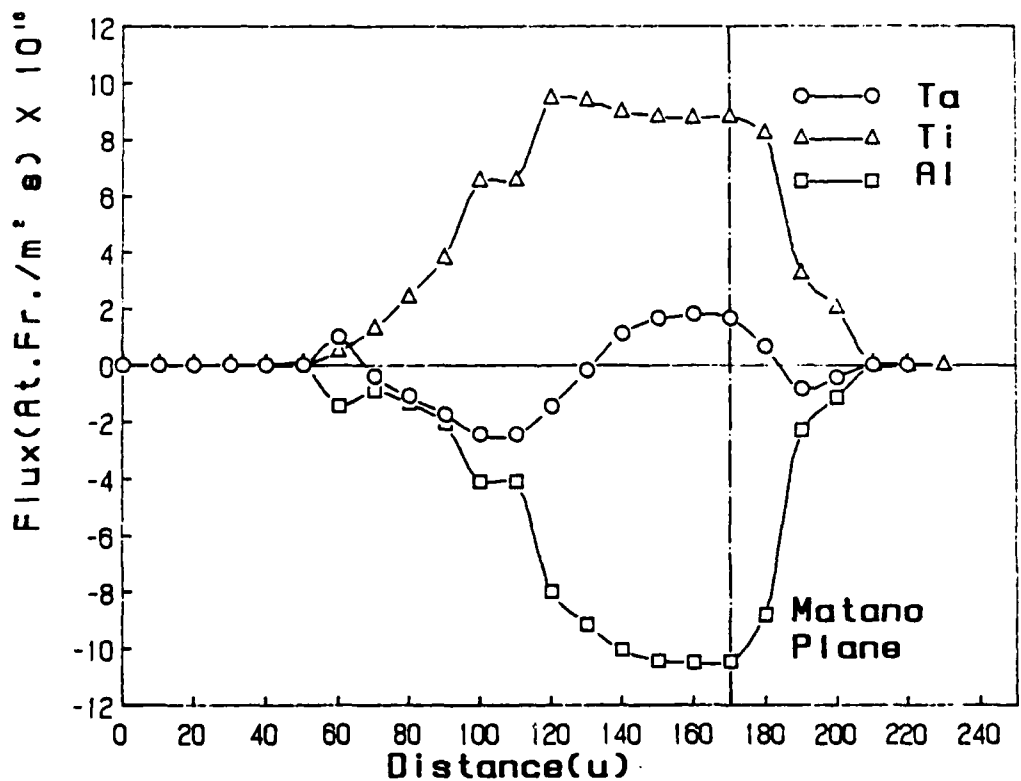
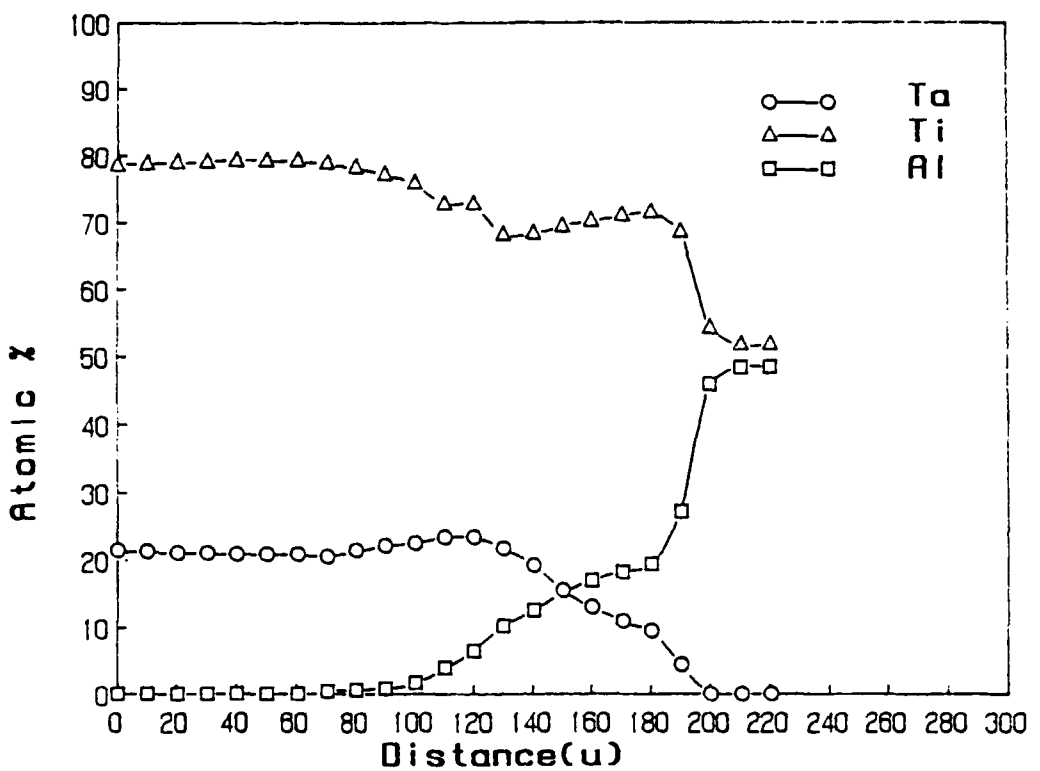


Figure 29 Composition profile and Matano analysis of component fluxes for a $\beta(\text{Ta}_{28}\text{Ti}_{72})/\gamma$ couple annealed at 1100°C for 1 hr.

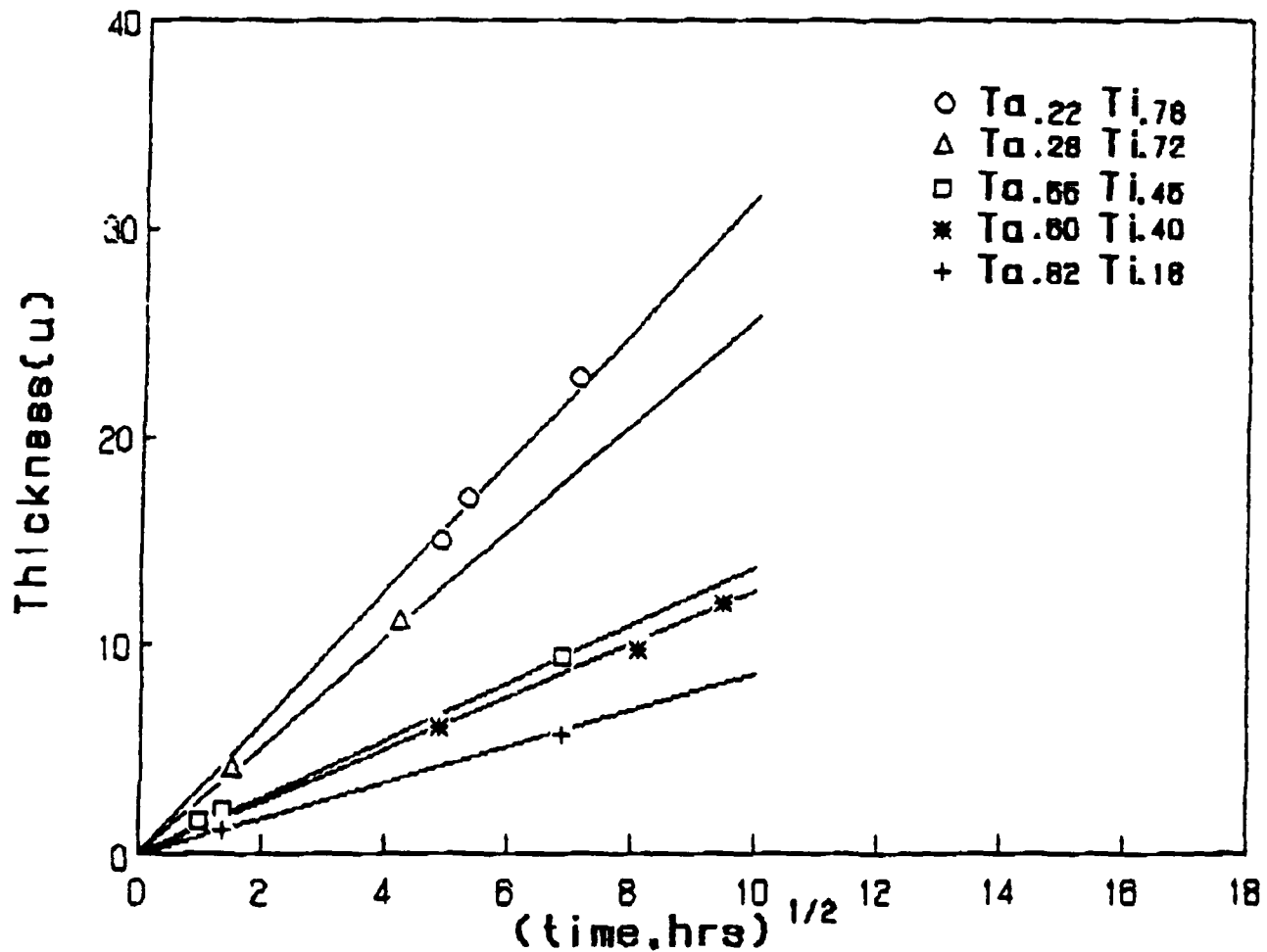


Figure 30 Summary of α_2 layer growth kinetics in several $\beta(\text{Ta}_{1-x}\text{Ti}_x)/\gamma$ diffusion couples.

COMBINED MODE I - MODE III FRACTURE TOUGHNESS OF ALUMINA PARTICULATE-REINFORCED ALUMINUM ALLOY-MATRIX COMPOSITES

S.V. Kamat*, J.P. Hirth* and R. Mehrabian**

* Mechanical and Materials Engineering Dept.
Washington State University, Pullman, WA 99164** Materials Department
University of California, Santa Barbara, CA 99231

(Received February 8, 1989)

Introduction

The relatively lower costs for fabrication and secondary processing of particulate-reinforced aluminum alloy matrix composites has made them attractive for certain aerospace applications where the very high strengths and elastic moduli offered by continuous fiber-reinforced aluminum alloy-matrix composites may not be required. The role of microstructural parameters on fracture toughness and tensile properties in such composites has been discussed in a previous paper (1). However, more often than not, practical structures are subjected to combined mode loading, which necessitates the study of crack initiation under such conditions. The objective of this paper is to determine how mode III loading superimposed on mode I, an example among several mixed-mode possibilities, affects the fracture toughness and failure mechanisms in alumina particulate-reinforced aluminum alloy-matrix composites.

There is a paucity of experimental data describing fracture under combined mode I - mode III loading conditions for any type of material let alone particulate-reinforced metal-matrix composites. Most investigators have reported (2-5) that an imposed mode III load contribution lowers the mode I component required to initiate fracture. However, Pook (6) found that mode I fracture toughness was independent of transverse shear for several high strength alloys and that fracture occurs when the resolved mode I component equals K_{Ic} . Recent investigations (7,8) have established that combined mode I - mode III behavior in steels could be characterized into two groups. In ductile steels, a mode III loading component seems to have a significant influence on the mode I fracture toughness whereas in relatively brittle steels the mode III component has very little influence on mode I fracture toughness. Thus it would be interesting to observe whether alumina particulate-reinforced aluminum alloy-matrix composites, which exhibit only a limited macroscopic ductility, follow a similar trend under combined mode I - mode III loading conditions.

Experimental Procedure

Mode I and combined mode I - mode III fracture toughness tests were performed on the composites listed in Table I with the matrices in the O condition and with nominally equiaxed particles as discussed in earlier work (9,10). The mode I and combined mode I - mode III specimen designs are illustrated in figures 1 and 2, respectively. The mode I specimen design is based on the standard compact tension design recommended by ASTM E-399 (11). The essential modification of the combined mode I - mode II design compared to the standard compact tension design is the slanted notch oriented at 45° to the load line, which causes the crack plane to adopt this slanted orientation at the onset of

crack initiation. The 45° angle was chosen because it results in equal amounts of mode I and mode III loading components. The w/B ratio in both the specimen designs is 6.4, which does not satisfy the recommended $2 \leq w/B \leq 4$, but is an acceptable alternative when the thickness of the as-received material is small.

For the combined mode I - mode III specimens, it was observed experimentally that the fatigue pre-cracks did not follow the initial slanted notch, and hence for consistency all the specimens, including the pure mode I specimens, were pre-cracked by means of electron discharge machining (EDM). Comparative tests with prefatigued and EDM notched mode I specimens gave identical results indicating that the EDM notch root was less than the process zone size. The specimens were pulled at a constant crosshead velocity of 10 $\mu\text{m/s}$ in a MTS servohydraulic testing machine and the load versus load-line displacement recorded. For a few combined mode specimens, the loading was interrupted at fixed intervals to measure the displacements normal to the load line (horizontal displacements) across the mouth of the specimens. The measurements correlated well with continuous measurements and final displacement measurements and hence the rest of the combined mode I - mode III tests were carried out continuously. The fracture surfaces of all the broken compact tension specimens were examined under a scanning electron microscope.

Results and Discussion

Mode I Stress Intensity Factor

The mode I stress intensity factor analysis was done according to ASTM E-399 (11). K_{IQ} was calculated by means of the following relationship:

$$K_{IQ} = (P_Q/B w^{1/2}) f(a/w) \quad (1)$$

The calculated values of K_{IQ} are listed in Table II. Each value listed is an average of two readings with a spread in the total data of 1.5 percent. For most cases, the K_{IQ} obtained satisfies the condition for the applicability of LEFM but does not satisfy the condition for plane strain. Thus, the stress intensity factors obtained here are meaningful fracture toughness parameters but not valid plane strain fracture toughnesses.

Combined Mode I - Mode III Stress Intensity Factor

There is no standard procedure for analyzing combined mode I - mode III data. In this investigation we have chosen to do the analysis using the resolution method. This method involves resolving the loads and the displacements into mode I and mode III components. From the geometry of figure 3, one can write:

$$P_I = P \sin\theta, \quad P_{III} = P \cos\theta \quad (2)$$

and,

$$\delta_I = \delta_v \sin\theta - \delta_h \cos\theta, \quad \delta_{III} = \delta_v \cos\theta + \delta_h \sin\theta \quad (3)$$

where δ_v is the measured vertical displacement or displacement parallel to the load line and δ_h is the measured horizontal displacement or displacement normal to the load line. It was experimentally found that $\delta_h = 0$ which reduces equation (3) to

$$\delta_I = \delta_v \sin\theta, \quad \delta_{III} = \delta_v \cos\theta \quad (4)$$

Representative P_I versus δ_I and P_{III} versus δ_{III} plots are shown in fig. 4. They are identical because θ was = 45° in this investigation, which results in P_{iQ} being equal to P_{iiiQ} . The resolved mode I stress intensity factor, K_{iQ} , was then calculated analogous to ASTM E-399 (11) by means of the following relationship:

$$K_{iQ} = (P_{iQ}/B' w^{1/2}) f_I(a/w) \quad (8)$$

where $B' = B/\sin\theta$. This is because the slanted crack makes the effective thickness of the crack plane larger than the specimen thickness.

A similar type of analysis could be used to calculate the resolved mode III stress intensity factor, K_{iiiQ} , with K_{iiiQ} given by:

$$K_{iiiQ} = (P_{iiiQ}/B' w^{1/2}) f_{III}(a/w) \quad (9)$$

However, the problem is that there are no explicit solutions available for $f_{III}(a/w)$, for compact tension specimens loaded in mode III conditions. This problem was solved by finding the ratio of the stress intensity factors under mode III and mode I conditions for a geometry, illustrated in figure 5, which approximates closest to a compact tension geometry and assuming that the same ratio holds true for the compact tension case. The ratio K_{iii} / K_i was calculated for the above geometry using the stress intensity factors given in ref. 12 and was found to be equal to 0.833. Thus

$$K_{iiiQ} = 0.833 K_{iQ} \quad (10)$$

The values of K_{iQ} and K_{iiiQ} so obtained are listed in Table II along with the value of the total stress intensity factor for the combined mode case, K_{totalQ} , which was calculated by means of the following relationship:

$$K_{totalQ}^2 = K_{iQ}^2 + K_{iiiQ}^2 / (1 - \nu) \quad (11)$$

Each value listed is an average of two readings with a spread in the total data of 1.5 percent.

Effect of Crack Angle on Fracture Parameters

Figure 6 a) and b) show the bar graphs of K_{iQ} and K_{totalQ} for the two crack angles, respectively. K_{totalQ} and K_{iQ} are identical for the pure mode I case. The imposed mode III loading component slightly lowered the mode I stress intensity factor required for crack initiation, however, the total stress intensity factor was higher in the combined mode I - mode III case as compared to the mode I case. This implied that the crack initiation was more difficult in the combined mode I - mode III orientation as compared to the mode I orientation. This result was consistent with the macroscopic observation of crack rotation towards mode orientation immediately following crack initiation. The observation of fracture surfaces of both the mode I and combined mode I - mode III compact tension specimens under the SEM revealed essentially the same general features as shown in figure 7. The combined mode I - mode III specimen fracture surfaces did not show any voids elongated in the shear (mode III) direction. All of the above observations tend to indicate that the fracture in such composites was mainly governed by tensile (mode I) stresses and not by mode III shear. Thus, it appears that there is no apparent change in the failure mechanism in such composites with the introduction of a mode III loading component. These observations are consistent with the results reported by other investigators (7,8,12,13) for other materials exhibiting limited ductility. The higher value of K_{totalQ} in combined mode I - mode III loading compared to K_{iQ} also suggested that in alumina-particulate reinforced aluminum alloy-matrix composites, at least for the combined mode I - mode III loading, K_{Ic} may be a good conservative estimate of the fracture toughness for design purposes.

Conclusion

- 1) The imposed mode III loading component slightly lowered the mode I stress intensity factor required for crack initiation. However, crack initiation was more difficult in the combined mode I - mode III case as compared to the pure mode I case as reflected by the higher total stress intensity factor at crack initiation.
- 2) There was no apparent change in the failure mechanism with the introduction of the mode III loading component. Mode III shear did not play a significant role in the failure process which was mostly influenced by mode I tensile stresses.

Acknowledgement

This research was supported by the DARPA University Research Initiative at the University of California, Santa Barbara, under ONR Contract No. N00014 - 86 - K - 0753.

References

1. S.V. Kamat, J.P. Hirth, and R. Mehrabian, Submitted for publication.

2. R.C. Shah, ASTM STP 560, p. 29, (1974).
3. Y. Ueda, K. Ikeda, T. Yao, and M. Aoki, Eng. Fract. Mech. 18, p. 1131, (1983).
4. W.K. Wilson, Westinghouse Research Report, (1969).
5. J.G. Schroth, J.P. Hirth, R.G. Hoagland, and A.R. Rosenfield, Metall. Trans. 18A, p. 1061, (1987).
6. L.P. Pook, Eng. Fract. Mech. 3, p. 205, (1971).
7. M. Manoharan, Ph.D Thesis, Ohio State University, (1988).
8. S. Raghavachary, Ph.D Thesis, Ohio State University, (1988).
9. F.M. Hosking, F. Folgar Portillo, R. Wunderlin, and R. Mehrabian, J. of Mater. Sci. 17, p. 1105, (1982).
10. C.G. Levi, G.J. Abbaschian, and R. Mehrabian, Metall. Trans. 9A, p. 697, (1978).
11. ASTM Annual Book of Standards, Am. Soc. Test. Mat., E-399, p. 680, (1987).
12. A.R. Rosenfield and W.H. Duckworth, Int. J. of Fract. 32, p. R59, (1987).
13. S. Suresh and E.K. Tscheegg, J. Am. Cer. Soc. 70, p. 726, (1987).

Table I. Alumina particulate size D and volume fraction f for Composites Investigated

Matrix	D (μm)	f	Matrix	D (μm)	f
2014	5	0.02	2024	5	0.02
2014	5	0.05	2024	5	0.05
2014	15	0.05	2024	5	0.20
			2024	50	0.20

Table II. Mode I and combined mode I - mode III fracture toughness of the composites in the O condition

Composite Matrix	D μm	f	Mode I K		Combined Mode I - Mode III K	
			K _{IQ} MPa ^{1/2} m ⁻¹	K _{iIQ} MPa ^{1/2} m ⁻¹	K _{IIIQ} MPa ^{1/2} m ⁻¹	K _{totalQ} MPa ^{1/2} m ⁻¹
(A) 2014	5	0.02	14.6	12.8	10.7	18.1
(B) 2014	5	0.05	13.5	11.5	9.6	16.2
(C) 2014	15	0.05	13.9	11.9	9.9	16.7
(D) 2024	5	0.02	16.5	13.2	11.0	18.6
(E) 2024	5	0.05	15.8	11.8	9.8	16.7
(F) 2024	5	0.20	12.2	9.3	7.7	13.1
(G) 2024	50	0.20	13.2	10.0	8.3	14.1

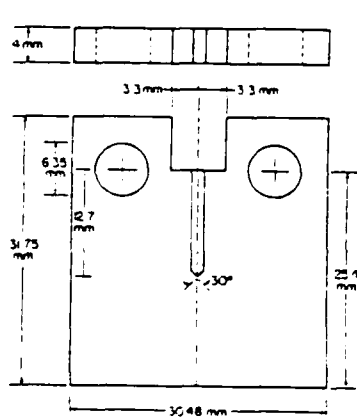


FIG. 1. Mode I compact tension specimen design.

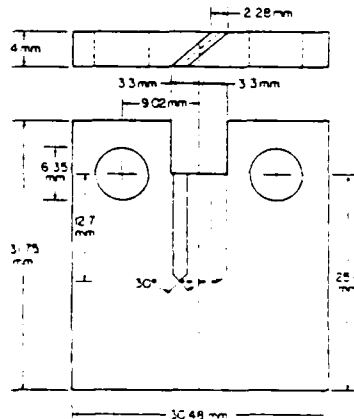


FIG. 2. Combined Mode I - Mode III compact tension specimen design.

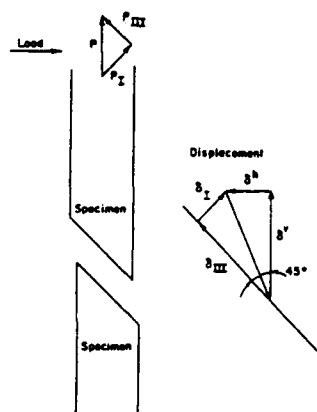


FIG. 3. Resolution of load and displacement into mode I and mode III components

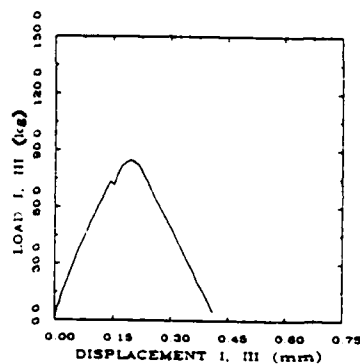
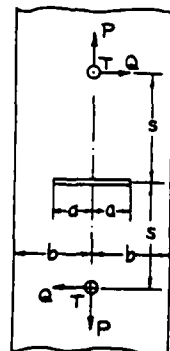


FIG. 4. Representative resolved load versus resolved displacement plots.

Figure 5. Geometry used for calculating K_{III}/K_I .

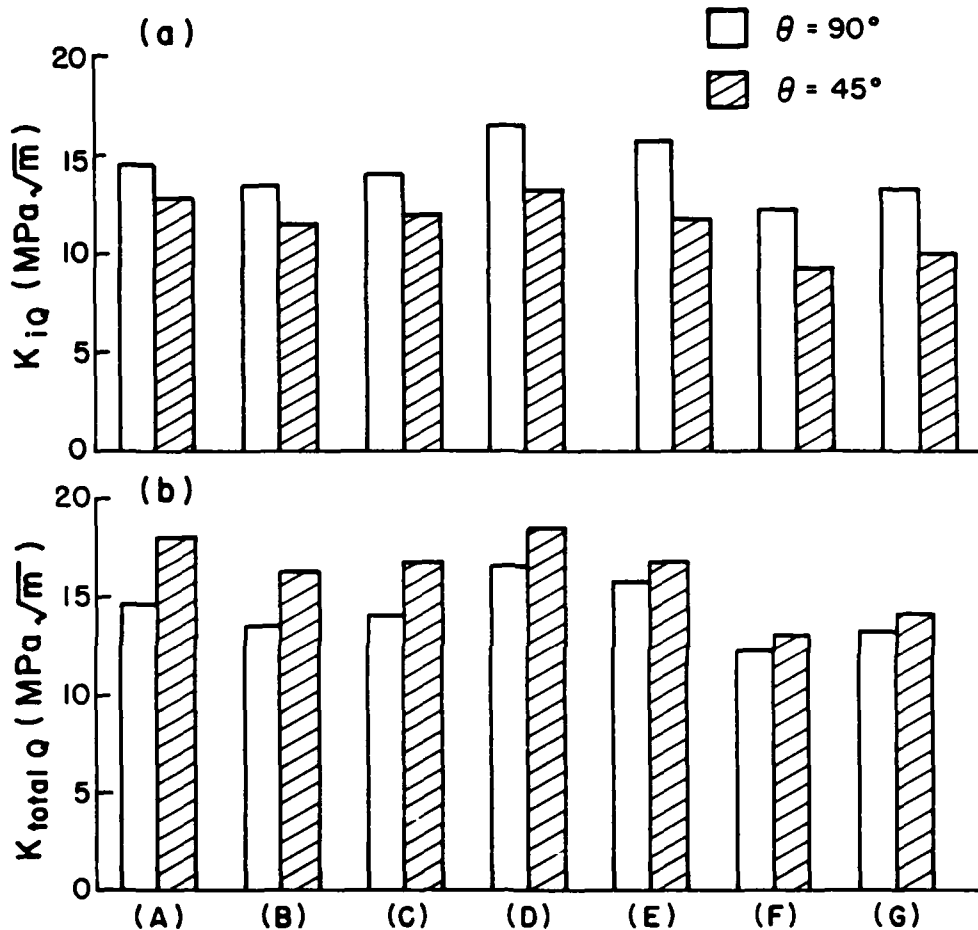


FIG. 6. Bar graphs illustrating a) mode I stress intensity factors and b) total stress intensity factors, for the two crack angles for all the composites investigated.

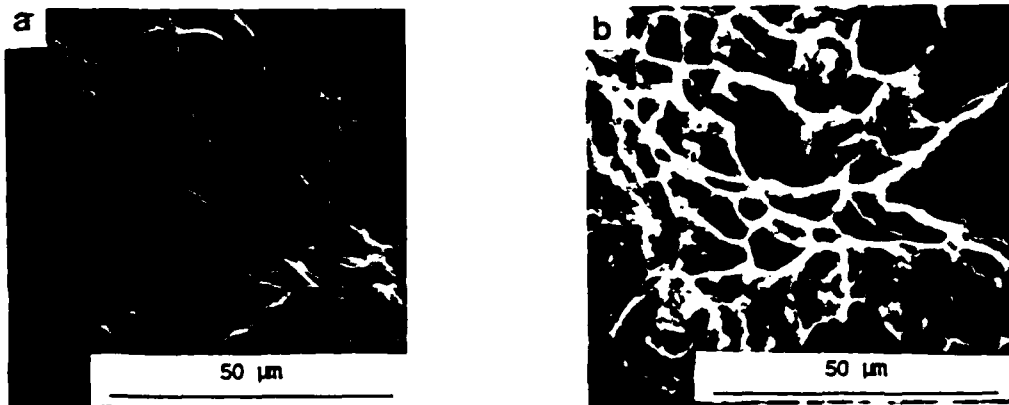


FIG. 7. SEM micrographs showing the general fracture surface features for a) mode I case and b) combined mode I - mode III case.